FATIGUE BEHAVIOR AND XFEM BASED LIFE PREDICTION OF TUBULAR X-JOINTS WITH CONCRETE FILLED CHORD

KITTIKUN JITPAIROD

(***B. Eng.*** **(*Hons*), *Chiang Mai University*)**

A THESIS SUBMITTED FOR

THE DEGREE OF DOCTOR OF PHILOSOPHY

DEPARTMENT OF CIVIL AND ENVIRONMENTAL ENGINEERING

NATIONAL UNIVERSITY OF SINGAPORE

2015

DECLARATION

I hereby declare that this thesis is my original work and it has been written by me in its entirety. I have duly acknowledged all the sources of information which have been used in the thesis.

This thesis has also not been submitted for any degree in any university previously.

Kittikun Jitpairod

20 February 2016

ACKNOWLEDGEMENT

The research work reported in this thesis has been carried out at the Department of Civil and Environmental Engineering, National University of Singapore.

I wish to express my deepest gratitude to my supervisor Professor Somsak Swaddiwudhipong and co-supervisor Associate Professor Qian Xudong, for their supports and guidance through my study in NUS. Their patience and support helped me overcome many tough situations. Thank you for commenting, thoroughly reading and countless revising of my thesis.

Very special thanks go to Professor Choo Yoo Sang and Dr. Kuang Sze Chiang, for their meaningful comments and advices.

It is my privilege to thanks teacher Udom Chatsirikul who encouraged me to come to NUS.

I thank my helpful, cheerful, and joyful friends and colleagues Dr. Yuthdanai Petchdemaneengam, Mr. Mochamad Raditya Pradana, Dr. Xiangbo Liu, Dr. Wah Yi Feng, Dr. Yeoh Ker-Wei, Dr. Harrif Santo, Dr. Zheng Jiexing and Dr. Abraham Christian. Thanks for the wonderful time and fun we have had during the last 5 years.

I would also like to thank all CEE administrative staffs and NUS structural lab staffs.

Sincerely thanks are expressed to the research scholarship provided by the National University of Singapore.

Lastly, the encouragement and best wishes from my parents, brother, and teachers are appreciated.

TABLE OF CONTENTS

SUMMARY

In welded circular hollow section (CHS) structures, fatigue cracks most likely initiate along the weld toe due to high stress concentration. Many approaches have been introduced to enhanced fatigue performance of these structures. Concrete grouting is one of the economic and promising methods to strengthen hollow structures and ultimately reduces overall stress of the welded sections. Another interesting method is to create smooth transition between the weld and the base materials. This method not only improves weld toe condition but also removes material defects. However, the benefits of these improvement methods are not well documented in design guidelines, and study on this topic is limited. This leads to a series of experimental investigation of fatigue performance of CHS X-joints with concrete-filled chord and post-weld toes grinding. Experimental program includes two CHS X-joints fabricated using the newly proposed full capacity tubular joint welds. The chord member of both specimens is filled with ultra-high performance concrete Densit Ducorit D4. The first X-joint is tested in as-welded condition, whereas chord weld toes of the second joint is burr-ground prior fatigue test. The post-weld toe grinding is performed strictly follow the International Institute of Welding (IIW) recommendation. The two CHS X-joints are subjected to constant-amplitude cyclic brace in-plane bending until the fatigue crack depth reaches 80% of wall thickness. Stress concentration factors along weld toes are calculated and cracks depth are measured by potential drop technique. The test results reveal satisfactory fatigue performance of both X-joints comparing with the existing design S-N curves. The test results also show that fatigue crack propagation life contributes to a significant portion of the total fatigue life which raises the importance of remaining fatigue crack propagation life prediction.

Extended finite element method (XFEM) is adopted in this thesis to study fatigue crack propagation and estimate remaining fatigue crack propagation life structures based on Paris' law. The study begins by evaluating accuracy and robustness of XFEM in terms of stress intensity factor (SIF) calculation. The SIF results from 3-dimensional

XFEM are compared against available closed form SIF solutions of compact tension (C(T)), and finite plate with semi-elliptic crack specimens. Important parameters, such as element size, enrichment region and crack location relative to mesh are taken into account. Finally, fatigue propagation life of finite plate with semi-elliptic crack specimens, and CHS X-joints are predicted. The results show that XFEM give reasonably accurate SIF results for all studied specimens with relatively course mesh. Moreover, remaining fatigue crack propagation life estimated from XFEM compare reasonably well to experimental results.

LIST OF TABLES

LIST OF FIGURES

NOMENCLATURE

A	Cross sectional area
C	Material constant in Paris equation
C_x, C_y	Contour integral size
E	Modulus of elasticity
E_c	Modulus of elasticity of concrete
$F(x)$	Asymptotic near-tip enrichment function
G	Energy release rate
H	Height of specimen
$H(x)$	Heaviside function
I	Area moment of inertia
K	Stress intensity factor
K_c	Fracture toughness
L	Distance between two points
M	Mesh size in contour integral region
M_b	Applied bending moment
N	Number of load cycles
P	Applied load
R	Load or stress ratio
S_c	Cross-crack probe spacing
SD	Standard deviation
S_r	Intact probe spacing
T	Traction stress
U	Potential energy
V_c	Cross-crack voltage
V_{c0}	Initial cross-crack voltage
V_r	Reference voltage
V_{r0}	Initial reference voltage

a	Crack depth
a_i	Enrichment nodal variable
a_0	Initial crack depth
b_i	Enrichment nodal variable
c	Half crack width
h	Overclosure of the contact pair
k	Thickness exponent for S-N curves
l'	Support span length of J2 series setup
M	Material constant in Paris equation
N	Set of elements in the entire finite element model
n_{cr}	Set of elements cut by crack
n_{tip}	Set of elements containing the crack tip
$\vec{\mathbf{n}}$	Unit normal vector
p	Contact pressure
r_y	Size of plastic zone
t	Thickness
t_{ref}	Reference thickness
t_{sh}	Time of concrete drying (day)
u^{ENR}	Enriched displacement field
u^{FE}	Displacement field
u_i	Nodal displacement variable
w_e	Strain energy density
(x, y, z)	Cartesian coordinate system
(u, v, w)	Displacement components in (x, y, z)
x^*	Closet point to the crack segment
x_c	Point on the discontinuity
δ	Crack tip opening displacement
δ_{ij}	Kronecker delta function

$\varepsilon_{hot-spot}$	Hot-spot strain
ε_{nom}	Nominal strain
κ	Constant for plane-stress or plane-strain condition (Kolosov constant)
μ	Shear modulus
μ_s	Static coefficient of friction
ν	Poisson's ratio
ρ	Local angle on the brace
σ	Stress
σ_{amp}	Applied stress amplitude
$\sigma_{hot-spot}$	Hot-spot stress
σ_{ij}	Stress tensor
σ_{mean}	Mean stress
σ_{nom}	Nominal stress
σ_{notch}	Notch stress
σ_{ref}	Reference stress
σ_u	Ultimate tensile strength of material
σ_Y	Yield strength of material
$\phi(x)$	Signed distance function describes the location of the crack face
$\psi(x)$	Signed distance function locates the crack tip or crack front
ψ	Local dihedral angle
$\Delta\sigma$	Cyclic stress range
Δa	Crack depth increment
ΔN	Crack propagation cycle increment
τ	Shear stress
$\aleph$	Electric field

CHAPTER 1

INTRODUCTION

1.1 A brief history of fatigue

In the last two centuries, a large number of mysterious failure phenomena of components of machines, vehicles and structures subjected to repeated loading have been recorded. These failures occur although the stress level is below material yield strength. This process of failure due to repeated loading was officially named as the fatigue failure in 1839. In the 1850s, the Versailles rail accident motivated August Wöhler to develop design strategies to avoid fatigue failure. Since that time, fatigue failure has become a major concern of engineering design.

1.2 Fatigue failure in offshore industry

In the offshore industry, fatigue failure is also a major concern since offshore structures are extensively subjected to repeated loading for their service life. The repeated loadings result from wind, wave, current, and operational loadings. Figure shows that 25% of structures in the North Sea are subjected to fatigue damage, which is the majority cause of damage. The causes outlined in Figure 1.2-1 can be designated as accidental damage. The notable disaster in the North Sea in 1980 was the failure of the semi-submersible drilling rig Alexander L. Kielland. Although the disaster was a consequence of several circumstances, the root cause was a fatigue crack in a small fillet

weld at the surface of brace member. This accident initiated a large research effort into fatigue in Norway and worldwide.

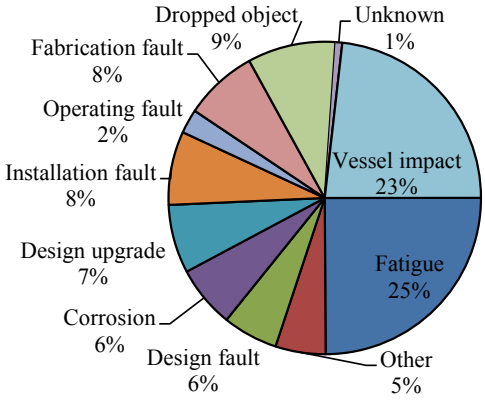

Figure 1.2-1: Causes of damage to North Sea during 1974-1992 (Jármai and Frakas, 1999)

1.3 Strengthening and repair of tubular offshore structures

The number of ageing offshore structures is increasing globally. A number of them remain in operation although they have exceeded their design life. This leads to the necessity of the strengthening and repair of existing structures. The strengthening and repair techniques are unique because of the different structural configurations, member sizes, joint details, and physical constraints of access to different water depths and different parts of the structure. The various grouted and mechanical repair techniques that have already been employed can be separated into three major groups; grouted clamp, grouted connection (double skin grouted joints) and infilled grouting as shown in Figure 1.3-1. Among the strengthening and repair techniques, the infilled grouting technique is the most convenient in construction and the most cost-effective. Some advantages of the infilled grouting technique are 1) full restored strength of the damaged section, 2) increased axial compressive strength of the member, 3) reduced stress concentration factor (SCF), 4) flexibility in water depth and 5) is being conveniently available.

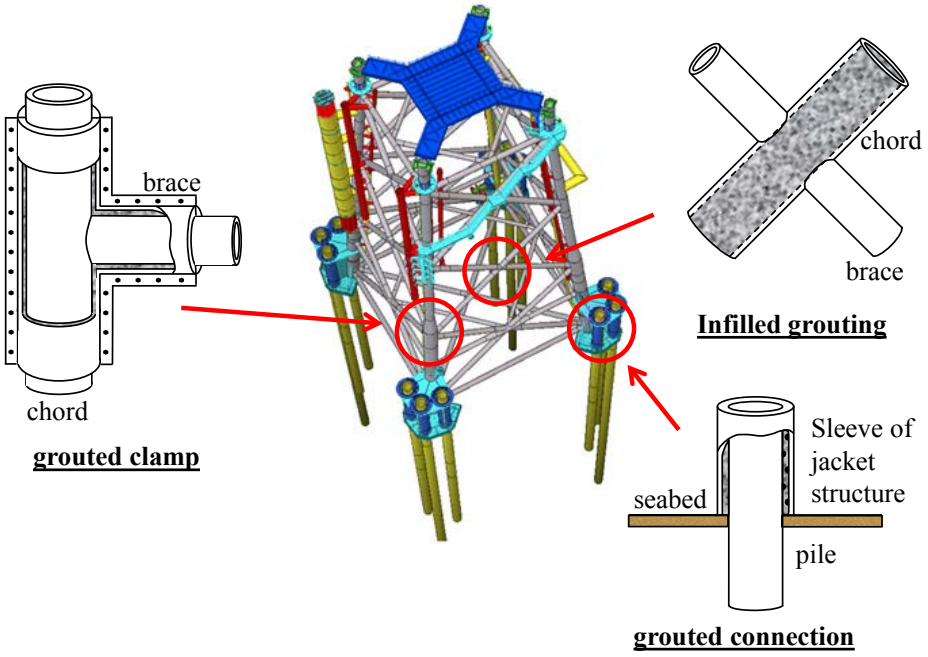

Figure 1.3-1: Example of strengthening and repair techniques

However, the use of grouting techniques is limited because of the shortage of fatigue design guidelines. For example, DNV (2011) recommends to treat the grouted joints as simple joints except that 1) original chord thickness is used to determine the stress concentration factors (SCFs) of the brace member and 2) the chord thickness is replaced by the equivalent chord thickness as shown in Equation 1.3-1 and Equation 1.3-2. Moreover, the same design S-N curves for ungrouted joints are recommended for grouted joints.

$$\text{Infilled grouting: } T_{eff} = T + 0.45T_{insert} \tag{1.3-1}$$

$$\text{Grouted connection: } T_{eff} = (5D + 134T)/144 \tag{1.3-2}$$

where, D and T are the chord diameter and thickness respectively, and

T_{eff} is the effective thickness, and T_{insert} is the thickness of the inserted pile.

1.4 Literature review

Concrete-filled steel sections have, over the recent years, become a popular approach to strengthen, reinforce and repair structural components on both onshore and offshore applications (Ellobody et al., 2006; Han et al., 2012; Harwood & Shuttleworth, 1998; Lohaus et al., 2013; Mao & Xiao, 2006; Patel et al., 2014; Valipour & Foster, 2010). Prior research work has led to the development of comprehensive design guidelines (British Standard Institute, 2004) for concrete-filled members focusing on their ultimate capacity under monotonic loading conditions. However, the fatigue failure of these concrete-filled structures, characterized by the initiation and propagation of fatigue cracks in critical structural components, may impose a potential threat to the safety of these structures experiencing cyclic loadings caused by environmental action, e.g., offshore structures, or traffic conditions, e.g., bridges. The fatigue assessment described in existing design guidelines, however, does not provide an explicit S-N curve for the concrete-filled welded tubular joints, essentially due to the lack of experimental data required for the development of such S-N curves.

The understanding on fatigue behavior of hollow section tubular joints has grown expansively over the last three decades, driven by extensive experimental work such as by the first and second phase of the United Kingdom Offshore Research Project (Failure Control Ltd. & Marine Technology Support Unit, 1999; UKOSRP-II Programme Steering Committee, 1987). Among the three types of S-N curves, namely the nominal stress S-N curve, the hot-spot stress S-N curve and the notch stress S-N curve, the hot-spot stress based S-N curve has evolved into a widely accepted and convenient approach which agrees closely with the experimental results (Chiew et al., 2004; Im et al., 2005). Recent developments by Dong and his team (Dong, 2005; Dong & Hong, 2012) have advanced into a validated, mesh-insensitive structural stress approach to calculate the hot-spot stresses near the weld toe of tubular joints. Dong's approach simplifies the procedure to calculate hot-spot stresses in contrast to the conventional extrapolation

method recommended in design guidelines (DNV, 2010), and bridges directly with the fracture mechanics assessment under mixed-mode conditions. Other experimentalists have recently uncovered some interesting findings on the fatigue performance of tubular joints. The fatigue tests on the welded tubular joints (Schumacher et al., 2009; Schumacher & Nussbaumer, 2006) have revealed the size effect on the estimated hot-spot stresses for tubular joints with large wall thicknesses. In contrast, Mashiri (2007) discuss the size effect on the fatigue life of thin-walled tubular joints with wall thickness less than 4 mm. Their study highlights that the conventional S-N approaches may lead to unsafe estimations on the fatigue life for thin-walled tubular joints. In line with the experimentally validated hot-spot stress S-N approach and the fracture mechanics based Paris method (Paris et al., 1961) to estimate the fatigue life of tubular joints, a number of recent research efforts (Ghanameh et al., 2004; Gho & Gao, 2004; Pang et al., 2009; Qian, 2009; Qian et al., 2005; Shao & Cao, 2005) have focused on developing reliable estimations of the stress concentration factors and the stress intensity factors for welded tubular joints. Barter et al. (2005) have examined the crack growth behavior for a multi-planar XX-joint. The growing crack size indicates a linear relationship with respect to the number of applied cycles in a log-log scale. In addition to the fatigue performance of tubular joints, a few other experimental works (Burdekin et al., 1988; Stacey et al., 1996; Talie-Faz et al., 2002) have ascertained the residual strength of circular hollow section (CHS) joints with a pre-existing surface-breaking or through-thickness crack, in an effort to deliver quantitative assessments on the static strength of cracked joints.

In contrast to the extensive work on the fatigue behavior of hollow section tubular joints, the public literature contains only limited studies on the fatigue performance of tubular connections with a concrete-filled chord member. Wang et al. (2013) have concluded, from an experimental investigation of eleven circular hollow section T-joints with a concrete-filled chord, that the presence of the concrete material within the chord member leads to significant reductions in the measured stress concentration factors near the weld toe and therefore enhances the fatigue performance compared to the corresponding hollow section joints. Mashiri and Zhao (2010) reported an ex-

perimental investigation on the fatigue of square hollow section (SHS) T-joints with a concrete-filled chord under cyclic in-plane bending actions. The concrete-filled SHS joints demonstrate improved fatigue strength compared to the hollow section SHS T-joints. Sakai et al. (2004) have reported an experimental study on three fatigue tests of the concrete-filled tubular K-joints and static tests for six concrete-filled and reinforced tubular K-joints. The presence of the normal strength concrete (with a 14-day compressive strength of 31 MPa) decreases significantly the stress concentration factors near the weld toes in the compression brace, but does not cause strong reductions of the SCF values near the weld toes of the tension brace.

More recently, Marshall et al. (2013) have proposed a new set of welding details, namely the full capacity tubular joint welds, also known as the welder-optimized complete joint penetration (CJP) welds, to enhance the quality control and workmanship requirement in the otherwise complete joint penetration (AWS, 2010) welds commonly practiced for CHS joints. Qian et al. (2013b, 2013c) have subsequently confirmed the fatigue performance of the welded circular hollow section X-joints fabricated using the proposed welding details. Qian et al. (2013a) have also demonstrated that the fracture mechanics based Paris law provides a close estimation of the fatigue crack propagation life compared to the monitored crack growth during the constant amplitude load tests.

Both off-shore and on-shore structures are subjected to repeated loading, i.e., winds, waves, or thermal, which may lead to fatigue failure. Much have been devoted to improve the finite element method to simulate crack propagation and predict fatigue life of structures. One traditionally used technique is to couple the re-meshing technique with the finite element method. The procedure automatically regenerates a mesh during crack growth stages. This technique requires the crack to be modeled explicitly in the structure. This may pose some difficulties if crack geometry is 3-dimensional and/or complicated. Moreover, projecting the current data onto the updated mesh may reduce the accuracy of the results. The element deletion method, on the other hand, does not require the crack to be explicitly modeled. Rather, the stiffness of the elements cut

by the crack is reduced close to zero. However this technique may result numerical difficulties because of the near zero stiffness of the elements cut by the crack.

Gifford & Hilton (1978) develop the enriched finite element method by embedding crack tip singularity solutions into the standard displacement field. The stress intensity factor (SIF) results not only agree well with the known solution, but are also relatively insensitive to the mesh around the crack tip. These advantages attract many researchers including Belytschko. In a series of publications, Belytschko and his coworker have proposed and developed the extended finite element method (XFEM) for the efficient study of stationary cracks and propagating cracks problem. In 1999, Belytschko and Black developed similar enrichment idea incorporating the discontinuous displacement field into the standard finite elements to cater for the presence of discontinuities such as cracks. This will involve significantly less effort in remeshing crack growth problems for finite element study. Later Moës et al. (1999) improved the aforementioned method by adopting the enrichment functions combining both discontinuous fields and near tip asymptotic fields to form the extended finite element method (XFEM). The discontinuity across the crack surface is represented by the Heaviside function. This method does not require any remeshing during the crack propagation simulation as the discontinuous field has been earlier included earlier in the finite element model. Sukumarz et al. (2000) apply the XFEM for 3-dimensional crack modeling. They have demonstrated the accuracy of this technique for three-dimensional static cracks using the same enrichment functions as adopted by Moës et al. (1999).

Belytschko et al. (2001) have presented a generalized technique for modeling arbitrary discontinuities. Updating the position of the discontinuity has been carried out by describing the surface of discontinuity using the signed distance function coupled with the level set method. Moës et al. (2002) and Gravouil et al. (2002) has presented the mechanical model and level set update for non-planar 3-dimensional crack growth based on the Hamilton-Jacobi equation. The level set is updated with the velocity extension approach. Ventura et al. (2002 and 2003) have developed the vector level set

method to describe the crack surface. The method is more robust and easy to implement as compare to the previous approach. Sukumar et al. (2003) have implemented the fast marching methods to simulate 3-dimensional planar fatigue crack growth that provides a faster analytical procedure.

Giner et al. (2008 and 2009) have implemented the extended finite element method for two-dimensional fracture problems within the finite element software ABAQUS by means of user element subroutine. XFEM generates a reasonably accurate stress intensity factor using relatively coarse meshes with no remeshing for crack growth simulations. Shi et al. (2010) has developed a 3-dimensional XFEM coupled with the fast marching method and implemented this in the ABAQUS finite element package via user subroutine.

In 2009, XFEM was available in the ABAQUS software package. This gives a good opportunity for researchers to study crack propagation using reliable software. Although, the XFEM in ABAQUS is more suitable for modeling crack propagation of specimens subjected to monotonic loading, users can extend the capability of ABAQUS to analyze specific problems, i.e., fatigue crack propagation, using subroutine or post-process scripts.

Currently, the studies on fatigue performance of concrete-filled chord tubular connections are limited. The benefits of concrete grouting methods are not well documented in design guidelines. This leads to a series of experimental investigations on the fatigue performance of CHS X-joints with concrete-filled chord.

1.5 Objective and scope

The objectives of this thesis are to (i) examine fatigue behavior and fatigue performance of the tubular X-joints with concrete filled chord and (ii) study fatigue crack propagation and estimate fatigue crack propagation based on XFEM.

In this research, fatigue behavior and fatigue performance of two large-scale grouted tubular X-joints using enhanced partial joint penetration (PJP+) welding profile are investigated. Both specimens are subjected to constant amplitude sinusoidal loadings. The purpose of the first joint (as-welded joint) is to study the effects of chord infilled grouting. For the second joint, the purpose is to study the effects of post-weld improvement. The weld toe on chord member is ground by a 3 mm radius grinding stone. Stress concentration factors (SCFs) along the weld toe on chord and brace members are measured to estimate the fatigue life by design S-N curves from various design guidelines. The measured SCFs are also compared to finite element results.

The stationary crack of C(T) and semi-elliptic surface crack specimen are studied using XFEM. The purpose is to study the appropriate mesh design which yield accurate stress intensity factor results. The crack propagation life prediction of semi-elliptical surface crack subjected uniform cyclic bending stress and tubular X-joints with concrete filled will be studied.

CHAPTER 2

OVERVIEW OF FRACTURE MECHANICS AND FATIGUE

2.1 Fracture mechanics

Fracture is the separation of a material into two or more parts under the applied stress. The separation occurs when the bonds that hold atoms together are broken by the applied stress.

2.1.1 Linear Elastic Fracture Mechanics (LEFM)

LEFM is derived based on linear elastic material and small scale yielding (SSY) assumptions. The cracked body follows the linear elastic response. The SSY restricts the plastic zone into a small region ahead of the crack tip which can be neglected from a macroscopic point of view. These two assumptions make LEFM applicable to many engineering problems.

2.1.1.1 Stress field near crack tip

In general, structures are subjected to complex loadings which cause complex crack openings. The complex crack opening can be extracted into three principal crack opening modes as shown in Figure 2.1-1. Mode I denotes a symmetric crack opening

where load is applied normal to the crack plane. Mode II is the sliding mode or the in-plane shear loading mode in which the load is applied normal to the crack front and results in an anti-symmetric crack opening. Mode III is the tearing mode or the out-of-plane shear loading mode. In this mode, load is applied tangent to the crack front resulting in a tearing-like crack opening. Each of these modes is associated with stress and strain fields as shown in Figure 2.1-2. Considering the two-dimensional body which contains a straight crack, the closed-form solution of stresses in the body is given in Equation 2.1-1 (Anderson, 1957) as:

$$\sigma_{ij} = \left(\frac{k}{\sqrt{r}}\right) f_{ij}(\theta) + \sum_{m=0}^{\infty} A_m r^{\frac{m}{2}} g_{ij}^{m}(\theta) \tag{2.1-1}$$

where, σ_{ij} is the stress tensor,

k is is constant,

$f_{ij}(\theta)$ is a dimensionless function,

r and θ are polar coordinate of the measuring point.

In the immediate vicinity to the crack tip $(r \to 0)$ the first term of Equation 2.1-2 (proportional to $1/\sqrt{r}$) results in a singular stress, while the second term (higher order term) approaches zero. This region is called *singularity dominated zone*. Therefore, stresses close to the crack tip are solely described by the singularity term. Replacing k with the stress intensity factor K $\left(K = k\sqrt{2\pi}\right)$ of each crack opening mode, Equation 2.1-1 can be re-written as (Anderson, 1957):

$$\begin{aligned}
\lim_{r\to 0} \sigma_{ij}^{I} &= \frac{K_I}{\sqrt{2\pi r}} f_{ij}^{I}(\theta), \\
\lim_{r\to 0} \sigma_{ij}^{II} &= \frac{K_{II}}{\sqrt{2\pi r}} f_{ij}^{II}(\theta), \text{ and} \\
\lim_{r\to 0} \sigma_{ij}^{III} &= \frac{K_{III}}{\sqrt{2\pi r}} f_{ij}^{III}(\theta).
\end{aligned} \tag{2.1-2}$$

With the linear elastic assumption, the principle of linear superposition of the individual loading mode is applicable to solve mixed-mode problems, as shown in Equation 2.1-3 (Anderson, 1957).

$$\sigma_{ij}^{total} = \sigma_{ij}^{I} + \sigma_{ij}^{II} + \sigma_{ij}^{III} \tag{2.1-3}$$

The analytical solutions of stress and displacement fields in the singularity dominated zone are summarized in Appendix A.

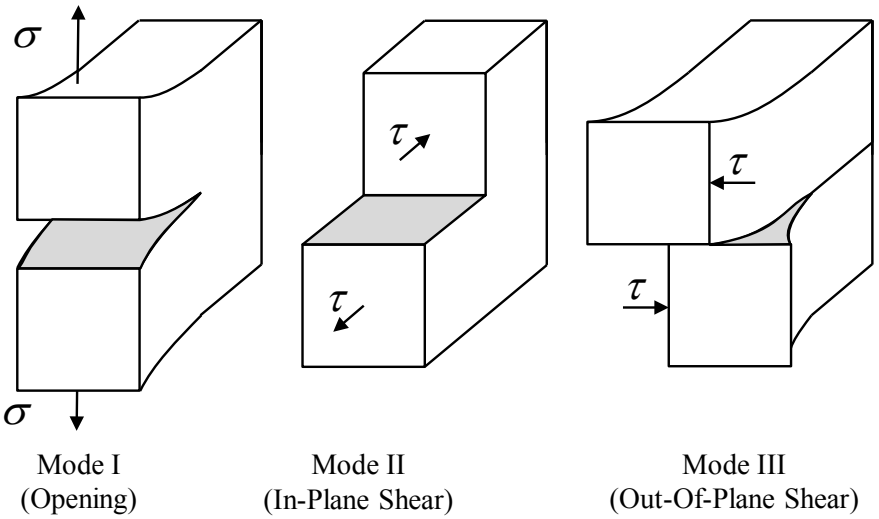

Figure 2.1-1: Three principal crack opening modes (Anderson, 1957)

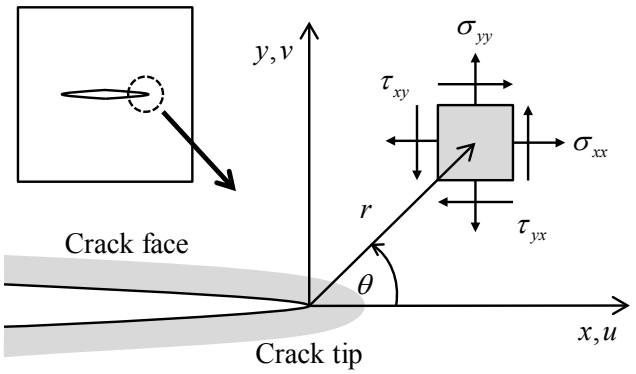

Figure 2.1-2: Notation for crack tip stress field (Anderson, 1957)

2.1.1.2 Stress intensity factor

Stress intensity factor (SIF) is used to predict stresses in the region close to the crack tip. The magnitude of SIF depends on the geometry of the cracked body, loading mode and magnitude of loads on the body. As can be seen in the previous section, the stress and displacement field close to the crack tip are uniquely described by the single parameter K. Therefore, the determination of K is necessary. Consider an infinite plate

with a through crack (Figure 2.1-3), K for mode I loading (K_I) is given by Equation 2.1-4.

$$K_I = \sigma\sqrt{\pi a} \tag{2.1-4}$$

When the crack size becomes larger or the plate size decreases, the crack tip is influenced by the outer boundaries. An appropriate correction factor which depends on geometry and loading mode must be introduced to Equation 2.1-4. A general form of SIF of a finite plate is given as (Anderson, 1957):

$$K_{(I,II,III)} = f\left(\frac{a}{W}\right)\sigma\sqrt{\pi a} \tag{2.1-5}$$

where, $f\left(\frac{a}{W}\right)$ is a dimensionless correction factor.

SIF can also be considered as a state variable of the region near the crack tip. When K reaches a critical value (K_c), it is a circumstance of crack extension or fracture of materials. K_c is an intrinsic material property. It is independent of dimensions of the body and loading modes as long as the SSY condition is satisfied. This makes K_c an appropriate parameter of fracture criteria. K_c is also known as fracture toughness.

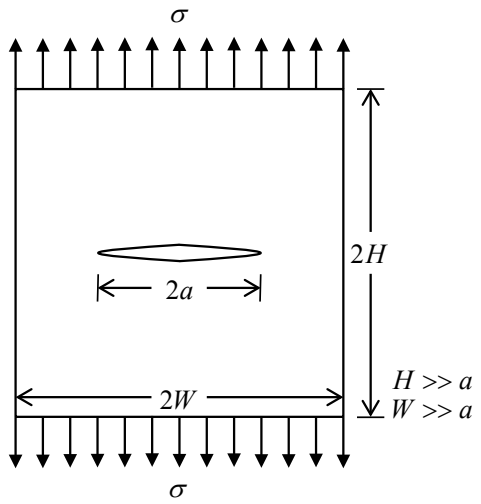

Figure 2.1-3: Infinite plate with through-thickness crack (Anderson, 1957)

2.1.1.3 The energy release rate

The energy release rate or the crack extension force, G, is the change in the potential energy, U, of the system per unit increase in crack area, A. The energy release rate can be expressed as (Anderson, 1957):

$$G = -\frac{dU}{dA} \tag{2.1-6}$$

The energy release rate is related to the stress intensity factor as,

$$\text{Mode I} \quad \begin{aligned} G_I &= \frac{K_I^2}{E} \text{ for plane stress} \\ G_I &= \frac{K_I^2\left(1-\nu^2\right)}{E} \text{ for plane strain} \end{aligned} \tag{2.1-7}$$

$$\text{Mode II} \quad G_{II} = \frac{\kappa+1}{8\mu}K_{II}^2 \tag{2.1-8}$$

$$\text{Mode III} \quad G_{III} = \frac{K_{III}^2}{2\mu} \tag{2.1-9}$$

where, $\kappa = \frac{3-\nu}{1+\nu}$ for plane stress,

$\kappa = 3-4\nu$ for plane strain,

μ is shear modulus of material, $\mu = \frac{E}{2(1+\nu)}$.

2.1.2 Elastic-Plastic Fracture Mechanics

2.1.2.1 Crack tip plasticity

The validity of LEFM is held for the case of small-scale yielding, where plastic zone is small compared to K-dominance zone, which is limited to high strength and low fracture toughness materials. For materials that exhibit nonlinear behavior or undergo large plastic deformation, the assumptions of LEFM become invalid and the results are inaccurate. For mode I loading, the plastic zone shape can be estimated by equating the von Mises stress (Anderson, 1957):

$$\sigma_{eq} = \sqrt{\frac{(\sigma_{xx}-\sigma_{yy})^2 + (\sigma_{xx}-\sigma_{zz})^2 + (\sigma_{yy}-\sigma_{zz})^2}{2} + 3\left(\tau_{xy}^2 + \tau_{xz}^2 + \tau_{yz}^2\right)}, \quad \text{(2.1-10)}$$

to material yield stress. Substituting stress components (listed in Appendix A) into Equation 2.1-10 yields:

$$\begin{aligned} r_y(\theta) &= \frac{1}{4\pi}\left(\frac{K_I}{\sigma_Y^2}\right)\left[1+\cos\theta+\frac{3}{2}\sin^2\theta\right], \text{ for plane stress, and} \\ r_y(\theta) &= \frac{1}{2\pi}\left(\frac{K_I}{\sigma_Y^2}\right)\left[(1-2\nu)^2(1+\cos\theta)+\frac{3}{2}\sin^2\theta\right], \text{ for plane strain.} \end{aligned} \quad \text{(2.1-11)}$$

The plastic zone size can be approximated by setting $\theta = 0^\circ$

$$\begin{aligned} r_y &= \frac{1}{2\pi}\left(\frac{K_I}{\sigma_Y}\right)^2 \text{ for plane stress} \\ r_y &= \frac{1}{6\pi}\left(\frac{K_I}{\sigma_Y}\right)^2 \text{ for plane strain} \end{aligned} \quad \text{(2.1-12)}$$

2.1.2.2 Crack tip opening displacement

The crack tip opening displacement (CTOD), δ, concept originates from the experimental work of Wells (1961) who showed that the LEFM could not describe the crack tip behavior of high fracture toughness (K_c) materials such as structural steels. Moreover, an initial sharp crack tip is blunted due to the plastic deformation. The degree of crack blunting is proportional to the fracture toughness of material. These findings led to the relation of CTOD and fracture toughness. In the framework of LEFM, Irwin (1961) showed that the behavior of a blunted crack tip (due to plastic deformation) and a sharp crack tip lengthened by r_y (first-order plastic zone size) are similar. Therefore, CTOD is estimated by the displacement (given in Appendix A) at r_y behind the crack tip, as shown in Figure 2.1-4.

For plane stress condition at $r = r_y$ (estimated by Equation 2.1-12) and $\theta = 180°$,

$$\delta = \frac{4}{\pi} \frac{K_I^2}{\sigma_Y E} \tag{2.1-13}$$

CTOD can also be defined by other definitions such as the displacement at the original crack tip and at the 90° intercept (Rice, 1968), as shown in Figure 2.1-5.

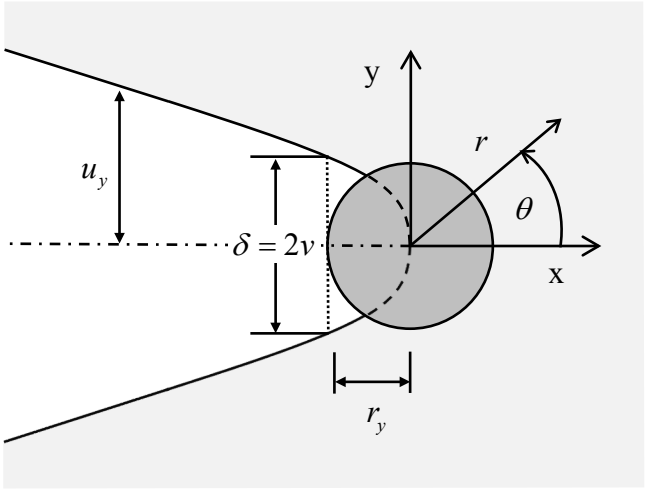

Figure 2.1-4: Estimation of CTOD using LEFM (Anderson, 1957)

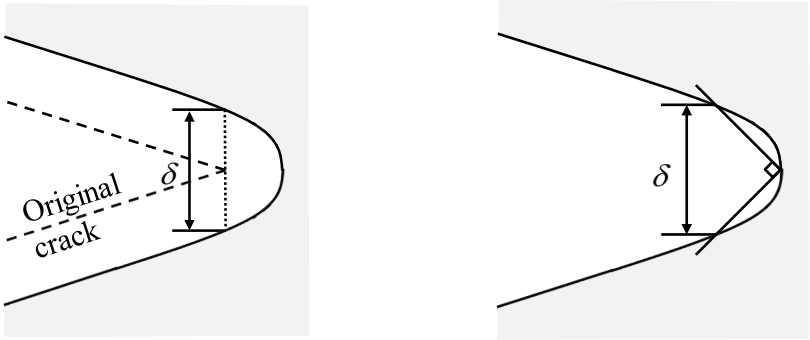

(a) at original crack tip **(b) at 90° line intercept**

Figure 2.1-5: Definition of CTOD as the displacement (Anderson, 1957)

2.1.2.3 J-integral

Rice (1968) proposed a J-integral concept which is a path-independent contour integral for a cracked body. The J-integral is the energy release rate for nonlinear elastic materials as follows (Anderson, 1957):

$$J = \int_{\Gamma} \left(w_e dy - T_i \frac{\partial u_i}{\partial x} ds \right) \tag{2.1-14}$$

where, w_e is the strain energy density,

$$w_e = \int_0^{\varepsilon_{ij}} \sigma_{ij} d\varepsilon_{ij} \tag{2.1-15}$$

T_i is the traction applied along the boundary of the contour,

$$T_i = \sigma_{ij} n_j \tag{2.1-16}$$

σ_{ij} and ε_{ij} are stress and strain tensors respectively,

n_i is the unit vector normal to the boundary Γ,

u_i are the components of the displacement vector, and

ds is the length of an infinitesimal segment along the contour Γ.

The J-integral is equivalent to the strain energy release rate, G, for linear elastic materials as (Anderson, 1957):

$$\begin{aligned} J = G &= \frac{K^2}{E} \text{ for plane stress,} \\ J = G &= \frac{K^2 \left(1 - \nu^2\right)}{E} \text{ for plane strain.} \end{aligned} \tag{2.1-17}$$

2.2 Fatigue mechanics

2.2.1 Fatigue crack growth mechanism

Fatigue is a damage process due to repeatedly applied stresses and strains. Generally, the fatigue process is divided into three phases: crack initiation, crack growth, and final fracture. Cracks usually initiate on the surface of the material where stresses are concentrated, such as scratches, sharp changes in the cross section, pits, inclusions, or embrittled grain boundaries, or even in the absence of a surface defect. The source of fatigue cracks is the formation of persistent slip bands (PSBs) which are driven by the maximum shear stress (approximately 45° to the principal stress direction). The back-and-forth movement of the slip bands causes microscopic extrusions and intrusions on the surface of material and eventually leads to the formation of microcracks, as shown in Figure 2.2-1.

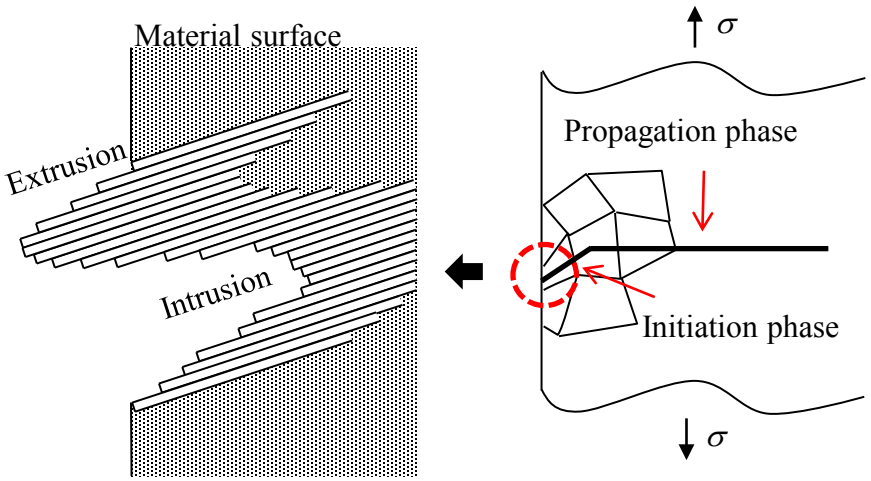

Figure 2.2-1: Formation of extrusions and intrustion (Campbell, 2008)

After the crack extends to several grain sizes, it will propagate in a direction perpendicular to the maximum principal stress direction. This mark is the transition from the initiation to propagation phase, in which the crack is considered a macrocrack. The crack growth in this phase is steady and often produces striations which are the ridges on the fracture surface. The process of striation is described by the crack front sharpening followed by blunting as shown in Figure 2.2-2.

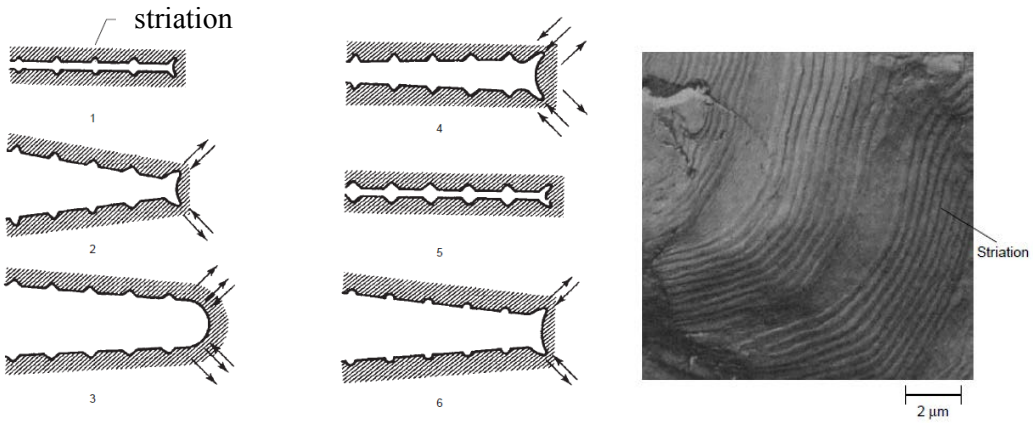

Figure 2.2-2: Formation of striationduring crack growth (Campbell, 2008)

The final fracture occurs when the crack size becomes large enough such that the remaining ligament of the cross section can no longer sustain the applied load.

2.2.2 Cyclic loading

In engineering applications, there are 2 types of cyclic loading: constant amplitude cyclic loading, and variable amplitude cyclic loading. Constant amplitude loading (Figure 2.2-3) describes the situation when the magnitude of the maximum stress and the minimum stress relative to the mean stress are equal and constant in the loading spectrum. The terminologies used to describe the loading are:

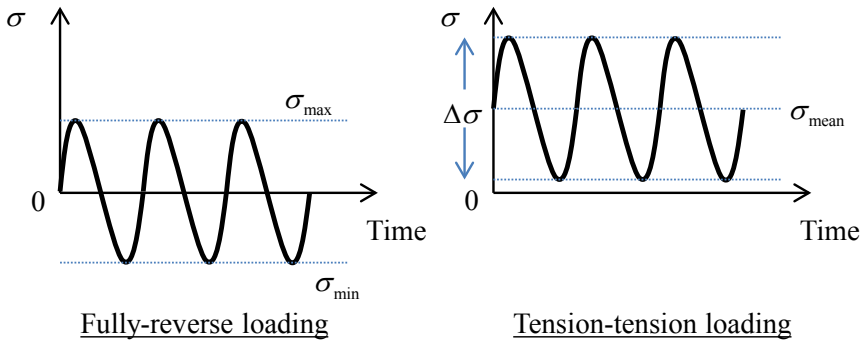

Figure 2.2-3: Constant amplitude loading (Anderson, 1957)

$$\text{Cyclic stress range: } \Delta\sigma = \sigma_{\max} - \sigma_{\min} \tag{2.2-1}$$

$$\text{Cyclic stress amplitude: } \sigma_{amp} = \frac{\sigma_{\max} - \sigma_{\min}}{2} \tag{2.2-2}$$

$$\text{Mean stress: } \sigma_{mean} = \frac{\sigma_{\max} + \sigma_{\min}}{2} \tag{2.2-3}$$

$$\text{Stress ratio: } R = \frac{\sigma_{\min}}{\sigma_{\max}} \tag{2.2-4}$$

Variable amplitude loading describes the situation where the amplitude and the wavelength are varied in the loading spectrum.

2.2.3 Cyclic stress-strain behavior

Under cyclic strain-controlled fatigue in which the strain amplitude is constant, the materials can undergo cyclic strain hardening, cyclic strain softening or remain stable. Cyclic hardening leads to increasing peak stresses with increasing cycles, while cyclic softening results in decreasing stress levels with increasing cycles, as shown in Figure 2.2-5. Dislocation microstructure of the material plays an important role in cyclic stress-strain behavior. For soft materials that exhibit cyclic strain hardening, cyclic strain increases the dislocation density. The higher dislocation density increases the amount of elastic strain and the stress on the material. In contrast, hard materials exhibit cyclic strain softening because cyclic strain leads to a more stable dislocation arrangement. Therefore, the stress is reduced when plastic deformation occurs. Typically, the material is cyclically hardened if σ_Y/σ_u>1.4 and cyclically softened if σ_Y/σ_u<1.2, where σ_u is monotonic ultimate tensile strength and σ_Y is monotonic yield strength (Manson, 1964).

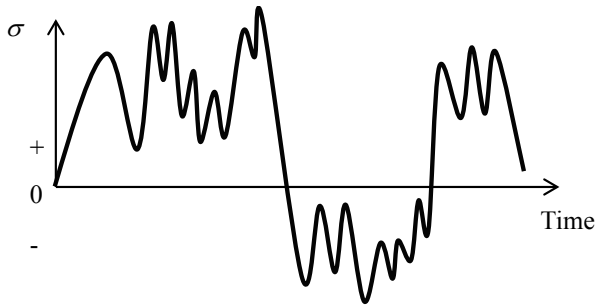

Figure 2.2-4: Variable amplitude loading (Anderson, 1957)

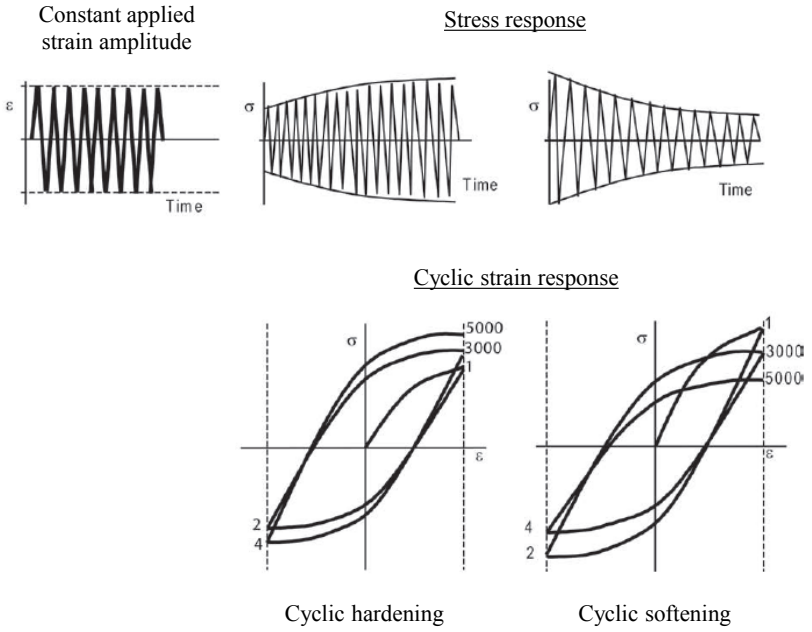

Figure 2.2-5: Cyclic hardening and cyclic softening (Campbell, 2008)

2.2.4 Definition of various stresses

2.2.4.1 Nominal stress

Nominal stress is defined as the sectional stress regardless of any local stress rising effect, such as the effect of the welding profile. In fracture mechanics, it is sometimes called the remote stress. Nominal stress can be simply calculated using classical theory, such as the beam theory. For a CHS X-joint subjected to in-plane bending in the brace (secondary) members, the bending stress in the brace is considered the nominal stress in this particular loading type, which is expressed as:

$$\sigma_{nom} = \frac{M_b(d/2)}{I}, \tag{2.2-5}$$

where, M_b is the in-plane bending moment,

d is the distance from nutria axis to brace outer surface,

I is the area moment of inertia.

2.2.4.2 Notch stress (Local stress)

Notch stress is a total stress at the weld toe. It includes the stress resulting from the geometry of the joint and the nonlinear stress field due to the notch profile at the weld toe. It includes geometric stresses and stresses which are affected by the welding profile. Any small change of welding profile can substantially affect the notch stress. In reality, even a certified welder cannot produce identical welding profiles for two duplicated specimens. As a result, notch stress can be significantly different although the global dimensions of the compared joints are the same. On the other hand, to compute notch stress numerically, a very precise welding profile has to be modeled in the finite element model which is rather difficult and almost impossible, especially for tubular joints. Practically, a stress which is not affected by welding profile has to be defined.

2.2.4.3 Hot-spot stress (Geometric stress)

The hot-spot stress includes the uneven stress distribution caused by the joint geometry and loading type, but excludes influences related to fabrication, such as the configuration of the weld (flat, convex or concave) and the local condition of the weld toe (radius of weld toe, undercut, etc.). In other words, the non-linear peak stress which is caused by the local notch at the weld toe is excluded. The hot-spot stress and its location represent the highest geometric stress in the joint and the location where cracks are always initiated.

2.2.4.3.1 Determination of hot-spot stress

For welded joints, the hot spot stress can be determined by extrapolating the stress from the stress field outside the region influenced by the local stress to the weld toe position as shown in Figure 2.2-6.

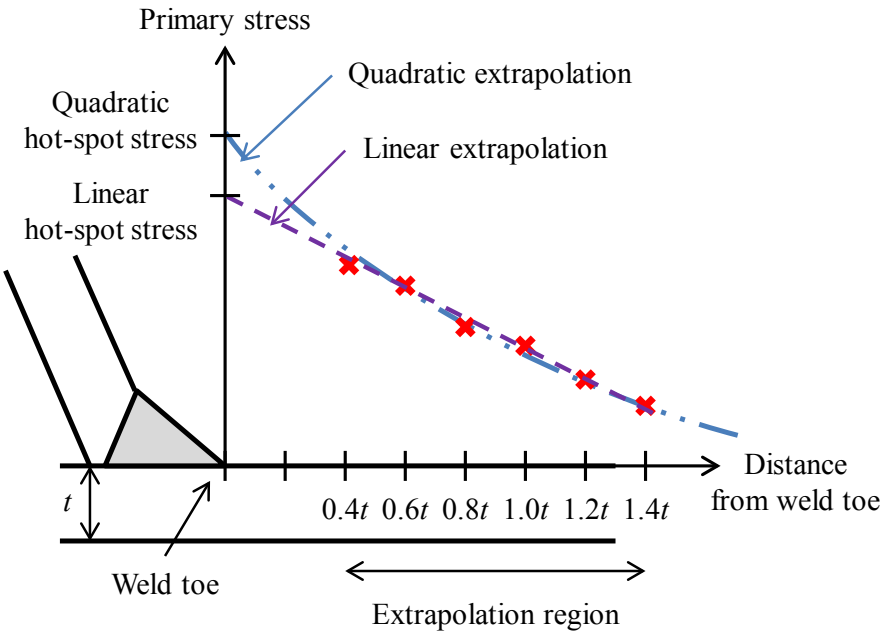

Figure 2.2-6: Hot-spot stress definition

2.2.4.3.2 Extrapolation region

The chosen extrapolation region must be adequately far from the weld toe position in order to get rid of the effect of the nonlinear stress field. In addition, this region must represent the strain gradients affected by the global geometry. Many standards, such as IIW (Hobbacher, 2007), CIDECT (Zhao et. al., 2001) and ABS (2010), have proposed boundaries depend on the dimension of the joint, such as the thickness and the radius of each member. Overall, the closest position should be at least 4 mm away from weld toe. However, the furthest position is different in each standard. In this study, the recommendation from IIW (Hobbacher, 2007) is adopted. The minimum and maximum distances from the weld toe are $0.4t$ and $1.4t$ respectively, where t is the thickness of the member.

2.2.4.3.3 Extrapolation method

The hot-spot stress can be calculated by extrapolating the stress in the extrapolation region to the weld toe in order to eliminate the effect of weld configurations. The two extrapolation methods normally used are linear extrapolation and quadratic extrapolation. The extrapolation method must be chosen depending on the nonlinearity of the stress field in the extrapolation region. For a circular hollow section (CHS) joint, the linear extrapolation method is recommended since stresses vary linearly. For a rectangular hollow section joint (RHS), stress in the extrapolation region varies non-linearly. Therefore, the quadratic extrapolation method is more appropriate (Zhao et. al., 2001 and DNV, 2011).

2.2.4.4 Stress component

From fracture mechanics, mode I crack opening usually governs the failure of structures. Therefore, the direction of the extrapolated stress has to be perpendicular to the weld toe and lying on the parent member surface. The stress normal to the weld line is considered the fatigue crack opening stress. For a simple geometries specimen, such as a welded plate subjected to tensile loading, the direction of the maximum principal stress is almost perpendicular to the weld toe. Therefore, maximum principal stress is a good representative of hot-spot stress. In contrast, for a complicated geometrical specimen, the principal stress may deviate from the direction normal to the weld toe. To get more reasonable results, stress perpendicular to the weld toe shall be used as the hot-spot stress instead of the maximum principal stress. In addition, most of the fatigue crack initiation originates along the weld line.

2.2.5 Stress concentration factor and strain concentration factor

For the convenience of calculation of the hot-spot stress for other structures which have the same geometry or the same structure subjected to different applied load levels, a relationship between the hot-spot stress and nominal stress is established. The stress concentration factor is defined by the ratio of the hot-spot stress over the nominal stress as expressed in Equation 2.2-6 In other words, it is a normalized factor which gives an idea of the hot-spot stress level depending on the applied load.

$$SCF = \frac{\sigma_{hot-spot}}{\sigma_{nom}} \tag{2.2-6}$$

Similar to the stress concentration factor, the strain concentration factor is defined by the ratio of the hot-spot strain over the nominal strain as expressed in Equation 2.2-7.

$$SNCF = \frac{\varepsilon_{hot-spot}}{\varepsilon_{nom}} \tag{2.2-7}$$

From Equation 2.2-6 and Equation 2.2-7, the stress concentration factor and the strain concentration factor can be related through Hooke's law as follows:

$$E = \frac{\sigma_{nom}}{\varepsilon_{nom}}, \tag{2.2-8}$$

yields,

$$\frac{SCF}{SNCF} = \frac{1}{E}\frac{\sigma_{hot-spot}}{\varepsilon_{hot-spot}}. \tag{2.2-9}$$

From continuum mechanics, material constitutive (stress-strain) relationship is expressed as:

$$\sigma_{ij} = \frac{2G\nu}{1-2\nu}\delta_{ij}\varepsilon_{kk} + 2G\varepsilon_{ij} \tag{2.2-10}$$

where, δ_{ij} is the Kronecker delta function which = 1 for i=j, otherwise = 0, and

$G = \frac{E}{2(1+\nu)}$

Substituting Equation 2.2-10 into Equation 2.2-9 yields:

$$\frac{SCF}{SNCF} = \frac{1}{1+v} + \frac{v}{(1+v)(1-2v)}\left(1+\frac{\varepsilon_{22}}{\varepsilon_{11}}+\frac{\varepsilon_{33}}{\varepsilon_{11}}\right) \tag{2.2-11}$$

where ε_{11} is the extrapolated strain in the direction perpendicular to the weld toe,

ε_{22} is the extrapolated strain in the direction parallel to the weld toe and tangent to the member surface,

ε_{33} is the cross product of ε_{11} and ε_{22} $\varepsilon_{33} = \varepsilon_{11} \times \varepsilon_{22}$.

Since fatigue damage often initiates at the surface of the members, which is a free surface, the stress perpendicular to the member surface should be zero. Therefore Equation 2.2-11 can be simplified to a two-dimensional plane-stress case.

$$\frac{SCF}{SNCF} = \frac{1}{1-v^2}\left(1+v\frac{\varepsilon_{22}}{\varepsilon_{11}}\right) \tag{2.2-12}$$

The SNCF can thus be converted to the SCF using the following equation:

$$SCF = 1.15 \times SNCF \tag{2.2-13}$$

2.2.6 Existing parametric equations for determination of SCF

Many researchers have proposed parametric equations based on finite element solutions and/or experimental results to calculate the stress concentration factor for tubular joints. These equations are presented for the maximum outer surface stress concentration factor on both the chord and brace using dimensionless geometric joint ratios. They cover a wide range of geometric joint ratios for simple joint configurations commonly found in offshore structures. Moreover, many load configurations, such as axial load and in-plane bending, are also considered. The stress concentration factors from this approach are normally given at four locations on the joint, such as at the crown and saddle position of the brace and chord as a function of geometric parameters (α, β, γ, τ, and θ) as defined in Equation 2.2-14. The typical geometry of the X-joint is

shown in Figure 2.2 7. In this section, only the parametric equations of tubular X-joints subjected to in-plane bending will be represented.

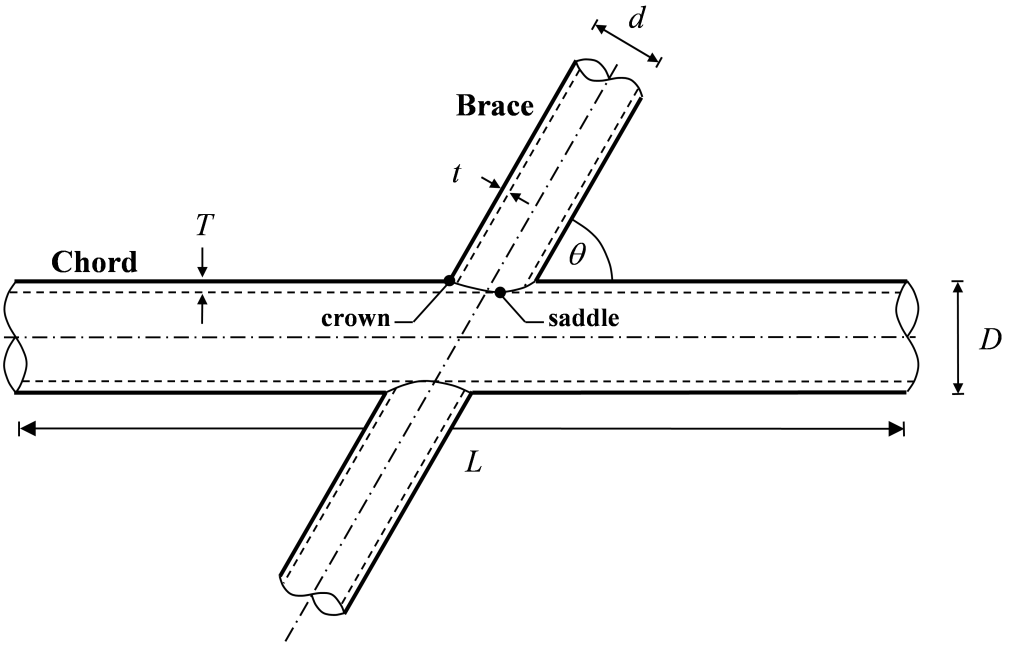

Figure 2.2-7: Typical geometry of tubular X-joint

α is the ratio of the chord length to the chord radius $= \dfrac{2L}{D}$

β is the ratio of the brace diameter to the chord diameter $= \dfrac{d}{D}$

γ is the ratio of the radius to wall thickness ratio of chord member $= \dfrac{D}{2T}$ (2.2-14)

τ is the ratio of the brace thickness to chord wall thickness $= \dfrac{t}{T}$

θ is the angle between the chord and brace $(\text{less than } 180^\circ)$

2.2.6.1 Efthymiou formulae

Efthymiou and Durkin (1985) published a series of parametric equations covering T/Y and gap/overlap K-joints and Efthymiou (1988) published a comprehensive set of simple joint parametric equations covering T/Y, X, K and KT simple joint configurations. Stress concentration factors were analyzed based on the maximum principal stress and linearly extrapolated to the weld toe. The proposed parametric equations for in-plane bending are as follows:

$$
\begin{aligned}
SCF_{CC} &= 1.45\beta\tau^{0.85}\gamma^{1-0.68\beta}\sin^{0.7}\theta \\
SCF_{BC} &= 1+0.65\beta\tau^{0.40}\gamma^{1.09-0.77\beta}\sin^{0.06\gamma-1.66}\theta \\
SCF_{CS} &= \text{negligible} \\
SCF_{BS} &= \text{negligible}
\end{aligned}
\tag{2.2-15}
$$

The equations are valid in the following regions:

$$
\begin{aligned}
&6 \le \alpha \le 40 \\
&0.2 \le \beta \le 1.0 \\
&8 \le \gamma \le 32 \\
&0.2 \le \tau \le 1.0 \\
&20^\circ \le \theta \le 90^\circ
\end{aligned}
$$

2.2.6.2 Chang and Dover expressions

Chang and Dover (1996) studied the stress concentration factors of tubular X and DT joints. In their study, eight-noded quadrilateral thin-shell elements with reduced integration and six-noded triangular thin-shell elements were employed. The intersection between brace and chord of thin-shell finite element models was modeled as the intersection of their mid-planes. Weld profile was neglected. The proposed parametric equations for in-plane bending are as follows:

$$
\begin{aligned}
SCF_{CC} &= 2.0647\alpha^{-0.0486}\beta^{-0.0468}\gamma^{0.377}\tau^{0.971}\sin^{0.644}\theta \\
SCF_{BC} &= 6.0497\alpha^{-0.0784}\beta^{0.295}\gamma^{0.798-0.369/\theta}\,\tau^{0.617}e^{-1.37\beta-0.0195\gamma-0.748\tau}\sin^{-1.36}\theta \\
SCF_{CS} &\approx 0 \\
SCF_{BS} &\approx 0
\end{aligned}
\tag{2.2-16}
$$

The equations are valid in the following regions:

$$6 \leq \alpha \leq 40$$
$$0.2 \leq \beta \leq 0.8$$
$$7.6 \leq \gamma \leq 32$$
$$0.2 \leq \tau \leq 1.0$$
$$35^\circ \leq \theta \leq 90^\circ$$

2.2.6.3 Lloyd's Register of Shipping formulae

Lloyd's Register of Shipping (1997) proposed parametric equations based on experimental results of steel and acrylic joints. The equations cover stress concentration factors of T/Y, X, K and KT-joints. The proposed parametric equations for in-plane bending are as follows:

$$\begin{aligned} SCF_{CC} &= 1.23\gamma^{0.5\beta^{-0.5}}\tau^{0.8}\beta\left(1-0.32\beta^5\right)\sin^{0.5}\theta \\ SCF_{BC} &= 1.12+1.12\gamma\tau^{0.8}\beta\left(0.32-0.25\beta\right)\sin^{1.5}\theta \\ SCF_{CS} &= \text{negligible} \\ SCF_{BS} &= \text{negligible} \end{aligned} \tag{2.2-17}$$

The equations are valid in the following regions:

$$\alpha \geq 4$$
$$0.13 \leq \beta \leq 1.0$$
$$10 \leq \gamma \leq 35$$
$$0.25 \leq \tau \leq 1.0$$
$$30^\circ \leq \theta \leq 90^\circ$$

The 3 formulae take β, γ, τ, and θ into account. Only Chang and Dover formulae take effect of chord length into account by including α. The applicable range geometric parameters of the 3 formulae are close. The comparison of SCF results determined from the 3 formulae with fixed $\alpha = 6.0$ and $\theta = 90^\circ$ is illustrated in Figure 2.2 8. The SCF results from the 3 formulae increase with increasing τ and γ value. The ef-

fect of τ and γ to SCF values is more pronounce on the chord crown position than those on the brace crown position. The changes of SCF values at chord crown respect to β value determined using Chang and Dover formulae is rather flat as compared to those determined from Efthymiou and Durkin and Lloyd's Register of Shipping formulae. It should be noted that, in this comparison, the SCF values at chord crown are slightly changed in the cases of $\beta > 0.6$.

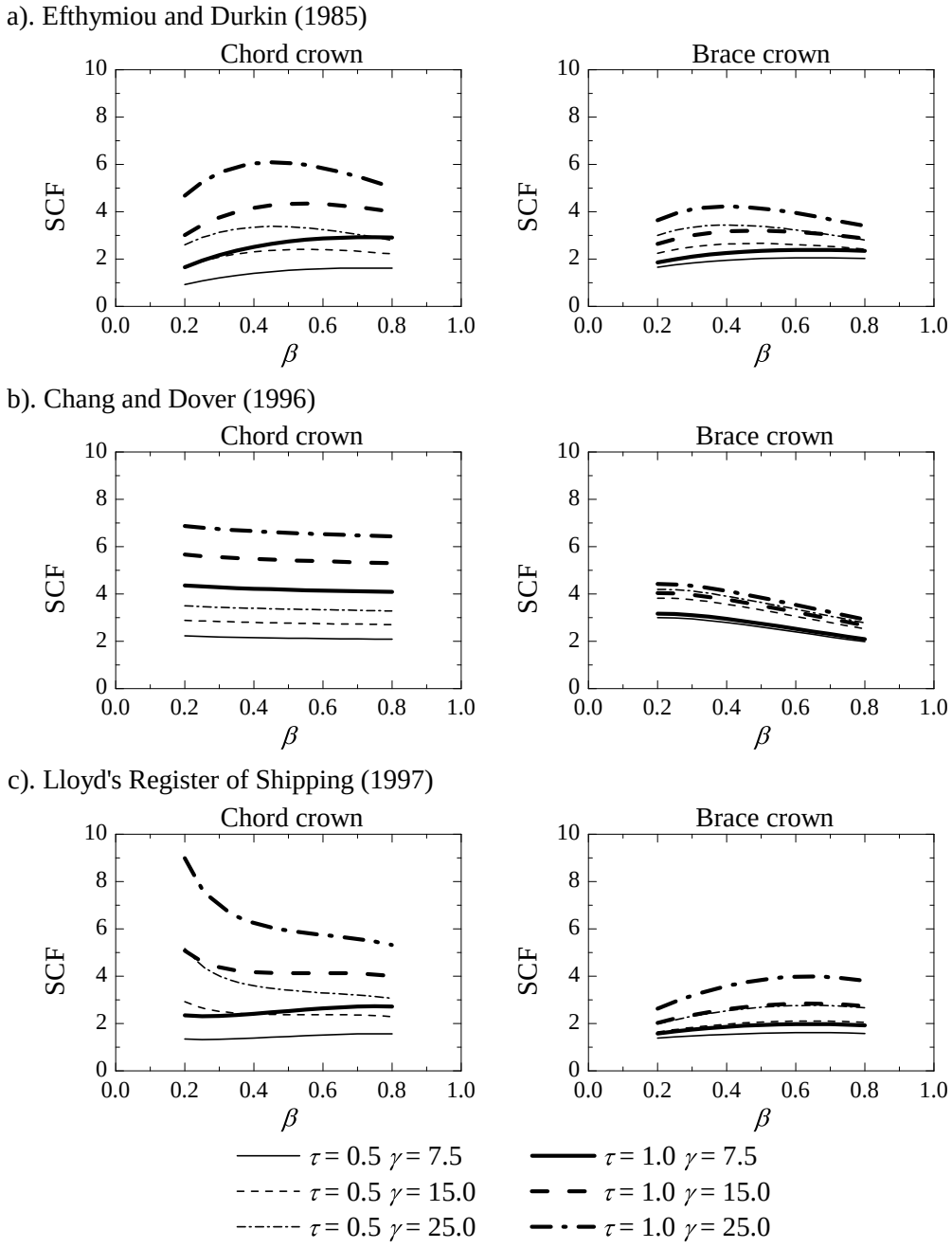

Figure 2.2-8: Comparison of SCF values from parametric quations

2.3 Fatigue assessment using S-N approach

S-N approach is widely used to estimate the fatigue life of offshore structures. The fatigue life directly relates to the interested stress level by means of S-N curves which are normally presented in a $\log_{10} - \log_{10}$ scale. The basic design S-N curve is given as:

$$\log N = \log \bar{a} - m \log \Delta\sigma \tag{2.3-1}$$

or

$$N = \bar{a}(\Delta\sigma)^{-m} \tag{2.3-2}$$

where, N is the predicted number of cycles to failure,

$\Delta\sigma$ is the stress range,

m is the negative inverse slope the S-N curve, $\log \bar{a}$ is the intercept of S-N curve with $\log N -$ axiz,

$$\log \bar{a} = \log a - 2SD_{\log N} \tag{2.3-3}$$

$\log a$ is the intercept of the mean S-N curve with $\log N -$ axiz, and

$SD_{\log N}$ is the standard deviation of $\log N$.

Thickness of a material greatly influences the fatigue strength. For material thickness which is different from reference thickness, the S-N curve has to be adjusted as follows:

$$\log N = \log \bar{a} - m \log \left(\Delta\sigma \left(\frac{t}{t_{ref}} \right)^{k} \right) \tag{2.3-4}$$

where, t is the material thickness,

t_{ref} is the reference thickness, and

k is the thickness exponent.

Various design guidelines proposed different concept of S-N curves depending on the most appropriate stress definitions which can be determined in the structures.

Stresses must be calculated in accordance with the stress definition used to derive a particular S-N curve. There are three types of S-N curves normally used in welded structures, the hot-spot stress S-N curve, notch stress S-N curve and nominal stress S-N curve. Figure 2.3-1 shows an example of the hot-spot S-N curves with and without thickness correction.

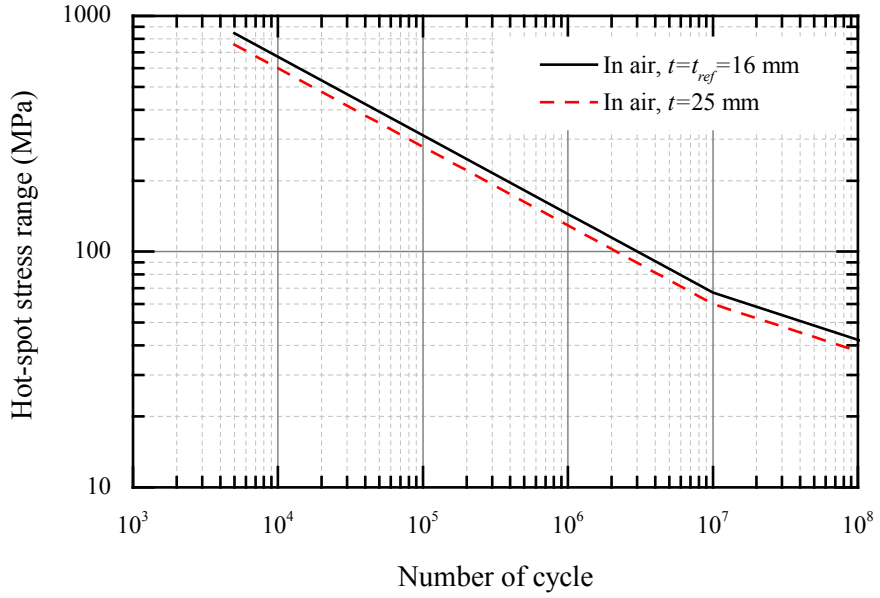

Figure 2.3-1: Hot-spot stress S-N curve, API 2009

The International Institute of Welding (Hobbacher, 2007) design guideline provides various nominal stress S-N curves based on material, structural detail and fatigue class. Table 2.3-1 shows the values of the constants in Equation 2.3-1 for two fatigue classes: FAT71 and FAT50. FAT71 and FAT50 are recommended for full penetration weld and partial penetration weld or fillet weld respectively.

Table 2.3-1: Constants for nominal stress S-N curves

Fatigue class	$\bar{a}$	m	t_{ref} [mm]	k
FAT71	7.158×10^{11}	3	-	0.25
FAT50	2.500×10^{11}	3	-	0.25

The hot-spot stress S-N curve is recommended by many design guidelines. The American Petroleum Institute (API, 2007) provides the hot-spot stress S-N curves for tubular connections subjected to regular cyclic loading in atmospheric service for both the as-welded profile(X curve) and for the controlled weld profile (X' curve). The S-N relation is given as follows,

$$N = 2 \times 10^6 \left(\frac{\Delta\sigma}{\Delta\sigma_{ref}} \right)^{-m} \tag{2.3-5}$$

Table 2.3-2 shows the values of the constants in Equation 2.3-5.

Table 2.3-2: Constants for hot-spot stress S-N curves (API 2005)

API 2005	$\Delta\sigma_{ref}$ [MPa]	m	t_{ref} [mm]	k
X	100	4.38	16	0.25
X'	79	3.74	25	0.25

The Comité International pour le Développement et l'Etude de la Construction Tubulaire (Zhao et. al., 2001) recommends S-N curves with thickness correction formulae established by van Wingerde et. al. (1997c, 1998a) as follows,

$$\log(\Delta\sigma) = \frac{1}{3}(12.476) - \log(N) + 0.06\log(N)\log\left(\frac{16}{t}\right) \tag{2.3-6}$$

or

$$\log(N) = \frac{12.476 - 3\log(\Delta\sigma)}{1 - 0.18\log\left(\frac{16}{t}\right)} \tag{2.3-7}$$

This formula is applicable to circular hollow section joints with member thickness between 4 mm to 50 mm.

The American Petroleum Institute (API, 2007) and Det Norske Veritas (DNV, 2011) also provide hot-spot stress S-N curves in the form of Equation 2.3-1. The constants for S-N relationship are listed in Table 2.3-3.

Table 2.3-3: Constants for hot-spot stress S-N curves (API 2007, DNV 2011)

CODE	$\log \bar{a}$	m	t_{ref} [mm]	k
API 2009	12.480	4.38	16	0.25
DNV 2011	12.164	3.74	32	0.25

Notch stress S-N curves provided by International Institute of Welding (Hobbacher, 2007) recommends using the FAT225 curve and Det Norske Veritas (DNV, 2011)

Table 2.3-4: Constants for notch stress S-N curves

CODE	$\log \bar{a}$	m	t_{ref} [mm]	k
IIW FAT225	11.653	3	N.A.	N.A.
DNV 2011	13.358	3	N.A.	N.A.

CHAPTER 3

EXPERIMENTAL INVESTIGATION

Steel structures using circular hollow sections (CHS) are widely used in offshore and onshore structures. They provide relatively high strength-to-weight ratios when compared to concrete structures. Moreover, they have good bending and torsion resistance in all directions. In steel structures, there are many joint configurations such as T-joints, Y-joints, K-joints and X-joints. Qian et al. (2013a and 2013b) conducted a series of experiments to examine the fatigue performance of CHS X-joints fabricated from newly proposed weld profiles (PJP+), also named as the full capacity tubular joint welds, and reported good fatigue performance. However, fatigue performance of CHS X-joints with concrete-filled chord and post-weld toe grinding has not been examined.

This chapter starts with a brief introduction of the full capacity tubular joint welds. The following section is an overview of the experimental program. Sections 3.3 and 3.4 report and discuss experimental results. Finally, section 3.5 concludes the main findings from the series of experimental studies.

3.1 Full capacity tubular joint welds

Welding is one of the most common joining methods for metallic structures. In the offshore structures, especially the offshore-jacket structures, there are two welding profiles commonly adopted: the partial joint penetration (PJP) welding profile and the complete joint penetration (CJP) welding profile. The PJP welding profile (Figure

3.1-1a) is a groove weld that does not extend completely through the thickness of the components joined. The increasing unwelded portion leads to a lower load transmitting capacity. Moreover, it induces crack-like defects at the weld root which may lead to an undetectable root crack.

The CJP welding profile (Figure 3.1-1b) is a groove weld that extends completely through the thickness of the components joined. Therefore, full-load transmitting capacity is recovered. This welding profile is commonly used in offshore jacket structures in which the connection weld details allow welding from the outside surface only. The single-side welding requires GR6 welders and rigorous quality control and inspection (AWS, 2010). An alternative approach is to use the inside backing plate (Figure 3.1-1c) to prevent the unfavorable weld root discontinuities in the small groove angle region.

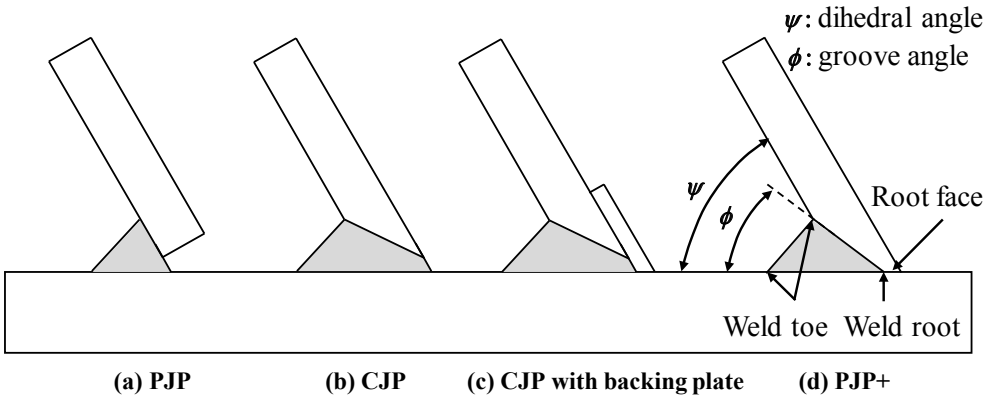

Figure 3.1-1: Comparison of traditional welding profiles in offshore structures and the newly proposed PJP+ welding profile

The combination of the backing plate and CJP leads to the newly proposed welding profile called the enhanced partial joint penetration (PJP+) welding profile which aims to improve the PJP welding profile to meet the level of the CJP welding profile and to reduce the workmanship requirement in the welding procedure. Figure 3.1-2 shows the details of the PJP+ welding profile. The PJP+ provides strict weld root size which serves as the backing plate during the welding procedure. In addition, the beveling root face allows the secondary components to rest onto the primary components before welding. Moreover, the PJP+ provides sufficient weld deposit and a large groove angle. All

the aforementioned features of the PJP+ welding profile will reduce the workmanship requirement and make it an alternative to the CJP welding profile.

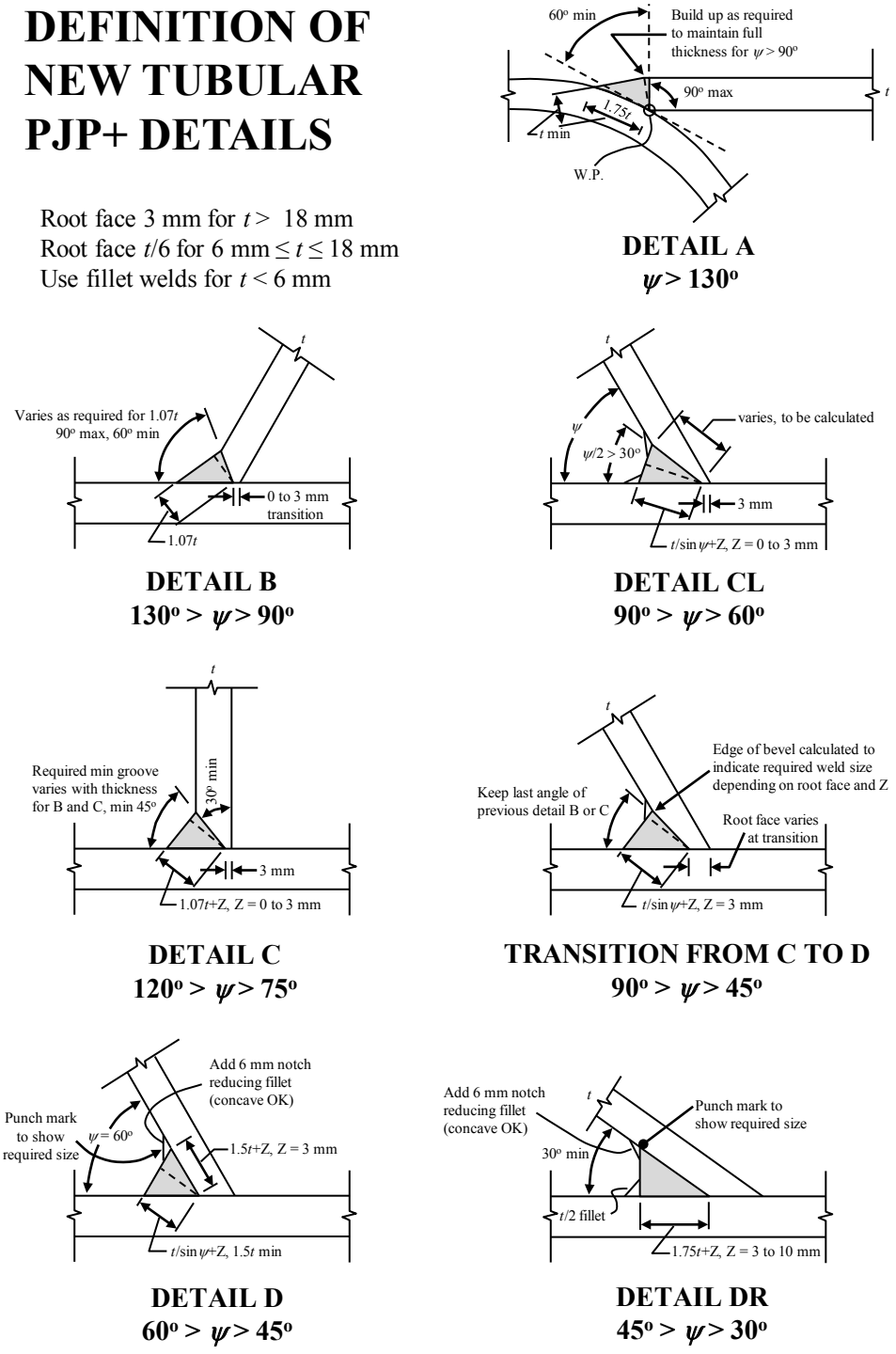

Figure 3.1-2: Enhanced partial joint penetration weld details (Qian et al., 2009)

3.2 Overview of experimental program

3.2.1 Description of the test specimens

The tubular X-joints which are used to investigate the fatigue performance of the newly proposed enhanced partial joint penetration (PJP+) welding profile are fabricated from S355 structural steel. The drawing of the joint is illustrated in Figure 3.1-2. The brace members have an outer diameter of 406.4 mm with a 25 mm wall thickness. The span length of the two braces is 4,024 mm as measured from the center of one diaphragm plate to another. The diaphragm plates are fillet-welded to both ends of the brace members at the support position. These diaphragm plates are used to prevent an excessive local deformation due to highly concentrated reaction force from supports. The cold rolled chord member has an outer diameter of 750 mm with 25 mm wall thickness. The chord length is 1,750 mm. The brace members intersect the chord member at a 60° angle. Load is applied to the chord through a reusable fixture to simulate the in-plane bending in the brace members. The chord members are filled with high strength concrete (Densit Ducorit® D4) and enclosed with two partition plates at the top and bottom. The experimental program investigates fatigue performance of 2 X-joints denoted as J2-1 and J2-2. Both X-joints share the same geometry as indicated in Table 3.2-1.

Table 3.2-1: Geometry and non-dimensional parameters of test specimen

Specimen	Chord [mm]			Brace[mm]			α	β	γ	τ	θ
	D	T	L	d	t	l	$2L/D$	d/D	$D/2T$	t/T	deg
J2-1, J2-2	750	25	1750	406.4	25	4024	4.67	0.54	15	1	60

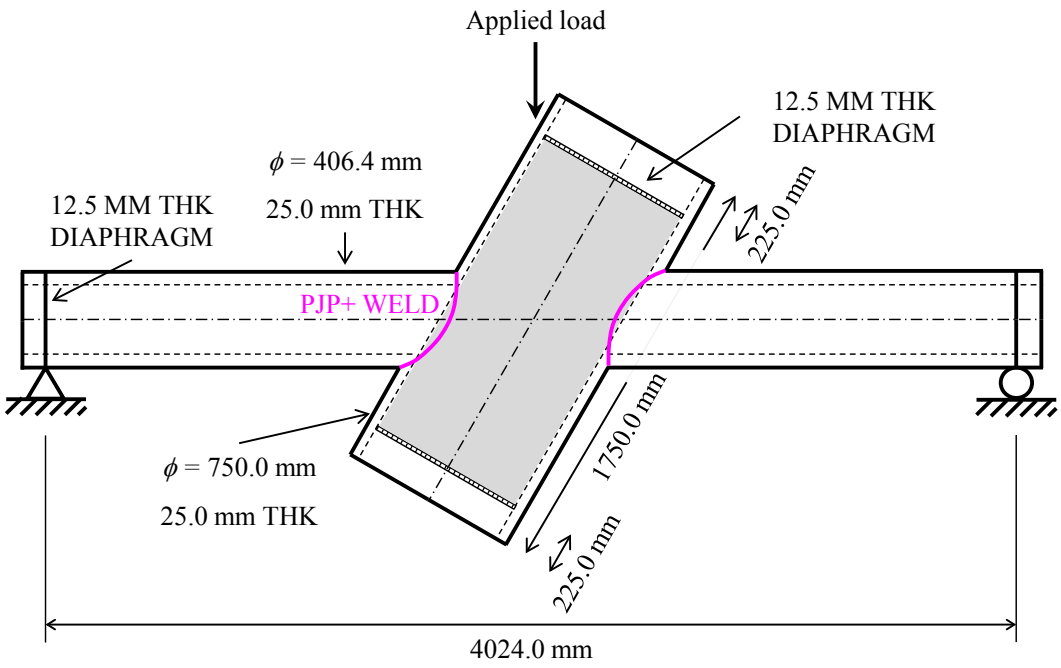

Figure 3.2-1: Drawing of the tubular X-joint

3.2.2 Experimental setup

The tubular X-joints were tested at the structural engineering laboratory in the National University of Singapore. The joint is securely installed in the 2000 kN test rig as shown in Figure 3.2-2a. The left brace rests on a pinned support (Figure 3.2-2b). The right brace rests on a roller support (Figure 3.2-2c). A circular plate is fillet-welded to the brace end at the support locations (Figure 3.2-2d). The rigid loading fixture (Figure 3.2-2e) is fixed firmly to a 2000 kN actuator and placed on the top of the chord member to transfer the load from the actuator.

All of the tubular X-joints are fabricated with high quality control and tight tolerances. However, the delivered joints have consistent fabrication errors. The two braces which should be co-planar, leveled and aligned are found to be co-planar but misaligned. When the joint is installed in the test rig, the left hand side brace is level but the right hand side brace tilt upward by 0.93° towards the joint. This misaligned configuration is called misalignment type A. Suppose that the joint is rotated 180° about

its out of plane axis, the left brace will tilt upward by 0.93° towards the left support and the right brace will level. This misaligned configuration is called misalignment type B. The two misalignment types are shown in Figure 3.2-3. The effects of brace misalignment to performance of structure will be discussed in Chapter 4.

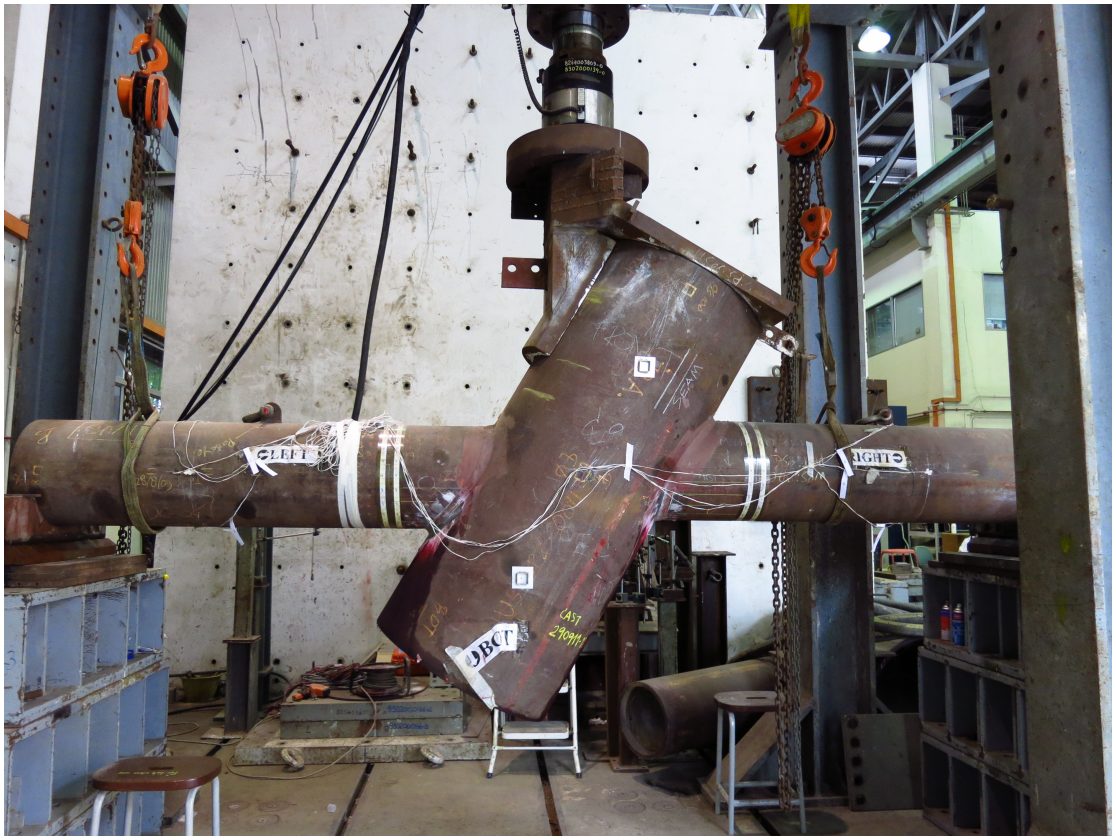

(a) Tubular X-joint

(b) Pinned support at the left brace

(c) Roller support at the right brace

(d) Plate stiffener at the brace end

(e) Loading fixture

Figure 3.2-2: Test specimen setup

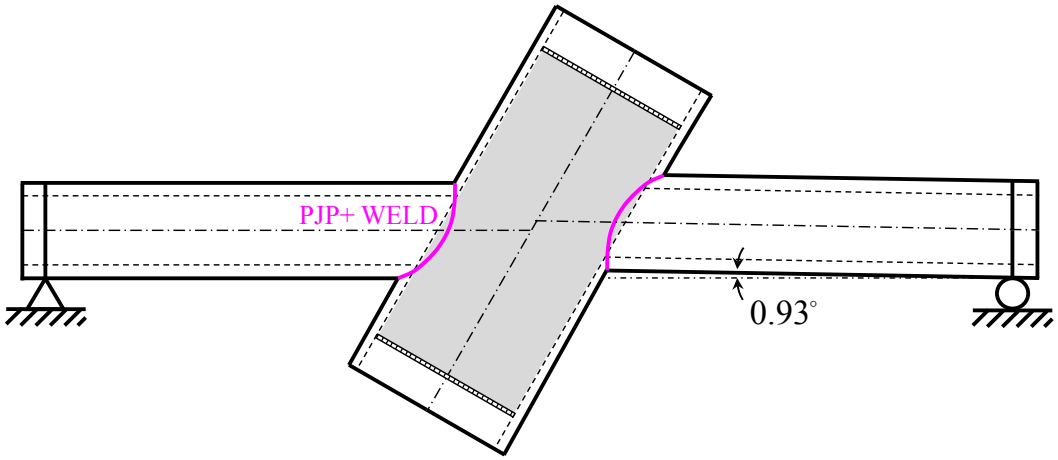

(a) Misalignment type A

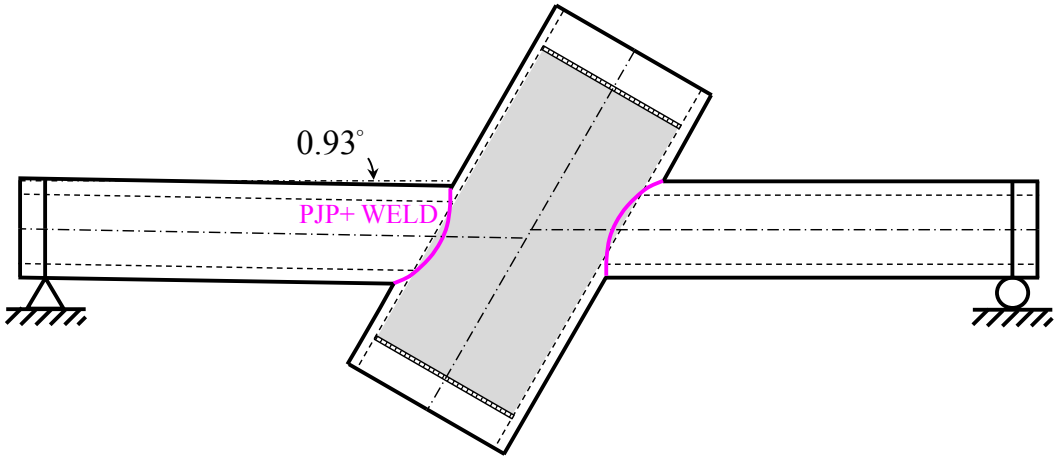

(b) Misalignment type B

Figure 3.2-3: Two possible brace misalignment types

3.2.3 Instrumentation

The principal acquired data in this experiment are values of strain at various locations. They can be measured by strain gauges. The other important data are the values of crack depth along the weld toe. The Alternating Current Potential Drop (ACPD) is used to measure the crack depth and the Linear Variable Differential Transformer (LVDT) or transducers are placed at various positions to track the movement of the specimen. Additional information of the testing instruments is given in the following section.

3.2.3.1 Strain gauge

As its name implies, the strain gauge is a device used to measure values of strain on specimens under load. The deformation of the attached strain gauge alters its electrical resistance that can be acquired. These changes in electrical resistance values of the strain gauges are related to the mechanical strain by the gauge factor which is provided by strain gauge manufacturer.

In this testing series, we adopted 3 types of strain gauges (Figure 3.2-4) where each one is used for specific measurement. The first type is the strip gauge which is a set of small strain gauges packed together as a unit arranged and set in a specific direction. The advantages of the strip gauge are 1) all gauges are always parallel to each other and 2) the gauge spacing is known and consistence. With those advantages the strip gauge is best suited to measure strains in the extrapolation region for subsequent determination of the SCF values. It is not only reducing operator works but also reduce human errors when dealing with multiple small single strain gauges. In this testing series, the 5-element single-axis strip gauge is used. The gauge length of the strip gauge is 1 mm and the gauge pitch is 2 mm. According to the IIW (2007) recommendation, the first gauge is placed at 10 mm ($0.4t$) away weld toe perpendicular to it. The strip gauges are attached at strategic locations of interest in the vicinity of the weld along the weld toe on both brace and chord members along the region from $\rho = 90^\circ$ to $\rho = 270^\circ$.

The second type of strain gauge is the 1 mm single strain gauge as shown in Figure 3.2-4b. This small strain gauge is used specifically for measuring strain as close as possible to the weld toe (less than 1 mm). This measured strain is then used to determine NSCF. Similarly to strip gauge, the 1 mm single strain gauges are placed in the perpendicular direction to the weld toe.

The third type of the strain gauge used in the experiment is the 10 mm single strain gauge. The single gauges are attached to the brace at 600 mm away from the supports at every 90° from the top most of the brace ($\rho = 0°$). The nominal stress, σ_{nom}, is verified using these single strain gauges.

Throughout testing, the number of strain measuring locations is limited to 200 as this is the maximum number of channels available on the data acquisition unit. The example of strain gauges placement is demonstrated in Figure 3.2-4a. However, the strain gauge locations in each specimen may differ.

3.2.3.2 Alternating Current Potential Drop (ACPD)

Potential drop (PD) is an electromagnetic technique that directly estimates the crack depth based on the difference in the potential (voltage) passing through defective (V_c: cross crack voltage) and intact regions (V_r: reference voltage). The two potentials are measured by a two point contacting probe (Figure 3.2-5a). A decrease in the potential implies an initiation and propagation of the defect. Both forms of currents, direct current (DC) and alternating current (AC), are normally used. AC provides better estimation for skin cracks due to the skin effect of electrical conductors which force the current to flow in a thin layer close to the surface of the material (Lugg, 2002).

The V_c and V_r are related to crack depth through:

$$V_c = \aleph\,(S_c + 2a) \tag{3.2-1}$$

$$V_r = \aleph\,(S_r) \tag{3.2-2}$$

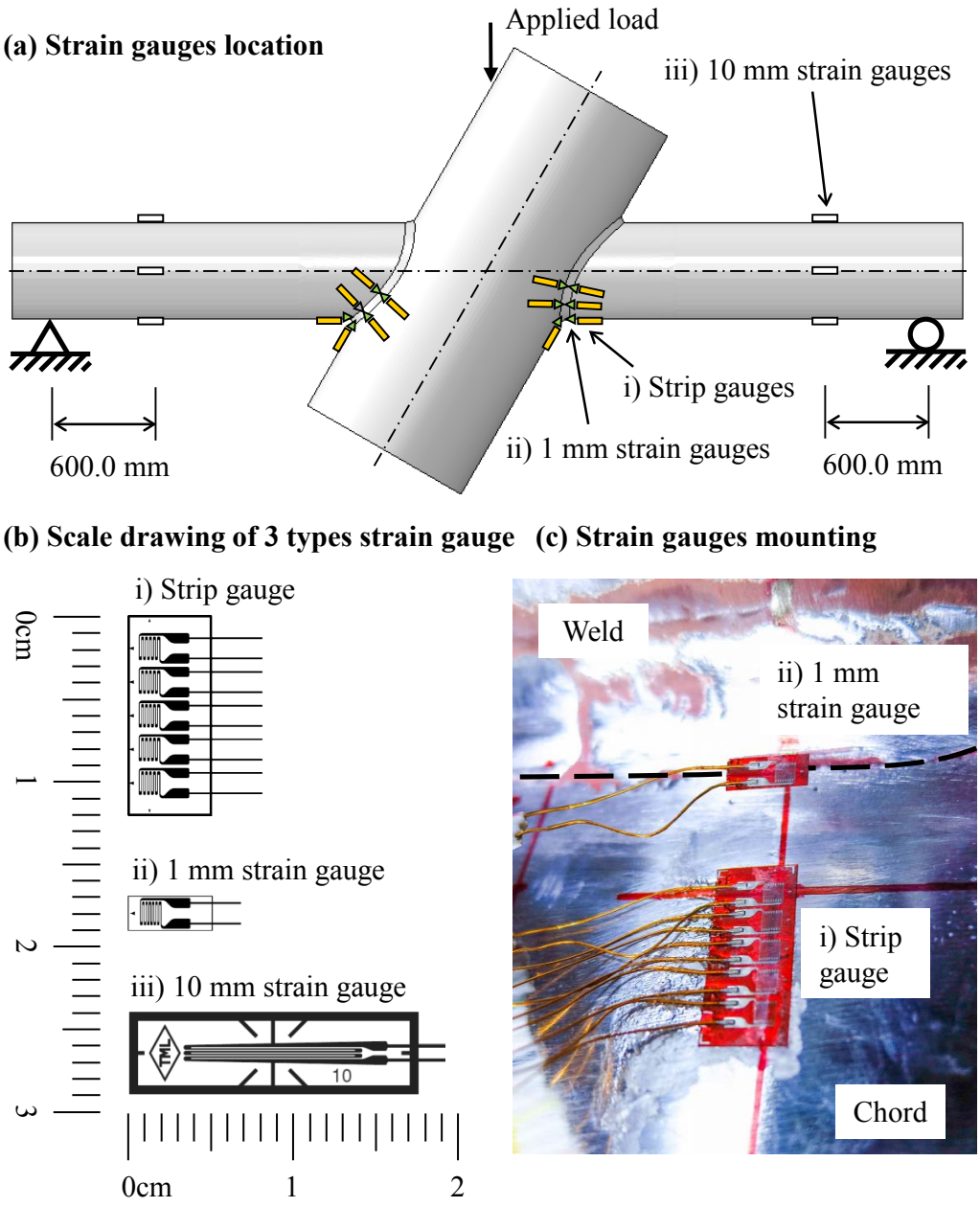

Figure 3.2-4: Type of strain gauge used in the experiment and example of strain gauge attachment to measure strains at the weld toe and extrapolation region

where, $\aleph$ is the electric field,

S_c is the cross-crack probe spacing,

S_r is the intact probe spacing, and

a is the crack depth.

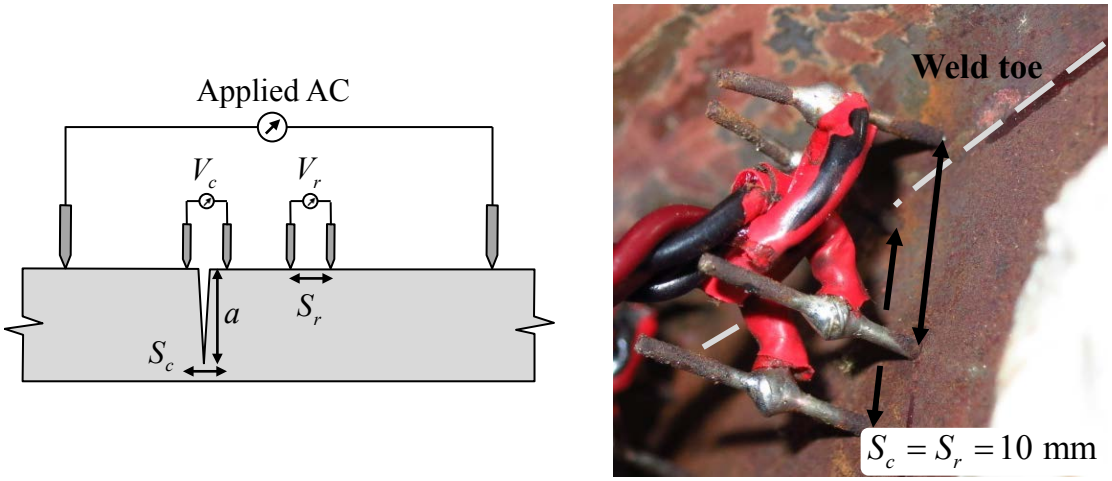

(a) Notation **(b) ACPD attachment in the experiment**

Figure 3.2-5: Applications of ACPD

The crack depth, a, can be calculated by solving Equation 3.2-1 and Equation 3.2-2 which yields:

$$a = \frac{S_r}{2}\left(\frac{V_c}{V_r} - \frac{S_c}{S_r}\right) \tag{3.2-3}$$

In this experiment, S_c and S_r are chosen to be 10 mm (Figure 3.2-5). This leads to:

$$a = 5\left(\frac{V_c}{V_r} - 1\right) \tag{3.2-4}$$

Practically, surface roughness and/or inaccurate probe spacing cause unavoidable initial crack depth. Therefore, crack depth must be initialized at the beginning of the test using the following equation:

$$a_{initialized} = a - a_0 = 5\left(\frac{V_c}{V_r} - \frac{V_{c_0}}{V_{r_0}}\right) \tag{3.2-5}$$

Equation 3.2-5 can be used to track the crack advancement in each cycle, as shown in Equation 3.2-6.

$$\Delta a = a_i - a_{i-1} = 5\left(\frac{V_{c_i}}{V_{r_i}} - \frac{V_{c_{i-1}}}{V_{r_{i-1}}}\right) \tag{3.2-6}$$

The ACPD device from TSC Inspection System (Figure 3.2-6) is used to measure the crack depth along the weld toe throughout the experiment. This test kit is able to monitor the crack depth at various locations simultaneously by spot-welding multiple probes onto the specimen. The spot-welded probes are called fixed probes. The test kit also comes with manual probe which can be employed to access the current crack depth at any location of interest.

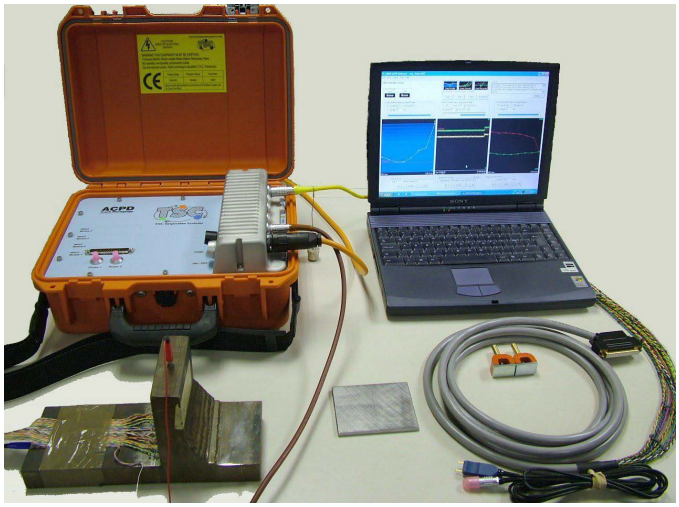

Figure 3.2-6: TSC ACPD Crack Microguage test kit

3.2.3.3 Linear Variable Differential Transformer (LVDT)

All movements of the joint either in-plane or out-of-plane are tracked using LVTD, to ensure a proper setup. There are 12 LVDTs installed during the fatigue test, as shown in Figure 3.2-7. LCDT numbers 1, 2, 7, and 8 track the displacement of the specimen in the vertical direction. The out-of-plane displacement is checked via the recorded displacement result of LVDT number 3 to 6. The displacement results from these LVDTs are used to check against the results from finite element analysis. LVDT numbers 11 and 12 track the movement of the support to ensure that the supports are firmly fixed onto ground, the LVDT record the horizontal displacement of the supports.

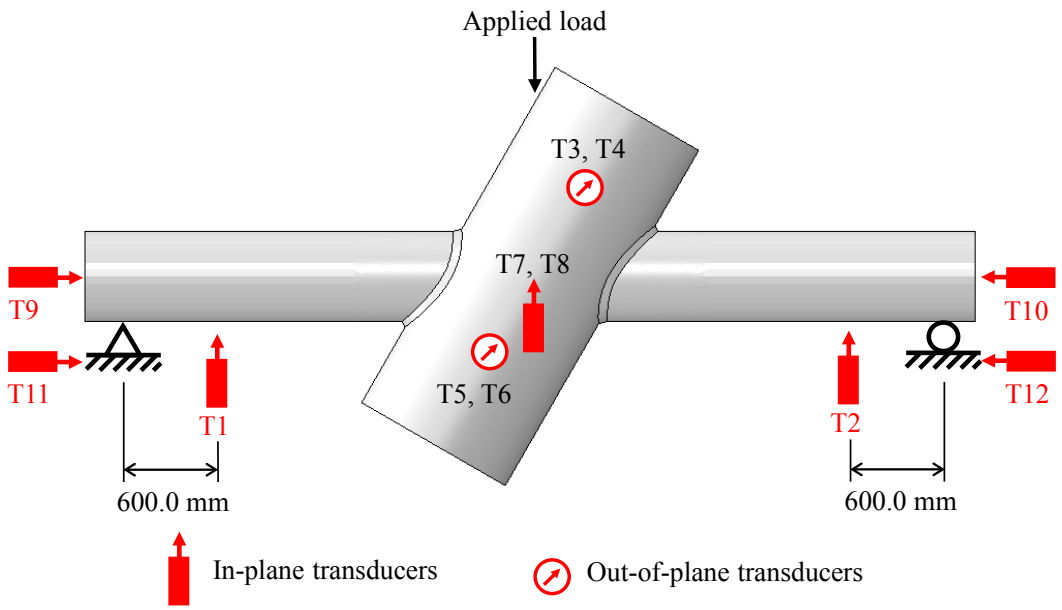

Figure 3.2-7: Locations of LVTD

3.2.4 Experimental procedure

The experimental program for each specimen involves 2 fatigue tests. The experimental procedure of each fatigue testing has two main phases, namely 1) preparation phase, and 2) fatigue testing phase. In the preparation phase, the X-joint is set up on the test rig and equipment is installed. Strain measurement is carried out to monitor the variation of strains at the weld line due to the various stages of specimen preparation including the grouting of the chord and the weld toe grinding. Thereafter, the fatigue testing phase begins. In the fatigue testing phase, the X-joint is subjected to constant-amplitude cyclic load. The loading frequency is fixed at 0.75 Hz and cyclic load ratio (minimum load to maximum load) is 0.1. The load cycle is normally paused at a certain number of cycles (11,250 and 10,000 cycles) to enable the ACPD manual probe measurement and visual inspection to counter-check the ACPD fixed probe readings. During cyclic loading, the crack depths are monitored and tracked by the ACPD instrument in real time. The fatigue testing is terminated after the deepest crack reaches 80% of the wall thickness. Subsequently the specimen is flipped by about its out of plane axis to perform the second fatigue test which follows the same procedure as described

earlier. The specimen in the J2 flipped configuration is denoted by the –F suffix. It is worth to mention that the specimen in the first cyclic test has brace misalignment type A (Figure 3.2-3a), whereas the specimen in the second cyclic test (with –F suffix) has brace misalignment of type B (Figure 3.2-3b).

The first fatigue test of the J2-1 specimen has 2 preparation stages before and after concrete grouting, denoted as J2-1 and J2-1G respectively. The second fatigue test of the J2-1 specimen is denoted as J2-1GF. For the J2-2 specimen, there are 4 preparation stages: as-welded specimen (J2-2), specimen with weld toes grinding (J2-2X), specimen with diaphragm plates installed (J2-2XP), and specimen with concrete-filled chord (J2-2XPG). The second fatigue test of the J2-2 specimen has 2 preparation stages: before and after weld toes grinding, denoted as J2-2PGF and J2-2XPGF respectively. All the preparation stages are summarized in Table 3.2-2. In the weld toes grinding preparation stage, weld toes on the chord member of the J2-2X and J2-2XPGF are ground along the tension side of the brace-to-chord intersection (from $\rho = 90^\circ$ to $\rho = 270^\circ$). In the concrete-filled grouting stage, the concrete is cured in-place for 28 days, allowing the compressive strength to be fully developed. During the curing process, temperatures on the skin of the chord at various locations are continuously measured for 36 hours. After 12 hours, the maximum temperature on the chord skin reaches its peak at 55°C which is lower than the operational temperature of the strip gauges and adhesive of 80°C (TML strain gauges datasheet). Therefore, all strain gauges are envisaged not to be damaged by heat generated during the concrete curing process.

The maximum applied cyclic load during fatigue testing is calculated based on the maximum tensile SCF from finite element analysis (see Section 4.3 and 4.4.7 for more details). To ensure that the material at the hot-spot location does not yield, the hot-spot stress is set to equal the material yield stress. The maximum applied load can be calculated by substituting Equation 2.2-5 into Equation 2.2-6. The maximum applied load can be expressed as:

$$P = \frac{2\sigma_Y I}{SCF \cdot l'd/2} \tag{3.2-7}$$

where σ_Y is the yield stress of S355 structural steel. In this study, the σ_Y of 355 MPa (BS EN 10025:1993) is used. The applied load for J2-2G and J2-2XG are as shown in Table 3.2-3.

Table 3.2-2: SCF measurement corresponding to preparation stages of J2-1 and J2-2 specimens

Specimen	Test	SCF measurement	Preparation stage			
			Weld toes condition		Diaphragm plates installed	Concrete-filled chord
			As-welded	Post-weld grinding		
J2-1	1st test: J2-1G	J2-1	✓			
		J2-1G	✓		✓	✓
	2nd test: J2-1GF	J2-1GF	✓		✓	✓
J2-2	1st test: J2-2XPG	J2-2	✓			
		J2-2X		✓		
		J2-2XP		✓	✓	
		J2-2XPG		✓	✓	✓
	2nd test: J2-2XPGF	J2-2PGF	✓		✓	✓
		J2-2XPGF		✓	✓	✓

Table 3.2-3: Applied cyclic load in fatigue test

Specimen	P_{max} [kN]	P_{min} [kN]	Load ratio, R	$\sigma_{nominal}$ [MPa]	Loading frequency [Hz]
J2-1	200	20	0.100	56.7	0.75
J2-2	235	25	0.106	66.2	0.75

3.2.5 Post weld improvement method

Fatigue cracks usually develop at the weld toe of a welded joint. Stresses along the weld toe are normally higher than the surrounding region due to geometrical discontinuity, defects left during the welding process and high tensile residual stress during the weld cooling process. Several improvement techniques have been developed to improve the fatigue properties of welds. IIW (Haagensen and Maddox, 2001) recommended four commonly used post-weld toe improvement techniques for all arc welded steel or aluminum components. They are 1) hammer peening, 2) needle peening, 3)

TIG (Tungsten Inert Gas) dressing, and 4) grinding. Besides the above improvement techniques recommended by IIW, it should be noted that Prof. Ummenhoferhas proposed the HiFIT (High Frequency Impact Treatment) method (Nüsse, 2010)which is more direct and easier to apply. However, the current study adopts the weld toe grinding as the post-weld improvement method as it requires less operator skill and special instruments. Therefore, current experiment of the grouted joint (J2-2G) adopts weld toe grinding as the post-weld improvement technique. For the weld toe grinding method, IIW (Haagensen and Maddox, 2001), grinding depth, d, and grinding radius, r, is shown in Figure 3.2-8. By controlling these 2 control parameters it is difficult to pinpoint exactly the area needed to be ground. Therefore, additional control parameter namely weld toe offset, s, is introduced to indicate the grinding location. Based on IIW recommendation (Haagensen and Maddox, 2001) for the weld toe grinding, the grinding depth, d, and grinding radius, r, were determined to be 0.5 mm and 3.0 mm respectively for this series of test. An additional control parameter, s, of 1.0 mm is introduced to precisely locate grinding region.

According to the guideline, the two-stage grinding approach is adopted to reduce a tendency of the burr to climb up the weld face and to get a more accurate grinding depth. Firstly, the 3 mm diameter grinding stone and tungsten carbide burr are used to establish a groove of the correct depth and position. Subsequently, the 6 mm diameter grinding stone is used to get the required grinding radius. The required instruments and an example of a ground weld toe are shown in Figure 3.2-9.

To measure strain before weld toe grinding, strip gauges are attached perpendicular to the weld toe with the first gauge at 10.0 mm away from the weld toe. For strain measurement at the weld toe of as-welded joint, single element strain gauges are attached as close to the weld toe as possible. However, the original weld toe after toe grinding is completely removed. A new strain measurement location in the middle of the ground weld as depicted in Figure 3.2-9 is introduced to represent strain of the ground weld. These measured strains are thereafter used to determine NSCF.

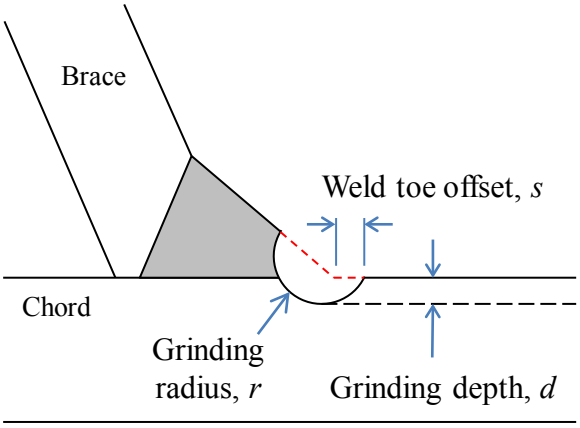

Figure 3.2-8: Guideline for weld toe grinding method (not to scale)

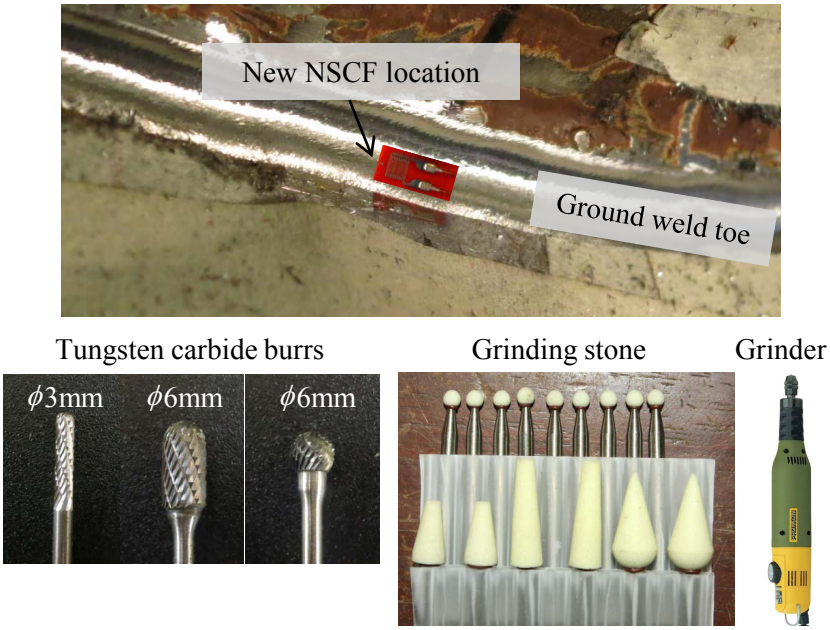

Figure 3.2-9: Example of ground weld toe with new strain measuring location and grinding instruments

3.2.6 Definitions of positions along chord-to-base intersection

Positions along the weld toe at the chord-to-base intersection are defined by the brace angle, ρ. The angle ρ is measured along the circumferential of the brace member and starts from the top fiber of the brace member. The convention adopted in this study is such that $0^\circ \leq \rho \leq 180^\circ$ in the front-half of the joint as shown in Figure 3.2-10.

For fast referencing, the brace and chord members on the left hand side are denoted as BL and CL respectively. Similarly, the brace and chord member on the right hand side are denoted as BR and CR. The member referencing may be followed by the ρ angle in order to indicate weld toe location on the referenced member, i.e., CL150 refers to the weld toe on the left hand side chord member at $\rho = 150^{\circ}$.

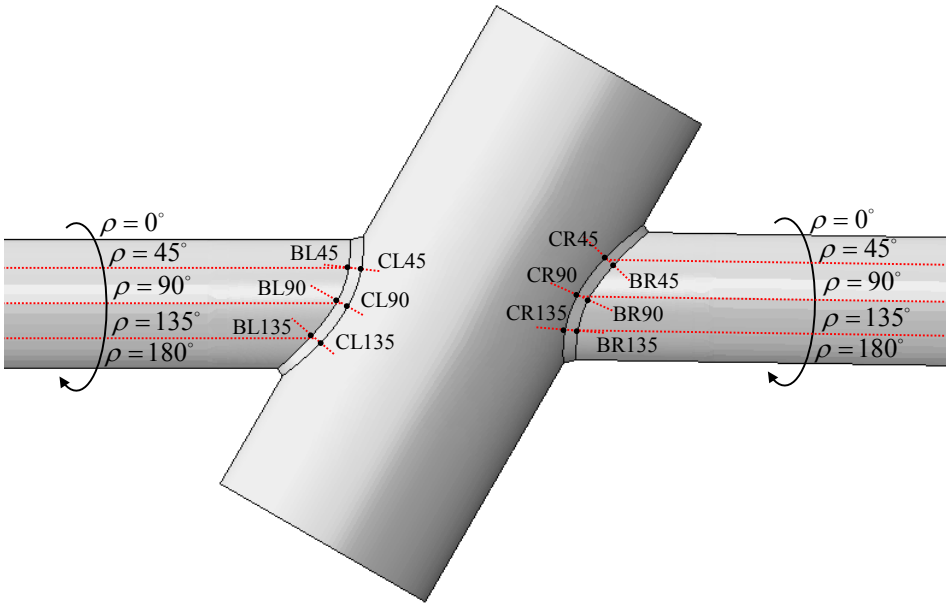

Figure 3.2-10: Weld toe positioning convention

3.3 Fatigue testing of J2-1 specimen

3.3.1 Stress concentration factors

Before the commencement of the experimental program, finite element analysis of the X-joint (to be discussed in chapter 4) is conducted to determine possible fatigue crack initiation location. The results show that stresses along the weld toe on the left side are higher than the right side of the X-joint. Therefore, more strain gauges are attached there. Throughout the fatigue testing of this specimen, 28 strain gauges were used in total. All of them are strip type strain gauges. Strip gauge locations of J2-1 joint are tabulated in Table 3.3-1.

Table 3.3-1: Location of strain gauges on J2-1 specimen

Strain gauge type	Strain gauge locations, ρ [deg]							
	J2-1, J2-1G				J2-1GF			
	BL	CL	BR	CR	BL	CL	BR	CR
Strip gauge at 0.4t from weld toe	120	120				120		120
	135	135	135	135	135	135	135	135
	150	150				150		150
	165	165				165		165
	180	180	180	180	180	180	180	180
	195	195				195		195
	210	210				210		210
	225	225	225	225	225	225	225	225
	240	240				240		240
Single gauge at < 1 mm from weld toe	180	180	180	180	180	180	180	180

The SCF and NSCF values at various preparation stages of the J2-1 specimen are tabulated in Table 3.3-2 toTable 3.3-4. The SCF values of the as-welded specimen J2-1 in Table 3.3-2 shows that SCF values on the BL and CL are higher than those on the BR and CR The hot-spot location of the J2-1 specimen is in the region between CL225 to CL240 where the SCF value is 4.28. It is also observed that, the CL member is also subjected to higher NSCF values. Both SCF and NSCF values indicate that the CL member is more prone to initial fatigue crack. After the chord member is filled with concrete, the overall SCFs around $\rho \approx 165^\circ - 195^\circ$ increase whereas the SCFs in the regions $\rho \approx 120^\circ - 165^\circ$ and $\rho \approx 195^\circ - 240^\circ$ decrease. It is observed that the rate of change of SCF values for the grouted specimen J2-1G is lower than those of the ungrouted specimen J2-1. The SCF reduction on the chord member is more significant than the SCF reduction on the brace member. As reflected in Table 3.3-3, the hot-spot location of the J2-1G is still on the CL member, and the location shifts to $\rho = 210^\circ$ with a smaller magnitude of 2.77. The J2-1GF specimen shows a similar SCF distribution trend as the J2-1G specimen. However, the overall SCFs are higher. The hot-spot

location of the J2-1GF is at CL195 with a magnitude of 3.29.

In summary, the concrete-filled approach reduces significantly the SCF values and improves substantially the fatigue performance of the J2-1G and J2-1GF specimens over the hollow section J2-1 specimen.

Table 3.3-2: Measured SCF values of J2-1 specimen

J2-1	Location	BL	CL	BR	CR
	120°	2.14	3.92		
	135°	2.24	4.05	1.41	3.65
	150°	2.08	3.16		
	165°	1.40	2.14		
SCF	**180°**	1.01	1.68	0.89	2.35
	195°	1.13	2.04		
	210°	1.63	3.40		
	225°	1.88	**4.28**	1.51	3.28
	240°	2.37	**4.28**		
NSCF	**180°**	2.47	4.18	0.84	1.24

Table 3.3-3: Measured SCF values of J2-1G specimen

J2-1G	Location	BL	CL	BR	CR
	120°	1.07	1.68		
	135°	1.45	2.17	1.09	2.57
	150°	1.93	2.50		
	165°	1.98	2.52		
SCF	**180°**	1.95	2.75	0.86	2.44
	195°	1.82	2.56		
	210°	1.63	**2.77**		
	225°	1.25	2.41	1.36	2.77
	240°	1.19	1.84		
NSCF	**180°**	4.82	9.79	2.23	2.86

Table 3.3-4: Measured SCF values of J2-1GF specimen

J2-1GF	Location	BL	CL	BR	CR
	120°		2.07		2.33
	135°	1.75	2.63	1.44	2.82
	150°		3.02		2.83
	165°		3.05		2.85
SCF	**180°**	2.27	2.91	1.34	2.95
	195°		**3.29**		2.81
	210°		3.02		2.9
	225°	1.66	2.52	1.45	2.75
	240°		1.83		2.39
NSCF	**180°**	4.03	5.22	1.94	3.84

3.3.2 Fatigue crack initiation and propagation of J2-1G specimen

Prior to the fatigue testing of J2-1G and J2-1GF specimens, the ACPD fixed probes are installed. The fixed probes which are used to send electrical currents to the joint are spot-welded at various locations along the weld toe. Since the preload test results show that crack is likely to initiate on the left chord in the vicinity of $\rho = 180°$, the fixed probes are densely spot-welded around that area. The locations of the fixed-probe are tabulated in Table 3.3 5. It can be observed that the precision of fixed probe locations are relatively high especially on CL of J2-1G specimen. Those fixed probe locations are in fact determined based number of probes needed in between two strain gauge locations. For example, between CL165-CL180 where there are 3 fixed probes in between, the fixed probe locations are in the increment of $\rho = 3.75°$ from CL165. To achieve the level of accuracy in the experiment, the ρ angle on the brace member is precisely divided and carefully projected onto the chord weld toe. The center of the probe is kept as close as to the projected ρ angle as possible. It is worthwhile to mention that the ρ angle of $1°$ is equivalent to approximately 5 mm which is relatively large as compare to the probe size ($\sim$1 mm in diameter). Therefore the accuracy of $\rho = 0.25°$ or 1.25 mm is achievable.

Table 3.3-5: ACPD fixed probe locations on J2-1G and J2-1GF specimen

Measuring equipment	ACPD fixed probe location, ρ [deg]							
	J2-1G				J2-1GF			
	BL	CL	BR	CR	BL	CL	BR	CR
ACPD	155	140	150	150	150	140	165	160
	160	145	165	165	157.50	145	195	170
	170	153.75	195	195	165	155		175
	175	157.50	210	210	172.50	157.50		185
	185	161.25			187.50	160		190
	190	168.75			195	170		200
	200	172.50			202.50	172.50		
	205	176.25			210	175		
		183.75				185		
		187.50				187.50		
		191.25				190		
		198.75				200		
		202.50				202.50		
		206.25				205		
		215				215		
		220				220		

In the fatigue test of J2-1G specimen, the first crack emerges on the CR member at $\rho = 145^\circ$ after 150,000 cycles. The second crack is observed at about 10,000 cycles after the first crack on the CL member at $\rho = 180^\circ$. The width of each crack is approximately 3 mm measured along the surface of chord. It is interesting to note that in this case, the first crack does not initiate at the hot-spot location. This is most likely due to the local effects or material defects in the vicinity.

During the fatigue test, the crack on the CR propagates downward from CR145 to CR180 and forms a single crack. The crack propagates until its width reaches $\sim$200 mm, and thereafter it stops propagating. The ACPD measurement in Figure 3.3-1 shows the deepest crack is at CR150 which is close to the first observed crack (CR145). The deepest crack location changes due to the fact that the SCF level rises towards $\rho = 180^\circ$.

Dye penetrant is performed during the fatigue test to check cracks which could not be observer or detected by ACPD instrument. The inspecting area is firstly cleaned by cleaning spray. Thereafter the penetrant (red color) are sprayed over the area and leave it around 30 minutes to allow the penetrant to soak into cracks. After the excessive penetrant has been removed, the developer (white color) is sprayed on top of the area. When the developer dried, it draws the penetrant from the crack out onto the surface to form visible indication, known as bleed-out. The more the bleed-out, the deeper the crack should be. The dye penetrant test performed at the end of the test as shown in Figure 3.3-2 reveals that the major crack on the CR member covers the area from CR140 to CR180. Moreover the dye penetrant result agrees well with the ACPD measurement.

On the left chord, the major crack at CL180 propagates upward in both left and right directions during fatigue test. At the same time multiple small cracks initiate over CL120 to CL240 and coalesce with the major crack to finally form a single large crack across CL140 to CL220. The ACPD measurement in Figure 3.3-3 shows that the crack covers a large area from CL140 to CL 220 and that the deepest crack is at CL175. The dye penetrant test in Figure 3.3-4 shows the same finding as the ACPD measurement.

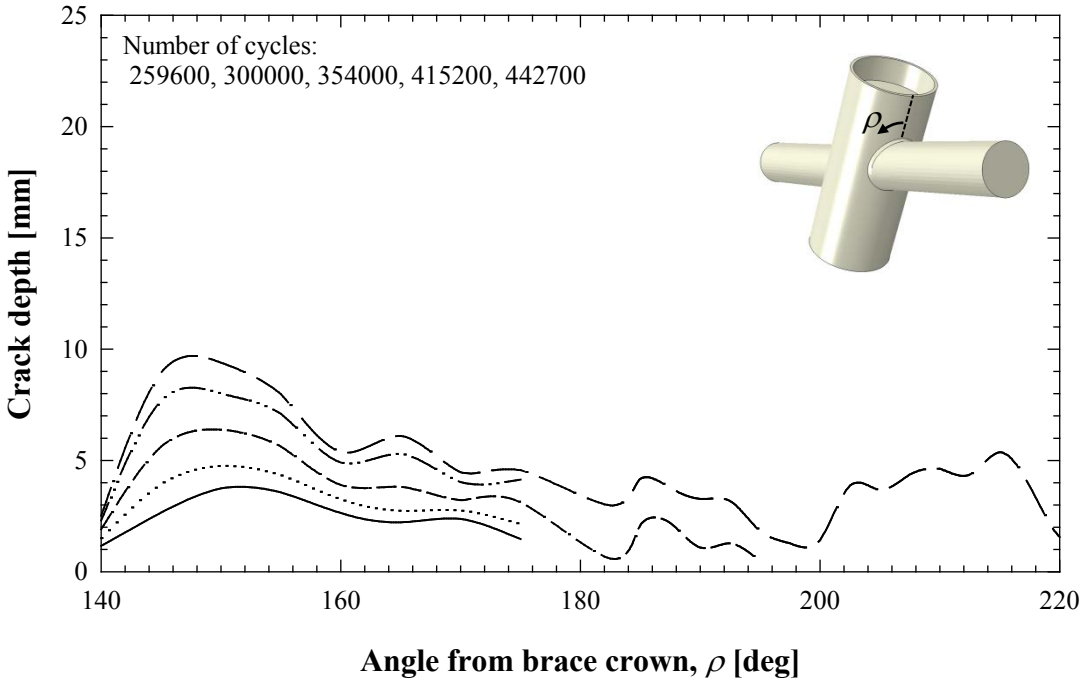

Figure 3.3-1: Crack profile on CR of J2-1G

Figure 3.3-2: Dye penetrant test on CR of J2-1G

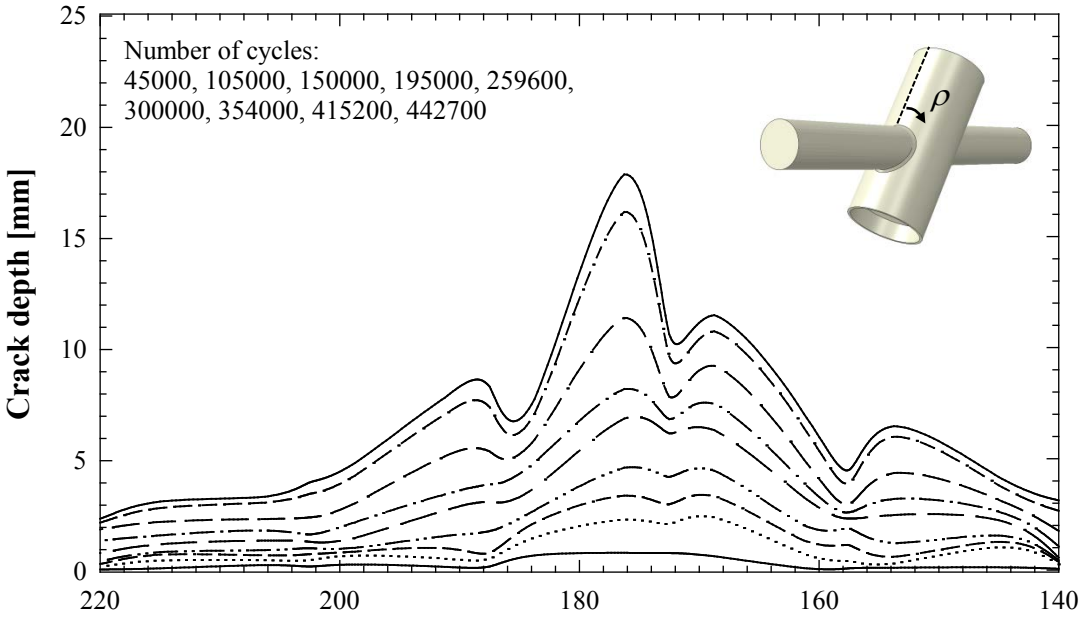

Figure 3.3-3: Crack profile on CL of J2-1G

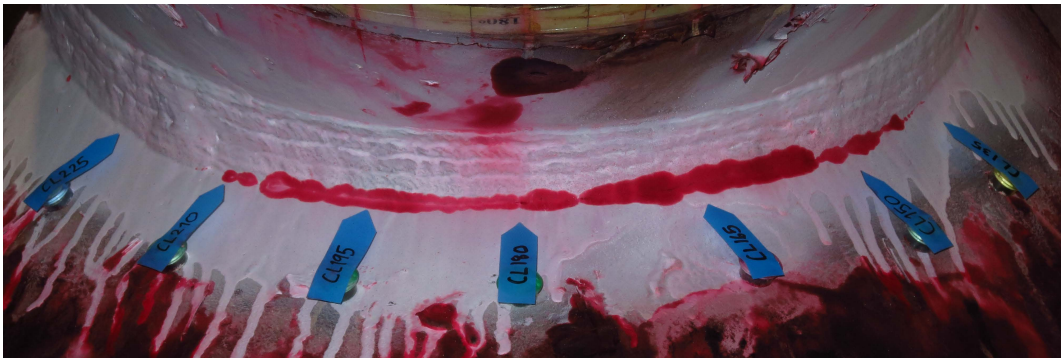

Figure 3.3-4: Dye penetrant test on CL of J2-1G

3.3.3 Fatigue crack initiation and propagation of J2-1GF specimen

The first observed crack in the J2-1GF fatigue test is at the hot-spot location, CL195. It is observed after 120,000 cycles, the width of the crack is 3 mm. The crack growth pattern is similar to what is observed in the previous test where the crack propagates upwards in both left and right directions. Towards the end of the test, the first crack coalesces with other cracks to form a single long crack. After the test is terminated, this crack covers the area from CL157.5 to CL220. ACPD measurements illustrated in Figure 3.3-5 indicate that the crack on the CL member covers the range CL157.5 to CL220 and that the deepest crack is at CL190. The width of the crack is approximately 200 mm measured along the chord member surface.

On the right chord, one crack emerges at CR190 after 180,000 cycles. This crack grows more slowly than the crack on the CL member. The final width of this crack is 25 mm. Two cracks emerged adjacent to the CR190 crack towards the end of the test. The ACPD measurement of the CR crack is shown in Figure 3.3-6.

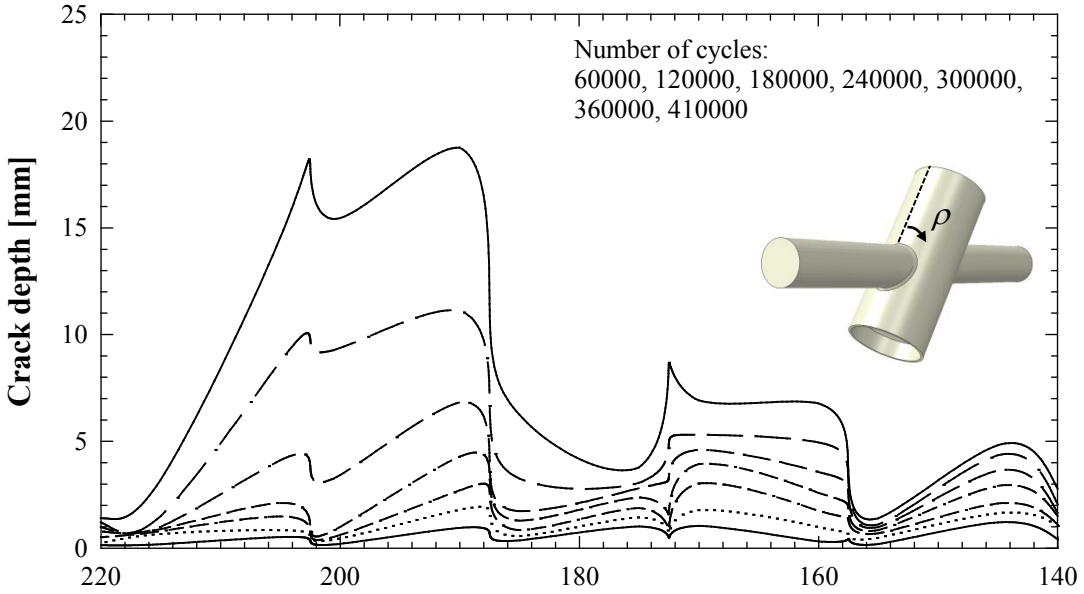

Figure 3.3-5: Crack profile on CL of J2-1GF

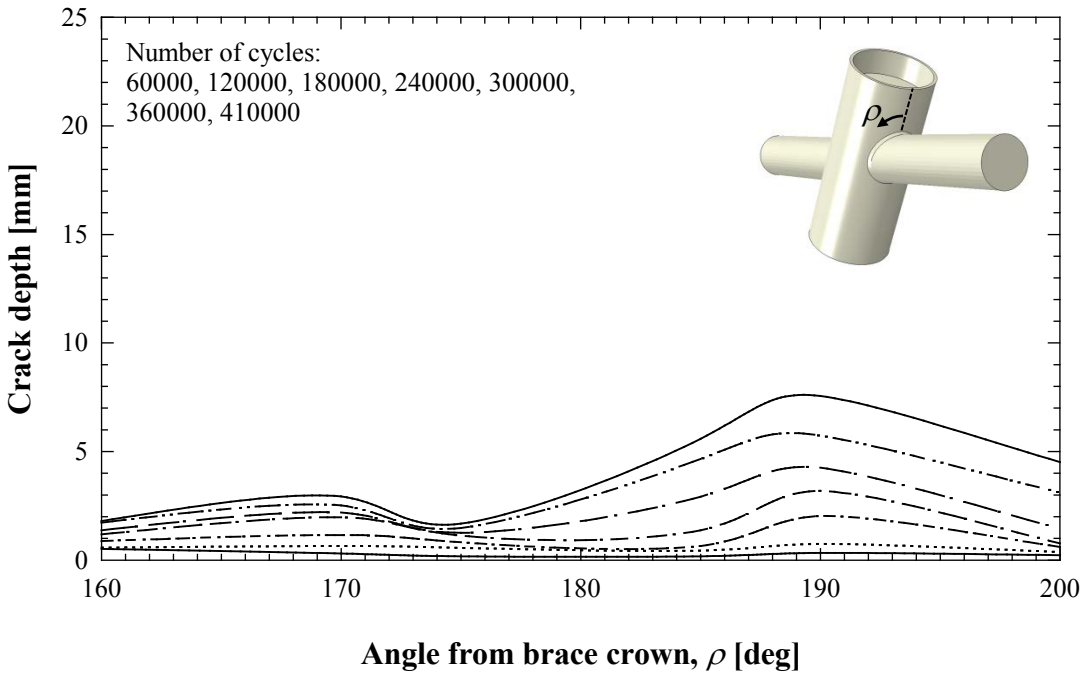

Figure 3.3-6: Crack profile on CR of J2-1GF

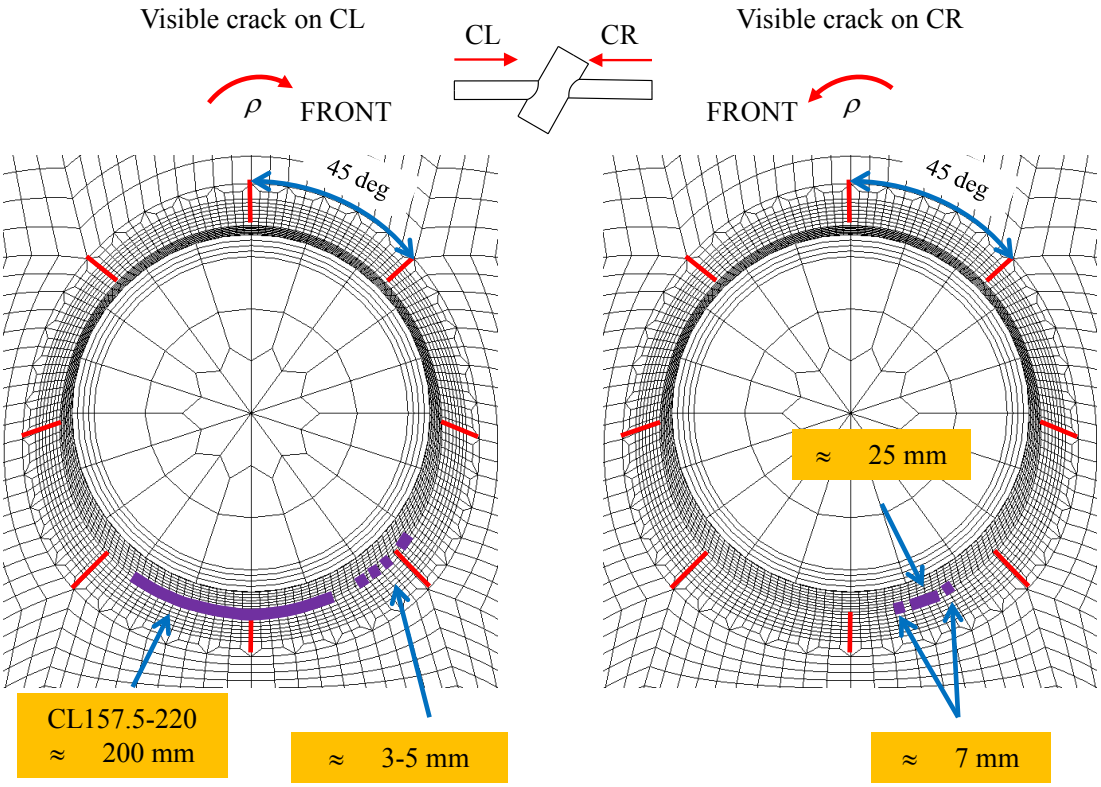

Figure 3.3-7: Visible crack from eye observation of J2-1GF

In practice, the fatigue crack initiation phase is difficult to justify and highly depends on the scale of measurement. ABS (2010) guidelines recommend that the crack is in the initiation phase if the crack depth is less than 0.5 mm ($a \leq 0.5$ mm). Therefore, the crack initiation in this study corresponds to the crack depth of 0.5 mm as measured by ACPD instrument. The crack growth curve of J2-1G specimen in Figure 3.3-8 shows that the crack initiation life of CL176.25 is only about 7% of the total fatigue life. Similarly, Figure 3.3-9 shows that fatigue crack initiation life of the CL190 crack is only 9% of the total fatigue life.

In the two fatigue tests, the fatigue crack on the left side of the chord member has a faster growing rate than the rest of the cracks observed during the test, especially near the final stage of the fatigue test. The faster crack propagation rate derives essentially from the higher stresses driving the fatigue crack initiation and propagation on the left side of the brace, as evidenced by the large SCF values on the left side of the joint

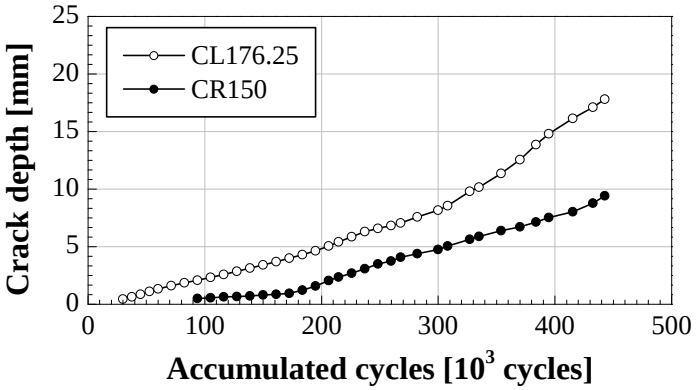

Figure 3.3-8: Fatigue crack growth of the two deepest cracks of J2-1G specimen

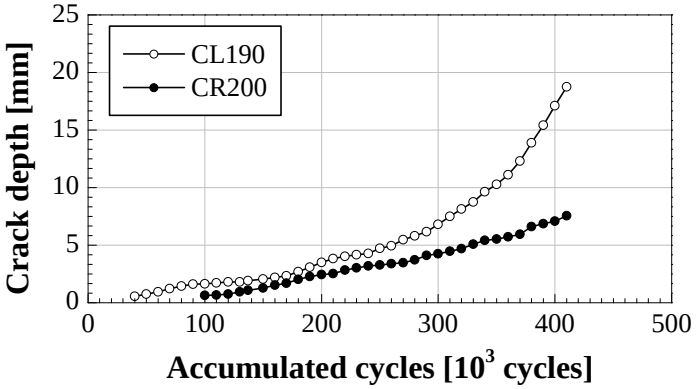

Figure 3.3-9: Fatigue crack growth of the two deepest cracks of J2-1GF specimen

3.3.4 Fatigue performance based on S-N curves

The fatigue performance can be determined from 3 different stress definition - hot-spot stress, notch stress, and nominal stress. Four hot-spot stress S-N curves are compared in this study - API RP 2A (2002) X and X' curves, API RP 2A (2007), and CIDECT (2001). For notch stress S-N curve, only the DNV RP C203 (2011) is used as a benchmark. In terms of nominal stress, AWS DT1.1 (2008) is chosen. All these standards takes the specimen thickness correction into account.

The comparison of fatigue life predicted using S-N curves from various design guidelines to the fatigue life from fatigue testing is illustrated in Figure 3.3-10 and Figure 3.3-11. In Figure 3.3-10, the number of cycles at the first point of each data corresponds to the number of cycles at fatigue crack initiation and the second (end) point indicates the number of cycles at the end of the test. The fatigue performance of the J2-1G specimen based on the hot-spot stress S-N curve clearly passes the requirements of API (2002) for both X and X' curves, whereas it is slightly lower than the requirements of DNV (2011), CIDECT (Zhao et. al., 2001) and API (2007). The fatigue performance based on notch stress passes the requirement of DNV (2011). Based on the nominal stress S-N curve, the fatigue performance of the joint is relatively far from the requirement of the IIW (Hobbacher, 2007) FAT 50 curve which is recommended for a partial penetration weld or fillet weld. In contrast, it meets the requirement of AWS (2008) which apply to circular sections with a CJP groove weld.

As illustrated in Figure 3.3-11, the flipped joint (J2-1GF) shows great fatigue performance using the hot-spot stress approach. It passes all the hot-spot stress S-N curves. In terms of the notch stress range (the highest NSCF of J2-1GF is around 60% of J2-1G), the performance of the joint does not meet the requirement of DNV (2011). Similar to J2-1G, the fatigue performance based on nominal stress approach remains below the estimate by the IIW (Hobbacher, 2007) FAT50 curve, as the small applied nominal stress range is expected to have a longer fatigue life. However, the test results

of J2-1GF pass the requirement of the DT curve stipulated by AWS (2008). The latter is recommended for tubular joints with a CJP groove weld.

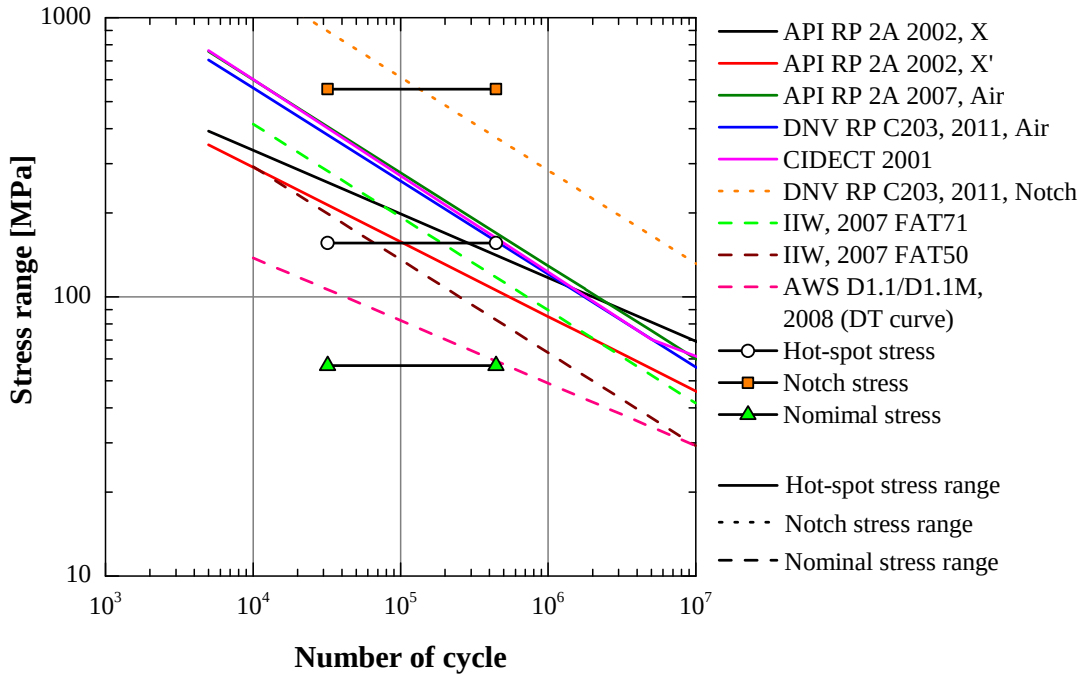

Figure 3.3-10: Fatigue performance of J2-1G joint based on S-N curves approach

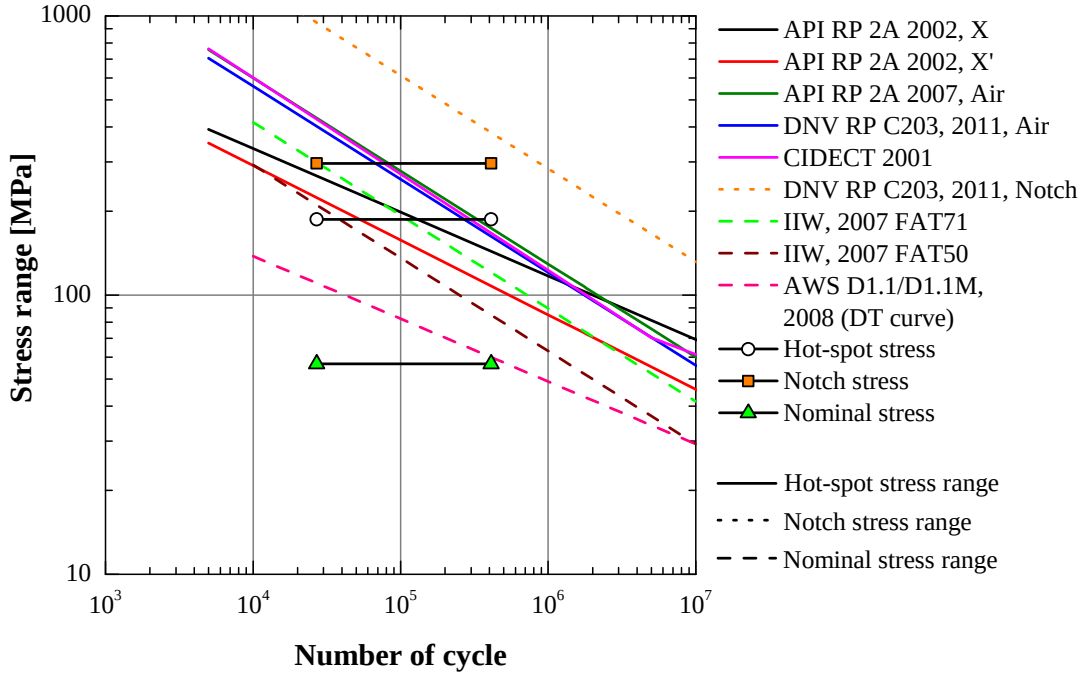

Figure 3.3-11: Fatigue performance of J2-1GF joint based on S-N curves approach

3.4 Fatigue testing of J2-2 specimen

3.4.1 Stress concentration factors

Similar to the previous J2-1 specimen, the possible crack initiation sites are predetermined by finite element analysis which will be discussed in Chapter 4. There are 38 strain gauges used in the fatigue test of this specimen: 22 of those are strip type strain gauges, and the remaining 16 are single element strain gauge. However, the locations are slightly different from those used in J2-1 specimen, as indicated in Table 3.4-1. The strain gauges are heavily placed on BL, CL, and CR as the measured SCF values of the J2-1 specimen are high in this region. The fatigue tests of J2-1 specimen also show that fatigue cracks developed in this area.

Table 3.4-1: Location of strain gauges on J2-2XG and J2-2XGF

Strain gauge type	Strain gauge locations, ρ [deg]			
	BL	CL	BR	CR
Strip gauge at 0.4*t* from weld toe		120		120
	140	140	140	140
	160	160		160
	180	180	180	180
	200	200		200
	220	220	220	220
Single gauge at < 1 mm from weld toe		240		240
	140	140	140	140
		160		160
	180	180	180	180
		200		200
	220	220	220	220

The measured SCF and NSCF values of the J2-2 specimen at various preparation stages are tabulated in Table 3.4-2 to Table Table 3.4-5. The as-welded joint J2-2 shows higher SCF values on the left-chord compared to the right-chord. The hot-spot location

is at CL240 with the magnitude of 4.81, as indicated in Table 3.4-2. The hot-spot SCF value and its location are comparable to those measured in the previous as-welded joint J2-1 reported earlier in Table 3.3-2.

After the weld toe grinding, the measured SCF values on chord members of the J2-2X joint decrease slightly. This indicates that the post-weld toe grinding does not significantly affect the stress strain field in the SCF extrapolation region. The hot-spot of the J2-2X joint is unchanged from the J2-2 joint. The NSCF values on the chord member of the J2-2X specimen are significantly higher than those measured in the J2-2 specimen. The NSCF values are around 2 times those observed in the J2-1 specimen. The trend is reasonable as a circular hole in the infinite plate induces the stress concentration by a factor of 3. It is interesting to see if the weld toe grinding which creates a smooth transition at the weld toe and removes weld toe imperfections will enhance fatigue performance of the joint.

The reduction of the SCF and NSCF values are more pronounced after the diaphragm plates are installed. Stiffening the chord by diaphragm plates relocate the hot-spot location to CL200 and the hot-spot SCF value is observed to decrease by 40%. In addition, variation of SCF values along the weld toes is gentler. Further stiffening of the chord by concrete-filled slightly decreases overall SCF and NSCF values.

The as-welded joint with concrete-filled chord J2-2PGF shows the higher SCF and NSCF values on the CR member. This differs from all the previously tested specimens where the SCF and NSCF values are more critical on the CL member. The hot-spot locations of this joint are at CR140 and CR180 with the SCF and NSCF values of 3.06 and 4.60 respectively. After performing the post-weld improvement, the overall SCF values drop by around 10% similar to what is observed in the J2-2X specimen. However, the SCF and NSCF values on the CR member remain more critical than those on the CL member. The hot-spot location of the J2-2XPGF remains at CR140.

Table 3.4-2: Measured SCF and NSCF values for J2-2

J2-2	Location	BL	CL	BR	CR
	120°		4.29		2.44
	140°	2.06	3.91	1.38	3.46
	160°	1.49	2.50		2.51
SCF	**180°**	0.97	1.26	0.81	2.05
	200°	1.27	2.86		2.16
	220°	1.97	4.52	1.23	2.59
	240°		**4.81**		1.95
	140°	4.23	6.48	1.85	4.30
	160°		3.80		4.34
NSCF	**180°**	1.45	2.32	1.32	3.67
	200°		3.81		3.96
	220°	3.69	6.44	1.38	3.96

Table 3.4-3: Measured SCF and NSCF values for J2-2X

J2-2X	Location	BL	CL	BR	CR
	120°		4.12		2.40
	140°	2.03	3.72	1.34	3.24
	160°	1.46	2.40		2.39
SCF	**180°**	0.97	1.15	0.81	1.88
	200°	1.26	2.73		2.05
	220°	1.91	4.19	1.25	2.46
	240°		**4.64**		1.91
	140°	4.22	11.1	1.82	7.30
	160°		7.23		7.17
NSCF	**180°**	1.45	5.02	1.33	5.60
	200°		6.88		6.19
	220°	3.61	11.82	1.41	6.07

Table 3.4-4: Measured SCF and NSCF values for J2-2XP

J2-2XP	Location	BL	CL	BR	CR
	120°		1.88		2.41
	140°	1.63	2.57	1.09	2.50
	160°	2.02	2.82		2.45
SCF	**180°**	1.92	2.19	1.01	2.25
	200°	1.89	**2.90**		2.29
	220°	0.84	2.68	1.30	2.42
	240°		1.86		1.92
	140°	3.42	8.08	1.53	5.85
	160°		8.72		7.48
NSCF	**180°**	2.89	9.50	1.63	6.94
	200°		7.48		7.07
	220°	2.79	7.95	1.51	6.19

Table 3.4-5: Measured SCF and NSCF values for J2-2XPG

J2-2XPG	Location	BL	CL	BR	CR
	120°		1.89		2.28
	140°	1.52	2.34	1.05	2.41
	160°	1.85	2.47		2.27
SCF	**180°**	1.72	1.91	1.00	2.07
	200°	1.70	**2.56**		2.16
	220°	0.76	2.46	1.21	2.30
	240°		1.90		1.82
	140°	3.18	7.41	1.46	5.56
	160°		7.70		7.02
NSCF	**180°**	2.62	8.42	1.59	6.53
	200°		6.63		6.78
	220°	2.58	7.37	1.43	5.89

Table 3.4-6: Measured SCF and NSCF values for J2-2PGF

J2-2PGF	Location	BL	CL	BR	CR
	120°		1.56		2.30
	140°	1.74	2.18	1.18	**3.00**
	160°	1.74	2.35		2.74
SCF	**180°**	2.22	2.71	1.30	**3.06**
	200°	1.69	2.47		2.83
	220°	1.61	2.48	1.30	2.57
	240°		1.93		1.72
	140°	2.01	2.98	1.90	4.15
	160°		2.94		3.69
NSCF	**180°**	3.07	3.12	1.97	4.60
	200°		3.16		3.91
	220°	2.62	2.95	1.50	4.02

Table 3.4-7: Measured SCF and NSCF values for J2-2XPGF

J2-2XPGF	Location	BL	CL	BR	CR
	120°		1.45		2.00
	140°	1.67	1.99	1.13	**2.93**
	160°	1.69	2.11		2.43
SCF	**180°**	2.16	2.42	1.24	2.78
	200°	1.68	2.33		2.64
	220°	1.57	2.24	1.29	2.23
	240°		1.69		1.55
	140°	1.98	6.76	1.87	6.98
	160°		6.11		8.45
NSCF	**180°**	3.01	6.94	1.89	6.10
	200°		6.87		7.67
	220°	2.53	6.87	1.44	7.00

3.4.2 Fatigue crack initiation and propagation of J2-2XPG specimen

The previous section reviews that the crack will most likely initiate on the left-chord. Therefore, ACPD fixed probes are heavily spot-welded in this region to capture the crack initiation event and track the propagation of the fatigue crack. The locations of the ACPD fixed in the J2-2XPG and J2-2XPG specimens are tabulated in Table 3.4-8.

Table 3.4-8: ACPD fixed probe locations of J2-2XPG and J2-2XGPF

Position	ACPD fixed probe location, ρ [deg]			
	Brace Left (BL)	**Chord Left (CL)**	**Brace Right (BR)**	**Chord Right (CR)**
ACPD	146.7	130	175	165
	153.4	135	185	170
	166.7	145		175
	173.4	150		185
	186.7	155		190
	193.4	165		195
	206.7	170		
	213.4	175		
		185		
		190		
		195		
		205		
		210		
		215		
		225		
		230		

In this test, two cracks are observed after 300,000 cycles. The first crack is at CL190 that is close to the hot-spot location (CL200). The second crack is at BL190. The widths of the CL190 and BL190 cracks are 15 mm and 30 mm respectively. The difference in the crack sizes seems to imply that the BL190 crack initiated before the CL190 crack. This is unexpected because not only is the SCF value at BL190 lower than at CL190, the NSCF value at BL190 is also lower than the NSCF value at CL190.

The crack on the left-chord member initiates at CL190 and subsequently propagates in both upward and downward directions. Another crack initiates at CL155 after 650,000 cycles with the width of 3 mm. Subsequently, these two cracks coalesce to form a single long crack covering the region of CL145 to CL225.

On the other hand, after the crack on the left-brace member initiates at BL190, the second crack on the left-brace is observed at BL165 after 380,000 load cycles with a width of 3 mm. Later, these two cracks coalesce to form a single crack. This crack starts from BL157.5 to BL190. Figure 3.4-1 and Figure 3.4-2 show ACPD measurement of the BL and CL crack. Figure 3.4-3 shows dye penetrant test after the fatigue test was terminated at 760,000 cycles.

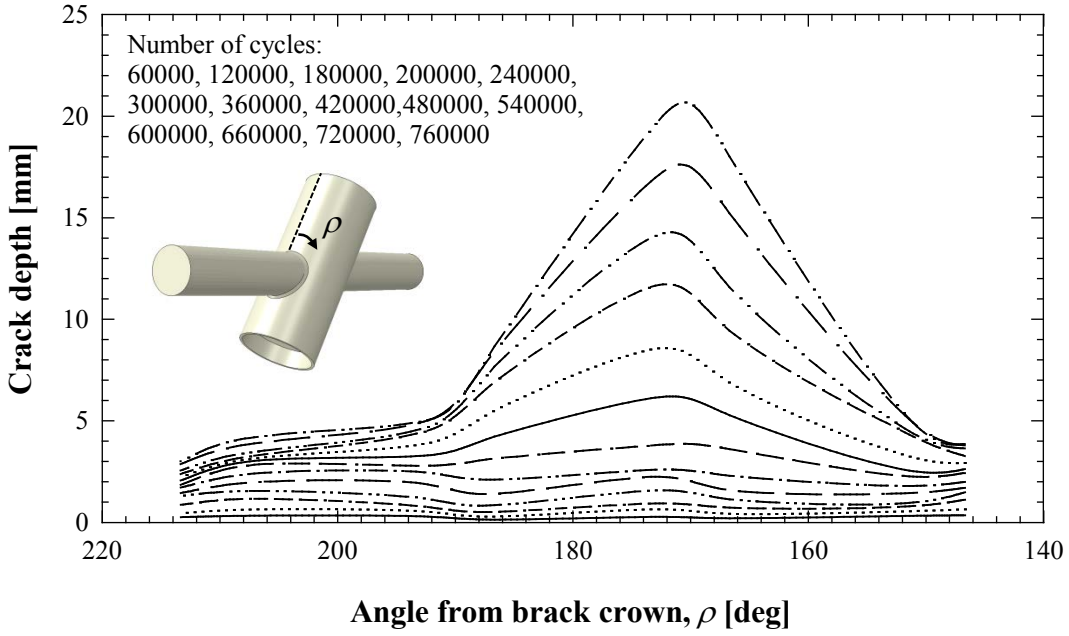

Figure 3.4-1: Fatigue crack growth profile on the left-brace of J2-2XPG

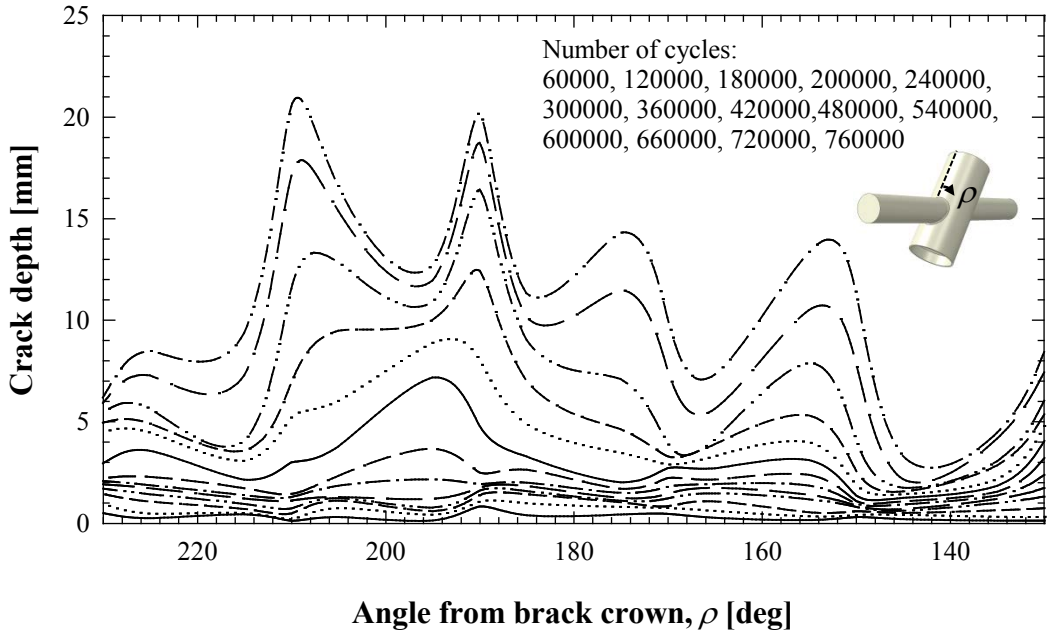

Figure 3.4-2: Fatigue crack growth profile on the left-chord of J2-2XPG

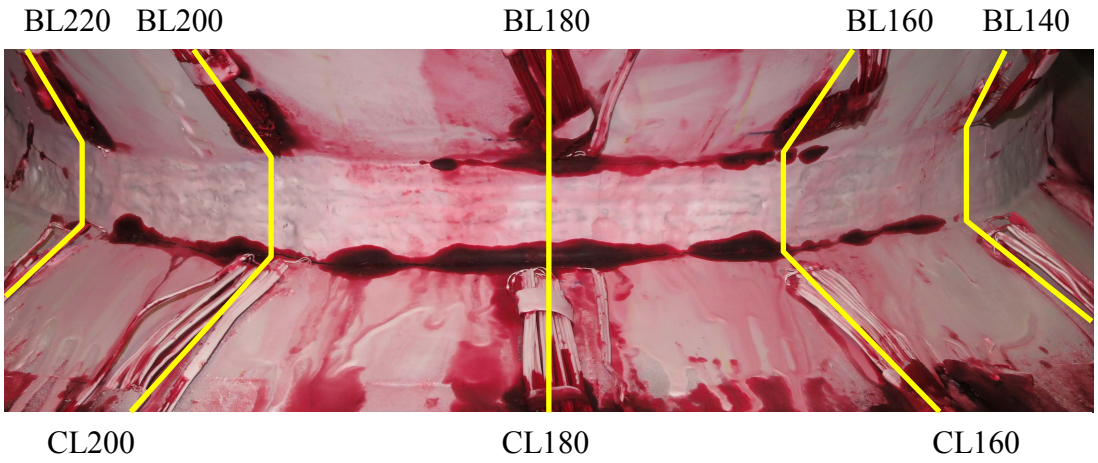

Figure 3.4-3: Final fatigue crack of J2-2XG on the left-side

3.4.3 Fatigue crack initiation and propagation of J2-2XPGF specimen

The ACPD locations adopted in this test are the same as those of the previous test (see Table 3.4-8). Although the number of probes on the left chord is more than that on the right chord, the same density of probes in the region between $\rho = 180^\circ$ and $\rho = 200^\circ$ is maintained. Based on the previous 3 fatigue tests, this is the region where

the critical fatigue crack initiates. If crack happens to initiate and tends to propagate outside the probe covering area, probe relocation will be performed.

After the fatigue test passes the 300,000 load cycles, the first fatigue crack is observed to initiate at CL190. The width of the crack is 4 mm. This location is close to the highest measured values of SCF and NSCF (CL180) on the left-chord. The second crack is noticed at 50,000 cycles after the first crack at CL135 with a width of 3 mm. This is an unexpected crack because both SCF and NSCF values at CL135 are smaller than those at the hot-spot location.

During the fatigue test, the first crack initiated at CL190 propagates in both upward and downward directions. After the termination of the fatigue test, this crack covers the region from CL170 to CL220 as shown in Figure 3.4-4 and Figure 3.4-5. The second crack covers a small area from CL130 to CL140 and does not propagate significantly further. Figure 3.4-4 illustrates the fatigue crack profile on the left-chord generated from the ACPD measuring data. The crack area from the ACPD fixed probe measurement agrees reasonably well with the actual crack. The ACPD results also show that the deepest crack locates at CL195 which is close to the location where the first crack initiated. The fatigue test is terminated after the CL195 crack reaches 20.55 mm at 980,000 load cycles.

At the end of the test, the deepest crack depth of the J2-2XPG specimen on the left-brace is 19.33 mm (located at BL173.3) and the deepest crack depth on the left-chord is 20.51 mm (located at CL210). The fatigue crack growth curves in Figure 3.4-6 indicate that crack growth rates of the BL173.3 and CL210 cracks are close up to 600,000 cycles. Thereafter the fatigue crack growth rate of the CL210 crack increases while the crack growth rate of the BL173.3 crack remains unchanged.

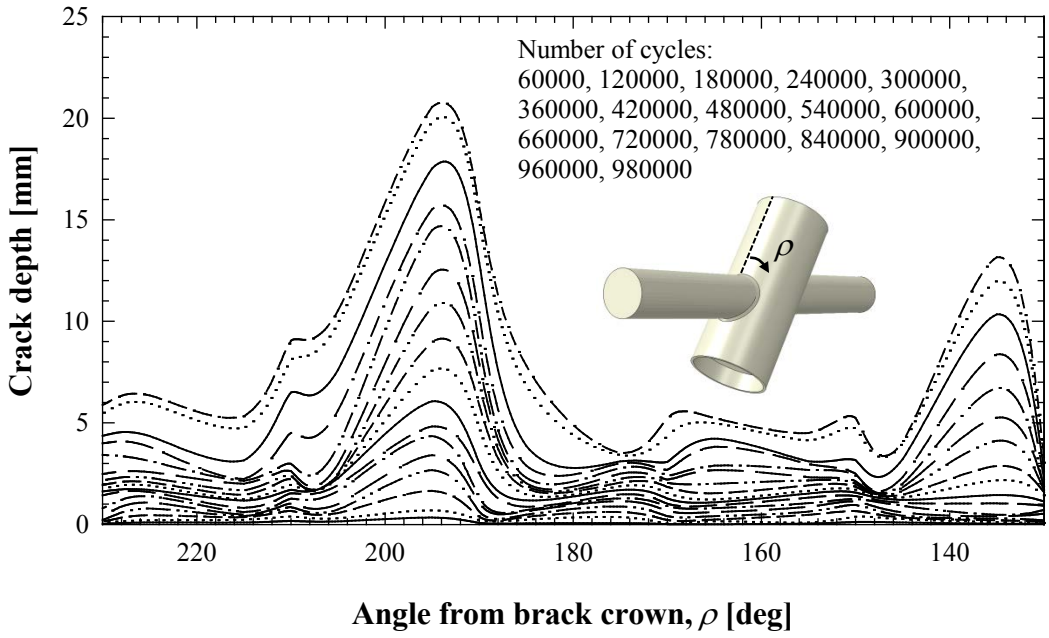

Figure 3.4-4: Fatigue crack growth profile on the left-chord of J2-2XPGF

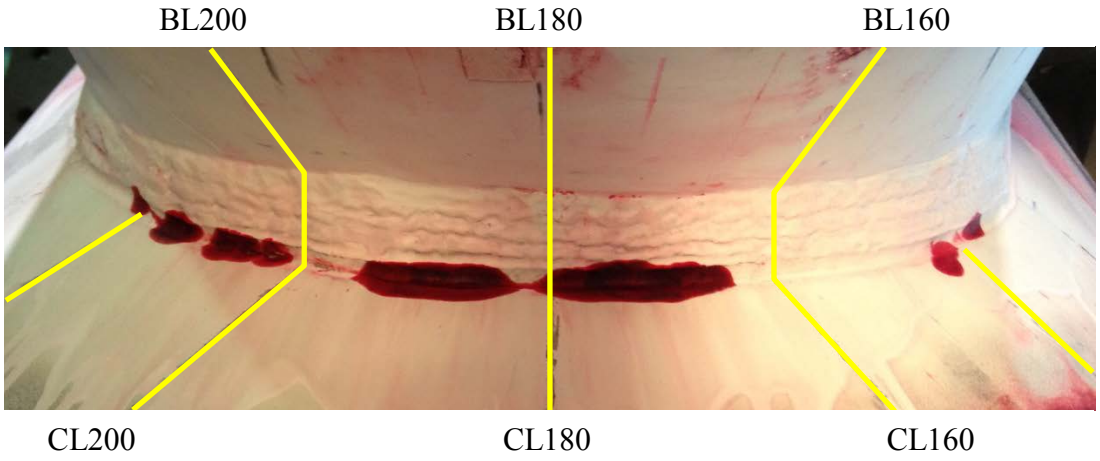

Figure 3.4-5: Final fatigue crack of J2-2XPGF on the left-side

The fatigue crack growth curves of J2-2XPG specimen at CL135 and CL195 are shown in Figure 3.4-7. The crack propagation rates at the two locations are approximately the same for the entire fatigue life. However, Figure 3.4-7 reveals that the CL195 crack initiated before the CL135 crack which agree with what is observed in the experiment. The fatigue crack initiation of the J2-2XPGF specimen, corresponding to the 0.5 mm crack depth of the CL195 crack, is at 103,000 loading cycles.

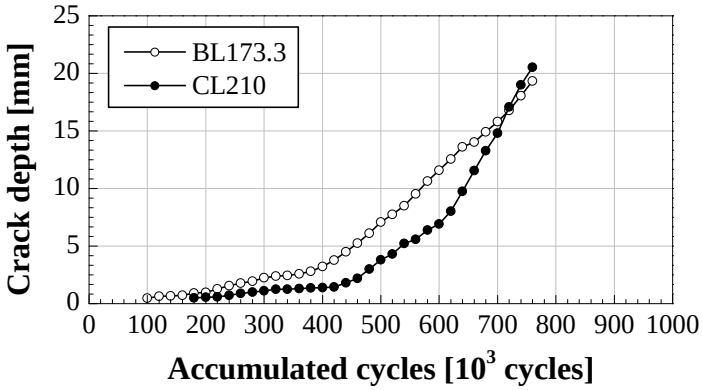

Figure 3.4-6: Fatigue crack growth of the two cracks of J2-2XPG specimen

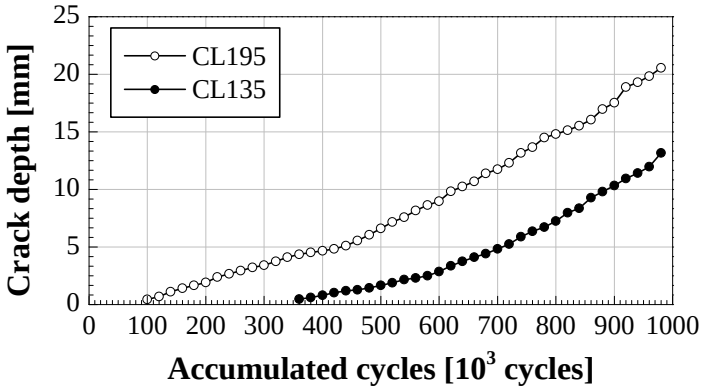

Figure 3.4-7: Fatigue crack growth of the two cracks of J2-2XPGF specime

3.4.4 Fatigue performance based on S-N curves

The fatigue performance of the J2-2XG joint compared to various recommended S-N curves is illustrated in Figure 3.4-8. In terms of hot-spot stress definition, the joint shows reasonably good performance. It passes all the recommended S-N curves. Moreover, it also shows an outstanding fatigue performance compared to the notch stress S-N curve. Based on the nominal stress S-N curve, the fatigue performance of the joint is far beyond the AWS DT curve.

Fatigue strength of the joint is determined by comparing the fatigue life to the recommended S-N curves. The measured SCF value at CL200 (adjacent to the deepest crack at CL195) is used to represent the highest SCF of the joint. In terms of hot-spot stress S-N curves, Figure 3.4-9 shows that the J2-2XGF joint perform reasonably well.

Its fatigue life is far beyond the API RP 2A (2007) which is the highest recommended hot-spot stress S-N curve in this comparison. Compared to the notch stress S-N curves, its performance is much better than the requirement from DNV RP C203 (2011). The fatigue performance of this specimen based on the nominal stress approach as compared to the AWS (2008) DT curve is well covered and its total fatigue life extends far beyond the requirements stipulated by the code.

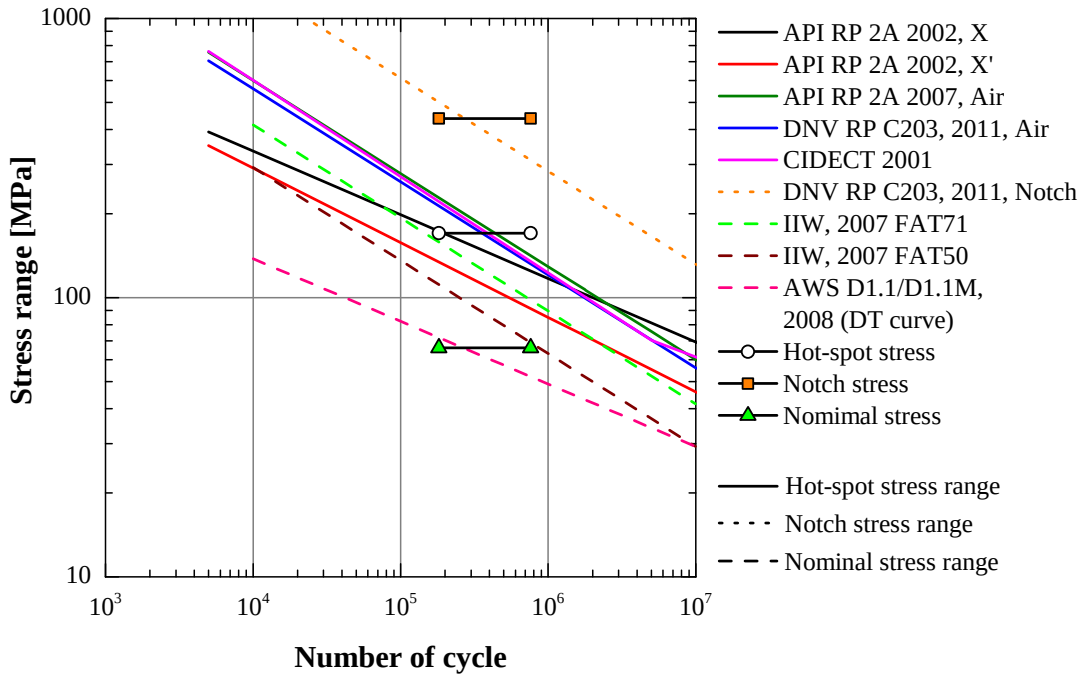

Figure 3.4-8: Fatigue performance of J2-2XPG joint based on S-N curves approach

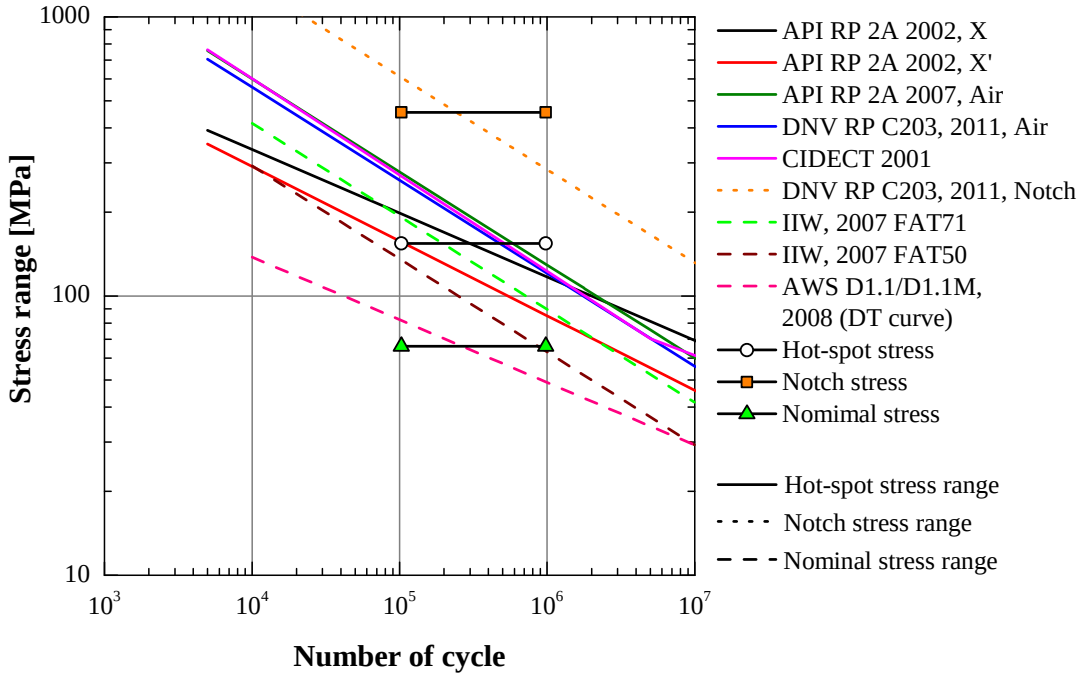

Figure 3.4-9: Fatigue performance of J2-2XGF joint based on S-N curves approach

3.5 Discussion on the entire fatigue test results conducted at NUS

The fatigue performance of the newly proposed weld profile PJP+ is examined by a series of fatigue tests conducted at the NUS structural laboratory. In total, five tubular X-joints are tested. Three of them have 12.5 mm brace wall thickness and are classified as the J1 group. The other two of 25.0 mm brace wall thickness are considered as J2. The objective of each test of these X-joints is stipulated below:

1. The test on the J1-1 joint is to study the fatigue performance of the as-welded joint

2. The test on the J1-X joint is to establish the fatigue performance under controlled weld profile condition

3. The test on the J2-1G joint is intended to observe the effect of fully chord infilled grouting on the fatigue performance

4. The intention of testing the J2-2XG joint is to examine the effect of fully chord infilled grouting and post weld improvement on the fatigue performance

Each joint is subjected to sinusoidal load with different load ranges and frequencies until the deepest crack depth reaches 80% of the parent member wall thickness. The details and applied load range of each specimen are summarized in Table 3.5-1.

Table 3.5-1: Details and applied load to the X-joints

Specimen	Brace wall thickness, t [mm]	Load range [kN]	Frequency [Hz]	Overloading	Grouting	Weld toe treatment
J1-1	12.5	235-25	0.50	-	-	-
J1-X	12.5	235-25	0.50	-	-	Profile control
J1-2	12.5	180-20	0.50	J1-2F (270kN)	-	-
J2-1	25.0	200-20	0.75	-	Yes	-
J2-2X	25.0	235-25	0.75	-	Yes	Post-weld toes grinding

There are two fatigue tests performed for each specimen. Every specimen is set up such that it has misalignment type A configuration in the first fatigue test, and misalignment type B configuration in the second fatigue test. In total, there are 10 fatigue tests.

3.5.1 Effects of brace wall thickness and concrete-filled chord grouting

The major difference between the J1 and J2 series is the brace wall thickness. The specimens in the J1 series have 12.5 mm brace wall thickness, whereas in those of the J2 series the brace is 25.0 mm thick. Intuitively, the thicker brace member should render the joint stiffer and be able to transfer more stress to the chord member. However, SCFs on the chord member increase. Figure 3.5-1 shows the measured SCF value of the J1-1, J1-2, J2-1, and J2-2 specimens. The specimens with thicker brace wall

J2-1 and J2-2 show slightly lower SCF values on the brace member, while the SCF values on chord member increase substantially. It has been observed, as expected, that the hot-spot locations of the J1-1 and J1-2 specimens are on BL members at around $\rho = 120° - 140°$ and $\rho = 220° - 240°$. The hot-spot locations of the J2-1 and J2-2 are, however, on the CL members at about the same ranges of location as those of the J1-1 and J1-2 specimens.

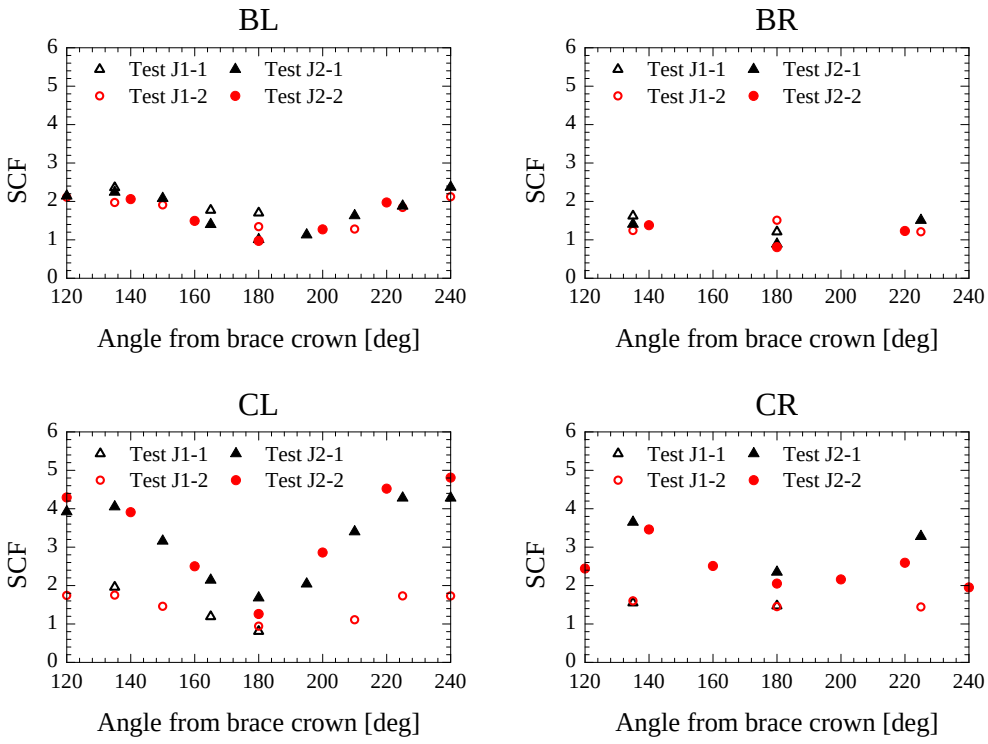

Figure 3.5-1: Comparison of SCFs of the X-joint with different brace wall thickness and weld toe treatments

Assuming that both specimens are subjected to the same load range, nominal stress (Equation 2.2-5) of the J1-1 specimen would be 1.94 times of the nominal stress of the J2-1 specimen. The magnitude of the hot-spot SCF value increases by 95% on average for the thicker brace wall. As a result of the aforementioned assumption, both J1-1 and J2-1 specimen will be subjected to approximately the same hot-spot stress.

The S-N curves in section 2.3 are used for hollow section joints with a specific reference wall thickness. For joints with different wall thickness, thickness correction factors must be introduced. Generally, the thicker the wall, the shorter the fatigue life.

According to recommended S-N curves from API RP 2A 2007, API RP 2A 2002 (X' curve), DNV 2011, and CIDECT 2001, the estimated fatigue life of the thicker brace wall J2-1 specimen will be 28%, 34%,41%, and 50% of those of J1-1 specimen respectively.

The grouted chord specimens J2-1G and J2-2XPG show significant reduction of SCF values. The hot-spot SCF values of the grouted joints with thicker brace wall J2-1G and J2-2XPG are estimated to be 25% higher than those of the ungrouted joints J1-1. However, the resultant hot-spot stress of the J2-1G and J2-2XPG specimens is 35% lower than that of the J2-1 specimen. This leads to at least 2 times longer fatigue life.

3.5.2 Comparison of fatigue test results

The fatigue test results of all 10 specimens are summarized in Table 3.5-2. The hot-spot locations of the J1 series are observed to be located around BL120 and BL240. Contrary to those of the J1 series, the highest hot-spot locations of J2 series lie between CL195 to CL210, except for the hot-spot location of the J2-2XPGF which is at CR140. These hot-spot locations are expected to be the fatigue crack initiation sites. However, observations from fatigue tests show that the first fatigue cracks of J1 series are initiated around CL230 to CL240 where the SCF values are lower than those of the hot-spot locations. In contrast to the J1 series, three fatigue tests of J2 series show that the crack initiation sites are where the major cracks develop in the vicinity of hot-spot locations.

The specimens with thicker brace wall and with concrete-filled chord J2-1G demonstrate at least 2 times longer fatigue life than the hollow chord specimen J1-1 as predicted in the previous section. The longer fatigue life is also observed for the specimens with post-weld toe treatment, namely, joints J1-X, J1-XF, J2-2XPG, and J2-2XPGF as compared to specimens with no weld toe treatment J1-1, J1-1F, J2-1G, and J2-1GF. This demonstrates the effectiveness of these techniques. The controlled weld profile technique applied to joints J1-X and J1-XF extends the total fatigue life

by 2 to 3 times as compared to that of specimens without any weld toe treatment, i.e., specimens J1-1 and J1-1F. The post-weld toe grinding technique applied to J2-2XPG and J2-2XPGF increases the total fatigue life by approximately 2 times. Table 3.5-2 also indicates that more than 50% of the total fatigue life is consumed by crack propagation life.

Table 3.5-2: Comparison of fatigue test results

Specimen	Hot spot location (experiment)	Crack initiation location	Deepest crack location	SCF*	NSCF*	$\Delta\sigma_{nom}$ [MPa]	$\Delta\sigma_{hot}$ [MPa]	$\Delta\sigma_{notch}$ [MPa]	Total life (1,000 cycles)	Initiation life** (%)	Propagation life** (%)
J1-1	BL135	CL240	CL240	1.71	2.85	122	208	346	203	34.4	65.6
J1-1F	BL240	CL240	CL242.5	2.05	2.90	122	250	353	159	16.4	83.6
J1-X	BL120	CL227	CL235	2.15	2.97	122	261	360	485	36.1	63.9
J1-XF	BL240	CL230	CR185	1.80	2.43	122	218	296	600	49.2	50.8
J1-2	BL240	CL237	CL242	1.98	2.82	93	183	261	430	23.7	76.3
J1-2F	BL120	CL122	CL127	2.07	2.95	93	192	273	478	35.1	64.9
J2-1G	CL210	CR145	CL176.3	2.75	9.79	57	156	555	443	7.2	92.8
J2-1GF	CL195	CL195	CL190	3.29	5.22	57	187	296	410	9.0	91.0
J2-2XPG	CL200	CL190	CL210	2.56	6.63	66	170	439	760	23.9	76.1
J2-2XPGF	CR140	CL190	CL195	2.33	6.87	66	154	455	980	10.6	89.4

* corresponding to the deepest crack location

** Percentages of the total life

3.5.3 Comparison of fatigue performance

Fatigue performance of the tubular joints can be determined using S-N approach based on three different stress definitions; hot-spot stress, notch stress, and nominal stress. All the S-N curves used in this comparison have already taken the effect of member thickness into account. The fatigue crack initiation cycles at a crack depth of 0.5 and the total fatigue life are included and represented by the first and second symbol respectively. It is worth noting that the total fatigue life corresponds to the crack depth equal to about 70%-80% of wall thickness. The applied load range and stress range of each specimen are tabulated in Table 3.5-3.

Table 3.5-3: Comparison of applied stress range

Specimen	ΔP [kN]	Load ratio, *R*	$\Delta\sigma_{nom}$ [MPa]	$\Delta\sigma_{hot}$* [MPa]	$\Delta\sigma_{notch}$* [MPa]
J1-1	235-25	0.106	121.49	208.08	346.26
J1-1F			121.49	249.45	352.53
J1X			121.49	260.73	360.43
J1XF			121.49	218.11	295.63
J1-2	180-20	0.111	92.57	183.37	261.04
J1-2F			92.57	191.89	272.77
J2-1G	200-20	0.100	56.71	155.95	555.20
J2-1GF			56.71	186.58	296.03
J2-2XG	235-25	0.106	66.16	169.38	438.66
J2-2XGF			66.16	154.16	454.54

* corresponding to the deepest crack location

Comparison of the fatigue test results to the hot-spot stress S-N curves is shown in Figure 3.5-2. All specimens perform reasonably well. Their fatigue performances far exceed the life estimation by API RP 2A 2002 X and X' curves. The concrete-filled chord J2-1G, and J2-1GF specimens perform as well as the hollow section J1-1, and J1-1F specimens. The specimens with post-weld treatment show outstanding fatigue performance, especially the J1-X and J1-XF specimens.

In terms of notch stress definition, it is shown in Figure 3.5-3 that most of the specimens do not meet the requirements of DNV RC C203 (2011). The grouted joints J2-1G, J2-2XG, and J2-2XGF possess superb fatigue performance. They fall on the safe side of the S-N curve. Most specimens perform well when compared with the IIW (2007) FAT165 curve.

Compared to the nominal stress S-N curves (Figure 3.5-4), the J1X-1 and J1X-1F joints still show very good fatigue performance compared to the others. The J1 series pass the S-N curve even before the crack has initiated. The J2 series also perform reasonably well in terms of nominal stress range. Although the J2-1G and J2-1GF fall on the unsafe side, the deepest crack penetrates through only 80% of the wall thickness.

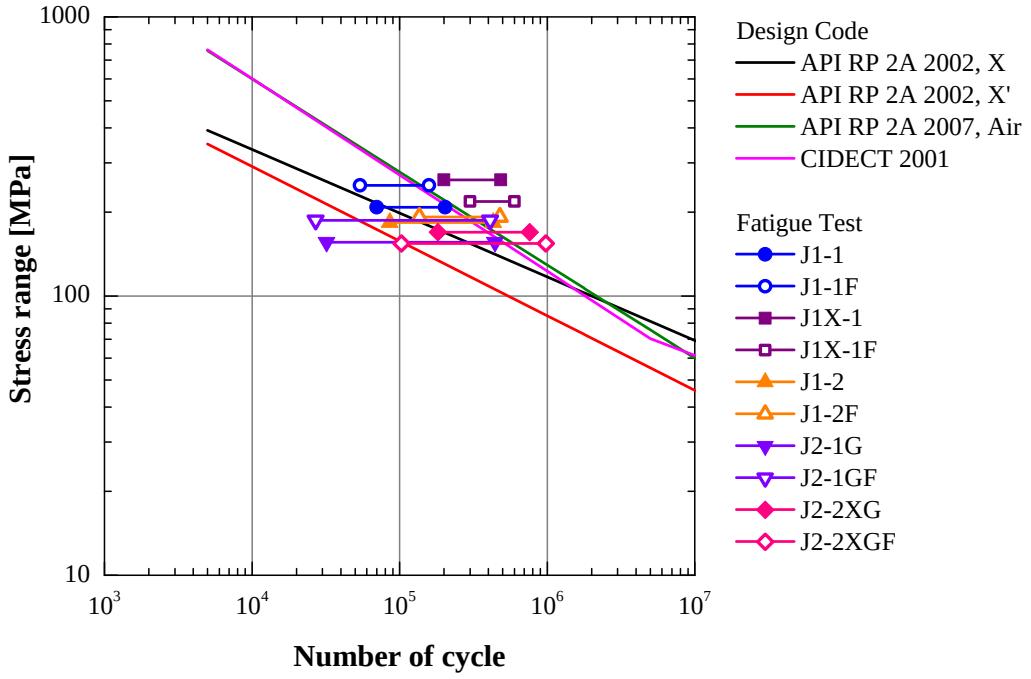

Figure 3.5-2: Fatigue performance of the J1 and J2 series based on hot-spot stress S-N curves approach

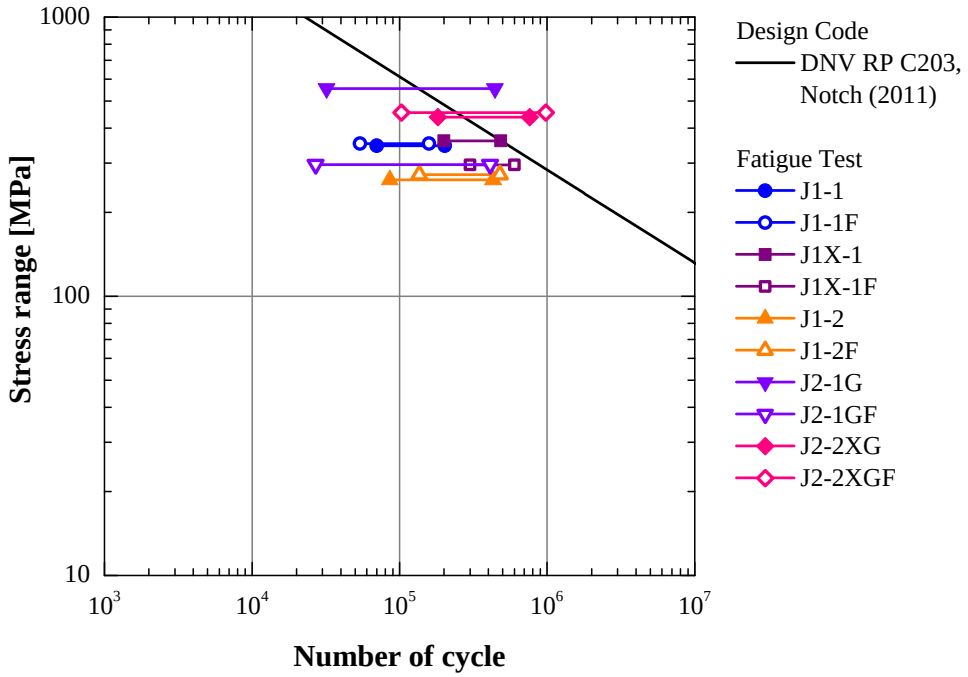

Figure 3.5-3: Fatigue performance of the J1 and J2 series based on notch stress S-N curves approach

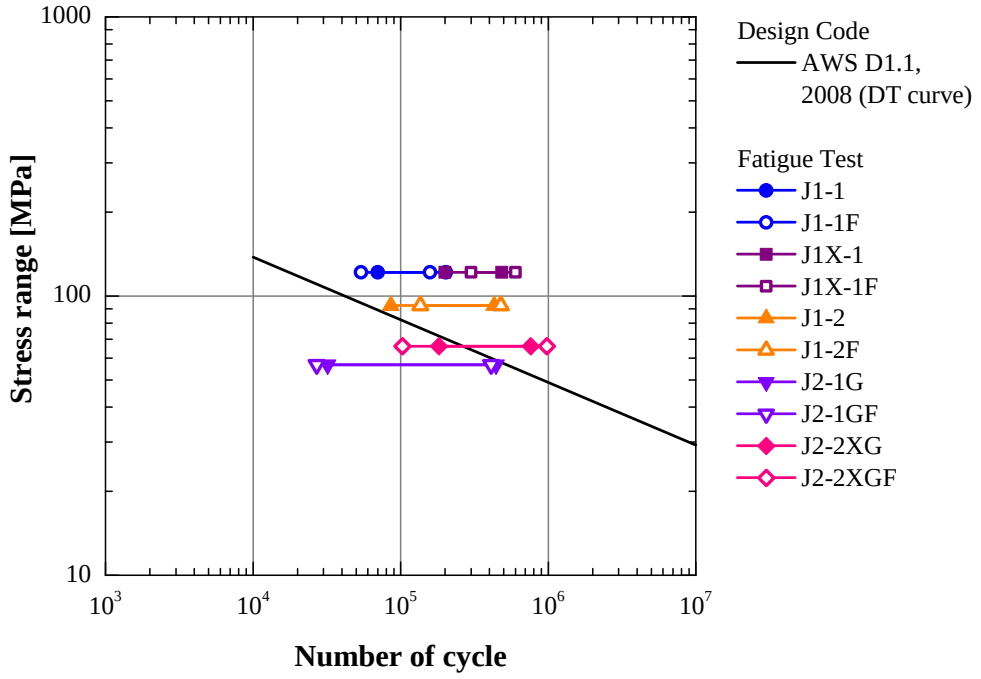

Figure 3.5-4: Fatigue performance of the J1 and J2 series based on nominal stress S-N curves approach

3.6 Conclusion

This chapter presents and discusses results from the experimental investigation of fatigue behavior of two CHS X-joints with concrete-filled chord and weld toe grinding. The observation and findings from the experimental work are as follows:

- Increase in brace wall thickness results in a significant increase of SCF values along the weld toes of the chord member, whereas SCF values along the brace weld toes are marginally decreased.
- Stiffening the chord member by introducing internal diaphragm plates or ultra-high strength concrete grouting significantly reduces SCF values along the weld toes of both brace and chord members. Moreover, the hot-spot location shifts from $\rho = 120^\circ - 135^\circ$ and $\rho = 225^\circ - 240^\circ$ toward the bottom crown point $\rho = 160^\circ - 220^\circ$.

- All of the fatigue cracks found in this study initiate near the weld toe of the chord member at multiple locations and coalesce with adjacent cracks. The first initiated crack almost always becomes the major crack in the specimen.

- The specimens with concrete-filled chord show longer fatigue life than the hollow section specimens. The increase in fatigue life is more pronounced in specimens with post-weld treatment. From all conducted fatigue tests, it can be seen that more than 50% of the total fatigue life is consumed by the crack propagation life. This highlights the importance of the accurate estimation of remaining fatigue life of structures.

- Compared with the three types of S-N curves originally developed for hollow section tubular joints fabricated with complete joint penetration (CJP) welds, the fatigue life of the concrete-filled joints agrees with the fatigue life estimation based on these S-N curves.

CHAPTER 4

FINITE ELEMENT STUDY OF SCF AND NSCF

Finite element analysis is adopted in this chapter to numerically determine SCF values of the CHS X-joints with concrete-filled chord. Section 4.1 presents on overview of the finite element analysis of CHS X-joints. The preliminary study of SCF and NSCF calculation in section 4.2 and 4.3 respectively. Lastly the numerical study of SCF and NSCF values is discussed in section 4.4 and 4.5 respectively.

4.1 Overview of finite element analysis

4.1.1 Finite element model

The stress concentration factors along brace and chord weld toe are computed from linear elastic finite element analyses. The half-symmetric finite element models (FE model) are employed in this study. The FE models with and without brace misalignment are illustrated in Figure 4.1-1. The difference between models with the absence and presence of partition plates in the chord member is illustrated in Figure 4.1-2. The FE model of the specimens with 3 mm radius ground weld toe is shown in Figure 4.1-3. The in-filled concrete model which is used in concrete-filled chord specimens is shown in Figure 4.1-4. These FE models utilize 20-node brick elements with reduced integration (C3D20R). There are four elements across the thickness of brace and chord members. Weld toes along brace-to-chord intersections contain 80 elements,

each element corresponding to an angle of $\rho = 2.25^{\circ}$. The SCF extrapolation zone comprises 5 elements distributed evenly from $0.4t$ to $1.4t$ away from the weld toe in perpendicular direction. The filled concrete model meshes at the surface of the filled concrete are compatible with the inner surface of the chord member.Number of nodes and elements of each FE models are listed in Table 4.1-1.

Table 4.1-1: Number of nodes and elements of FE models

FE model	Number of nodes	Number of elements	Smallest element size [mm]
X-joint without partition plates	228,417	48,450	0.72
X-joint with partition plates	230,697	48,770	0.72
X-joint with partition plates and weld toe grinding	298,477	63,168	0.72
Infilled concrete	123,527	25,600	0.04

4.1.2 Boundary conditions

Since only one-half of the tubular joint is modeled, the displacement in the z-direction (and rotation about the x and y axes) are restrained for all the nodes lying on the symmetric plane ($z = 0$). A pinned support and a roller support are applied at the ends of the left brace and right brace, respectively. Since a high reaction force might result in excessive deformation at applied boundary condition nodes, the material property in this region has to be numerically modified to be rigid compared to the material properties of other parts. Therefore, semi-circular diaphragm plates with Young's modulus of 1000E (205000 GPa) are introduced. Moreover, the Young's modulus in a small region around the applied point load position is changed to 1000E as well. Boundary conditions and the regions of modified material property Figure 4.1-5.

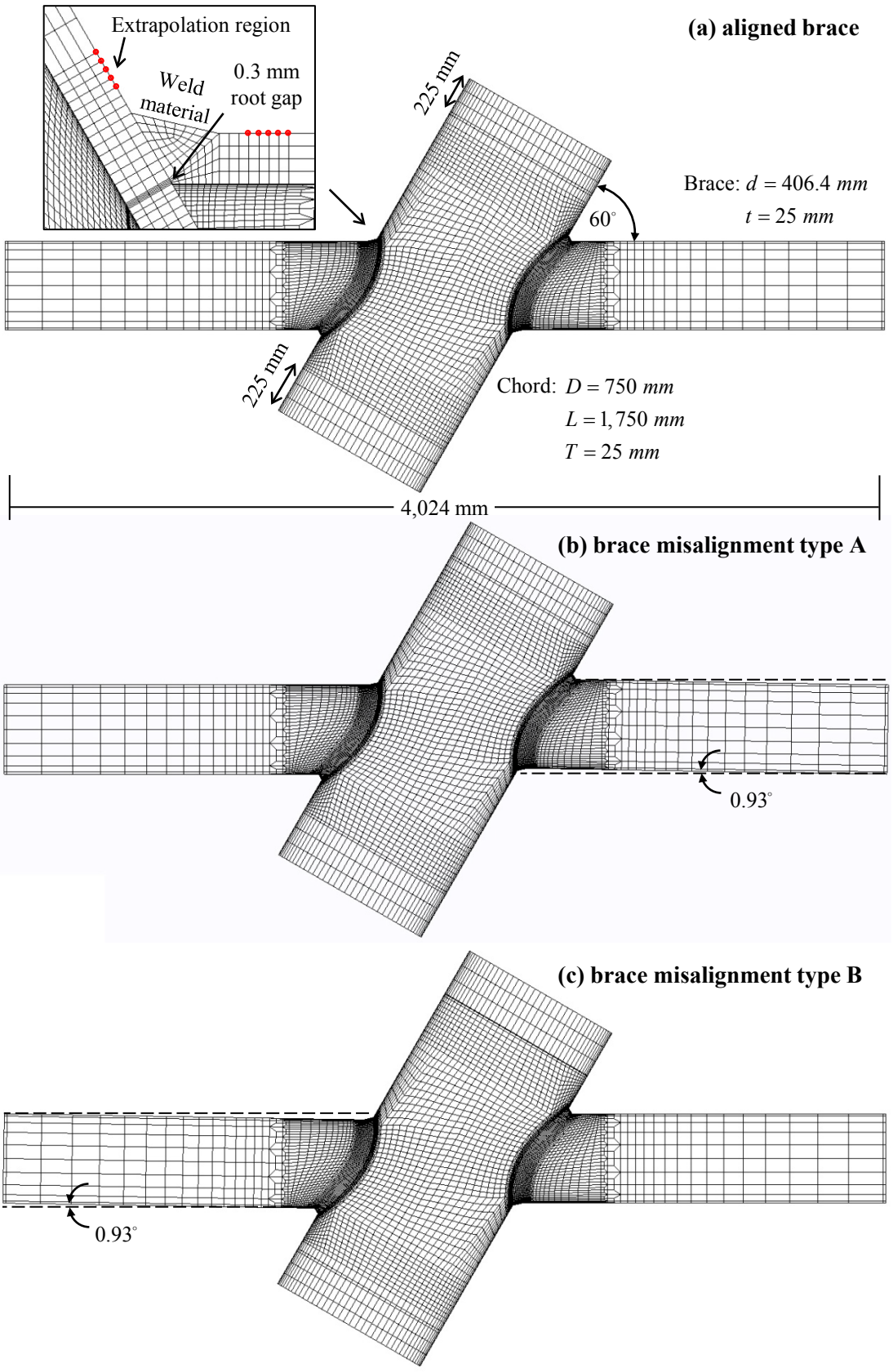

Figure 4.1-1: Finite element model of X-joint specimen

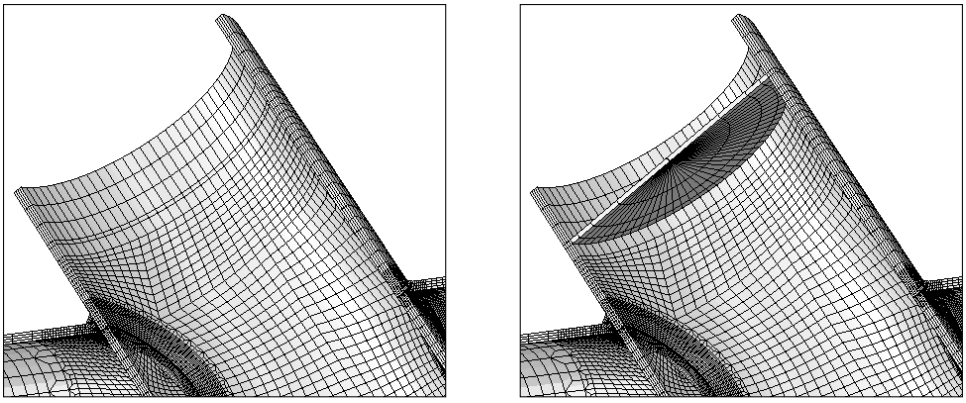

(a) absence of partition plates **(b) presence of partition plates**

Figure 4.1-2: Partition plates in chord member of finite element model

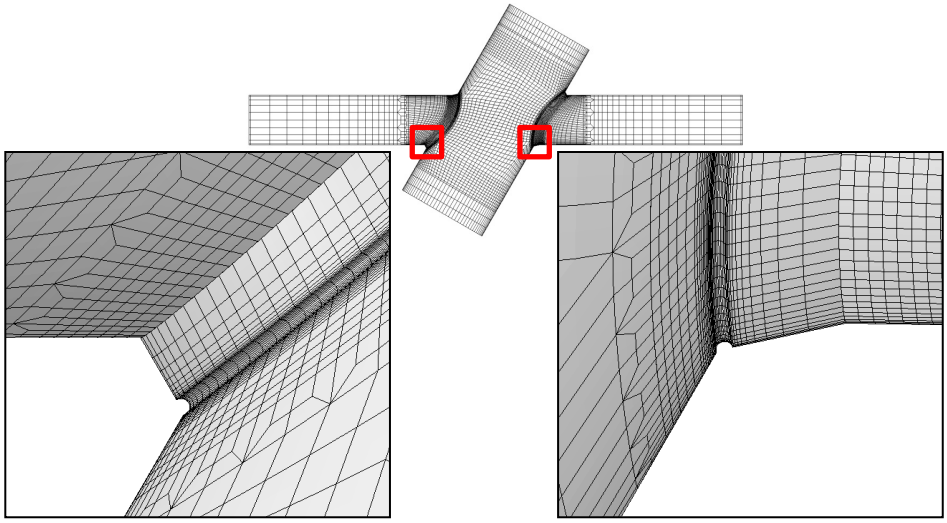

Figure 4.1-3: Finite element model of specimens with post-welded toe grinding

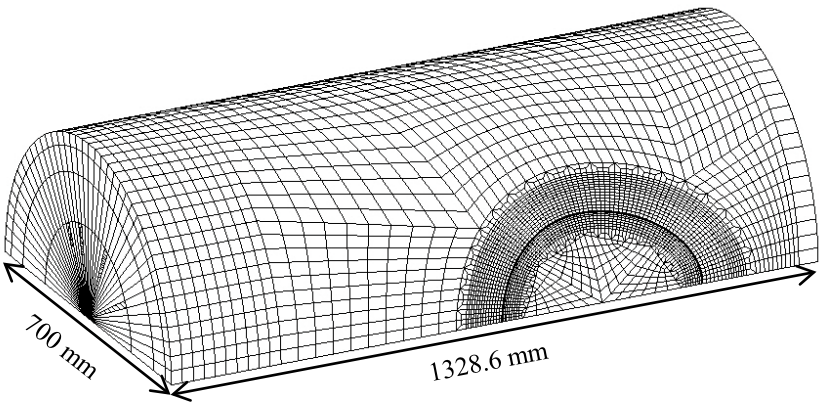

Figure 4.1-4: Finite element model of in-filled concrete

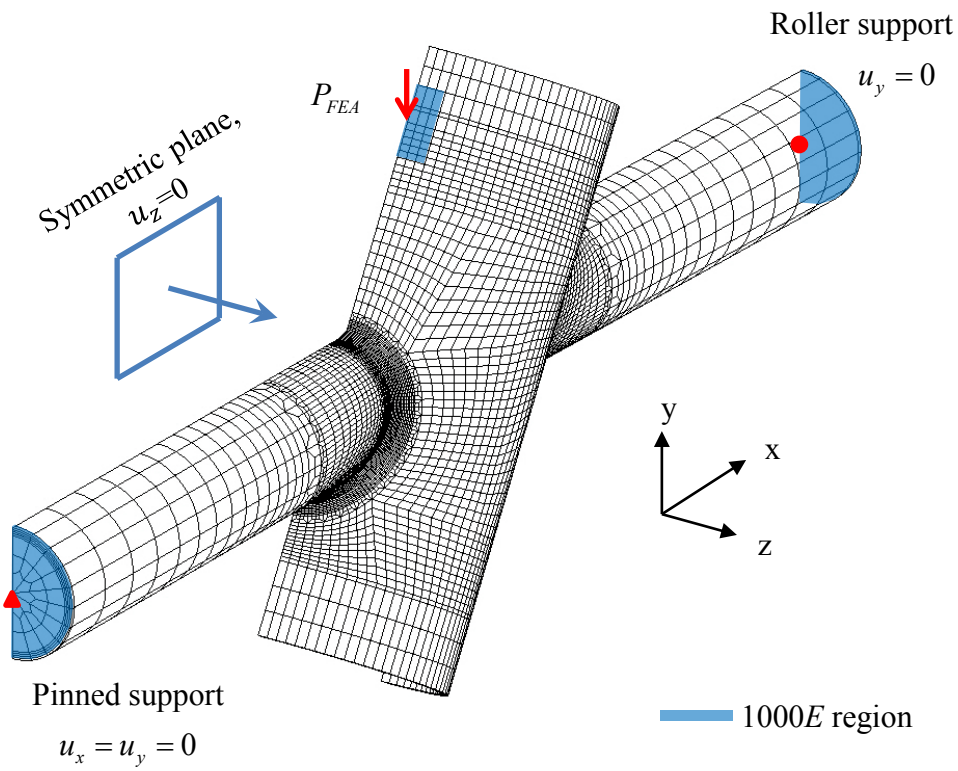

Figure 4.1-5: Boundary conditions imposed in finite element models

4.1.3 Material properties

The test specimen is fabricated from S355 structural steel for both brace and chord members. For the J2-1G specimen, the chord is filled by ultra-high performance concrete (UHPC), Densit Ducorit® D4, which is extensively used for strengthening and repair of offshore structures. Mechanical properties of S355 structural steel and Densit Ducorit® D4, infilled concrete, are tabulated in Table 4.1-2.

Table 4.1-2: Mechanical properties of S355 steel and Densit Ducorit® D4

Mechanical properties	**S355 steel**	**Densit Ducorit® D4**
Modulus of elasticity, *E*	205 GPa	70 GPa
Poisson's ratio, ν	0.3	0.19
Yield strength	355 MPa	-
Compressive strength	-	200 MPa
Static coefficient of friction, μ_s	-	0.60

4.1.4 Interaction properties between chord member and infilled concrete.

Interaction properties in ABAQUS (2012) are defined as geometric property and mechanical property. The geometrical property is defined by node sliding tracking approach and discretization method of contact pair: master surface and slave surface. All nodes on the slave surface are restrained not to penetrate into the master surface. In contrast, nodes on the master surface can penetrate into the slave surface. The latter undesirable phenomenon is mitigated via the symmetric master-slave contact pair technique described in the end of this section. The surface-to-surface discretization method, which provides accurate stress and pressure results (ABAQUS, 2012), and finite-sliding tracking approach are used in this analysis.

Mechanical properties are defined by the normal and tangential behavior. The normal behavior is described by the contact pressure-overclosure relationship. The hard contact, which is used in this analysis, instantaneously provides contact pressure between the two surfaces when they are closed, as described in the following equations (ABAQUS, 2012):

$$\begin{aligned} p &= 0 \text{ for } h > 0 \ \text{(open)} \\ p &> 0 \text{ for } h = 0 \ \text{(close)} \end{aligned} \tag{4.1-1}$$

where, p is the contact pressure, and

h is the overclosure of the contact pair.

The tangent behavior provided in ABAQUS is governed by the isotropic Coulomb friction model. According to this model, no slip can occur if the friction stress is smaller than the critical friction stress.

$$\tau_{crit} = \mu_s p \tag{4.1-2}$$

where, μ_s is the friction of coefficient.

In order to get the best contact condition, two techniques are introduced. One is the compatible mesh technique. The master and slave surfaces share an identical mesh pattern. The second is the symmetric master-slave contact pair technique. In the second approach, the two surfaces are defined by two contact pairs which switch the role of the master and slave surfaces. The symmetric contact pair approach also solves the inter-penetration problem between the two surfaces. These two techniques are reported to improve the accuracy of the model (ABAQUS, 2012).

4.2 Preliminary study of SCF calculation in finite element analysis

The definition of SCF adopted in this study is the ratio of hot-spot stress to nominal stress. The stresses or strains components in extrapolation region ($0.4t$-$1.4t$) are linearly extrapolated back to the weld toe to determine hot-spot stress. To calculate perpendicular stresses, one needs to determine the unit vector normal to the weld toe and thereafter calculate resultant stress in that direction. This section investigates the effects of different methods to calculate unit vector normal to weld toe and hot-spot stress on the SCF values.

4.2.1 Determination of unit vector normal to weld toe

As elaborated in section 2.2.6, SCF can be determined by parametric equations. Unfortunately, these equations provide the SCF values only at the chord crown (CC) and brace crown (BC) positions while the rest are ignored. For circular hollow section (CHS) joints, the hot-spot location may not be at the crown or saddle point but somewhere in between. Detail finite element analysis is required to determine the maximum SCF value and its corresponding location. As expressed in Equation 2.2-6, SCF is a ratio of hot-spot stress to nominal stress. Determination of hot-spot stress in finite element analysis is similar to what is done in the experiment. The stresses in the extrapolation region are linearly extrapolated to the weld toe and thereafter transform into

the direction normal to the weld toe by pre- and post-multiply by the directional vector as illustrated in Figure 4.2-1. The resultant stress is the hot-spot stress which can be expressed in general form as:

$$\sigma_{hot-spot} = \sigma_{11} = \vec{\mathbf{n}}_{11}^{T} \boldsymbol{\sigma} \vec{\mathbf{n}}_{11} = \begin{bmatrix} n_x \\ n_y \\ n_z \end{bmatrix}^{T} \begin{bmatrix} \sigma_{xx} & \sigma_{xy} & \sigma_{xz} \\ \sigma_{yx} & \sigma_{yy} & \sigma_{yz} \\ \sigma_{zx} & \sigma_{zy} & \sigma_{zz} \end{bmatrix} \begin{bmatrix} n_x \\ n_y \\ n_z \end{bmatrix} \tag{4.2-1}$$

where, $\boldsymbol{\sigma}$ is the linear-extrapolated the stress tensor,

$\vec{\mathbf{n}}_{11}$ is the unit vector in the direction perpendicular to the weld toe and tangent to the member surface,

x, y, z denotes global coordinates system, and

$1, 2, 3$ denotes weld toe local coordinates system as shown in Figure 4.2-2

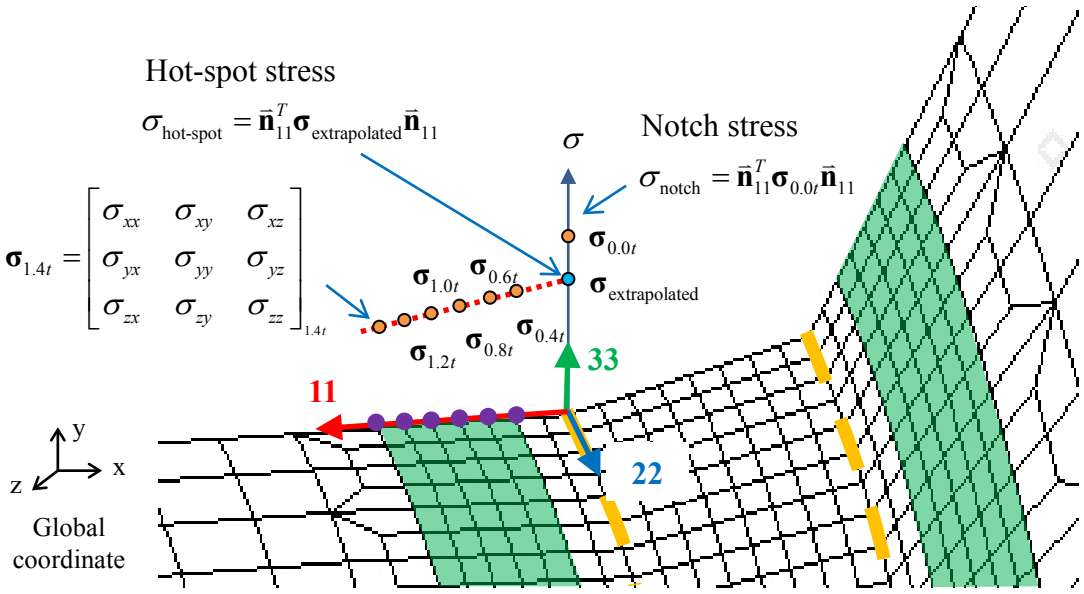

Figure 4.2-1: Determination of hot-spot stress and notch stress using finite element analysis

The stress tensors at various locations in the extrapolation region are determined using finite element method, whereas the unit vector normal to the weld toe, $\vec{\mathbf{n}}_{11}$, is however has to be determined manually. Determination of $\vec{\mathbf{n}}_{11}$ can be done by utilizing the secant direction vector of two adjacent points: one is a point A on the weld toe and the other is an adjacent point B along the line perpendicular to the weld toe as illustrated in Figure 4.2 2. This method is named here as simplified method as it simply utilizes the secant direction vector. The unit normal vector in this simplified method can be expressed as:

$$\vec{\mathbf{n}}_{11} = \vec{\mathbf{n}}_{BA} = \frac{x_B - x_A}{L}\vec{i} + \frac{y_B - y_A}{L}\vec{j} + \frac{z_B - z_A}{L}\vec{k} \tag{4.2-2}$$

where, L is the distance between point A and B.

$$L = \sqrt{(x_B - x_A)^2 + (y_B - y_A)^2 + (z_B - z_A)^2} \tag{4.2-3}$$

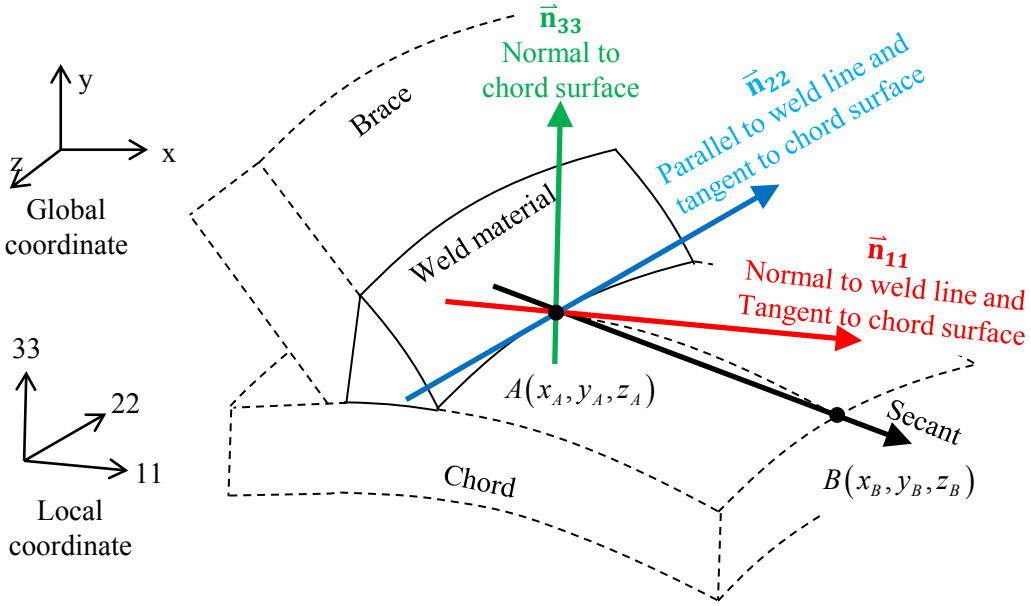

Figure 4.2-2: Vector normal to weld toe of detailed method and simplified method

The simplified method can yield results with certain degree of inaccuracy. If the distance between point A and point B is large, a more precise method to calculate unit normal vector is necessary.

As illustrated in Figure 4.2-2, the vector $\vec{\mathbf{n}}_{11}$ is a cross product of the vectors $\vec{\mathbf{n}}_{22}$ and $\vec{\mathbf{n}}_{33}$. The vectors $\vec{\mathbf{n}}_{22}$ and $\vec{\mathbf{n}}_{33}$ can be derived once the equation of the curves along the weld toe is known. However, the curves along the weld toe are difficult to derive mathematically. Therefore, the chord-to-brace intersection curves are used instead. The following assumptions are made:

1. The curves along the weld toe are parallel to the chord-to-brace intersection curves

2. The curvature of the curves along the weld toe is the same as compared to the curvature of the brace-to-chord intersection curves

With the above assumptions, the vector $\vec{\mathbf{n}}_{22}$ can be found by differentiating the parametric equation representing the chord-to-brace intersection curve, i.e. $\vec{R}(\alpha)$, with respect to the free parameter, α. Since there are infinite vectors normal to the curve, only the normal to the chord-to-brace intersection curve and normal to the member surface ($\vec{\mathbf{n}}_{33}$) is considered. Finally the normal vector, $\vec{\mathbf{n}}_{11}$, can be calculated from the cross product of the $\vec{\mathbf{n}}_{22}$ and $\vec{\mathbf{n}}_{33}$ vectors. The details of the derivation are shown in Appendix B.

The computed SCF values using two different unit normal vector computational methods are shown in Figure 4.2-3 and Figure 4.2-4. Both methods lead to similar estimations of SCF values along the weld toes for of both J2-1 and J2-1G specimens. The SCF values from the simplified method deviate slightly from those values obtained by the precise method in the region between $\rho = 10^\circ - 30^\circ$ and $\rho = 140^\circ - 170^\circ$. This is because the curvature of line perpendicular to the weld toe is relatively large and hence the precise method is preferred. Subsequent numerical determinations of unit vector normal to the weld toes follow the precise method.

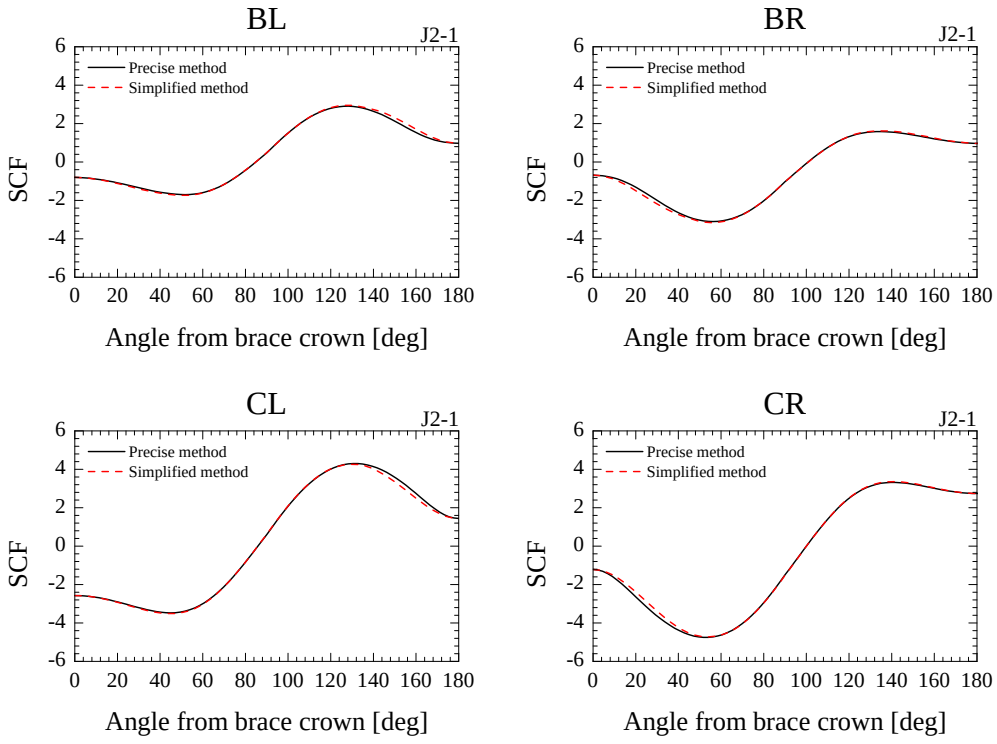

Figure 4.2-3: Comparison of numerically computed SCF values of J2-1 specimen using different unit normal vector computational methods

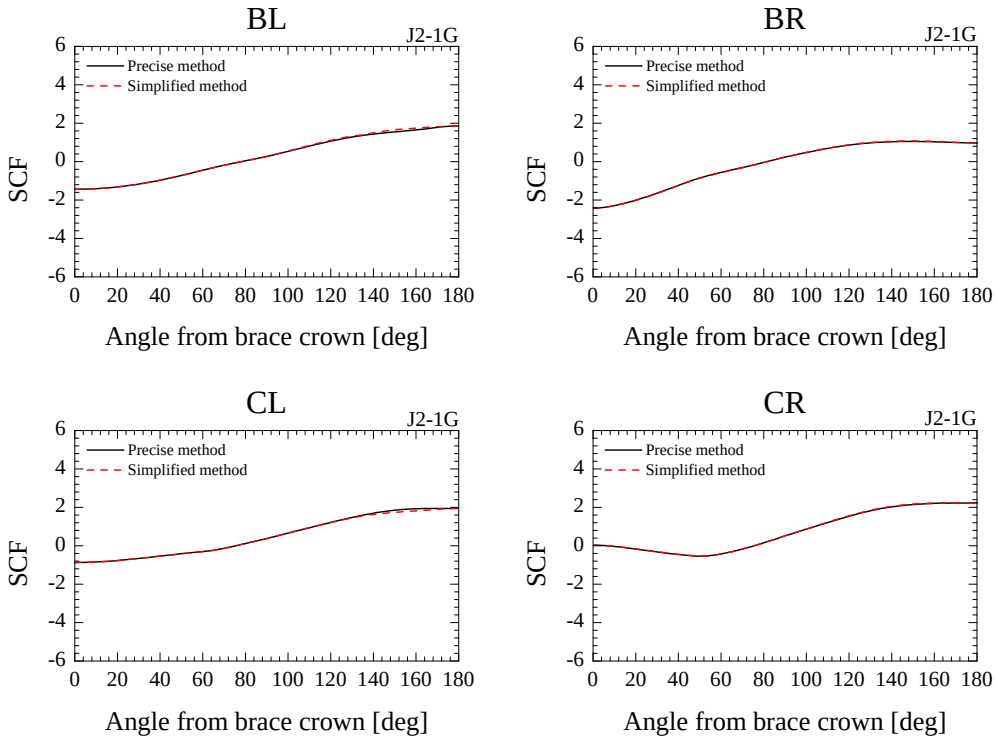

Figure 4.2-4: Comparison of numerically computed SCF values of J2-1G specimen using different unit normal vector computational methods

4.2.2 Determination of hot-spot stress

In the previous subsection, the stresses along the weld toes were determined by extrapolating stresses over the extrapolation zone to the weld toe, and subsequently hot-spot stress and SCF values were determined using Equation 4.2-1 and Equation 2.2-6 respectively. This determination of SCF values is named here as the *stress based* method. Alternatively, hot-spot stress can be determined based on strain results. The hot-spot strain can be determined by extrapolating strains over the extrapolation zone to the weld toe, and thereafter the hot-spot stress are determined using Equation 2.2-11 or Equation 2.2-12. The latter approach of extrapolating strain values is called the *strain based* method and the *strain based - plane stress* method respectively.

From Figure 4.2-5 and Figure 4.2-6, it can be observed that all hot-spot stress determination methods either based on stress values or strain values yield close estimation of SCF values along the weld toes of J2-1 and J2-1G specimens. Subsequent numerical determination of SCF values using finite element analysis in this thesis follows the *stress based* method.

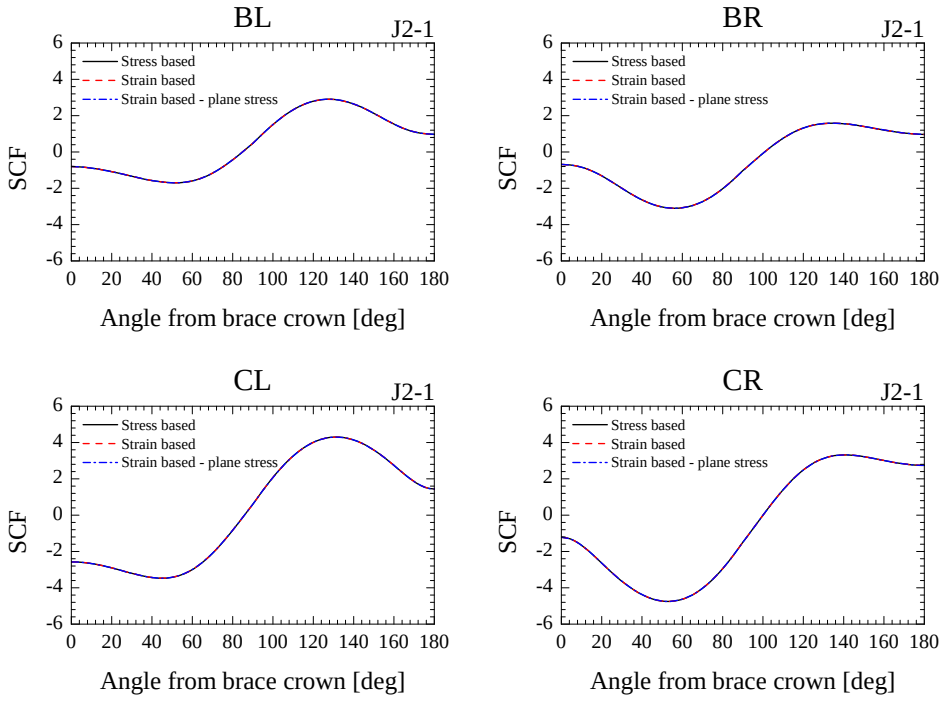

Figure 4.2-5: Comparison of numerically computed SCF values of J2-1 specimen using different hot-spot stress determination methods

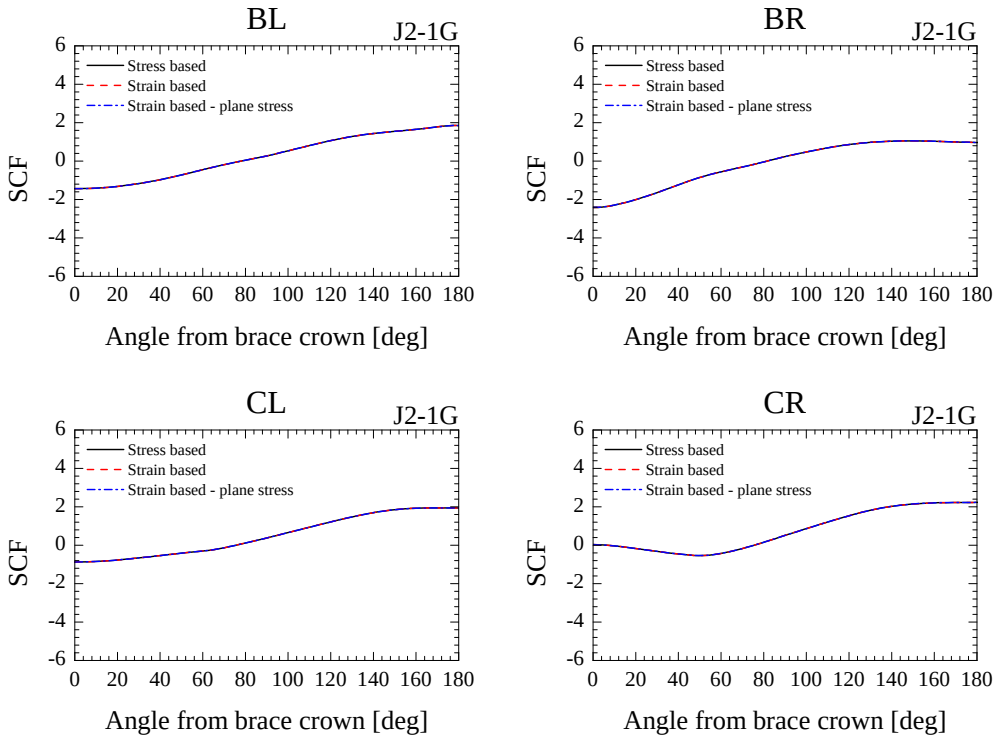

Figure 4.2-6: Comparison of numerically computed SCF values of J2-1G specimen using different hot-spot stress determination methods

4.3 Preliminary study of NSCF calculation in finite element analysis

The definition of NSCF is similar to the definition of SCF where NSCF is ratio of stress at the weld toe in perpendicular direction to weld toe to nominal stress. The perpendicular stress at the weld toe can be determined using Equation 4.2-1. However, the stress tensor, $\boldsymbol{\sigma}$, in this case is stress tensor at the weld toe, $\sigma_{0.0t}$.

For the specimen with as-welded weld toe condition, J2-1, the unit vector normal to the weld toe can be determined using simplied method or detailed method as discussed in Section 4.2.1. For the specimen with ground weld toe, J2-2, the direction vectors calculated from both methods are identical. Consider 3 points on the circular ground curve as shown in Figure 4.3-1, if the arch length between point $i-1$ and i, and point i and $i+1$ are equal, the secant vector between point $i-1$ and $i+1$ will be

identical to tangent vector calculated at point i. As a result, the normal vector can be expressed as:

$$\vec{\mathbf{n}}_{\perp_i} = \frac{x_{i+1} - x_{i-1}}{L}\vec{i} + \frac{y_{i+1} - y_{i-1}}{L}\vec{j} + \frac{z_{i+1} - z_{i-1}}{L}\vec{k} \tag{4.3-1}$$

where, L is the distance between point $i+1$ and $i-1$.

$$L = \sqrt{(x_{i+1} - x_{i-1})^2 + (y_{i+1} - y_{i-1})^2 + (z_{i+1} - z_{i-1})^2} \tag{4.3-2}$$

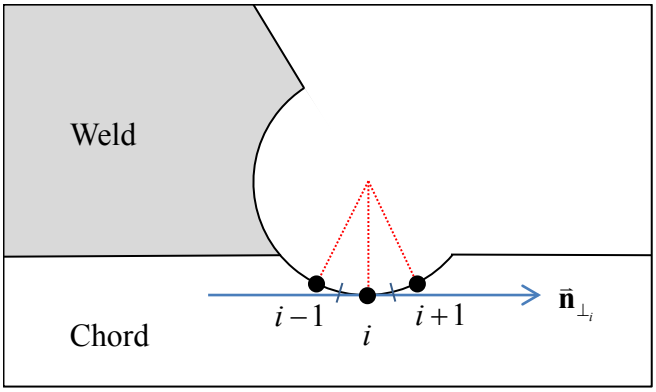

Figure 4.3-1: Unit normal vector along ground weld toe curve

The finite element model for the specimen with ground weld toe, J2-2, is modeled such that there are 16 elements across the cross section ground weld toe curve. Nodes along the ground weld toe curve are evenly distributed as shown in Figure 4.3-2. For referencing, the location #0 implies the node locates at the surface of weld material. The location number increases towards the surface of chord member which reference as #16. The middle of the ground weld toe curve is at location #8.

The NSCF distributions along the ground weld toe curve as shown in Figure 4.3-3 demonstrate that location #10 has the highest NSCF value and the NSCF values decrease towards weld material and chord surface. The location #10 is close to the middle of the ground weld toe curve (#8) where the strains are measured during the experiment for NSCF calculation. As the strain gauges are placed at the middle of the ground weld toe curve (#8), the subsequent determination of NSCF values for the specimen with ground weld toe, J2-2, will be referred to NSCF values at the middle of ground weld toe curve (location #8).

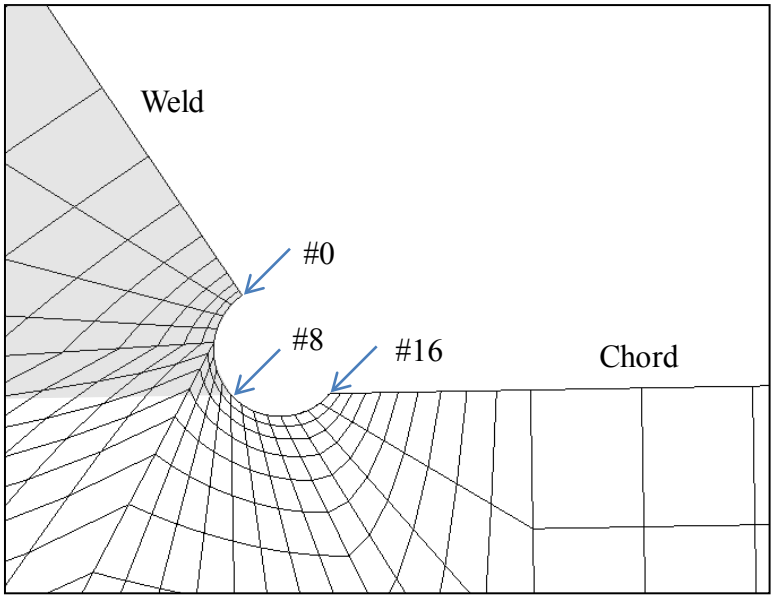

Figure 4.3-2: Reference calculating NSCF location along ground weld toe

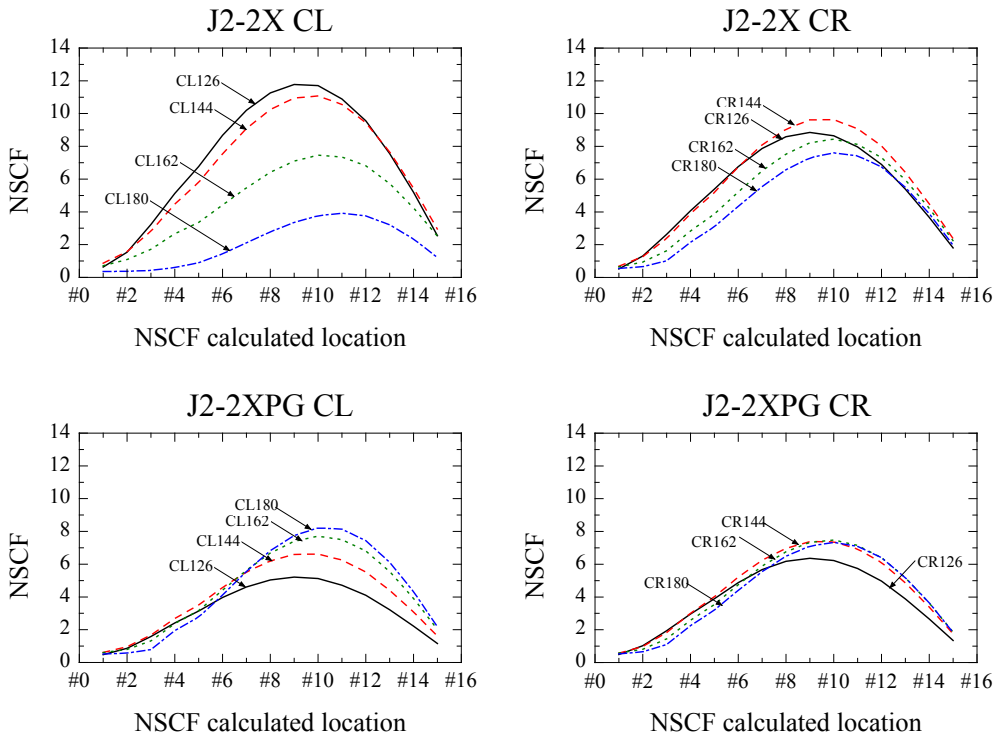

Figure 4.3-3: Distribution of NSCF values along the ground weld toe

4.4 Numerically computed SCF values

This section presents SCF values of J2-1 and J2-2 specimens from finite element analysis. The SCF values are determined based on stress results from finite element analyses and the unit normal vector calculated using the precise approach as discussed in the previous section. This section also compares the computed SCF values to the experimentally measured SCF values and investigates possible causes that may lead to the deviation between the computed SCF values and the experimentally measured SCF values.

4.4.1 J2 specimen with misaligned brace

In the experiment, it was found that one of the brace member misaligned. The specimen setup where the right hand side brace tilt upward by 0.93° towards the joint is called misalignment type A (Figure 4.1-1b), whereas the specimen setup where the left hand side brace tilt downward by 0.93° towards the joint is called misalignment type B (Figure 4.1-1c). The SCF results from FE analyses of J2 specimen with no concrete filled chord as shown in Figure 4.4-1 indicate that the brace misalignment type A does not significantly affect the SCF values along the BL, CL, and BR weld toe, whereas those in the region of $\rho = 40^\circ - 120^\circ$ on CR decrease by 3%. Overall the brace misalignment type A insignificantly affects the maximum SCF value. It can also be observed from Figure 4.4-1 that the brace misalignment type B increases the SCF values in the region of $\rho = 70^\circ - 150^\circ$ on CL and the maximum SCF value is increased by 5%. Among the two type of brace misalignment, the J2 specimen with brace misalignment type B is more concern.

The comparison of SCF values of the grouted J2 specimen without brace misalignment (Figure 4.1-1a) to the grouted J2 specimen with two types of brace misalignment is shown in Figure 4.4-2. It can be seen that both misalignment type A and type B

insignificantly influence the SCF distribution along the weld toes of J2 specimen with chord infilled grouting. Although the SCF values of the grouted J2 specimen are insignificantly affected by the brace misalignment, the FE models in subsequent sections take brace misalignment into account.

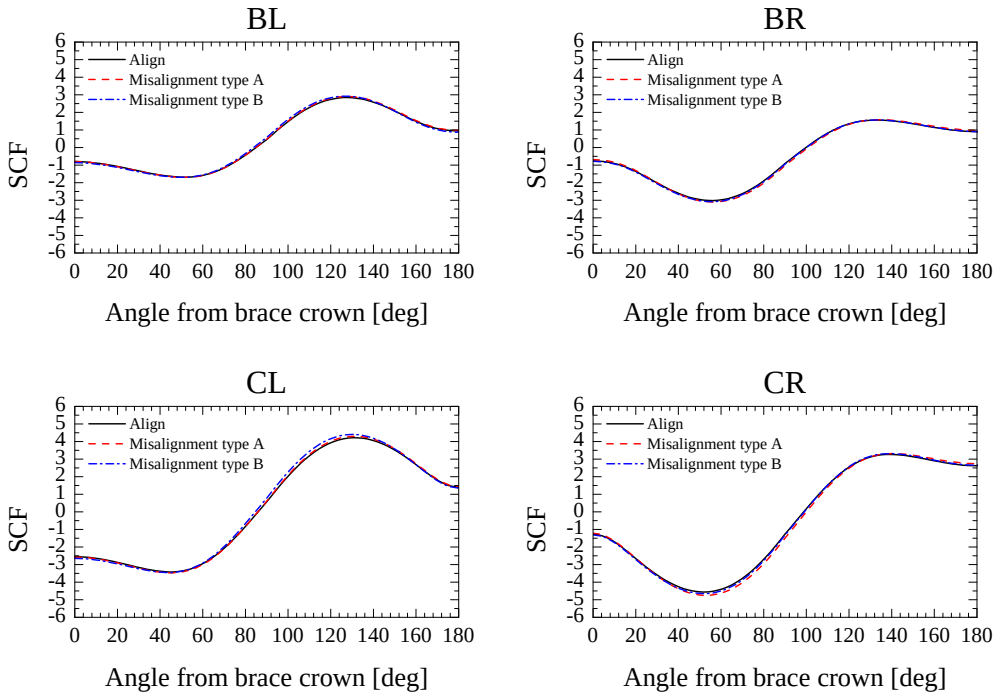

Figure 4.4-1: Effects of brace misaligmnent to SCF values of J2 specimen

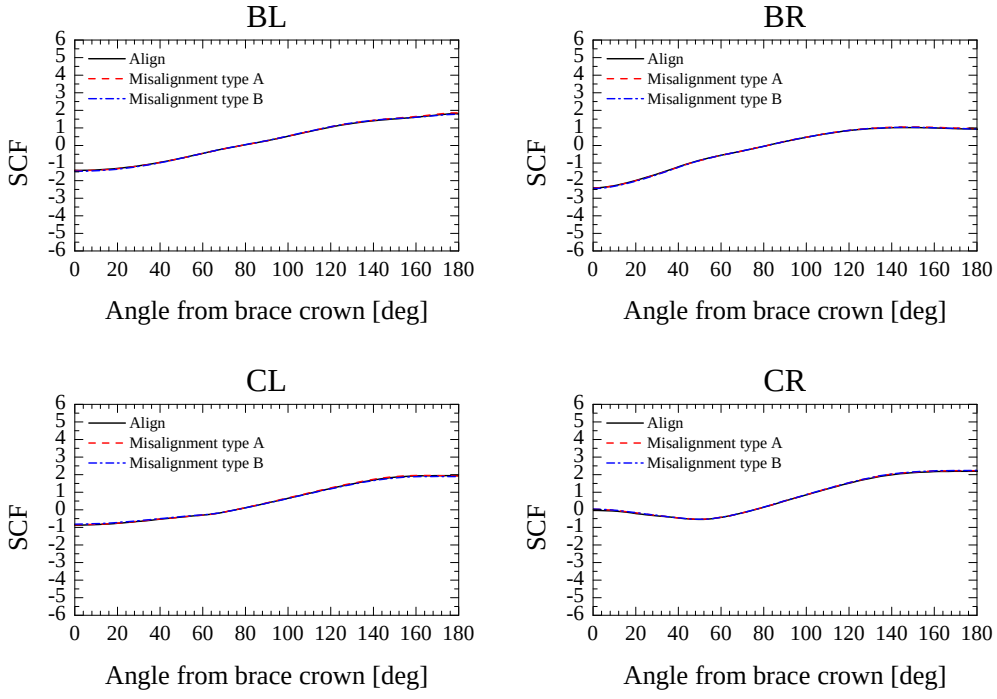

Figure 4.4-2: Effects of brace misaligmnent to SCF values of J2-G specimen

4.4.2 Numerically computed SCF values of J2-1 specimen

Comparison of numerically computed SCF values of the hollow section specimen, J2-1, and those of the concrete-filled chord specimens, J2-1G and J2-1GF, is illustrated in Figure 4.4-3. The numerical results of the J2-1 specimen agree well with the SCF values measured along the weld toes on both brace and chord members. For J2-1G and J2-1GF, numerical results demonstrate that the presence of concrete-filled and partition plates the in chord member significantly reduces the SCF values in both brace and chord members. The numerically computed SCF values on brace members agree reasonably well with the measured SCF values, whereas the calculated SCF values underestimate significantly the measured SCF values on the chord member. This discrepancy is likely due to:

1. Variation in the elastic modulus of concrete
2. Coefficient of friction between infilled concrete and inner chord surface
3. Gap between infilled concrete and inner chord surface
4. The simplified SCF and SNCF relationship

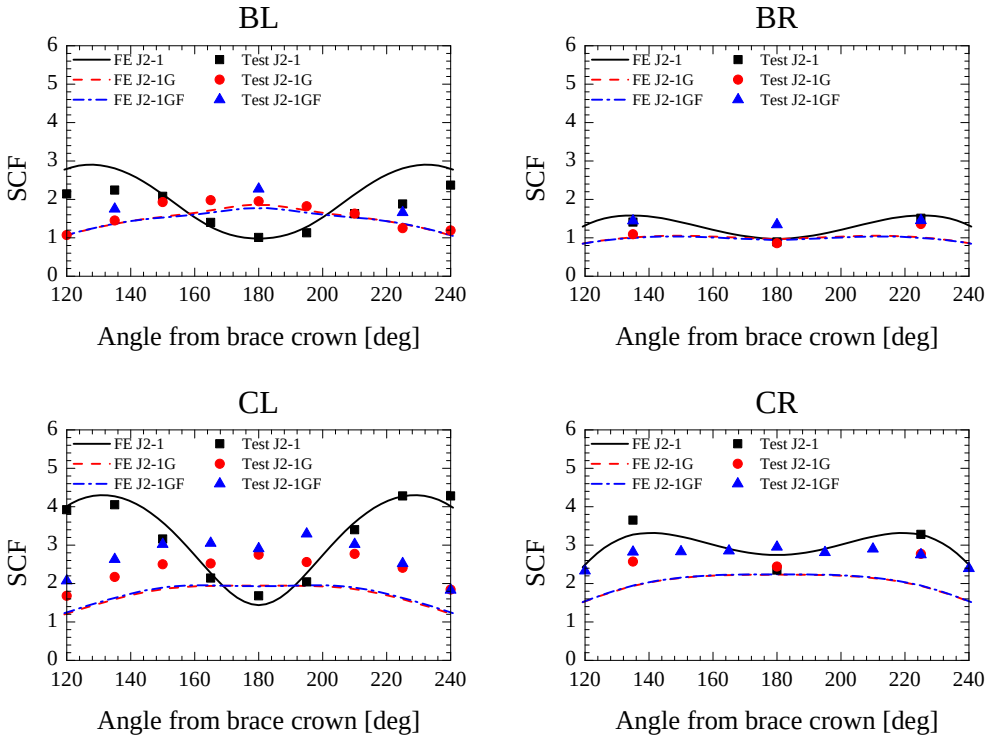

Figure 4.4-3: Comparison of SCF values of ungrouted and grouted specimens

4.4.3 Effect of infilled concrete properties on SCF values

Concrete is a composite construction material comprising primarily aggregate, cement and water. Water plays a critical role, particularly the amount used. Concrete mixed with less water gives higher strength. However, it may not achieve proper workability. In contrast, the micro-pore structure of concrete mixed with excess water is weakened by the water unconsumed in the hydration reaction, resulting in a decrease of concrete strength. The sensitivity of SCF values to the strength of concrete is investigated in this section.

In this study, the behavior of the J2-1G specimen is simulated via finite element analysis. The Young's modulus of concrete, Ec, which is dependent on the strength of concrete, is chosen to be 50 GPa, 60 GPa, 70 GPa and 80 GPa. The four selected cases cover most of the cases which might be encountered in practice and in actual experiment. The model with $E_c = 70$ GPa is the reference case. The two models with $E_c = 50$ GPa and 60 GPa represent the cases of concrete with lower strength while the model with $E_c = 80$ GPa is for cases of higher concrete strength beyond what is recommended. The analysis is based on the Misalignment type A model.

Simulated finite element results for various values of E_c are depicted in Figure 4.4-4, and tabulated in Table 4.4-1. As can be observed in Figure 4.4-4, the variation of the values of E_c does not seem to affect the values of SCF significantly for all locations along the weld line. For chord members, the deviation of SCF values is larger in the compressive region (negative SCF values) compared to those in the tensile region (positive SCF values). Increasing E_c can reduce SCF values in compressive zone. The reduction is greater in the vicinity of the top ($\rho = 0^\circ$) of the chord member. The sensitivity of the SCF values to the variation of E_c values in the study range as tabulated in Table 4.4-1 reflects the same trend. Both SCF values and the deviations, Δ (%), from control case ($E_c = 70$ GPa) at critical locations are presented. For brace members, the variations are insignificant in the range of $\pm 1\%$. For the left-side chord at $\rho = 0^\circ$, 17%

increament of the SCF values is noted when E_c is reduced to 50 GPa. However, fatigue cracking and/or fracture of material is of less concern in the structure subjected to compressive load.

In summary, the variation in the elastic modulus of concrete does not create noticeable differences in the computed SCF values at the weld toes on the left side of the chord member for the specimens with concrete-filled chord.

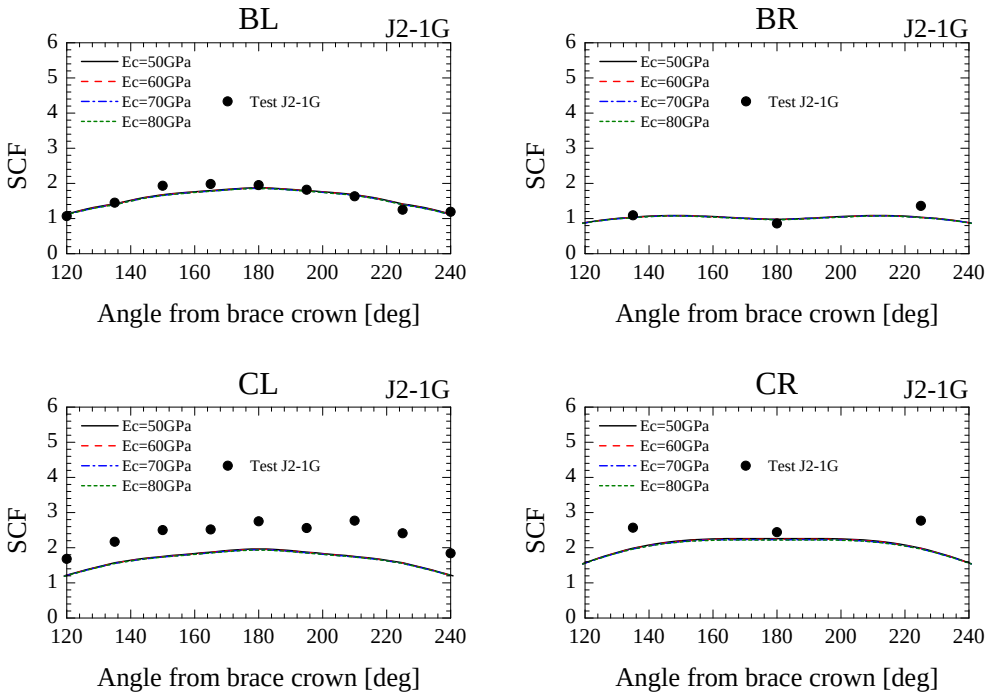

Figure 4.4-4: Effect of Young's modulus of concrete on SCF values

Table 4.4-1: Sensitivity of SCF values to Young's modulus of concrete

E_c (GPa)	ρ	BL		CL		BR		CR	
		SCF	Δ (%)	SCF	Δ (%)	SCF	Δ (%)	SCF	Δ (%)
50	0°	-1.42	-0.26	-1.03	17.51	-2.41	-0.08	-0.09	*
	180°	1.87	0.74	1.96	1.14	0.98	0.92	2.26	1.38
60	0°	-1.43	-0.11	-0.94	7.74	-2.41	-0.05	-0.02	*
	180°	1.86	0.31	1.95	0.43	0.97	0.31	2.24	0.63
70	0°	-1.43	-	-0.87	-	-2.41	-	0.03	-
	180°	1.85	-	1.94	-	0.97	-	2.23	-
80	0°	-1.43	0.04	-0.82	-6.19	-2.41	-0.03	0.07	*
	180°	1.85	-0.25	1.93	-0.47	0.96	-0.52	2.22	-0.44

*Absolute reference values of 0.03 is too small to give any meaningful values of deviation

4.4.4 Effect of friction between steel and concrete

Friction between steel and concrete is controlled by the coefficient of friction, μ_s. The friction affects the mechanical properties of contact interaction. The variation of μ_s values might contribute to the change in SCF values. This section investigates the effect of μ_s on the variation of SCF values. The Misalignment type A model with $\mu_s =$ 0.2, 0.4, 0.6 and 0.8 is assumed in the study.

Results as depicted in Figure 4.4 5 demonstrate the insignificant effects of μ_s in the study range on SCF values in all structural members at all locations. This effect will be disregarded in the present study.

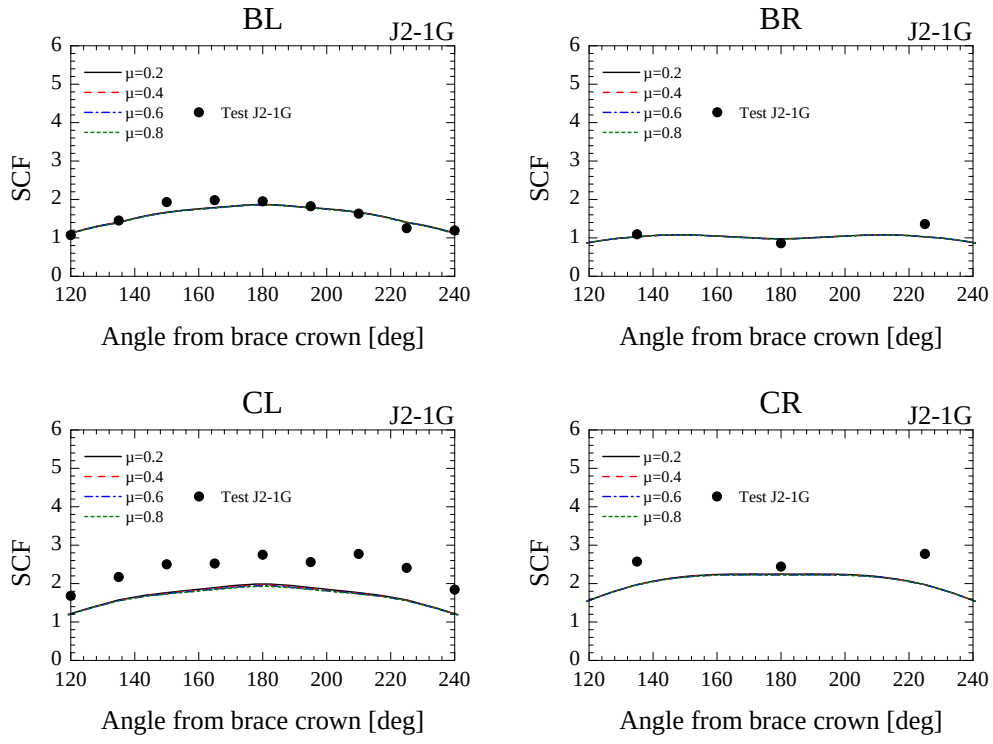

Figure 4.4-5: Effect of friction of coefficient on SCF values

4.4.5 Effect of gap between chord inner surface and concrete surface

The ultra-high strength concrete materials experience a certain amount of autogenous shrinkage during the curing stage (Kim & Koo, 2013) which leads to gap between chord inner surface and concrete surface. Shrinkage is the decrease of concrete volume with time due to the loss of moisture (free water) of the concrete. There are two types of shrinkage which are most likely to occur in this study; drying shrinkage and autogenous shrinkage. Drying shrinkage occurs after the concrete has already hardened. In drying environment (low relative humidity), the difference in the moisture content between concrete and the surrounding environment initiates the evaporation of free water, resulting in shrinkage strain. Similar to drying shrinkage, autogenous shrinkage occurs in hardened concrete. Autogenous shrinkage occurs as a result of the continuous cement hydration in concrete. For normal concrete, autogenous shrinkage is rather small compared to the drying shrinkage. In contrast, for high strength concrete with low water-to-cement ratio, autogenous shrinkage may exceed drying shrinkage (Newman and Choo, 2003). Since only the determination of the drying shrinkage is available in the ACI committee 209, the magnitude of drying shrinkage is firstly determined to get an idea of what would be the magnitude of gap to be considered. The determination of the drying shrinkage of concrete is as follows:

$$(\varepsilon_{sh})_{t_{sh}} = \frac{t_{sh}}{\phi + t_{sh}} (\varepsilon_{sh})_u \gamma_c \tag{4.4-1}$$

where, $(\varepsilon_{sh})_{t_{sh}}$ is the shrinkage after t_{sh} days of drying,

$(\varepsilon_{sh})_u$ is the ultimate drying shrinkage,

ϕ is the empirical constant depending on curing conditions.

It is worthwhile to mention that there might be other effects that contribute to the shrinkage of ultra-high strength concrete. The shrinkage determined using Equation 4.4-1 is considered here as a reference value.

Disregarding the volume change in the axial direction, Equation 4.4-1 gives a shrinkage gap of around 0.05 mm. The gap between chord inner surface and concrete surface to be covered in this study is therefore 0.05 mm, 0.10 mm, 0.20 mm, and 0.30 mm. Figure 4.4 6 shows finite element models of the shrunk infilled concrete. The J2-1G model together with zero gap in the concrete is the control case.

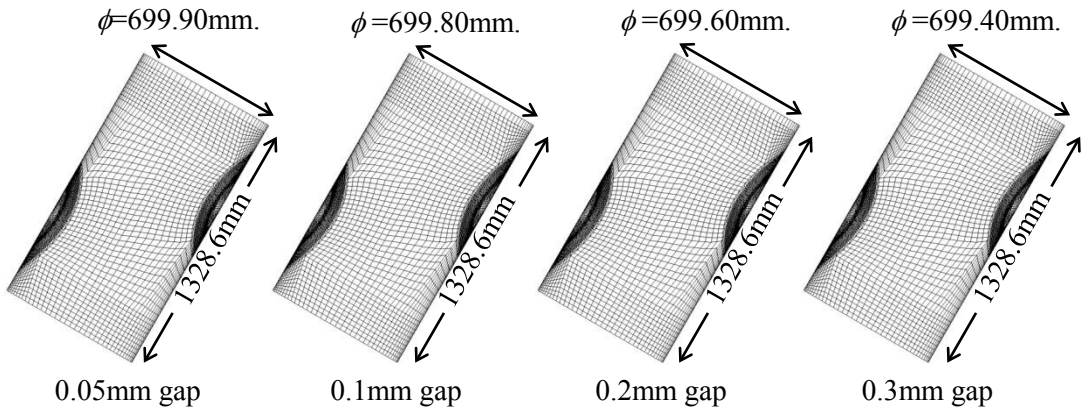

Figure 4.4-6: Shrunk infilled concrete model

It can be observed in Figure 4.4-7 that the presence of a finite gap between the concrete and steel surfaces leads to strong variations in the SCFs calculated along the weld toe especially in the chord member and the SCF values are significantly more sensitive to the size of gap between chord inner surface and concrete surface as compared to other material properties and friction. A small gap of only 0.05 mm can significantly raise the SCF values at various locations along the weld toe. The bottom of the brace right seems to be the least affected by the gap whereas the gap affects significantly the SCF values at all other locations and those of other members. The results in Figure 4.4-7 reveal the calculated SCF values converge as the gap between chord inner surface and concrete surface exceeds 0.20 mm and the SCF values calculated using assumed 0.10 mm gap between chord inner surface and concrete surface shows reasonable agreement of SCF values to the measured SCF values from the experiment. The post-test sectioning and measurement using a feeler gauge confirms an average gap of 0.18 mm between steel and the concrete surface.

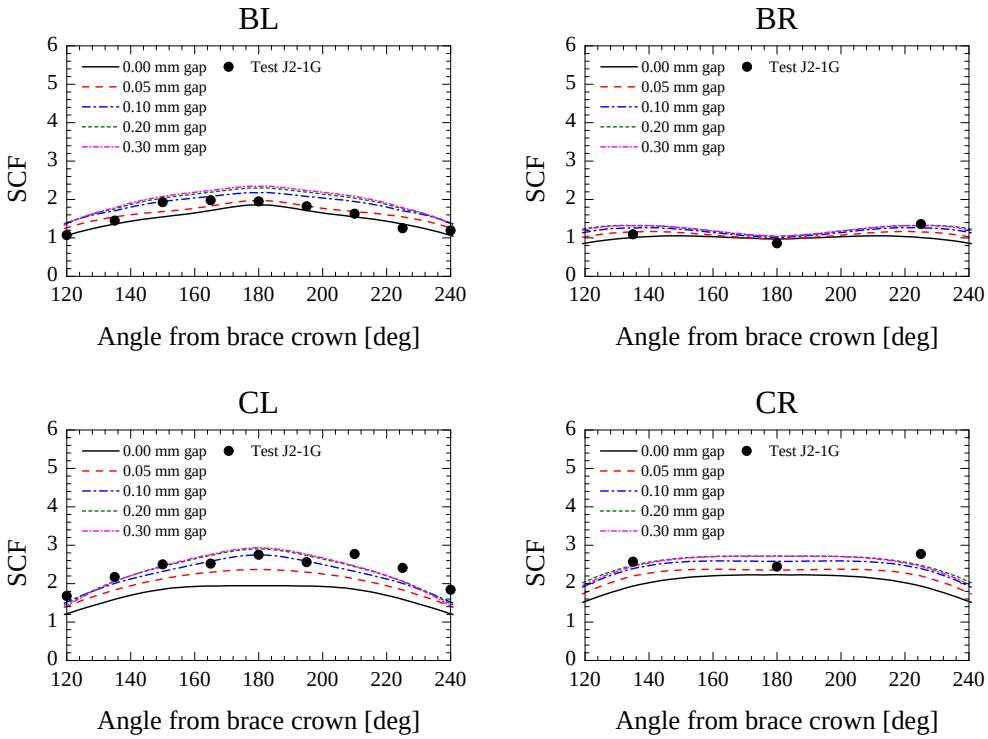

Figure 4.4-7: Effect of gap between chord inner surface and concrete surface to SCF values of J2-1G specimen

The minimum SCF = 2.0 is recommend for SCF calculation using parametric equation for the unspecified location. This minimum is significantly underestimate maximum SCF values of the CHS X-joints used in this study. The parametric equations also cannot capture this high SCF as it is not locate at crown position. Higher minimum of 4.0 is recommended otherwise detail FE analyses has to be conducted. The idea of minimum SCF value is probably more appropriate for the grouted CHS X-joint as the variation of SCF values is less pronounce in the high SCF region ($130^\circ \leq \rho \leq 230^\circ$). The minimum SCF = 3.0 would be recommended value for the grouted CHS X-joints with similar geometry to the studied joints.

4.4.6 Effect of simplified SCF-SNCF relationship

As discussed in Section 2.2.5, the relationship between SCF and SNCF can be derived using the constitutive law as shown in Equation 2.2-11. This equation can be simplified to a two-dimensional plane stress case (Equation 2.2-12) since all stresses and strains are measured at the material surface (stress perpendicular to material surface = 0). The ratio calculated from Equation 2.2-11 and Equation 2.2-12 will be called 3D ratio and 2D ratio respectively.

The variations of the 2D ratio and 3D ratio along the weld toe of J2-1 (ungrouted joint) model are illustrated in Figure 4.4-8a. For all members, the calculated 2D ratio and 3D ratio agree wilth the recommended value of 1.15 over a small region of $\rho \approx 60^\circ - 120^\circ$. On the other hand, the ratios at the locations where fracture or fatigue cracks are most likely to occur ($\rho \approx 180^\circ$) are greater than 1.15 for both chord and brace members. At the latter locations, the recommended value underestimates the SCF values by 14%. This should be borne in mind during the design process as it may lead to overestimation of fatigue life of the joint by the S-N approach. A small deviation of SCF values may lead to a substantial deviation in the permissible number of cycles to failure. Similar to J2-1 model, J2-1G (grouted joint) model shows that only a small region of BR and CR agrees with the guided value of 1.15 ($\rho \approx 90^\circ - 110^\circ$), as shown in Figure 4.4-9. The deviations are more pronounced on the BL and CL members. Figure 4.4-8b and Figure 4.4-9b demonstrate the differences of the results from 2D ratio as compared to the 3D ratio model.

The improvement of the fatigue performance of J2-1G where the more precise SCF-SNCF relationship is adopted is illustrated in Figure 4.4-10. The outcomes meet all the requirements stipulated in AIP (2002 and 2007), DNV (2011), and CIDECT (Zhao et al., 2001).

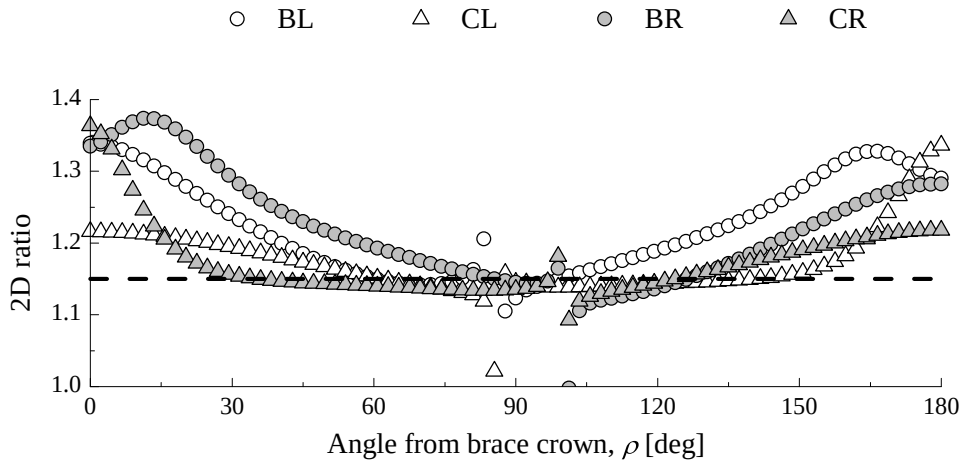

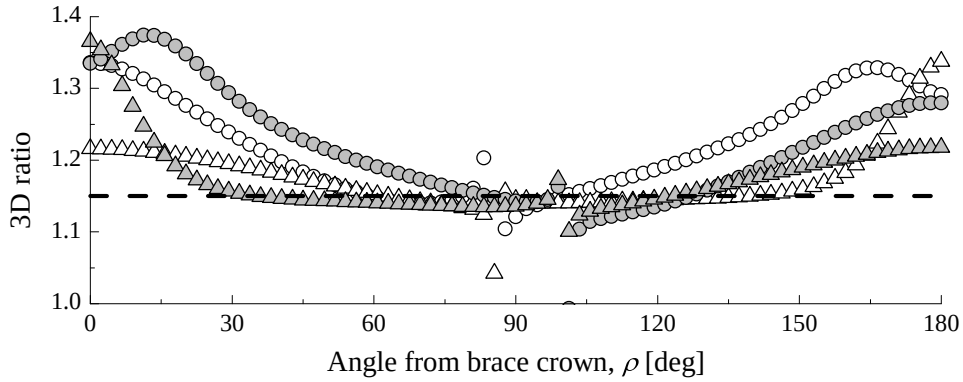

(a) Variation of 2D ratio and 3D ratio

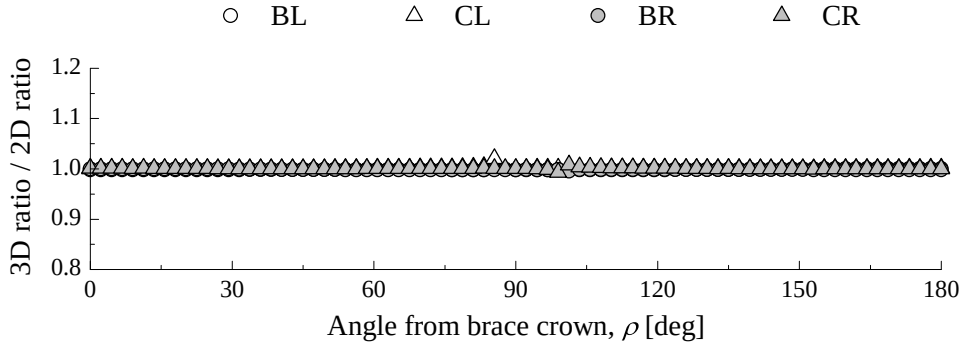

(b) Comparison between 2D ratio and 3D ratio

Figure 4.4-8: Comparison of SCF and SNCF values of J2-1

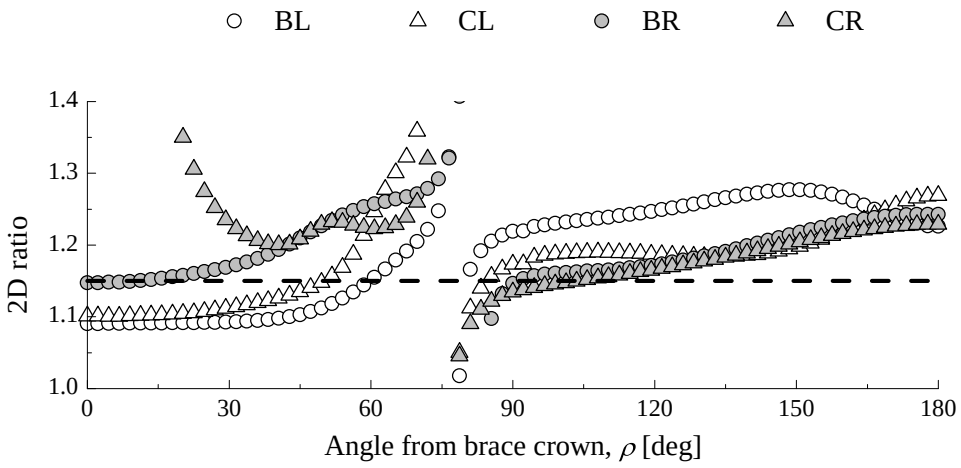

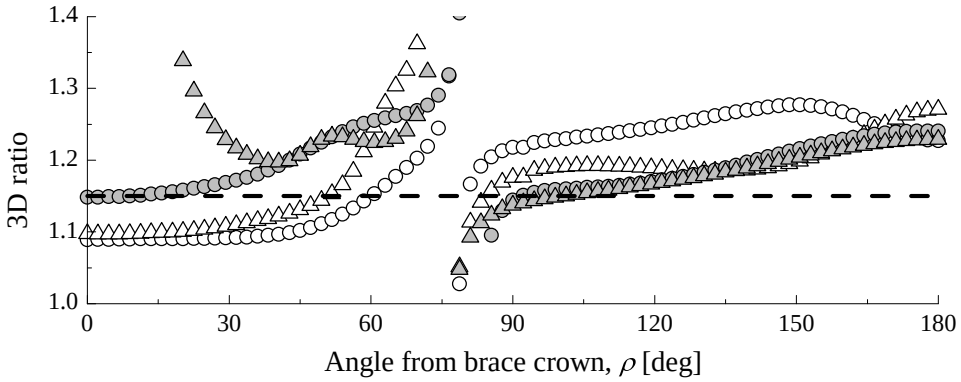

(a) Variation of 2D ratio and 3D ratio

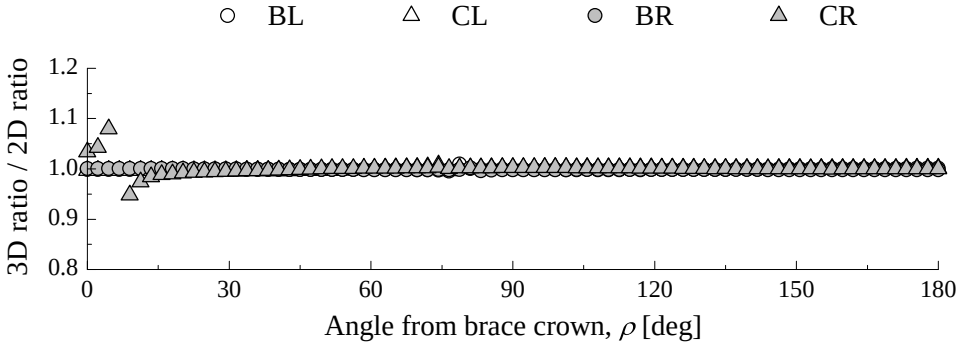

(b) Comparison between 2D ratio and 3D ratio

Figure 4.4-9: Comparison of SCF and SNCF values of J2-1G

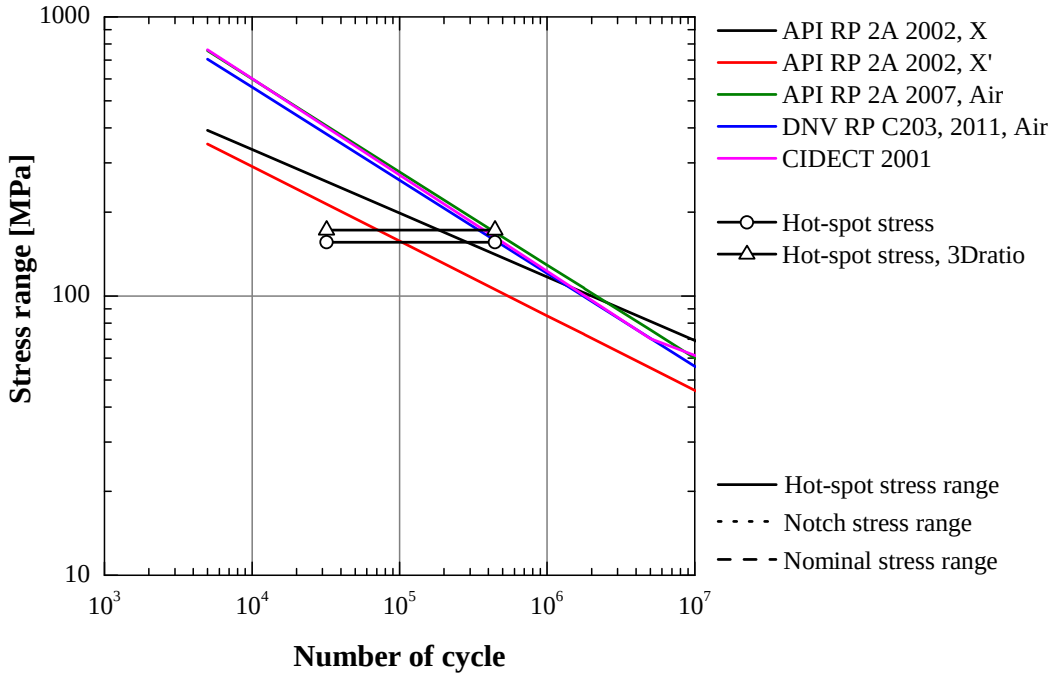

Figure 4.4-10: Fatigue performance based on the more precise SCF-SNCF relationship of J2-1G

4.4.7 Numerically computed SCF values of J2-2 specimen

The comparison of the computed and experimentally measured SCF values at various preparation stages of the J2-2 specimen is illustrated in Figure 4.4-11 and Figure 4.4-12. It is observed that the SCF values on chord member from the finite element model with ground weld toe J2-1X and J2-2XPFG are lower as compared to those from model without toe grinding J2-1 and J2-2PGF. In addition, the computed SCF values of those joints compare well with experimental results. The SCF values from finite element model with a 0.1 mm gap between chord inner surface and infilled concrete surface also agree well with the measured SCF values from the experiment. The computed SCF values in Figure 4.4-11 for J2-2P and J2-2PG confirm the postulations that (i) the presence of the internal diaphragm significantly reduces SCF values on the chord member, and (ii) further stiffening the chord marginally reduces SCF values of the joint.

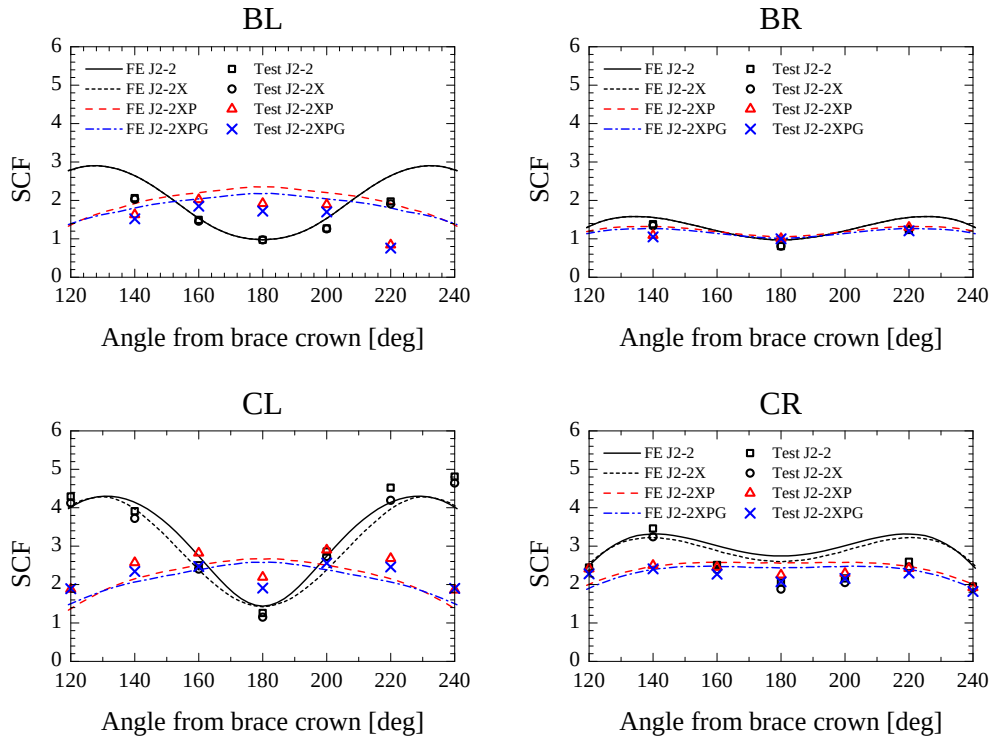

Figure 4.4-11: Comparison of numerically computed SCF values and experimentally measured SCF values of J2-2 specimen

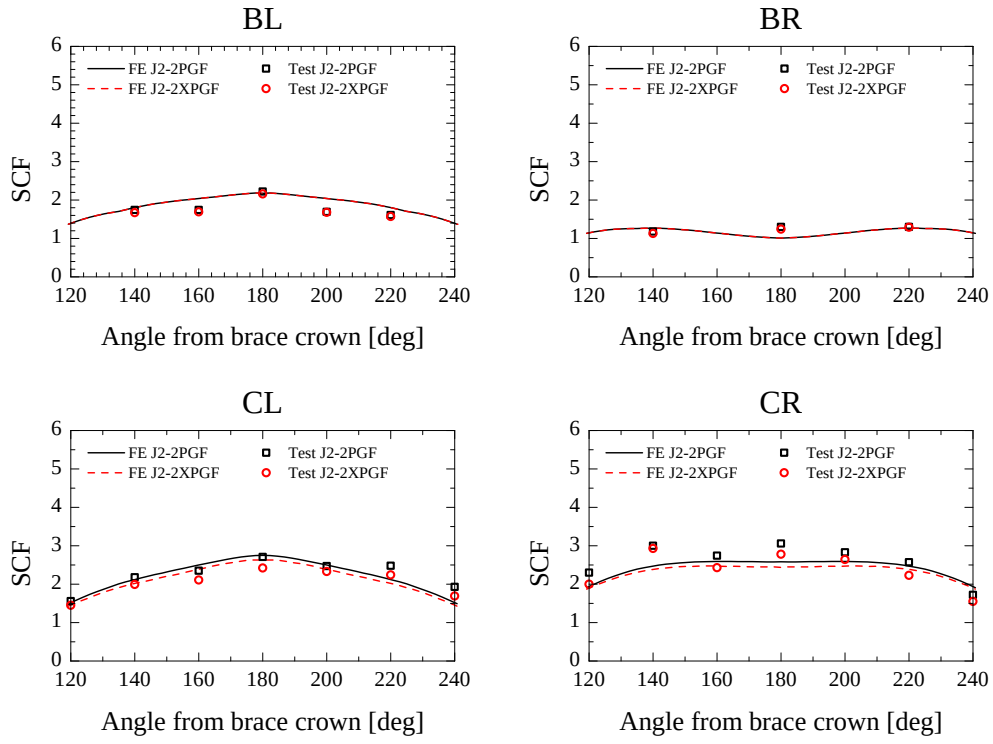

Figure 4.4-12: Comparison of numerically computed SCF values and experimentally measured SCF values of J2-2F specimen

4.5 Numerically computed NSCF values

This section presents NSCF values of specimen with as-welded weld toe condition and specimen with ground weld toe condition. The NSCF values are determined using Equation 4.2-1. The presented NSCF values for the specimen with ground weld toe condition correspond to the NSCF values at the middle of the ground weld toe curve (location #8). The numerically computed NSCF values are compared with NSCF values from experimental measurement.

The comparison of NSCF values in Figure 4.5-1 - Figure 4.5-3 show that the calculated NSCF values is in close agreement with the experimental measured NSCF values for all specimens with and without post weld toe grinding. Both calculated NSCF values and the experimental measured NSCF values in Figure 4.5-1 illustrate that the post-weld toe grinding increase substantially the NSCF values. The maximum NSCF value of the specimen with post-weld toe grinding on both CL and CR increases by almost 2 times as compared to those specimen with as-welded weld toe condition. The corresponding maximum NSCF location remains in the same region after grinding was implemented. The specimen with concrete-filled chord also shows similar findings as compared to the specimen without concrete-filled chord. The maximum NSCF values increased by almost 2 times and its corresponding location remains in the same region as illustrated in Figure 4.5-2. The overall NSCF values of the specimen with concrete-filled chord are lower than those of the specimen without concrete-filled chord as the presence of 2 internal diaphragm plates and ultrahigh strength concrete increases substantially the stiffness of chord member. As a result, the NSCF values decreased.

The NSCF values in Figure 4.5-3 show similar behavior as compared to the behavior of SCF values. Internal stiffening chord member by 2 internal diaphragm plates introduces significant reduction of NSCF values near the weld toe of the chord member. Further stiffening of the chord member by internal ultrahigh strength concrete causes only marginal decreases in the NSCF values.

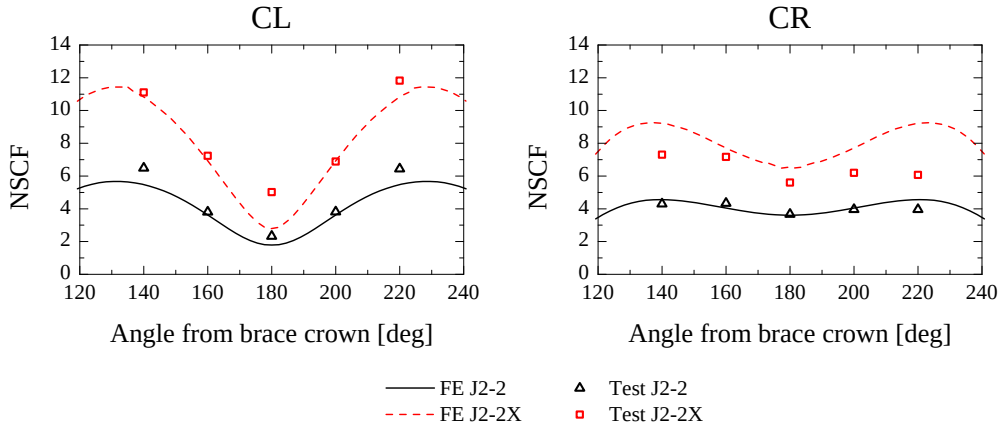

Figure 4.5-1: Effect of post-weld toe grinding to NSCF values of specimen without concrete filled chord

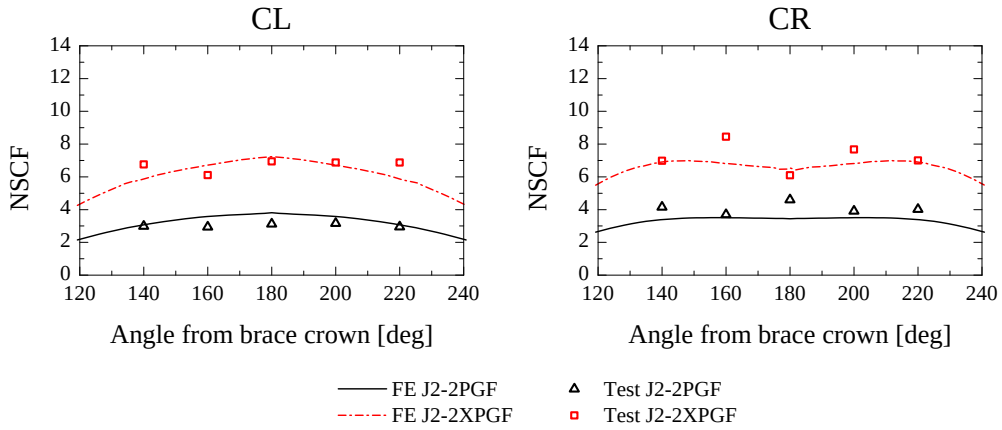

Figure 4.5-2: Effect of post-weld toe grinding to NSCF values of specimen with concrete filled chord

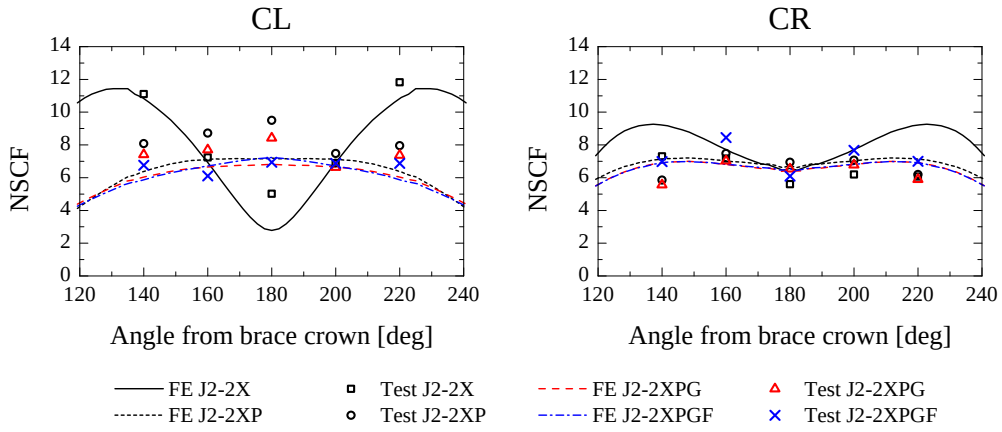

Figure 4.5-3: Comparison of numerically computed NSCF values and experimentally measured NSCF values of J2-2 specimen

4.6 Conclusion

Measured SCF values along the weld toe on brace members from the experiment agree well with the FE results for both J2-1G and J2-1GF joint specimens. However, the measured SCFs on the chord member are higher than the FE results. Gap between infilled concrete and the chord inner surface is most likely the cause of the discrepancy. The finite element analysis shows that the 0.10 mm gap significantly affects the computed SCF values and provides better convergence with the experimental results.

The strength of infilled concrete and coefficient of friction between infilled concrete and chord inner surface are less likely the cause of the discrepancy between SCF values obtained experimentally and the results from FE analyses.

The recommended SCF and SNCF relationship underestimates the SCF values at most locations along the weld toe of brace and chord members. This relation should be more precisely calculated since it greatly influences the fatigue life of structures. The SCF and SNCF relationship can be simplified to a more efficient 2D plane stress problem without significant loss of accuracy

CHAPTER 5

EXTENDED FINITE ELEMENT BASED FATIGUE LIFE EXTIMATION

5.1 Introduction

Studying fracture and fatigue behavior of cracked structures is an important task in structural integrity assessment and damage tolerance analyses. The conventional finite element method divides a continuous physical model into a series of elements. Problems arise when one wants to incorporate internal discontinuities, e.g., interfaces, cracks, voids, and inclusions. The discontinuity cannot be arbitrarily embedded into a finite element domain due to the continuous nature of FEM. As a result, the finite element domain has to coincide with the geometric edge of the discontinuity. This poses difficulties in the meshing process especially if the geometry of the discontinuity is complicated or the discontinuity is small compared to the structure size. This type of discontinuity requires dense and small elements which ultimately lead to excessive computational cost. Though these meshing difficulties are taken care of in advanced finite element software, the conventional finite element method is still not suitable for modeling cracks and their propagation. Problems involving cracks require special higher order elements with quarter nodes near the crack tip to enhance its ability to capture the singularity field at the crack tip. The analysis involves a constant re-meshing process during crack propagation.

In 1999 Belytschko and Moës proposed a new computational method called the extended finite element method (XFEM). XFEM is an enhancement of conventional FEM while holding all the basic concept of FEM, such as the partition of unity concept. The main idea of XFEM is to locally apply appropriate enrichment functions or prior known analytical solutions describing the field behavior to the domain of interest. Therefore, the domain of interest is fully capable of capturing features of interest, and accurate results can be obtained even when using a relatively coarse mesh. As an example, a discontinuous function is introduced to capture the discontinuity of field variables in the domain, and hence the description for the discontinuous field is consequently mesh-independent.

This chapter presents the formulation of XFEM in section 5.2. Crack representation using the vector level-set method is discussed in section 5.3. Section 5.4 describes crack modeling using XFEM in ABAQUS. Subsequently the studies of XFEM mesh design and fatigue crack propagation simulation are presented in section 5.5 and 5.6 respectively.

5.2 XFEM formulation

5.2.1 Displacement approximation

The displacement filed in XFEM comprises two parts, (i) the conventional FEM displacement field, u^{FE}, and (ii) the enriched displacement field, u^{ENR}:

$$u = u^{FE} + u^{ENR} = \sum_{i \in n} N_i u_i + \sum_{j \in n_{cr}} N_j H(x) a_j + \sum_{k \in n_{tip}} N_k \left(\sum_{l=1}^{4} F_l(x) b_l^k \right) \qquad (5.2\text{-}1)$$

where, n is the node number of elements in the entire model,

n_{cr} is the node number whose element completely cut by crack,

n_{tip} is the node number whose element contain crack tip,

u_i is the nodal displacement variable,

a_j and b_k are the nodal enrichment variables.

The literature is silent on the physical meaning of a_j, and b_k , but they may be viewed as the amount of *displacement* caused by the crack line and tip, respectively.

5.2.2 Enrichment function

For cracks problem, two sets of enrichment functions are used to handle the presence of a crack: a discontinuous function (jump function) describing the crack line and a set of asymptotic functions (crack tip functions) describing the crack tip.

5.2.2.1 Jump function

The jump function or Heaviside function is used to describe the elements which are completely cut by the crack (split into two).

$$H(x,y) = \begin{cases} 1 \text{ for } (x - x*) \cdot \vec{\mathbf{n}} > 0 \\ -1 \text{ for } (x - x*) \cdot \vec{\mathbf{n}} < 0 \end{cases} \tag{5.2-2}$$

where, x is the point of interest,

$x*$ is a point on the crack segment closet to point x, and

$\vec{\mathbf{n}}$ is a unit normal vector at the point $x*$.

5.2.2.2 Asymptotic near-tip enrichment function

For elements that contain the crack tip, the Heaviside function does not sufficiently describe crack tip conditions. The missing crack tip characteristic is stress singularity. A possible additional enrichment function is the asymptotic near-tip enrichment function. The displacement field available from Linear Elastic Fracture Mechanics (LEFM) is used to enrich these elements. The near tip displacement fields for combined modes I and II loading are:

$$
\begin{aligned}
u(x,y) =& \frac{K_I}{2\mu}\sqrt{\frac{r}{2\mu}}\cos\left(\frac{\theta}{2}\right)\left[\kappa - 1 + 2\sin^2\left(\frac{\theta}{2}\right)\right] \\
&+ \frac{K_{II}}{2\mu}\sqrt{\frac{r}{2\mu}}\sin\left(\frac{\theta}{2}\right)\left[\kappa + 1 + 2\cos^2\left(\frac{\theta}{2}\right)\right] \\
v(x,y) =& \frac{K_I}{2\mu}\sqrt{\frac{r}{2\mu}}\sin\left(\frac{\theta}{2}\right)\left[\kappa + 1 - 2\cos^2\left(\frac{\theta}{2}\right)\right] \\
&+ \frac{K_{II}}{2\mu}\sqrt{\frac{r}{2\mu}}\cos\left(\frac{\theta}{2}\right)\left[\kappa - 1 - 2\sin^2\left(\frac{\theta}{2}\right)\right]
\end{aligned}
\tag{5.2-3}
$$

where, K_I and K_{II} are stress intensity factors for crack opening mode I and mode II,

r and θ are polar-coordinates with the origin at the crack tip, and

$\kappa = \frac{3-\nu}{1+\nu}$ for plane stress and $\kappa = 3 - 4\nu$ for plane strain

Belytschko and Black (1999) have been shown that the above displacement field is contained in the span of the following functions:

$$
F(r,\theta) = \left\{\sqrt{r}\sin\frac{\theta}{2}, \sqrt{r}\cos\frac{\theta}{2}, \sqrt{r}\sin\theta\sin\frac{\theta}{2}, \sqrt{r}\sin\theta\cos\frac{\theta}{2}\right\} \tag{5.2-4}
$$

5.3 Vector level-set method

The level set method is a numerical technique to track moving discontinuities. It was proposed by Osher and Sethian (1988) and implemented into finite element method by Belytschko et al. (2001). The basic idea of the level set method is to provide a geometrical description of discontinuous surface. In the level set method, discontinuity is represented as a zero level set function. One of the frequently used methods for construction level set function is the signed distance function expressed as follows:

$$
f(x) = \pm \min|x - x_c| \tag{5.3-1}
$$

where, x is any evaluation point, and

x_c is a point on the discontinuity.

The physical meaning of the signed distance function is the closet distance from a point to the discontinuity. The signed distance function vanishes at the discontinuity. It gives positive values on one side of the discontinuity and negative values on the other. The interface is represented by a zero level set function at a particular time, t.

In crack problems, one signed distance function is insufficient to describe crack geometry. Two signed distance functions are introduced: $\phi(x)$, and $\psi(x)$. The first signed distance function, $\phi(x)$, describes the location of the crack face, whereas the second signed distance function, $\psi(x)$, locates the crack tip or crack front. Generally the two signed distance functions are assumed to be orthogonal:

$$\phi \cdot \psi = 0 \tag{5.3-2}$$

With the two signed distance functions as illustrated in Figure 5.3-1, cracks can be described as:

$$\forall \psi \rightarrow \phi \begin{cases} > 0 & \text{upper crack face} \\ = 0 & \text{crack face plane} \\ < 0 & \text{lower crack face} \end{cases}, \quad \forall \phi \rightarrow \psi \begin{cases} > 0 & \text{ahead of crack tip} \\ = 0 & \text{crack tip plane} \\ < 0 & \text{before crack tip} \end{cases} \tag{5.3-3}$$

The level set function not only helps in tracking discontinuities arbitrarily aligned with the finite element mesh but also helps in defining the position of a point at the crack tip polar coordinate system

The vector level set method (Ventura et al. 2002, 2003) is one of the simple and straightforward level set methods. This method is based only on the geometry of discontinuity. The signed distance function is expressed in a general form as:

$$f(x) = |\mathbf{d}| H\left(\mathbf{d} \cdot \vec{\mathbf{n}}\right) \tag{5.3-4}$$

where, $\mathbf{d}$ is distance vector joining evaluation point x and its projection point x_c on the crack line,

$H\left(\mathbf{d} \cdot \vec{\mathbf{n}}\right)$ is the Heaviside function returning sign of the $\mathbf{d} \cdot \vec{\mathbf{n}}$ product.

$$H\left(\mathbf{d}\cdot\vec{\mathbf{n}}\right)=\begin{cases}1 & \text{if} \quad \mathbf{d}\cdot\vec{\mathbf{n}}\geq 0\\ -1 & \text{if} \quad \mathbf{d}\cdot\vec{\mathbf{n}}<0\end{cases} \tag{5.3-5}$$

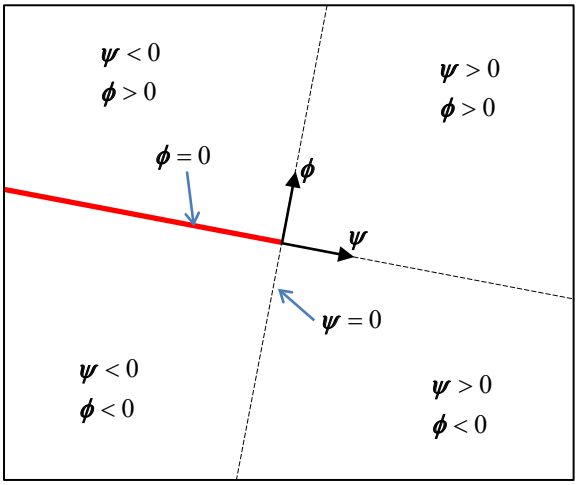

Figure 5.3-1: Definition of signed distance function

The two signed distance determination approaches (i) secant approach and (ii) tangent approach approaches is demonstrated in Figure 5.3-2. The secant approach assumes that the crack is straight within the cuts the element. The assumed straight crack is established by joining the crack tip point to a point where the crack cut element edge. The local crack tip coordinates are therefore parallel and perpendicular to the assumed straight crack. One can determine the signed distance function as expressed in Equation 5.3-4. However, finding x_c for all 4 nodal points takes more computational effort. Alternative signed distance function determination is to decompose vectors joining nodal point to crack tip point, $\vec{v}_i$, to the local crack tip coordinates. Therefore, the signed distance functions for the secant approach are expressed as:

$$\phi_i=\vec{v}_i\cdot\vec{u}_\phi \tag{5.3-6a}$$

$$\psi_i=\vec{v}_i\cdot\vec{u}_\psi \tag{5.3-6b}$$

where, i is node number,

$\vec{u}_\phi$ and $\vec{u}_\psi$ are the unit normal vectors to local crack tip coordinates.

The tangent approach, on the other hand, is more accurate than the former approach. This approach uses the actual crack geometry to calculate signed distance function and strictly follows Equation 5.3-4. The local crack coordinates are parallel and perpendicular to crack line. The signed distance functions for the tangent approach are expressed as:

$$\phi_i = \left|\vec{\phi}_i\right| H\left(\vec{\phi}_i \cdot \vec{n}_i\right) \tag{5.3-7a}$$

$$\psi_i = \left|\vec{\psi}_i\right| H\left(\vec{\psi}_i \cdot \vec{u}_\psi\right) \tag{5.3-7b}$$

Contour plots of the signed distance function ϕ_i with two different element sizes is shown in Figure 5.3-3. Element sizes in Figure 5.3-3a is wider than that in Figure 5.3-3b. With the same element size, the zero level set function from two approaches match well to the actual crack geometry (solid black line). It is noted that the crack is better represented for a more refined mesh.

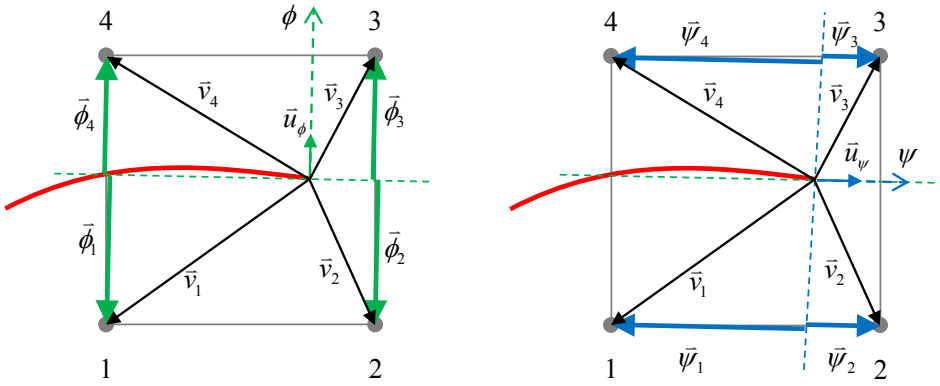

(a) Secant approach

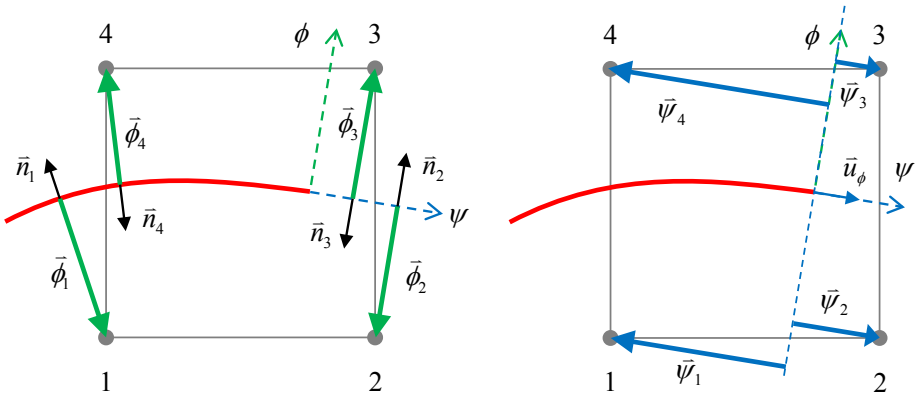

(b) Tangent approach

Figure 5.3-2: The two signed distance determination approaches

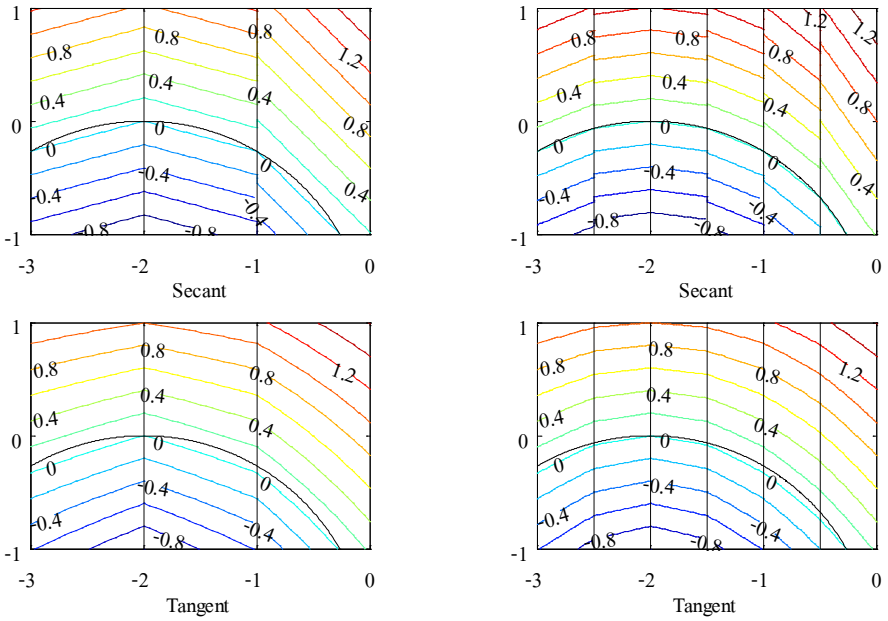

(a) 1×2 **unit** **(b)** 0.5×2 **unit**

Figure 5.3-3: Signed distance function ϕ with two different element sizes

5.4 Modeling XFEM in ABAQUS

This section describes the necessary parameters and features that have to be defined for stationary cracks in ABAQUS. Basically, users have to generate 3-dimensional model, specify material properties, create steps, assign boundary conditions, and create loads. To a create XFEM crack, the following steps have to be done.

- Creating crack body

  ABAQUS requires a 3-dimensional shell to represent a crack. The position of the crack relative to the model is automatically generated using the Level set method. The complexity of the crack is limited by the ability of ABAQUS itself to create a 3-dimensional shell. Users can also manually define cracks using sign-distance values by editing the input file (.inp extension).

- Choosing crack domain

  The crack domain defines the possible area/volume that enrichment functions can be added. Only elements that are cut by the crack and are within the crack domain will be enriched with appropriate enrichment functions as described earlier.

- Specifying enrichment radius

  The enrichment radius is the radius from the crack tip whereby elements inside this radius are enriched by the crack tip enrichment function and are involved in contour integral calculation. By default, this radius equals three times the characteristic element length.

- Requesting contour integral output

  There are 3 types of contour integral available in XFEM: the J-integral, stress intensity factors, and T-stress. It is worthwhile to mention that ABAQUS provides the interaction integral method to compute stress intensity factors for cracks under mixed-mode loading. The process of finding a set of elements that forms contour rings is automatically handled by ABAQUS. The number of contour rings is, however, specified by the user.

- Requesting output parameters for viewing crack

  User must request field output for the signed distance function, PHILSM (ϕ), otherwise the crack will not be visible. PSILSM (ψ) is an optional but useful parameter which helps users to locate the crack tip.

5.5 Study of XFEM mesh design

This section presents the investigation on the accuracy of XFEM results with various mesh designs. The XFEM results are compared with conventional FEM and available closed form solutions with the aim of providing practical guidelines on applying XFEM in the numerical study of SCF.

The investigation program starts with the convergence study. The convergence analysis is conducted to investigate how XFEM models with different mesh sizes and various input parameters, and how they affect the accuracy of SIF solutions. The second part of the program investigates how well XFEM handles different mesh patterns. Details of the investigations are presented in section 5.5.1and 5.5.2.

5.5.1 Mesh design for straight cracks

The standard CT specimen with 25 mm (1T) thickness is adopted in this study. The finite element model is generated following the dimensions as shown in Figure 5.5-1 with symmetry at half of the specimen thickness. The specimen is partitioned into two regions. The first region is the contour integral region as shown in Figure 5.5-2. Elements in this region are in a square shape of $M \times M$ mm. The area of the contour region is $2C_x \times 2C_y$ mm which is scaled to cover all the contour integral rings to ensure the best contour integral results. The second region is the area out of the contour integral region. The dimension of elements in this region is automatically determined by the sweep mesh technique in ABAQUS. The 8 nodes brick element (C3D8) is adopted.

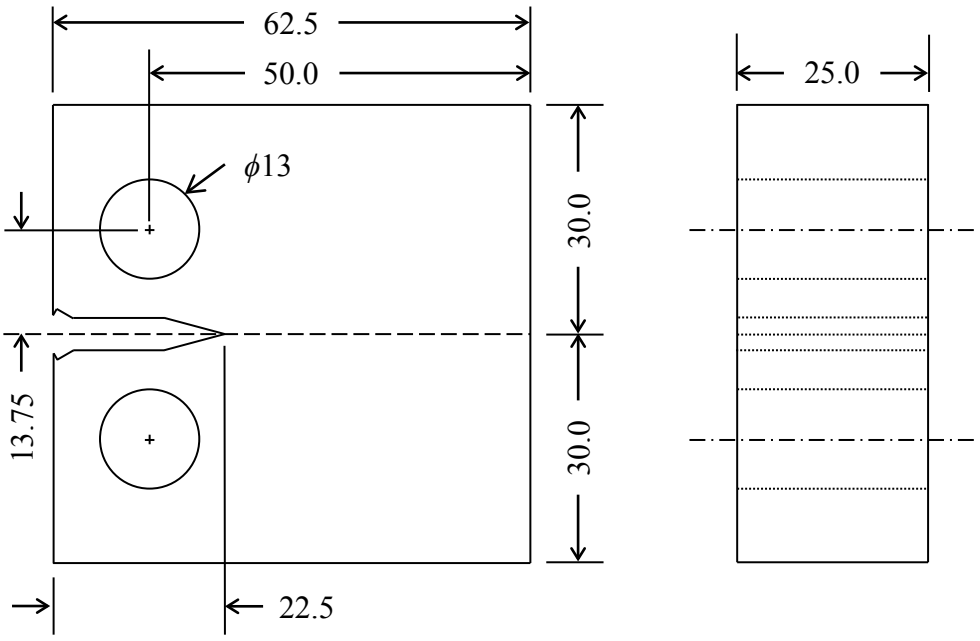

Figure 5.5-1: Typical dimension of the 1TC(T) specimen

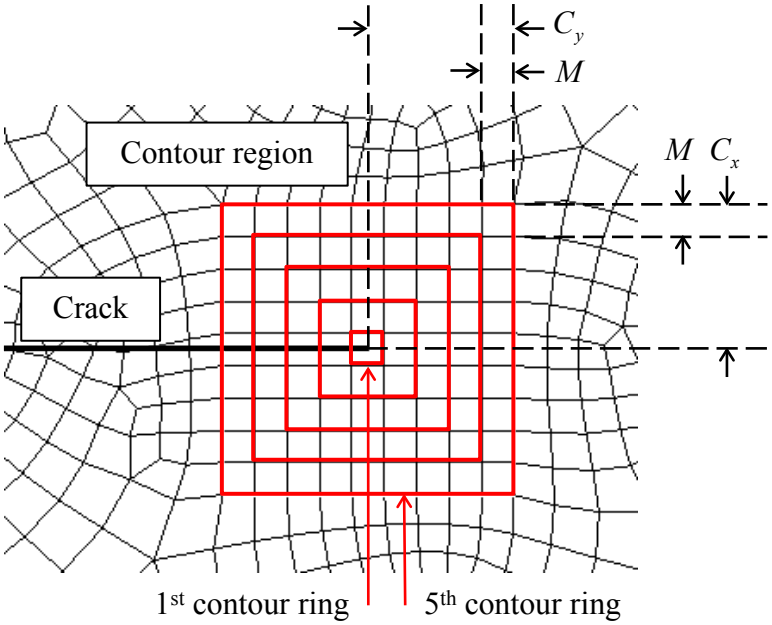

Figure 5.5-2: Dimension of contour integral region

For current investigation the element size, M, are varied between 0.01 to 0.5 mm to review element size sensitivity. Two crack tip locations with respect to the elements are considered. The first case involves the crack cutting through the element at the middle of the element whereas the second case is when the crack aligns with the element face as illustrated in Figure 5.5-3. The contour region is prepared such that it can support up to 10 contour rings. This results in the size of the contour region of $2C_x \times 2C_y$ being $20M \times 19M$ and $20M \times 20M$ for CASE1 and CASE2 respectively. The crack tip enrichment radius, ER, is simultaneously increased from $2M$ to $30M$. The cases with the default ER values calculated by ABAQUS are included and are denoted here as default values. Two crack depths, 10.5 mm and 20.0 mm, are considered.

It is worthwhile mentioning that the sign-distance function, ϕ, of the four bottom nodes in the CASE2 are of non-zero value. They cannot be zero otherwise the numerical integration which needs to be implemented on both sides of crack face will fail. The solution is to set the ϕ values of those nodes to a small value such as 10^{-6} as suggested by ABAQUS.

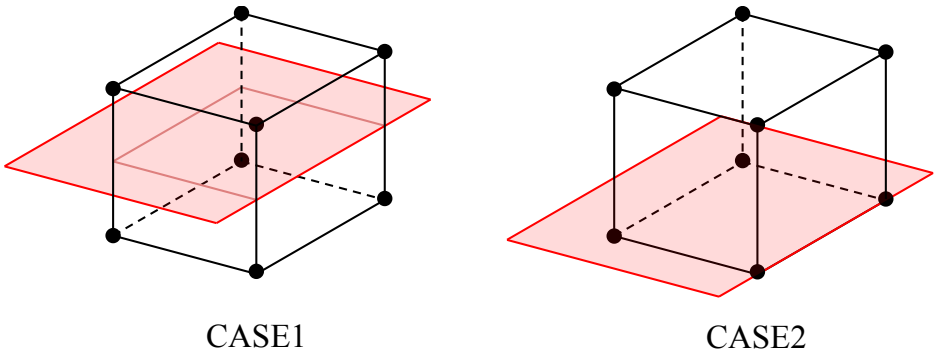

Figure 5.5-3: Two crack tip placement locations

The SIF results from finite element analysis are generally given at various points along the crack front. The through thickness average SIF following Equation 5.5-1 is introduced to determine the average SIF value. From the LEFM theory, K is proportional to the square root of the J-integral. The weighted-average normalized K can be written as:

$$K_{avg} \approx \sqrt{\frac{\sum_{i=1}^{n_z} (J_i)\, b_i}{\sum_{i=1}^{n_z} b_i}} \approx \sqrt{\frac{\sum_{i=1}^{n_z} (K_i)^2 b_i}{\sum_{i=1}^{n_z} b_i}} \tag{5.5-1}$$

where, n_z is the number of nodes in the thickness direction,

J_i is the J-integral value,

K_i is the stress intensity factor value, and

b_i is the distance between two elements adjacent to the node i.

The SIF results from ABAQUS are normalized by the closed-form solution, K_{cal}, (ASTM E 647-13a):

$$K_{\text{cal}} = \frac{P}{B\sqrt{W}} \frac{2+\alpha_c}{(1-\alpha_c)^{3/2}} \left(0.886 + 4.64\alpha_c - 13.32{\alpha_c}^2 + 14.72{\alpha_c}^3 - 5.6{\alpha_c}^4\right) \tag{5.5-2}$$

where, α_c equals a/W, and

P is the applied load.

The normalized K values (K_{avg}/K_{cal}) of the CASE1 crack tip placement tabulated in Table 5.5 1 indicate that, the K results from XFEM are about 30% larger than the K_{cal} for the cases involving shallow crack depth of $a = 10.5$ mm with ER values greater than 0.5 mm, whereas the cases with smaller ER show only 7% to 8% deviation. When ER is larger than 0.5 mm, for a shallow crack depth, the machine notched surfaces are also enriched by the crack tip enrichment functions, and consequently produce relatively high K values. The results also show that the combination of a shallow crack tip and the default ER values calculated by ABAQUS can lead to overestimation of K values regardless of the element sizes considered in this study. The normalized K values of a CASE2 crack tip placement are tabulated in Table 5.5 2. The overall results of the shallow crack depth of $a = 10.5$ mm case are similar to those of CASE1. This indicates that the 30% error of K_{avg} is a result of the shallow crack depth and that the ER being larger than 0.5 mm is not a result of crack tip placement.

For the cases when crack depth equals 20.0 mm, the results from CASE1 and CASE2 crack tip placement show higher K_{avg} values than those determined from Equation 5.5-2 by 5% to 9% regardless of the M and ER values. Moreover, the results show that the cases where ER equals $5M$ to $10M$ give the smallest normalized K values.

It is interesting that the element sizes adopted in the present study do not affect the K results significantly. This is most likely because the XFEM model with embedded crack tip enrichment functions provide the required singularity stress values at the crack tip. Therefore, the coarser mesh model can yield comparable K results to those of the finer mesh model.

The normalized K values from the conventional finite element method (FEM) which adopts 20 nodes brick element (C3D20) and quarter nodes singularity elements tabulated in Table 5.5 3 are slightly lower than the results of CASE1 and CASE2. The results from FEM do not show an improving trend as mesh size becomes smaller either. On the contrary, the finer mesh across the specimen thickness does not significantly improve the K_{avg} results as indicated in Table 5.5 4.

In summary, the study illustrates that the XFEM model with $M = 0.25$ mm and the *default ER* values do not produce results with adequate accuracy as compared to the theoretical solutions and care must be taken when choosing the *ER* for shallow cracks.

Table 5.5-1: Comparison of normalised *K* values with various *M* and *ER* (CASE1)

a [mm]	Element size, *M* [mm]	Normalized *K* values (K_{avg} / K_{cal})							
		2*M*	5*M*	10*M*	15*M*	20*M*	25*M*	30*M*	default
10.5	0.25	1.072	1.307	1.323	1.324	1.329	1.346	1.374	1.332
	0.10	1.071	1.070	1.311	1.327	1.327	1.325	1.333	1.332
	0.05	1.073	1.061	1.075	1.318	1.306	1.318	1.318	1.327
	0.01	1.076	1.065	1.079	1.077	1.080	1.079	1.076	1.329
20.0	0.25	1.050	1.039	1.055	1.055	1.060	1.060	1.061	1.054
	0.10	1.049	1.039	1.054	1.053	1.057	1.056	1.058	1.057
	0.05	1.047	1.037	1.052	1.051	1.055	1.054	1.054	1.051
	0.01	1.048	1.037	1.051	1.049	1.053	1.052	1.053	1.061

Table 5.5-2: Comparison of normalised *K* values with various *M* and *ER* (CASE2)

a [mm]	Element size, *M* [mm]	Normalized *K* values (K_{avg} / K_{cal})							
		2*M*	5*M*	10*M*	15*M*	20*M*	25*M*	30*M*	default
10.5	0.25	1.089	1.327	1.326	1.345	1.352	1.378	1.410	1.336
	0.10	1.087	1.081	1.321	1.328	1.334	1.337	1.339	1.334
	0.05	1.084	1.078	1.076	1.314	1.322	1.320	1.320	1.328
	0.01	1.085	1.080	1.077	1.079	1.079	1.078	1.077	1.330
20.0	0.25	1.065	1.059	1.056	1.061	1.062	1.064	1.068	1.061
	0.10	1.061	1.056	1.054	1.057	1.058	1.058	1.059	1.058
	0.05	1.059	1.053	1.051	1.055	1.055	1.055	1.057	1.058
	0.01	1.060	1.053	1.049	1.052	1.052	1.052	1.052	1.057

Table 5.5-3: Normalized *K* values from FEM with C3D20 element and quarter node element at crack tip

a [mm]	Element size, *M* [mm]	Normalized *K* values
10.5	0.25	1.061
	0.10	1.060
	0.05	1.062
	0.01	1.061
20.0	0.25	1.038
	0.10	1.038
	0.05	1.038
	0.01	1.037

Table 5.5-4: Normalized *K* values with refined mesh across the thickness of specimen cases

a [mm]	Crack placement	Normalized *K* values (K_{avg} / K_{cal})							
		2*M*	5*M*	10*M*	15*M*	20*M*	25*M*	30*M*	default
20	CASE1	1.059	1.054	1.051	1.055	1.055	1.055	1.056	1.056
20	CASE2	1.048	1.038	1.053	1.051	1.055	1.054	1.054	1.055

5.5.2 Flexibility of XFEM mesh design of curved cracks

The study in the previous section considers only straight cracks with meshes perpendicular to the crack front. Those mesh patterns are ideal for contour integral and are relatively easy to generate if the crack geometry is not complicated. However, it is normally more difficult to mesh the model such that it conforms the complex crack geometry. One of the advantages of XFEM is that it does not require the mesh to conform to the crack geometry. However the effects of the latter on the *K* results are not known. The study in this section aims to investigate the effects of mesh pattern on the accuracy of SIF calculation.

A semi-elliptical surface crack specimen with two mesh patterns are adopted in this study. The first mesh pattern is similar to what was used in the previous study where meshes in the contour integral region are parallel and at the same time perpendicular to the crack front. The second mesh is in a grid pattern which is more general, and easy to construct. For both mesh patterns, the crack cuts at the middle of elements and crack tip is at the element boundary.

The drawing of the semi-elliptical surface crack specimen is illustrated in Figure 5.5-44. The specimen width ($2W$), height ($2H$), and thickness (T) are 80.0 mm, 80.0 mm, 10.0 mm respectively. The mesh size, M, is fixed at 0.25 mm and the contour integral region $2C_x \times 2C_y$ equals $20M \times 19M$. The enrichment radius, ER, equals $10M$. The a/c ratios of 0.2, 0.4, 0.6, and 1.0 are considered. The specimen is subjected to uniform tensile stress loading, σ_t on the top and bottom surfaces.

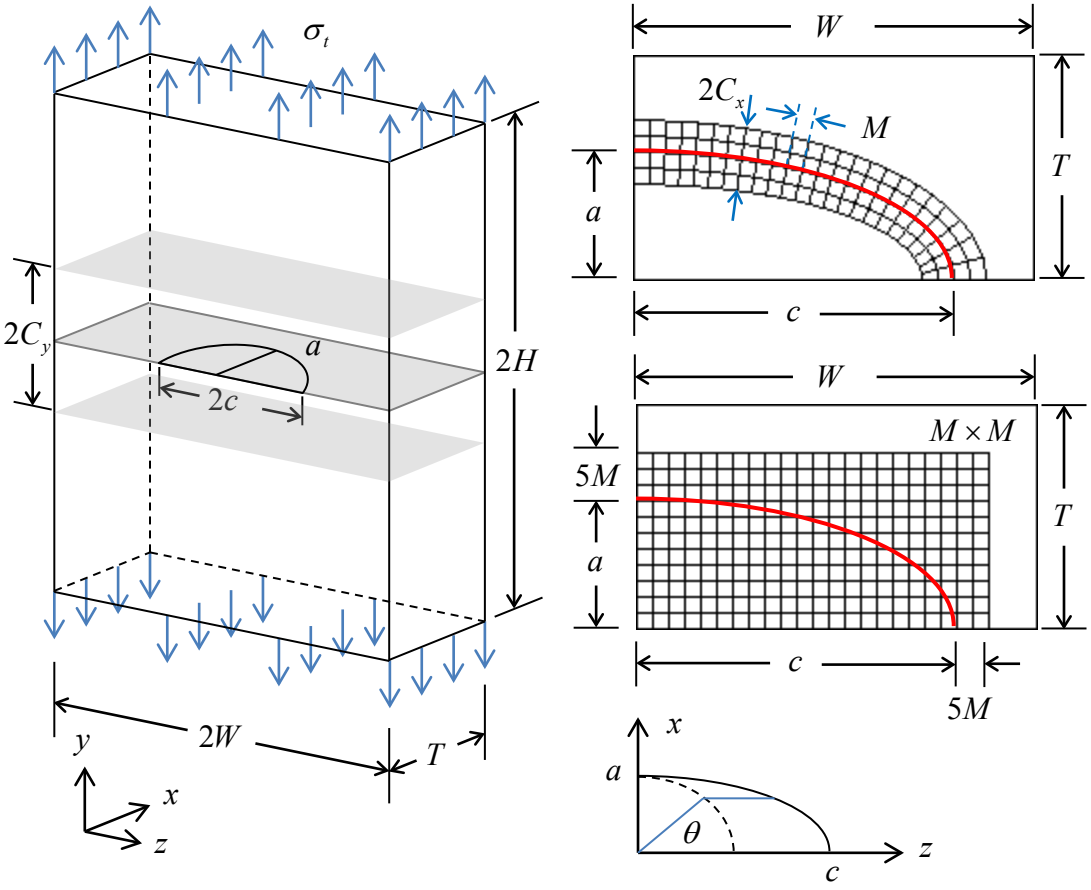

Figure 5.5-4: Typical dimension of semi-elliptical surface crack specimen

5.5.2.1 Normal and parallel mesh to crack line pattern

The K results obtained are compared against K values estimated using the empirical stress intensity factor equation proposed by Newman and Raju (1981) and K results from FEM. Figure 5.5-5 shows that the results from FEM gives around 1% larger K values than those estimated from the Newman and Raju equation, whereas the results from XFEM fluctuate around the Newman and Raju results. The fluctuation of K values from XFEM is more pronounced in the region of $\theta \approx 45^\circ$ to 90°, whereas the fluctuation dies down as θ decreases toward 0°.

Efforts try to reduce the fluctuation either by reducing element size and increasing ER, the fluctuation is still significant. Further investigation is performed by checking signed-distance function calculated by ABAQUS and it is found that the fluctuation of K results from XFEM in this case is mainly due to the slightly inaccurate model of the crack geometry. In ABAQUS, the shell surface is used to represent the crack geometry. The location of the shell with respect to its structure is represented by the signed distance function ϕ and ψ where the zero value of ϕ and ψ locate the crack face and crack tip respectively. The contour plot of the ψ signed distance function (denoted as PSILSM in ABAQUS) in Figure 5.5-6 shows that the zero ψ value locations of elements between $\theta = 70^\circ$ to 80° and $\theta = 80^\circ$ to 90° fall within elements. Moreover, the crack tip line joining the $\theta = 70^\circ$ to 80° and $\theta = 80^\circ$ to 90° are straight. This indicates that the shell which is used to represent crack geometry has a polygonal shape rather that an elliptical shape. As a result, immediate changes of the crack front might affect K calculation and cause those K fluctuations.

The vector level-set method is adopted to re-calculate the elliptical shape ψ signed distance function. The K results after the re-calculation included in Figure 5.5-5 (noted as XFEM_ψ_re-cal) are significantly smoother and compare well to the K values determined from the Newman and Raju equation and FEM results.

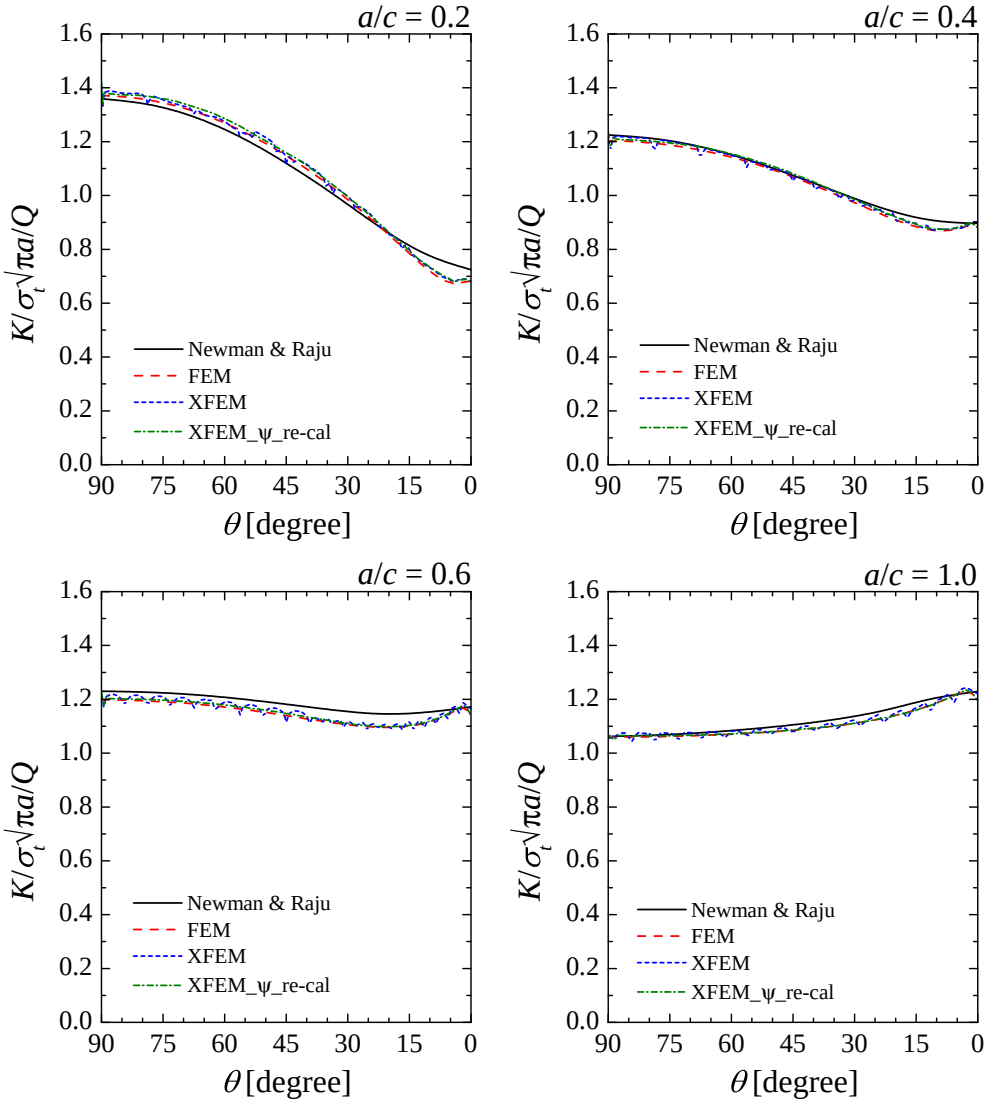

Figure 5.5-5: Comparison of normalized *K* values

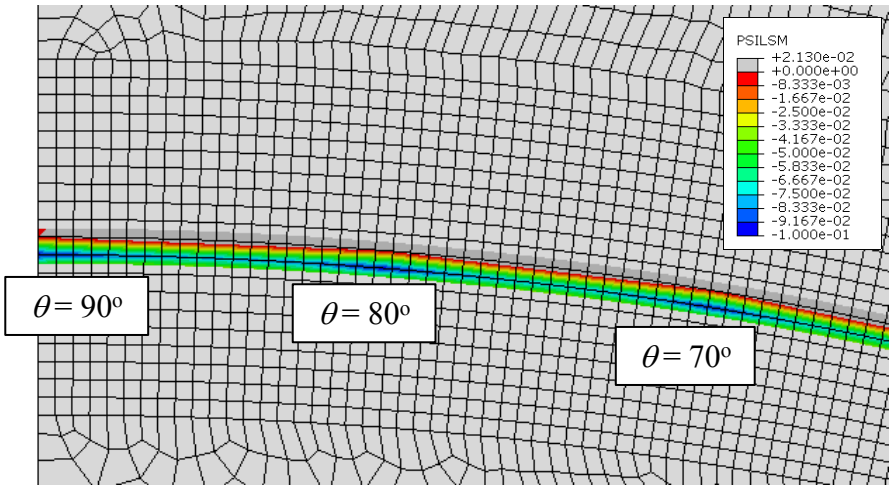

Figure 5.5-6: Contour plot of sign distance function *ψ*

5.5.2.2 Grid mesh pattern

In order to avoid inaccurate crack representation, the sign distance functions ϕ and ψ in this study are calculated using the vector level-set method. Figure 5.5-7 shows that the K values fluctuate at most θ locations along the crack front even though the two signed distance functions are recalculated. Varying the values of M, ER, C_x, and C_y, do not reduce the degree of fluctuation either. The source of this fluctuation may stem from the K calculation method. In ABAQUS, the direction of the contour ring is always perpendicular to the crack front and the set of elements which contribute to the calculation are automatically chosen. Although the perpendicular direction to the crack front is provided by the signed distance functions, it cannot be fully assumed that the distances from the crack tip to all the nodes that form the contour path are of the same order. The contour path at one crack tip point may pick up nodes closer to the crack tip and yield a slightly larger K value, whereas the adjacent crack tip point may give a slightly lower K value because the contour path may pick up nodes further away from the crack tip. As a result, the K values of the grid mesh pattern fluctuate.

The true remedy to minimize this fluctuation is most likely to revise the contour integral algorithm to be compatible with this mesh pattern and XFEM. The contour path may no longer follow element boundary but fixed at a radius away from the crack tip. Nodal stresses and strains are interpolated to the contour path to further calculate K. Writing a script or user subroutine calculating contour integral a number requires of testing and validation. A simpler remedy is preferred.

It is observed while performing parametric study that the XFEM results almost always fluctuate around FEM and Newman and Raju results. Proper polynomial curve fitting may produces accurate K results as compared to the reference. It is shown in Figure 5.5-7 that all the introduced polynomial curves fit quite well with the XFEM data. The 2nd and 3rd degree polynomials, however, underestimate K values in the region close to $\theta = 0^\circ$ in the a/t = 0.2 0.4 and 0.6 case.

The values of R^2 shown in Table 5.5-5 indicate that introducing more than 5 parameters to polynomial does not show significantly better fitting for all considered a/c ratio. Considering only R^2 may not justify if one model is better than the others because the model with more terms (higher R^2) will bend and twist more to come closer the data. The adjusted R^2 which takes the number of terms in a model relative to the number of data points into account is introduced. The adjusted R^2 in Table 5.5-6 indicate the highest adjusted R^2 values with 6^{th} degree polynomial and the adjusted R^2 decreases when the polynomial degree increases to 8. This indicate that the 8^{th} degree polynomial unnecessary high. Though the 6^{th} degree polynomial provides the highest R^2 and adjusted R^2 values, the magnitude is not significantly higher than the 4^{th} degree polynomial. Therefore, the 4^{th} degree polynomial is preferred because it well fit the data while involving least terms. Compared with the Newman and Raju results, the 4^{th} degree polynomial gives less than 5% error.

The K results from the normal and parallel mesh pattern and grid mesh pattern are comparable and the results are agree well with the closed from solutions obtained by the Newman and Raju equation. For stationary cracks the former mesh pattern is more favorable because curve fitting is not required. However, for propagating crack analysis, this mesh pattern requires more effort. It requires not only the FE model but also the crack front to be updated. The latter, the grid mesh pattern, substantially reduces the work load because only the crack representation needs to be updated.

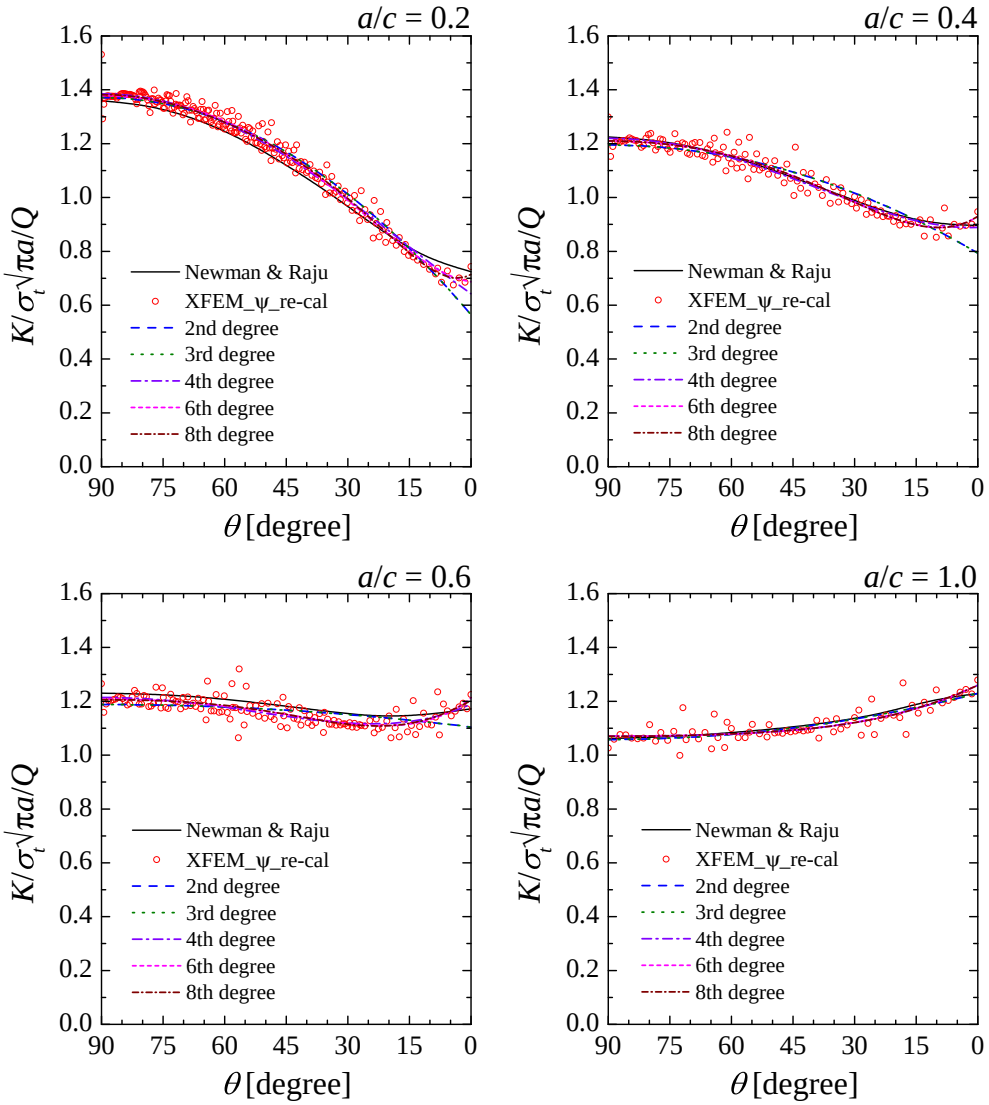

Figure 5.5-7: The *K* results from XFEM with grid mesh pattern

Table 5.5-5: R^2 values from polynomial curve fitting of XFEM results

a/*c*	R^2				
	2nd degree	3rd degree	4th degree	6th degree	8th degree
0.2	0.973	0.973	0.980	0.981	0.982
0.4	0.881	0.881	0.928	0.935	0.935
0.6	0.239	0.239	0.512	0.526	0.529
1.0	0.668	0.668	0.698	0.698	0.698

Table 5.5-6: Adjusted R^2 values from polynomial curve fitting of XFEM results

a/c	Adjusted R^2				
	2nd degree	**3rd degree**	**4th degree**	**6th degree**	**8th degree**
0.2	0.973	0.973	0.979	0.981	0.981
0.4	0.880	0.879	0.927	0.933	0.933
0.6	0.233	0.230	0.505	0.516	0.515
1.0	0.664	0.661	0.690	0.685	0.680

5.6 Fatigue crack propagation study

5.6.1 Fatigue crack propagation simulation procedure

The fatigue crack propagation simulation is started by calculating the signed distance function of the current crack geometry. Subsequently, the FE model with the updated signed distance function is analyzed by ABAQUS. The K results along the crack front are subsequently extracted and used to calculate crack propagation cycle ΔN and crack increment, Δa. Thereafter, a new crack profile is calculated by drawing the assumption that the crack propagation directions along the crack front are perpendicular to the current crack profile. The next analysis cycle will be continued if the deepest crack depth is less than the pre-defined deepest crack depth, a_max. The flow chart of the analysis procedure is shown in Figure 5.6-1.

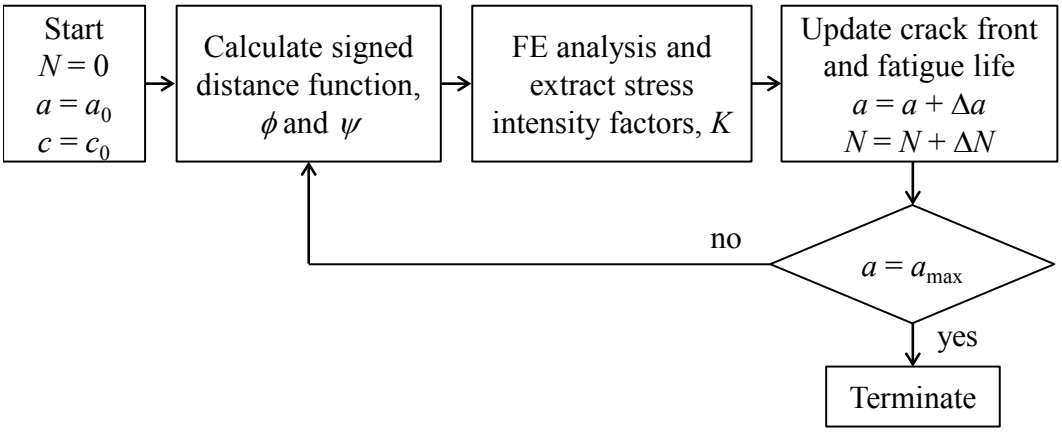

Figure 5.6-1: XFEM fatigue crack propagation analysis flow chart

The crack propagation simulation in this study is based on Paris' law. The crack propagation simulation is controlled by the crack increment, Δa, at a particular location depending on the specimen of interest, i.e. at the middle of the specimen for a CT specimen, or at the deepest crack location for the plate with a semi-elliptical surface crack. Assuming that the stress intensity factor range (ΔK) along the front is constant during crack increment, the fatigue crack propagation cycle, N, determined from Paris' law can be expressed in incremental form as:

$$\Delta N = \frac{1}{C\Delta K^m}\Delta a \tag{5.6-1}$$

where C and m are material constants. Once the ΔN is known, the Δa along the crack front can be calculated and finally the new crack profile is known.

5.6.2 Paris' law

Paris' law is used to calculate the crack propagation cycle, N, and the crack increment at various points along the crack front. The Paris's law is generally derived from experimental data of various specimens and materials. The British standard recommends Paris laws for steels with yield strength under 700 MPa operating in air or non-aggressive environments. They are denoted as the *Mean curve*, *Mean+2SD curve* and *simplified curve* which correspond to the mean, mean+2 standard deviation, and the upper bound of the experimental data.

Table 5.6-1: Paris' law constants recomended by BS7910

Paris' law	***C****	***m***
Mean curve	$3.98\text{x}10^{-13}$	2.88
Mean+2SD	$6.77\text{x}10^{-13}$	2.88
Simplified curve	$5.21\text{x}10^{-13}$	3.00

For da/dN in mm/cycle and ΔK in N/mm$^{3/2}$

5.6.3 Semi-elliptical surface crack propagation

In the literature, Hosseini and Mahmoud (1985), Varfolomeyev et al. (1991), Song et al. (2002), Liu et al. (2010), Shi et al. (2014), the semi-elliptcal crack is assumed to maintain a semi- elliptcal shape throughout the analysis, Paris' law at the deepest crack point and the free surface are defined independently, and the shape changes of the crack during fatigue growth are characterized by crack depth, a, and half crack length, c. The FE simulation shows good agreement with the experimental result. The drawback of the above literatures is that they require Paris' law at both deepest crack point and free surface.

Yamashita et al. (2004) carried out similar FE simulation to the aforementioned literatures. However they adopted the parametric values for Paris' law obtained from CT specimen to predict crack propagation. They reported that crack growth prediction showed good agreement with the experimental results if the Paris' law determined by CT specimen was appropriately adjusted. However, there was no clear reccomendation of how to do the adjustment.

McFadyen et al. (1990) conducted experimental and numerical study on surface crack growth in 28 mm thick steel plates loaded in pure bending. The adopted steel plate specimens are of the same dimension of $150 \times 400 \times 28$ mm in width, height, and thickness respectively. The initial semi-elliptical surface flaws with aspect ratios of $a/c = 0.1$, 0.25, 0.5 and 1.0 were studied. The initial flaws at the center of the specimens are introduced using a slitting saw or a spark discharged machine. The specimens were subjected to constant-amplitude bending stress which results initial stress intensity factor of 10 MPa$\sqrt{\text{m}}$ until failure. The development of the crack growth and crack shape were monitored via ACPD and the beach marking technique.

Though 10 specimens have been tested, only experimental results from 7 specimen, namely number 3, 4, 5, 6, 8, 9, and 10 were reported by McFadyen et al. (1990). These specimens were adopted in the present study and the XFEM solutions obtained

are compared with the reported test results. Details of the 7 specimens adopted in this study are tabulated in Table 5.6-2.

Table 5.6-2: Initial crack shape and loading

Specimen number	Initial crack shape		Initial K [MPa√m]	Stress range [MPa]	Stress ratio
	a [mm]	*c* [mm]			
3	1.0	8.5	10.5	179	0.080
4	1.0	8.5	10.9	189	0.050
5	0.5	3.9	9.5	185	0.083
6	0.9	1.0	10.1	283	0.097
8	0.9	1.0	9.9	277	0.057
9	1.0	4.5	10.0	186	0.018
10	1.0	0.7	9.6	199	0.015

Experimental results obtained from fatigue crack growth of all specimens reported by McFadyen et al. (1990) in a direction (the deepest point) and those in *c* directions (surface point) are shown in Figure 5.6-2. The hollow square symbols represent crack growth rate in *a* direction, while those in hollow triangular symbols represent crack growth rate in *c* direction Based on these results, McFadyen et al. (1990) proposed using the following Paris law:

$$\frac{da}{dN} = 2.9 \times 10^{-12} \Delta K_a^{3.0} \tag{5.6-2}$$

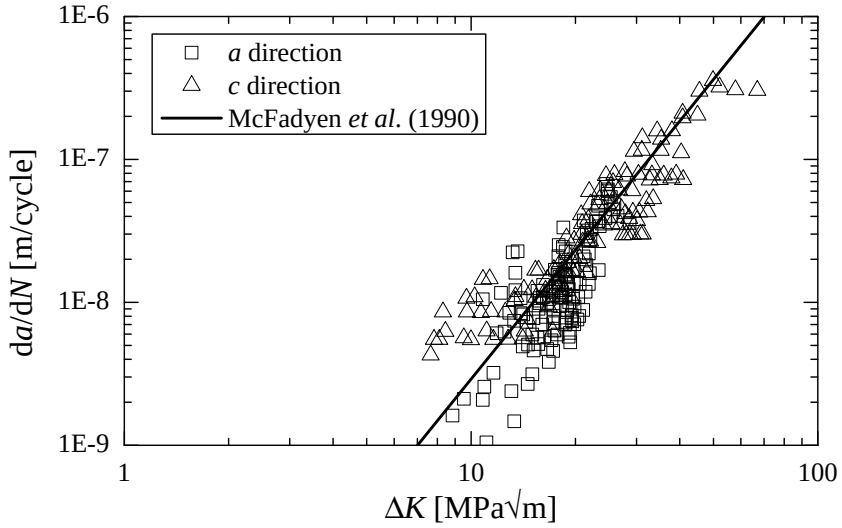

Figure 5.6-2: Fatigue crack growth rate results and the proposed Paris' law by McFadyen et al. (1990)

In this study, the proposed Paris' law in Equation 5.6-2 is adopted to study crack propagation of semi-elliptical surface crack using XFEM. The finite element model illustrated in Figure 5.6-3 is prepared with $M = 0.25$ mm, $2C_y = 20M$, and $ER = 10M$.

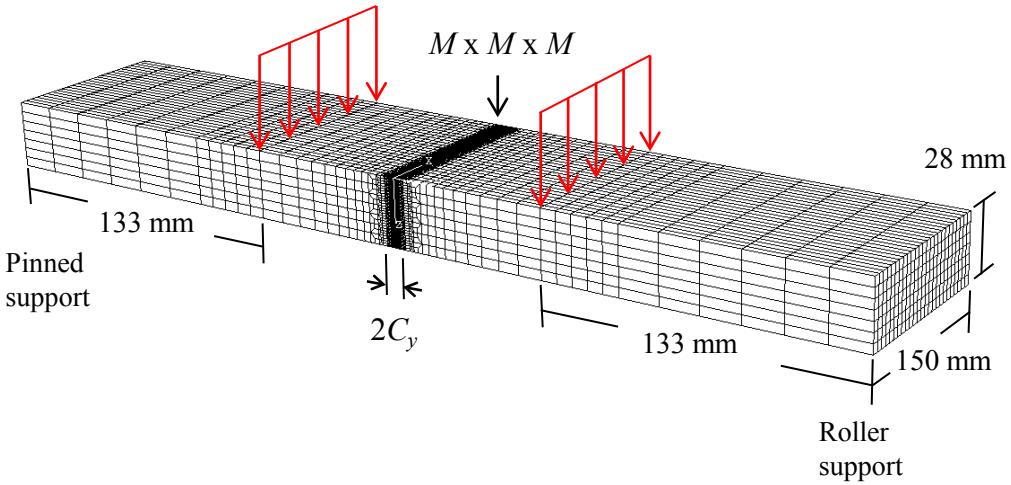

Figure 5.6-3: Semi-elliptical surface crack model

The predicted crack propagations in a direction at the deepest point and c direction at surface obtained from XFEM analysis are compared with tested data (McFadyen et al., 1990) in Figure 5.6-4 and Figure 5.6-5. The filled symbols represent the XFEM prediction and the hollow symbols refer to the experimental data of McFadyen et al. (1990). It can be observed that the XFEM results of specimens number 3, 5, 6, and 8-10 agree reasonably well with reported experimental results. Only those of specimen number 4 deviate significantly from experimental data after 15,000 loading cycles. This is unexpected as specimen 3 and 4 are quite similar and the behavior of the 2 specimens should be similar. This deviation is most likely due to experimental errors. This is clearly demonstrated in the performance of specimens number 6 and 8 which have the same initial crack size and are subjected to about the same stress range. We would expect the experimental results from these 2 specimens to be closed to each other and agree well with XFEM solutions.

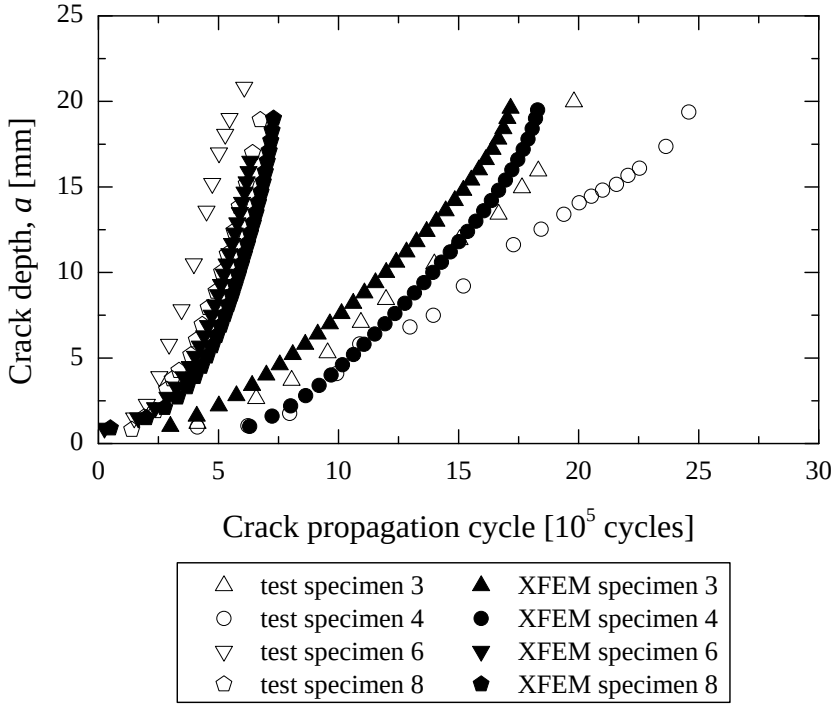

(a) Specimen number 3, 4, 6 , 8

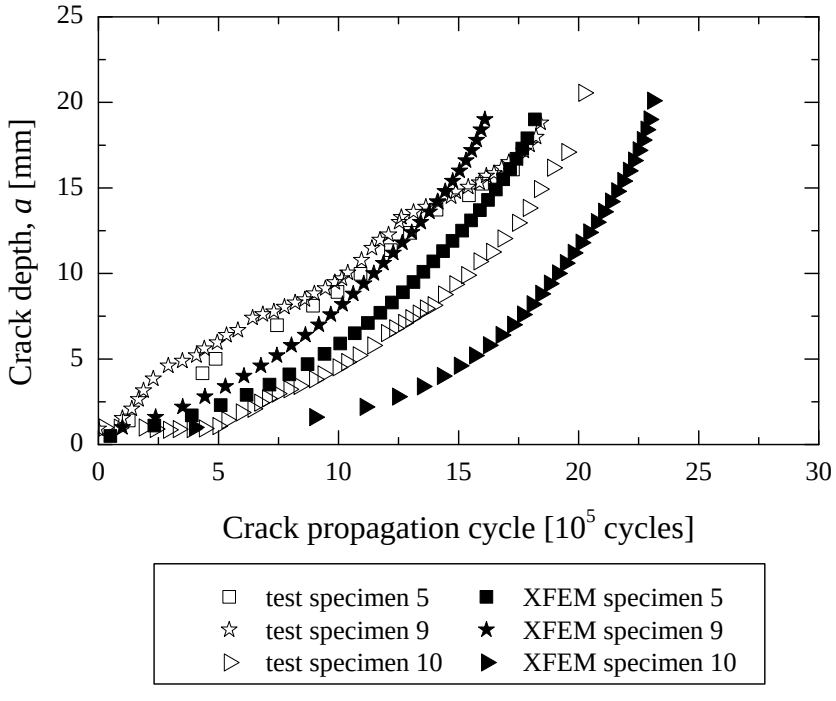

(b) Specimen number 5, 9, 10

Figure 5.6-4: Comparison of fatigue crack growth in *a* direction

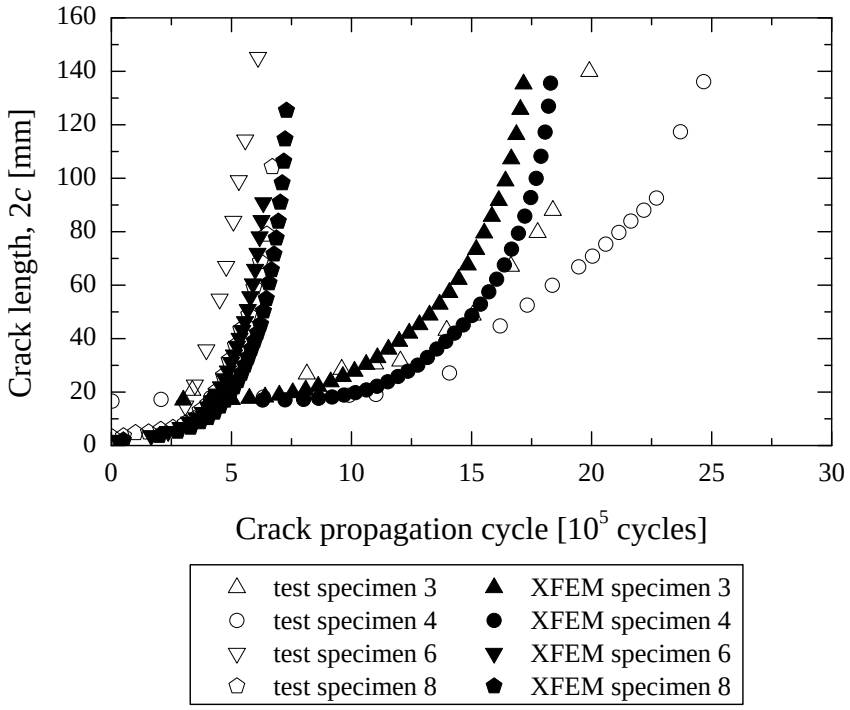

(a) Specimen number 3, 4, 6 , 8

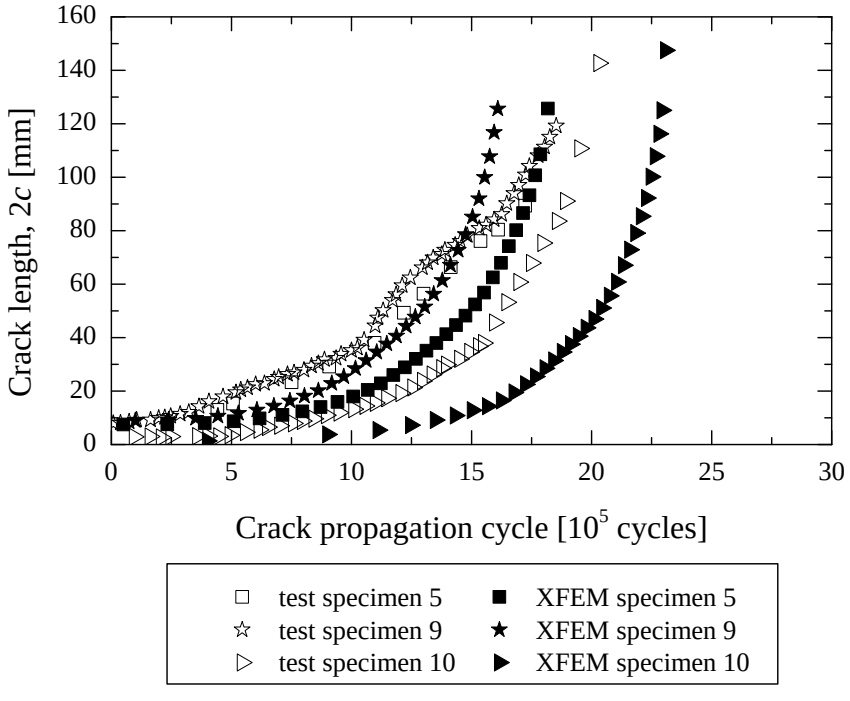

(b) Specimen number 5, 9, 10

Figure 5.6-5: Comparison of fatigue crack growth in *c* direction

5.6.4 Tubular X-joint

5.6.4.1 XFEM model

The tubular X-joint adopted in this section is identical to the X-joint discussed in chapter 3 and chapter 4. The material properties are tabulated in Table 4.1 2 and boundary conditions applied to the FE model are illustrated in Figure 4.1 5. However, the FE model of the X-joint in this study is a full model. The experimental results discussed in chapter 3 demonstrated that the final cracks in the chords of all specimens cover a large area from CL140 to CL220 across the symmetrical plane. To reduce mesh modeling effort the mesh tie is employed in this study. It is an efficient method in the study of local part (supermodel) with steep variation of stress that requires refined mesh for sufficiently accurate results. This technique ties two models with dissimilar mesh size together such that there is no relative motion between the tied surfaces. As a result, all the active degree of freedoms is correctly transferred. The finite element models of the X-joint and supermodels are illustrated in Figure 5.6-6.

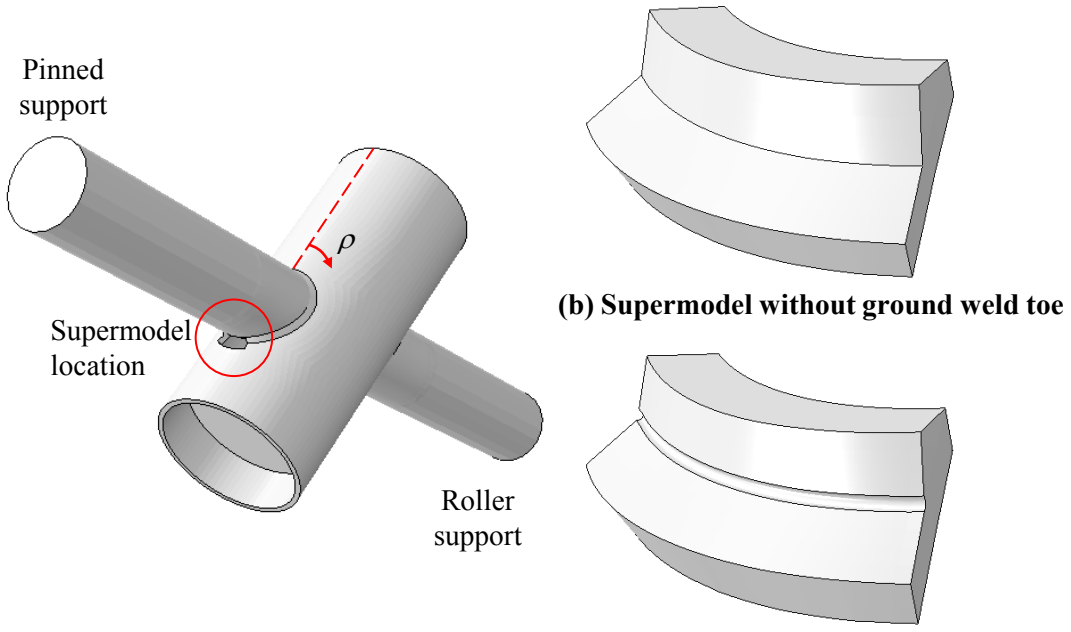

(a) Tubular X-joint model

(b) Supermodel without ground weld toe

(c) Supermodel with ground weld toe

Figure 5.6-6: Finite element models of the X-joint and supermodels

The supermodel in this study is prepared such that it covers the whole area of the actual crack of each specimen. The mesh size along the weld toe is approximately 0.5 mm which is equivalent to about 0.1° of ρ angle. The mesh size, $M \times M$, across the chord wall thickness of J2-1 specimen is of 0.25×0.25 mm, whereas the mesh size for the J2-2 specimen is reduced to 0.10×0.25 mm because space across the ground weld toe curve is limited. The detail of mesh of the supermodels are shown in Figure 5.6-7.

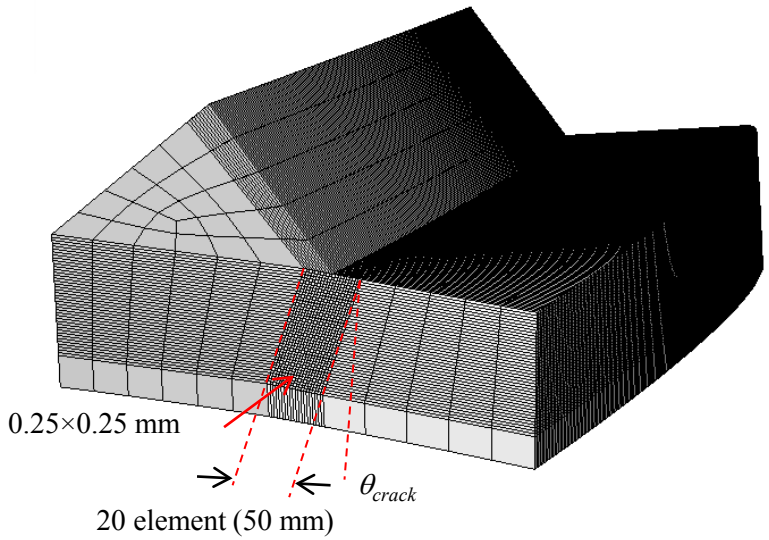

(a) Supermodel without ground weld toe

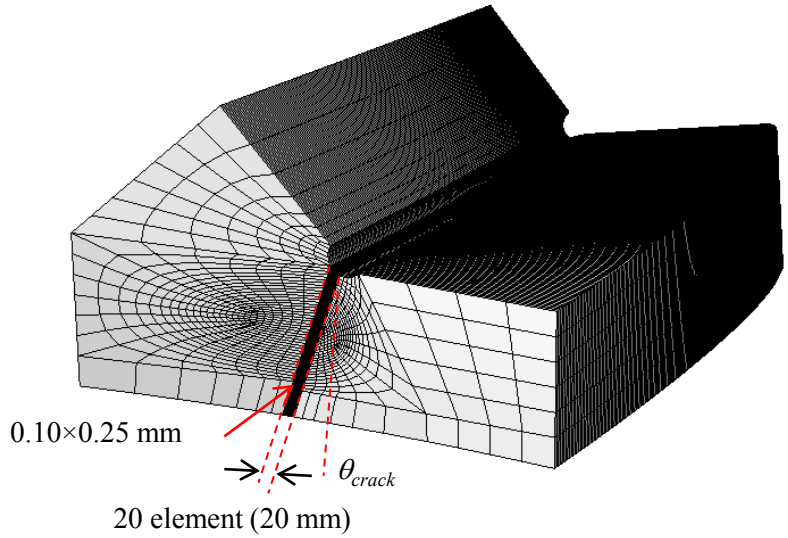

(b) Supermodel with ground weld toe

Figure 5.6-7: Detail of finite element of supermodels

5.6.4.2 Sensitivity of SIF along the crack front to crack angle

Crack angle, θ_{crack}, is the angle between crack surface and member surface (chord surface in this study). The positive crack angle is defined such that crack propagates towards the weld as shown in Figure 5.6-7. It has been observed in the post fatigue test specimen sectioning that the cracks do not propagate in the direction perpendicular to the member surface, but towards the weld (positive θ_{crack}). The crack angle of both the specimen J2-1GF and J2-2XFG is found to be around 20°. Petchdemaneengam (2011) also reported a similar value of θ_{crack}. As result the crack angle considered in this study is varied from 0° to 25°. The crack depth, a, adopted in this study is 3.0 mm and the crack width covers $\rho = 185° - 205°$.

The results in Figure 5.6-8 demonstrate that the model with $\theta_{crack} = 0°$ yields lowest K values and gradually increase with the increasing of θ_{crack} value. The K values reaching the plateau at $\theta_{crack} = 20°$ which is closed the measured value from the experiment. The K values decrease slightly when θ_{crack} is greater than 20°. The subsequent FE analysis adopt θ_{crack} of 20°.

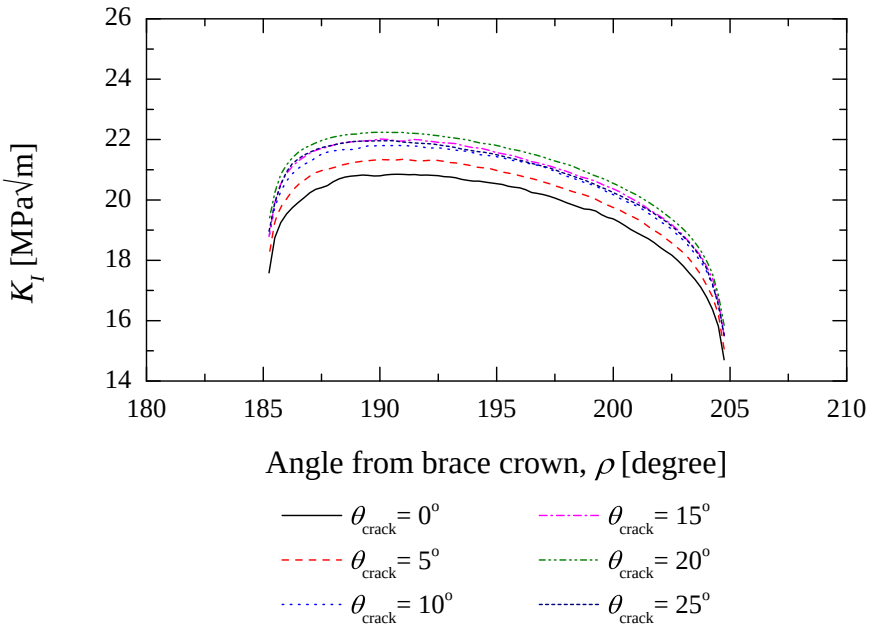

Figure 5.6-8: Sensivity of *K* values along the crack front to crack angle

5.6.4.3 XFEM crack propagation of chord filled grouted tubular joints

The initial crack depth, a, and the crack aspect ratio, a/c, adopted in this section is chosen to be 3.0 mm and 0.45 respectively. In the XFEM analyses, crack depth increment at the deepest point, Δa, is fixed at 0.50 mm per cycle and the crack angle, θ_{crack} of 20° is adopted throughout. The initial crack locations correspond to the deepest crack locations observed in the fatigue test of each specimen. The K values during crack propagation of all specimens are illustrated in Figure 5.6-9. It can be observed that the K values slightly increase with the increase in member loading cycles. The K values of the J2-2XPG and J2-2XPGF specimens are higher than those of the J2-1G and J2-1GF because of difference applied cyclic load range.

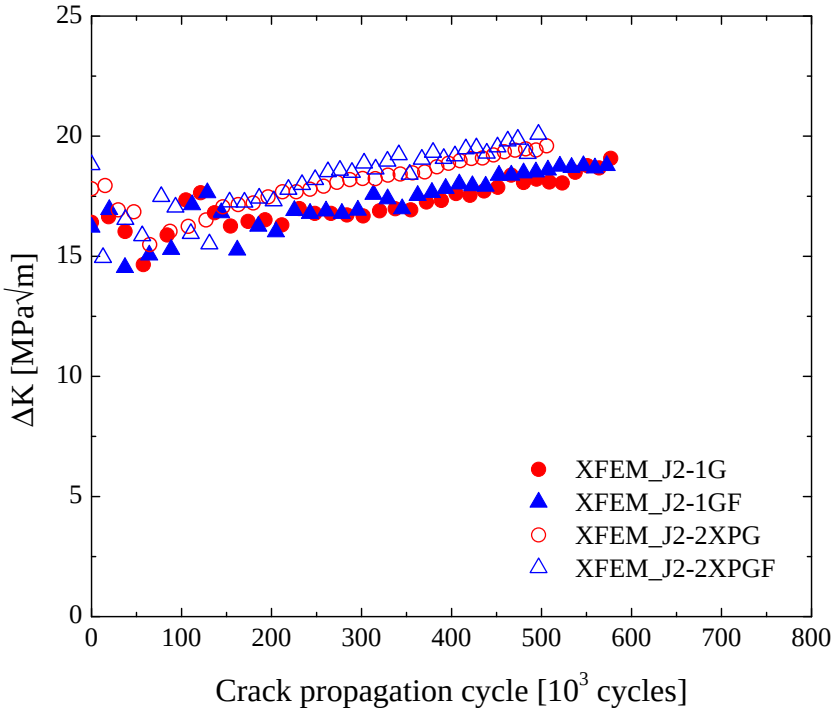

Figure 5.6-9: Development of *K* values at the deepest point during crack propagation

The crack propagation predictions from XFEM of the tubular X-joints with chord-filled concrete are illustrated in Figure 5.6-10. The group of thin lines in the figure represents the life prediction of the J2-1G and J2-1GF specimen whereas those of thick lines are the prediction results for J2-2XPG and J2-2XPGF specimens.

The predicted crack propagation of the J2-1G and J2-1GF (thin broken lines) from XFEM agree well with experimental results up to around $a = 8$ mm. Thereafter the crack propagation rate from XFEM becomes slower than the experimental result. Similarly, the XFEM prediction of the J2-2XPG (thick broken lines) falls below the experimental results. The deviation of the XFEM predictions from experimental results is most likely because the crack in the experiment initiates at multiple location and thereafter coalesce into a single crack. The interaction between multiple cracks and crack coalescing seems to increase the K values. According to Newman and Raju equation, the K values of a crack with low crack aspect ratio provide higher K values at the deepest crack depth location. Therefore, cracks in the experiment tend to propagate faster that the XFEM prediction.

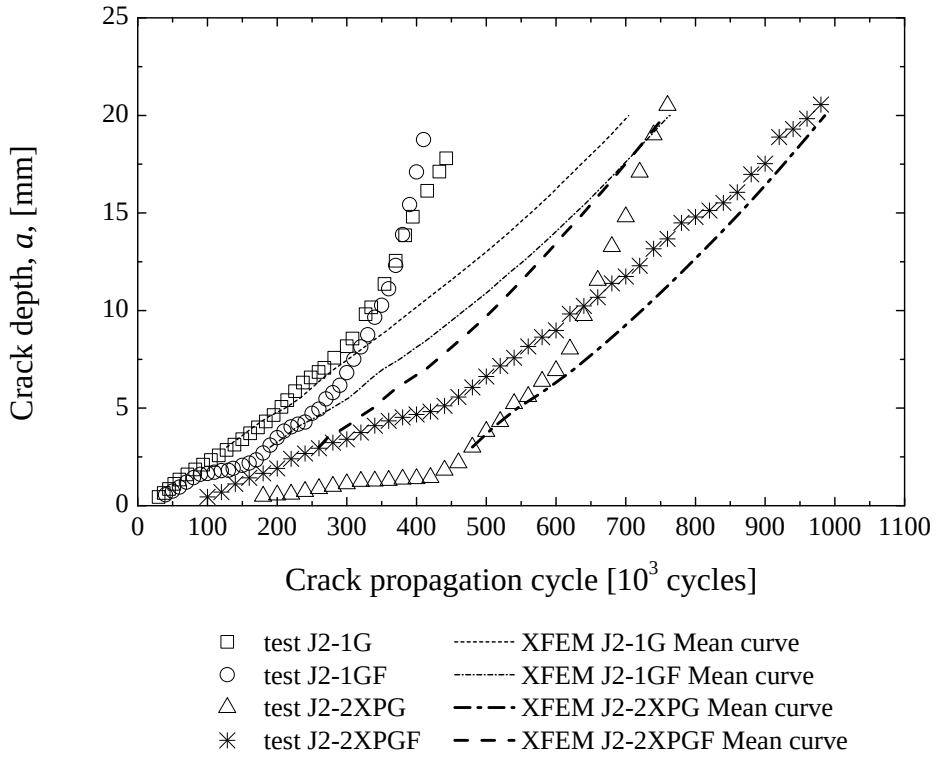

Figure 5.6-10: Fatigue life prediction of the grouted tubulat X-joint using XFEM

5.7 Conclusion

This chapter presents the studies of XFEM mesh design and XFEM based fatigue crack propagation life prediction. From the study, XFEM produces reasonable accurate K values as compared to those of FEM solutions at either shallow crack (with reasonable ER value) or deep crack. The XFEM mesh is simpler to model as compare to FEM mesh. However, the results tend to fluctuate. The fluctuation can be resolved by simple polynomial fitting. The studies of fatigue crack propagation using XFEM in collaboration with appropriate Paris' law show that the method predicts reasonably good fatigue crack propagation life and crack shape development of simple single crack as compares to experimental results. For more complicated fatigue crack propagation which involve multiple cracks, multiple cracks propagation and crack coalescing should be taken into account.

CHAPTER 6

CONCLUSIONS AND PROPOSED FUTURE WORKS

6.1 Conclusions from present research

This thesis focuses on the fatigue behavior of tubular X-joints with chord-filled grouting and XFEM based fatigue life prediction. Two tubular X-joints are tested under constant amplitude in-plane bending until the deepest crack reaches 80% of the member thickness. One of the joints was tested with the as-welded weld toe condition whereas post-weld toe grinding was performed on the other joint. The stress concentration factors (SCF) along the welds toe were determined through finite element analysis and compared with experimental results. Various factors which might contribute to the variation of SCF values were considered. Fatigue lives of the tubular X-joints were predicted using the extended finite element method (XFEM).

The fatigue tests of the two tubular X-joints with chord-filled grouting reveal that the specimens with concrete-filled chord member show longer fatigue life than that of hollow section specimens. The increase in fatigue life is more pronounced in the specimen with post-weld treatment. It can be observed from the experiments that all of the fatigue cracks found initiate near the weld toe of the chord member at multiple locations and coalesce with adjacent cracks. Moreover, the first crack that initiates almost always becomes a major crack of the specimen. Compared with the three types of S-N curves originally developed for hollow section tubular joints fabricated with complete

joint penetration (CJP) welds, the fatigue life of the concrete-filled joints comply with the fatigue life estimation based on these S-N curves. From all conducted fatigue tests, it can be seen that more than 50% of the total fatigue life is consumed by the crack propagation life. This highlights the importance of the accurate estimation of the remaining fatigue life of structures.

The results from finite element analysis reveal that stiffening the chord member by introducing internal diaphragm plates or ultra-high strength concrete grouting significantly reduces SCF values along the weld toes of both brace and chord members. Moreover, the hot-spot locations shifts $\rho \approx 120^\circ - 135^\circ$ and $\rho \approx 225^\circ - 240^\circ$ shift toward the bottom crown point $\rho \approx 160^\circ - 220^\circ$. The SCF values determined from finite element analysis agree well with the measured SCF values along the weld toe on brace members. However, the measured SCF values on the chord member are higher than the FE results. The gap between the infilled concrete and the chord inner surface most likely contributes to this discrepancy. Finite element analysis shows that the 0.10 mm gap significantly affects the computed SCF values and provides better agreement with the experimental results. Other factors such as the strength of the infilled concrete and coefficient of friction between the infilled concrete and the chord inner surface marginally affect SCF values from finite element analysis.

The studies of stationary and propagating semi-elliptical surface cracks based on XFEM show that the XFEM gives as accurate stress intensity factor (SIF) values as the FEM if XFEM mesh conform the crack. The SIF values from simple grid mesh pattern fluctuate at most locations along the crack front. However, the trend is close to the available closed form solution proposed by Newman and Raju (1981). This SIF fluctuation can be simply eliminated by performing polynomial curve fitting. The fatigue crack propagation life predicted by XFEM is reasonably accurate as compare to the experimental results. Moreover, XFEM can also predict accurately the crack shape development.

6.2 Proposed future works

6.2.1 Improved fatigue crack propagation simulation

It has been shown in Section 5.6.4 that the comparison of XFEM results compared well to the experimental results only in the early part of the prediction. Thereafter, the XFEM results deviated from the experimental results. This is due to multiple cracks propagation and crack coalescing, which changes the crack aspect ratio, a/c, as observed in the fatigue testing presented in Chapter 3. The investigation of semi-elliptical crack in plate in section 5.6.3 reveals that crack with lower a/c ratio has higher the SIF value at the deepest point which results the higher crack propagation rate.

To simulate multiple cracks initiation at different stages, the crack initiation criteria must be implemented in the FE model. The continuum damage mechanics based crack initiation criteria is appropriate in this study. The damage of material accumulates cycle-by-cycle until it reaches the critical value. At this point, the crack initiates and starts to propagate. Alternatively, one may manually introduce crack to specific location after certain loading cycles based on experimental data. Each propagating crack will be treated independently and the crack propagation rate is determined based on the SIF value at deepest point of each crack. Once cracks propagate at multiple locations and once jointed, they will coalesce and form single large crack. The crack shape after coalescing becomes more complicated and requires systematic and effective level-set method to calculate the signed-distance functions. The vector level-set method and Hamilton–Jacobi based level-set method are applicable in this case.

In summary, the crack initiation criteria, multiple crack propagation algorithm, and crack coalescing algorithm are required to predict crack propagation more effectively.

6.2.2 Degree of bending in tubular X-joints

Conventional fatigue assessment utilizes S-N approach where S is the stress range that the structure is subjected to and N is the corresponding number of cycle to failure. Large number of fatigue testing of welded connection conducted by Connolly (1986) showed that the one-dimensional hot-spot stress could not be used to characterize all aspects of fatigue failures. Joints with different geometries or loading modes exhibited significantly different fatigue life though those joints subjected to similar hot-spot stress range. This was found to be due to the through thickness stress distribution which can be characterized by the degree of bending (DoB).

$$\text{DoB} = \frac{\sigma_b}{\sigma_b + \sigma_m} \tag{6.2-1}$$

where, σ_b is the through-thickness bending stress, and

σ_m is the through-thickness membrane stress.

It is anticipated that joints with higher through-thickness bending stress will exhibit longer fatigue life than those with similar hot-spot stress but with larger through-thickness membrane stress. This leads to a problem when using S-N approach. The S-N approach may over estimate the fatigue life of the joints with lower DoB than those used to derived the S-N curves.

The conventional approach to predict the remaining fatigue life of cracked structures is to adopt fracture mechanics concepts requiring accurate determination of SIF values which thereafter used to determined crack propagation rate. It is almost impossible to calculate analytically the SIF values for crack in tubular joint. In contrast, one needs to conduct detail finite element analysis to calculate the SIF values. Since the through-thickness stress distribution acting on the crack path can be characterized by DoB, it is possible to come up with an approach to estimate fatigue crack propagation rate based on SCF and DoB values and finally estimate the remaining fatigue life of cracked structures.

The goals are to (1) establish parametric equations determining DoB for tubular joints with different geometries and loading conditions, (2) propose an approach to estimate fatigue crack propagation rate based on SCF and DoB values, and (3) propose set of S-N curves corresponding to different DoB level. The procedures involve (i) conducting comprehensive finite element analysis to establish parametric equations for the determination of crack propagation rate based on SCF and DoB values, (ii) performing a series of fatigue tests to calibrate the obtained finite element results.

REFERENCES

ABAQUS (2012). *ABAQUS Theory Manual, Version 6.12*, Hibbitt, Karlsson and Sorensen Inc, Pawtucket, Rhode Island.

American Bureau of Shipping (ABS), *Fatigue Assessment of Offshore Structures*, 2010

American Petroleum Institute (API). *Recommended Practice for Planning, Designing and Constructing Fixed Offshore Platforms*, API RP 2A-LRFD, API RP 2A-WSD, 2002.

American Petroleum Institute (API). *Recommended Practice for Planning, Designing and Constructing Fixed Offshore Platforms*, API RP 2A-LRFD, API RP 2A-WSD, 2007.

Amerian Welding Society (AWS). *Structural Welding Code – Steel*, AWS D1.1/D1.1M, 2008.

American Welding Society (AWS). *Structural Welding Code – Steel*. AWS D1.1/D1.1 M, 22nd Ed, 2010.

Anderson, T. L. (1957). *Fracture mechanics: fundamentals and applications* (3rd ed.). New York: CRC press

ASTM E 647-13a. *Standard Test Method for Measurement of Fatigue Crack Growth Rates*, ASTM International, Philadelphia.

Barter, S., Molent, L., Goldsmith, N., & Jones, R. (2005). *An experimental evaluation of fatigue crack growth*. Engineering Failure Analysis, *12*(1), pp. 99-128.

Belytschko, T., & Black, T. (1999). Elastic crack growth in finite elements with minimal remeshing. *International Journal for Numerical Methods in Engineering*, *45*(5), pp. 601-620.

Belytschko, T., Moës, N., Usui, S., & Parimi, C. (2001). Arbitrary discontinuities in finite elements. *International Journal for Numerical Methods in Engineering*, *50*(4), pp. 993-1013.

British Standards Institution. (2004). *Eurocode 4:Design of composite steel and concrete structures – Part 1-1: general rules and rules for buildings*.

British Standards Institution. (2005). *BS 7910:2005: Guide to methods for assessing the acceptability of flaws in metallic structures*.

Burdekin, F. M., Yang, G. J., & Cao, J. J. (1988). *Assessment of fracture strength of cracked tubular joints*. Offshore Technology Report OTH 554. Health and Safety Executive.

Campbell, F. C. (2008). *Elements of Metallurgy and Engineering Alloys*: ASM International

Chang, E., & Dover, W. D. (1996). Stress concentration factor parametric equations for tubular X and DT joints. *International Journal of Fatigue*, *18*(6), pp. 363-387.

Chiew, S., Lie, S., Lee, C., & Huang, Z. (2004). Fatigue performance of cracked tubular T joints under combined loads. I: experimental. *Journal of Structural Engineering*, *130*(4), pp. 562-571.

Connolly MPM. (1986). *A fracture mechanics approach to the fatigue assessment of tubular welded Y and K-joints*. PhD thesis, University College London.

Dong, P. (2005). A robust structural stress method for fatigue analysis of offshore/marine structures. *Journal of Offshore Mechanics and Arctic Engineering*, *127*(1), pp. 68-74.

Dong, P., & Hong, J. K. (2012). Fatigue of tubular joints: hot spot stress method revisited. *Journal of Offshore Mechanics and Arctic Engineering*, *134*(3), pp. 471-483.

Det Norske Veritas (DNV). *Fatigue Design of Offshore Steel Structures*, DNV-RP-C203, 2010.

Det Norske Veritas (DNV). *Fatigue Design of Offshore Steel Structures*, DNV-RP-C203, 2011.

Efthymiou, M. (1988). Development of SCF formulae and generalized functions for use in fatigue analysis. *OTJ'99*, *Surrey*, UK.

Efthymiou, M., & Durkin, S. (1985). Stress concentration in T/Y and gap/overlap K-joints. *Elsevier Science Publishers, Amsterdam, The Netherlands*, pp. 429-440.

Ellobody, E., Young, B., & Lam, D. (2006). Behaviour of normal and high strength concrete-filled compact steel tube circular stub columns. *Journal of Constructional Steel Research*, *62*(7), pp. 706-715.

Failure Control Ltd., & Marine Technology Support Unit. (1999). *Background to new fatigue guidance for steel joints and connections in offshore structures*. Health and Safety Executive, Offshore Technology Report, OTH-92-390.

Ghanameh, M. F., Thevenet, D., & Zeghloul, A. (2004). Stress concentration in offshore welded tubular joints subjected to combined loading. *Journal of Materials Science & Technology*, *20*(Supl.), pp. 35-37.

Gifford, L. N., & Hilton, P. D. (1978). Stress intensity factors by enriched finite elements. *Engineering Fracture Mechanics*, *10*(3), pp. 485-496.

Giner, E., Sukumar, N., Denia, F. D., & Fuenmayor, F. J. (2008). Extended finite element method for fretting fatigue crack propagation. *International Journal of Solids and Structures*, *45*(22–23), pp. 5675-5687.

Giner, E., Sukumar, N., Tarancón, J. E., & Fuenmayor, F. J. (2009). An Abaqus implementation of the extended finite element method. *Engineering Fracture Mechanics*, *76*(3), pp. 347-368.

Goh, W. M., & Gao, F. (2004). Parametric equations for stress concentration factors in completely overlapped tubular K(N)-joints. *Journal of Constructional Steel Research*, *60*(12), pp. 1761-1782.

Gravouil, A., Moës, N., & Belytschko, T. (2002). Non-planar 3D crack growth by the extended finite element and level sets—part II: level set update. *International Journal for Numerical Methods in Engineering*, *53*(11), pp. 2569–2586.

Haagensen, P. J., & Maddox, S. J. (2001). Post weld improvement of steel and aluminium structures, *The International Institute of Welding*, XIII-1815-00.

Han, L.-H., He, S.-H., Zheng, L.-Q., & Tao, Z. (2012). Curved concrete filled steel tubular (CCFST) built-up members under axial compression: Experiments. *Journal of Constructional Steel Research*, *74*, pp. 63-75.

Harwood, R., & Shuttleworth, E. (1998). *Grouted and mechanical strengthening and repair of tubular steel offshore structures*. Department of Energy, Offshore Technology. Report, OTH-88-283.

Hobbacher, A. (2002), *Recommendations for Fatigue Design of Welded Joints and Components*. International Institute of Welding.

Hobbacher, A. (2007), *Recommendations for Fatigue Design of Welded Joints and Components*. International Institute of Welding.

Hosseini, A., & Mahmoud, M. A. (1985). Evaluation of stress intensity factor and fatigue growth of surface cracks in tension plates. *Engineering Fracture Mechanics*, *22*(6), pp. 957-974.

Im, S. W., Chang, I. H., Park, K. K., Jo, C. H., & Kim, K. Y. (2005). A Study On the Fatigue Crack In Large-Scale Tubular Joints For Offshore Structures. *Proceedings from the 15th International Offshore and Polar Engineering Conference*, Seoul, Korea, 19-24 June 2005, The International Society of Offshore and Polar Engineers.

Irwin, G. R. (1961). Plastic zone near a crack and fracture toughness, *Proceedings from 7th Sagamore Research Conference*, 4, IV63–1V78.

Jarmai, K., & Farkas, J. (1999). *Mechanics and Design of Tubular Structures*: Springer.

Kim, G., & Koo, K. (2013) Effects of hydration heat velocity on autogenous shrinkage of high strength concrete. *Magazine of Concrete Research*, *65*(23), pp.1385-1395.

Laird, C. (1979). *Mechanisms and theories of fatigue, in fatigue and microstructure*. 1978 ASM Material Science Seminar, St. Louis, ASTM, pp. 149-203

Liu, Y.-P., Chen, C.-Y., Li, G.-Q., & Li, J.-B. (2010). Fatigue life prediction of semi-elliptical surface crack in 14MnNbq bridge steel. *Engineering Failure Analysis*, *17*(6), pp. 1413-1423.

Lloyd's Register of Engineers. *Stress Concentration Factors for Simple Tubular Joints*. Volumes 1 to 5, Lloyd's Register of Shipping-Offshore Division, 1997.

Lohaus, L., Schaumann, P., Lochte-Holtgreven, S., Bechtel, A., Griese, R., & Lindschulte, N. (2013). Approvals for grouted joints in offshore substructures. *Bautechnik*, *90*(7), pp. 402-409.

Lugg, M. C. (2002). *An introduction to ACPD*, Retrieved from www.tscndt.com.

Mao, X., & Xiao, Y. (2006). Seismic behavior of confined square CFT columns. *Engineering Structures*, *28*(10), pp. 1378-1386.

Marshall, P., Qian, X., Nguyen, C. T., & Petchdemaneengam, Y. (2013). Welder-optimized CJP-equivalency welds for tubular connections. *Welding in the World*, *57*(4), pp. 569-579.

Mashiri, F. R., & Zhao, X.-L. (2010). Square hollow section (SHS) T-joints with concrete-filled chords subjected to in-plane fatigue loading in the brace. *Thin-Walled Structures*, *48*(2), pp. 150-158.

Mashiri, F. R., Zhao, X.-L., Hirt, M. A., & Nussbaumer, A. (2007). Size effect of welded thin-walled tubular joints. *International Journal of Structural Stability and Dynamics*, *7*(1), pp. 101-127.

McFadyen, N. B., Bell, R., & Vosikovsky, O. (1990). Fatigue crack growth of semi-elliptical surface cracks. *International Journal of Fatigue*, *12*(1), pp. 43-50.

Moës, N., Dolbow, J., & Belytschko, T. (1999). A Finite Element Method for Crack Growth without Remeshing. *International Journal for Numerical Methods in Engineering*, *46*(1), pp. 131–150.

Moës, N., Gravouil, A., & Belytschko, T. (2002). Non-planar 3D Crack Growth by the Extended Fnite Element and Level Sets—Part I: Mechanical Model. *International Journal for Numerical Methods in Engineering*, *53*(11), pp. 2549–2568.

Newman, J., & Choo, B. S. (2003). *Advanced Concrete Technology*: Oxford: Butterworth-Heinemann

Newman, J. C., & Raju, I. S. (1981). An empirical stress-intensity factor equation for the surface crack. *Engineering Fracture Mechanics*, *15*(1), pp. 185-192.

Nüsse, G. (2010). *REFRESH - extension of the fatigue life of existing and new welded steel structure*. Düsseldorf: Verlag und Vertriebsgesellschaft mbH.

Osher, S., & Sethian, J. A. (1988). Fronts propagating with curvature-dependent speed: algotirhms based on Hamilton-Jacobi formulations. *Journal of Conputational Physics*, *79*(1), pp. 12-49

Pang, N. L., Zhao, X. L., Mashiri, F. R., & Dayawansa, P. (2009). Full-size testing to determine stress concentration factors of dragline tubular joints. *Engineering Structures*, *31*(1), pp. 43-56.

Paris, P. C., Gomez, M. P., & Anderson, W. E. (1961). A rational analytic theory of fatigue, *The Trend in Engineering*, *13*(1), pp. 9-14.

Patel, V. I., Liang, Q. Q., & Hadi, M. N. S. (2014). Numerical analysis of high-strength concrete-filled steel tubular slender beam-columns under cyclic loading. *Journal of Constructional Steel Research*, *92*, pp. 183-194.

Petchdemaneengam, Y. (2011). *Plasticity-Induced Fatigue Crack Closure for Structural Steels in Offshore Applications*. PhD thesis, National University of Singapore, Singapore

Qian, X. (2009). Stress-intensity factors for circular hollow section V-joints with a rack-plate chord. *Fatigue & Fracture of Engineering Materials & Structures*, *32*(1), pp. 61-79.

Qian, X., Dodds, J. R. H., & Choo, Y. S. (2005). Mode Mixity for Circular Hollow Section X Joints With Weld Toe Cracks. *Journal of Offshore Mechanics and Arctic Engineering*, *127*(3), pp. 269-279.

Qian, X., Marshall, P. W., Cheong, W. K. D., Petchdemaneengam, Y. & Chen, Z. (2009). Partial joint penetration welds for tubular joints: fabrication and SCFs. *Proceedings of the 62nd Annual Assembly and International Conference of International Institute of Welding*, Singapore, 12-19 July.

Qian, X., Nguyen, C. T., Petchdemaneengam, Y., Ou, Z., Swaddiwudhipong, S., & Marshall, P. (2013a). Fatigue performance of tubular X-joints with PJP+ welds: II — Numerical investigation. *Journal of Constructional Steel Research*, *89*, pp. 252-261.

Qian X., Petchdemaneengam Y., Swaddiwudhipong, S., Marshall P. W., Ou Z., & Nguyen C. T. (2013b). Fatigue performance of tubular X-joints with PJP+ welds: I – experimental study. *Journal of Constructional Steel Research*, *90*, pp. 49-59.

Qian X., Swaddiwudhipong, S., Nguyen C. T., Petchdemaneengam Y., Marshall P. W., & Ou Z. (2013c). Overload effect on the fatigue crack propagation in large-scale tubular joints. *Fatigue and Fracture of Engineering Materials and Structures*, *36*(5), pp. 427-438

Raju, I. S., & Newman Jr, J. C. (1979). Stress-intensity factors for a wide range of semi-elliptical surface cracks in finite-thickness plates. *Engineering Fracture Mechanics*, *11*(4), pp.817-829.

Rice, J. R. (1968). A path independent integral and the approximate analysis of strain concentration by notches and cracks. *Journal of Applied Mechanics*, *35*(2), pp. 379-386.

Sakai, Y., Hosaka, T., Isoe, A., Ichikawa, A., & Mitsuki, K. (2004). Experiments on concrete filled and reinforced tubular K-joints of truss girder. *Journal of Constructional Steel Research*, *60*(3–5), pp. 683-699.

Schumacher, A., Borges, L. C., & Nussbaumer, A. (2009). A critical examination of the size effect correction for welded steel tubular joints. *International Journal of Fatigue*, *31*(8–9), pp. 1422-1433.

Schumacher, A., & Nussbaumer, A. (2006). Experimental study on the fatigue behaviour of welded tubular K-joints for bridges. *Engineering Structures*, *28*(5), pp. 745-755.

Shao, Y. B., & Cao, Z. B. (2005). Experimental and numerical analysis of fatigue behavior for tubular K-joints. *Structural Engineering& Mechanics*, *19*(6), pp. 639-652.

Shi, J., Chopp, D., Lua, J., Sukumar, N., & Belytschko, T. (2010). Abaqus implementation of extended finite element method using a level set representation for three-dimensional fatigue crack growth and life predictions. *Engineering Fracture Mechanics*, *77*(14), pp. 2840-2863.

Shi, K., Cai, L., Chen, L., & Bao, C. (2014). A theoretical model of semi-elliptic surface crack growth. *Chinese Journal of Aeronautics*, *27*(3), pp. 730-734.

Song, P. S., Sheu, B. C., & Shieh, Y. L. (2002). Prediction of semi-elliptical surface crack growth in 2024-T4 aluminium alloy. *International Journal of Pressure Vessels and Piping*, *79*(4), pp. 273-278.

Stacey, A., Sharp, J. V., & Nicholas, R. W. (1996). Static strength assessment of cracked tubular joints. *Paper presented at the Proceedings of the 15th International Conference on Offshore Mechanics and Arctic Engineering*.

Sukumar, N., Chopp, D. L., & Moran, B. (2003). Extended finite element method and fast marching method for three-dimensional fatigue crack propagation. *Engineering Fracture Mechanics*, *70*(1), pp. 29-48.

Sukumarz, N., Moesx, N., Moran, B., & Belytschko, T. (2000). Extended Finite Element Method for Three-Dimensional Crack Modelling. *International Journal for Numerical Methods in Engineering*, *48*(11), pp. 1549-1570.

Talie-Faz, B., Dover, W. D., & Brennan, F. P. (2002). *Static strengh of cracked high strength steel tubular joints*. Offshore Technology Report 2000/078, Health and Safety Executive.

UKOSRP-II Programme Steering Committee. (1987). *United Kingdom Offshore Research Project – Phase II (UKOSRP II) Final Summary Report*, HMSO, OTH-87-265.

Valipour, H., & Foster, S. (2010). Nonlinear static and cyclic analysis of concrete-filled steel columns. *Journal of Constructional Steel Research*, *66*(6), pp. 793-802.

Varfolomeyev, I. V., Vainshtok, V. A., & Krasowsky, A. YA.(1991) Prediction of part-through crack growth under cyclic loading. *Engineering Fracture Mechanics*, *40*(6), pp. 1007-1022

van Wingerde, A. M., van Delft, D. R. V., Wardenier, J., & Packer, J. A. (1997). Scale Effects on the Fatigue Behaviour of Tubular Structures. *IIW International Conference on Performance of Dynamically Loaded Welded Structures*, July, San Francisco, USA, pp. 123–135.

van Wingerde, A. M., Wardenier, J., & Packer, J. A. (1998). Commentary on the Draft Specification for Fatigue Design of Hollow Section Joints. *The Eighth International Symposium on Tubular Structures*, Singapore, August, pp. 117–127.

Ventura, G., Budyn, E., & Belytschko, T. (2003). Vector level sets for description of propagating cracks in finite elements. *International Journal for Numerical Methods in Engineering*, *58*(10), pp. 1571–1592.

Ventura, G., Xu, J. X., & Belytschko, T. (2002). A vector level set method and new discontinuity approximations for crack growth by EFG. *International Journal for Numerical Methods in Engineering*, *54*(6), pp. 923–944.

Wang, K., Tong, L., Zhu, J., Zhao, X., & Mashiri, F. (2013). Fatigue behavior of welded T-joints with a CHS brace and CFCHS chord under axial loading in the brace. *Journal of Bridge Engineering*, *18*(2), pp. 142-152.

Wells, A. A. (1961). Unstable crack propagation in metals: cleavage and fracture. *Proceedings of the Crack Propagation Symposium*, College of Aeronautics, Cranfield, 1, pp. 210-230.

Yamashita, Y., Shinozaki, M., Ueda, Y., & Sakano, K. (2004). Fatigue Crack Growth Life Prediction for Surface Crack Located in Stress Concentration Part Based on the Three-Dimensional Finite Element Method. *Journal of Engineering for Gas Turbines and Power*, *126*(1), pp. 160-166.

Zhao, X. L., Herion, S., Packer, J. A., Puthli, R. S., Sedlacek, G., Wardenier, J., Weynand, K., S., Wingerde, A. M. van., & Yeomans, N. (2001). *Design guide for circular and rectangular hollow section welded joints under fatigue loading*. CIDECT Series "Construction with Hollow Steel Sections", Serial No. 8, TUV-Verlag, Köln, Germany.

LIST OF PUBLICATIONS

Journal paper

Qian, X., Jitpairod, K., Marshall, P., Swaddiwudhipong, S., Ou, Z., Zhang, Y., & Pradana, M. R. (2014). Fatigue and residual strength of concrete-filled tubular X-joints with full capacity welds. *Journal of Constructional Steel Research*, *10*0, pp. 21-35.

Conference papers

Qian, X., Marshall, P. W. & Jitpairod, K. (2013). Welder-optimized CJP welds for tubular joints: effect of grout on the fatigue performance. *7th Asia-Pacific IIW International Congress*, Singapore.

Jitpairod, K., Qian, X., Swaddiwudhipong, S., & Marshall, P. (2013) Effects of weld toe grinding on fatigue performance of the grouted tubular X-joints. *The Twenty-Suxth KKTHCNN Symposium on Civil Engineering*, Singapore.

APPENDIX A

STRESS AND DISPLACEMENT NEAR THE CRACK

The following equations refer to the notations in Figure 2.1 2,

Mode I: Opening load

$$\begin{bmatrix} \sigma_{xx} \\ \sigma_{yy} \\ \tau_{xy} \end{bmatrix} = \frac{K_I}{\sqrt{2\pi r}} \cos\frac{\theta}{2} \begin{bmatrix} 1-\sin\frac{\theta}{2}\sin\frac{3\theta}{2} \\ 1+\sin\frac{\theta}{2}\sin\frac{3\theta}{2} \\ \sin\frac{\theta}{2}\cos\frac{3\theta}{2} \end{bmatrix} \tag{A-1}$$

$$\begin{bmatrix} u \\ v \end{bmatrix} = \frac{K_I}{2G}\sqrt{\frac{r}{2\pi}} \begin{bmatrix} \cos\frac{\theta}{2}\left(\kappa-1+2\sin^2\frac{\theta}{2}\right) \\ \sin\frac{\theta}{2}\left(\kappa+1-2\cos^2\frac{\theta}{2}\right) \end{bmatrix} \tag{A-2}$$

Mode II: In-plane shear

$$\begin{bmatrix} \sigma_{xx} \\ \sigma_{yy} \\ \tau_{xy} \end{bmatrix} = \frac{K_{II}}{\sqrt{2\pi r}} \begin{bmatrix} -\sin\frac{\theta}{2}\left(2+\cos\frac{\theta}{2}\cos\frac{3\theta}{2}\right) \\ \sin\frac{\theta}{2}\cos\frac{\theta}{2}\cos\frac{3\theta}{2} \\ \cos\frac{\theta}{2}\left(1-\sin\frac{\theta}{2}\sin\frac{3\theta}{2}\right) \end{bmatrix} \tag{A-3}$$

$$\begin{bmatrix} u \\ v \end{bmatrix} = \frac{K_{II}}{2G}\sqrt{\frac{r}{2\pi}} \begin{bmatrix} \sin\frac{\theta}{2}\left(\kappa+1+2\cos^2\frac{\theta}{2}\right) \\ -\cos\frac{\theta}{2}\left(\kappa-1-2\sin^2\frac{\theta}{2}\right) \end{bmatrix} \tag{A-4}$$

Mode III: Out-of-plane shear

$$\begin{bmatrix} \sigma_{zx} \\ \sigma_{zy} \end{bmatrix} = \frac{K_{III}}{\sqrt{2\pi r}} \begin{bmatrix} -\sin\frac{\theta}{2} \\ \cos\frac{\theta}{2} \end{bmatrix} \tag{A-5}$$

$$w = \frac{2K_{III}}{G}\sqrt{\frac{r}{2\pi}}\sin\frac{\theta}{2} \tag{A-6}$$

where, $G = \frac{E}{2(1+\nu)}$ is the shear modulus, and

$\kappa = \frac{3-\nu}{1+\nu}$ for the plane-stress condition,

$\kappa = 3-4\nu$ for the plane-strain condition.

APPENDIX B

DERIVATION OF VECTORS NORMAL TO WELD LINE

B.1 Derivation of vector tangent to the chord-to-brace intersection curve on the left hand side

The cylindrical surface of the left-side brace in Cartesian coordinate system can be ex press as:

$$y^2 + z^2 = r_1^2 \tag{B-1}$$

In the cylindrical coordinate system, the left-brace can be written as:

$$y = r_1 \cos\theta_1 \tag{B-2}$$

$$z = r_1 \sin\theta_1 \tag{B-3}$$

where, $r_1 = \tan^{-1}(z/y)$.

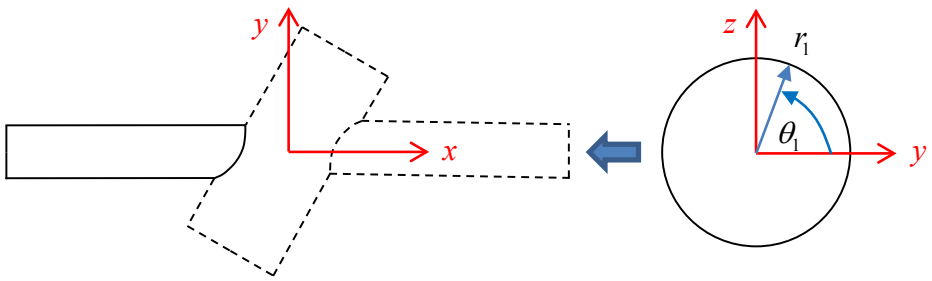

Figure B-1: Local coordinate of left-side brace

The cylindrical surface of lest-side chord in Cartesian coordinate system can be express as:

$$y'^2 + z'^2 = r_2^2 \tag{B-4}$$

In the cylindrical coordinate system, the left-brace can be written as:

$$y' = r_2 \cos\theta_2 \tag{B-5}$$
$$z' = r_2 \sin\theta_2 \tag{B-6}$$

where, $r_2 = \tan^{-1}(z'/y')$.

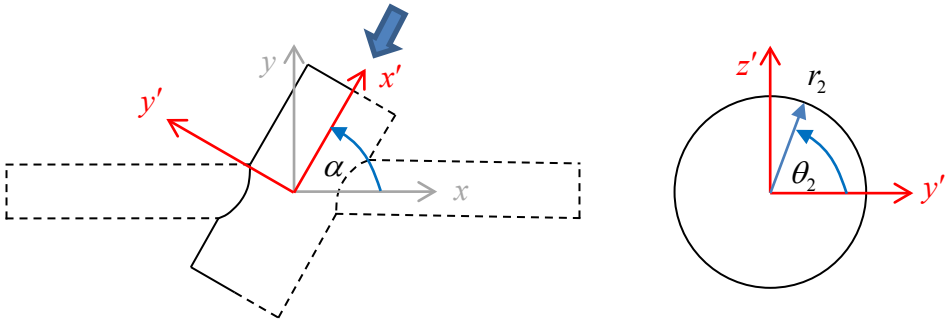

Figure B-2: Local coordinate of left-side chord

Introducing the coordinate transformation matrix:

$$\begin{Bmatrix} x' \\ y' \\ z' \end{Bmatrix} = \begin{bmatrix} \cos\alpha & \sin\alpha & 0 \\ -\sin\alpha & \cos\alpha & 0 \\ 0 & 0 & 1 \end{bmatrix} \begin{Bmatrix} x \\ y \\ z \end{Bmatrix} \tag{B-7}$$

yield,

$$x' = x\cos\alpha + y\sin\alpha \tag{B-8}$$
$$y' = y\cos\alpha - x\sin\alpha \tag{B-9}$$
$$z' = z \tag{B-10}$$

Substituting Equation B-6 and Equation B-9 into Equation Equation B-4 in order to find the intersection curve yield:

$$x = \frac{r_1\cos\theta_1}{\tan\alpha} \pm \frac{r_2\cos\theta_2}{\sin\alpha} \tag{B-11}$$

From Equation Equation B-10, the relationship between θ_1 and θ_2 can be expressed as:

$$\theta_2 = \sin^{-1}\left(\frac{r_1}{r_2}\sin\theta_1\right) \tag{B-12}$$

Equation B-2), Equation B-3, and Equation B-11 give the coordinate of points along the chord-to-brace intersection curve as a function of the free parameter θ_1. The general form of the parametric equation is given in Equation B-13. Therefore, the parametric equation representing the chord-to-brace intersection curve on the left-hand-side of the joint can be written as Equation B-14. The superscript L in Equation B-14 denotes left-hand-side of the joint.

$$\vec{R}(t) = f(t)\,\vec{i} + g(t)\,\vec{j} + h(t)\,\vec{k} \tag{B-13}$$

$$\begin{aligned} \vec{R}^{L}(\theta_1) &= x(\theta_1)\,\vec{i} + y(\theta_1)\,\vec{j} + z(\theta_1)\,\vec{k} \\ \vec{R}^{L}(\theta_1) &= \left(\frac{r_1\cos\theta_1}{\tan\alpha} \pm \frac{r_2\cos\theta_2}{\sin\alpha}\right)\vec{i} + r_1\cos\theta_1\,\vec{j} + r_1\sin\theta_1\,\vec{k} \end{aligned} \tag{B-14}$$

where, $\vec{i}$, $\vec{j}$, and $\vec{k}$ are the unit vector in x, y, and z direction respectively.

The vector tangent to curve, $\vec{T}(t)$, is defined as:

$$\vec{T}(t) = \vec{R}_{,t}(t) = f_{,t}(t)\,\vec{i} + g_{,t}(t)\,\vec{j} + h_{,t}(t)\,\vec{k} \tag{B-15}$$

where, $\partial\vec{R}_{,t}(t) = \frac{\partial\vec{R}(t)}{\partial t}$

From Equation B-14 we can get the vector tangent to the chord-to-brace intersection curve, $\vec{\mathbf{n}}_{22}^{L}$,as:

$$\begin{aligned} \vec{\mathbf{n}}_{22}^{L} = \vec{T}^{L}(\theta_1) = &\left(\frac{-r_1\sin\theta_1}{\tan\alpha} + \frac{r_2\sin\theta_2}{\sin\alpha}\frac{d\theta_2}{d\theta_1}\right)\vec{i} \\ &+ (-r_1\sin\theta_1)\,\vec{j} + (r_1\cos\theta_1)\,\vec{k} \end{aligned} \tag{B-16}$$

B.2 Derivation of vector tangent to the chord-to-brace intersection curve on the right hand side

For the chord-to-brace intersection curve on the right-hand-side, the local coordinate of brace is not only subjected rotation but also translation. The origin point of brace local coordinate using here is at the right support: $x_0 = 2012$ mm and $y_0 = 0$ mm.

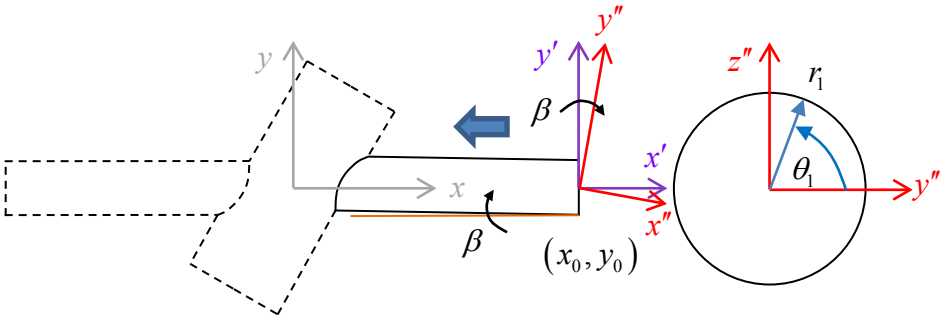

Figure B-3: Local coordinate of right-side brace

The cylindrical surface of the right-side brace in Cartesian coordinate system can be ex press as:

$$y''^2 + z''^2 = r_1^2 \tag{B-17}$$

In the cylindrical coordinate system, the left-brace can be written as:

$$y'' = r_1 \cos\theta_1 \tag{B-18}$$

$$z'' = r_1 \sin\theta_1 \tag{B-19}$$

where, $r_1 = \tan^{-1}(z''/y'')$

Introducing the coordinate transformation matrix:

$$\begin{Bmatrix} x'' \\ y'' \\ z'' \end{Bmatrix} = \begin{bmatrix} \cos\beta & \sin\beta & 0 \\ -\sin\beta & \cos\beta & 0 \\ 0 & 0 & 1 \end{bmatrix} \begin{Bmatrix} x' \\ y' \\ z' \end{Bmatrix} = \begin{bmatrix} \cos\beta & \sin\beta & 0 \\ -\sin\beta & \cos\beta & 0 \\ 0 & 0 & 1 \end{bmatrix} \begin{Bmatrix} x - x_0 \\ y \\ z \end{Bmatrix} \tag{B-20}$$

yield,

$$x'' = (x - x_0)\cos\beta + y\sin\beta \tag{B-21}$$

$$y'' = y\cos\beta - (x - x_0)\sin\beta \tag{B-22}$$

$$z'' = z \tag{B-23}$$

The cylindrical surface of the right-side chord in Cartesian coordinate system can be ex press as:

$$y''^2 + z'''^2 = r_2^2 \tag{B-24}$$

In the cylindrical coordinate system, the left-brace can be written as:

$$y''' = r_2\cos\theta_2 \tag{B-25}$$

$$z''' = r_2\sin\theta_2 \tag{B-26}$$

where, $r_2 = \tan^{-1}(z'''/y''')$

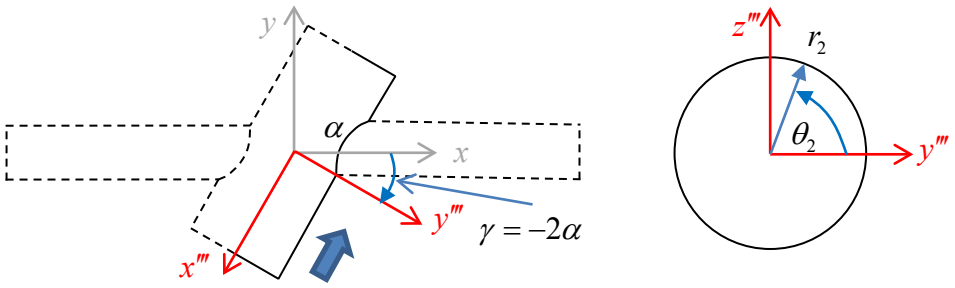

Figure B-4: Local coordinate of right-side chord

Introducing the coordinate transformation matrix:

$$\begin{Bmatrix} x''' \\ y''' \\ z''' \end{Bmatrix} = \begin{bmatrix} \cos\gamma & \sin\gamma & 0 \\ -\sin\gamma & \cos\gamma & 0 \\ 0 & 0 & 1 \end{bmatrix} \begin{Bmatrix} x \\ y \\ z \end{Bmatrix} \tag{B-27}$$

yield,

$$x''' = x\cos\gamma + y\sin\gamma \tag{B-28}$$

$$y''' = y\cos\gamma - x\sin\gamma \tag{B-29}$$

$$z''' = z \tag{B-30}$$

$$\gamma = -2\alpha$$

Equating Equation B-18 and Equation B-28 yield:

$$y = \frac{r_1 \cos\theta_1}{\cos\beta} + (x - x_0)\tan\beta \tag{B-31}$$

Substituting Equation B-31 into Equation Equation B-29 yield:

$$y''' = \frac{r_1 \cos\theta_1}{\cos\beta} + (x - x_0)\tan\beta\cos\gamma - x\sin\gamma \tag{B-32}$$

Substituting Equation B-26 and Equation B-32 into Equation B-24 in order to find the intersection curve yield:

$$x = \frac{1}{\tan\beta - \tan\gamma}\left(\pm\frac{r_2\cos\theta_2}{\cos\gamma} - \frac{r_1\cos\theta_1}{\cos\beta} + x_0\tan\beta\right) \tag{B-33}$$

Therefore, the parametric equation representing the chord-to-brace intersection curve on the left-hand-side of the joint can be written as:

$$\begin{aligned}\vec{R}^{R}(\theta_1) = &\frac{1}{\tan\beta - \tan\gamma}\left(\frac{r_2\cos\theta_2}{\cos\gamma} - \frac{r_1\cos\theta_1}{\cos\beta} + x_0\tan\beta\right)\vec{i} \\ &+ \left(\frac{r_1\cos\theta_1}{\cos\beta} + \frac{\tan\beta}{\tan\beta - \tan\gamma}\left(\frac{r_2\cos\theta_2}{\cos\gamma} - \frac{r_1\cos\theta_1}{\cos\beta} + x_0\tan\beta\right) - x_0\tan\beta\right)\vec{j} \\ &+ r_1\sin\theta_1\vec{k}\end{aligned} \tag{B-34}$$

The vector tangent to the chord-to-brace intersection curve, $\vec{\mathbf{n}}_{22}^{R}$,can be derived using Equation B-15.

$$\vec{\mathbf{n}}_{22}^{R} = \vec{T}^{R}(\theta_1) = \vec{R}^{R}{}_{,\theta_1}(\theta_1) \tag{B-35}$$

B.3 Derivation of vector normal to the chord and brace surface

Similar to the parametric equation of a curve, $\vec{R}(t)$, the parametric equation of a surface, $\vec{S}(t)$, can be derived from Equation B-13. The vector normal to surface is defined as:

$$\vec{N}(t) = \vec{T}_{,t}(t) = \vec{S}_{,tt}(t) \tag{B-36}$$

From Equation B-2 and Equation B-3, the parametric equation of the left-brace surface can be expressed as:

$$\vec{S}^{BL}(x,\theta_2) = x\vec{i} + r_1\cos\theta_1\vec{j} + r_1\sin\theta_1\vec{k} \tag{B-37}$$

The vector normal left-side brace surface, $\vec{\mathbf{n}}_{33}^{BL}$, is:

$$\vec{\mathbf{n}}_{33}^{BL} = \vec{N}^{BL}(\theta_1) = -r_1\cos\theta_1\vec{j} - r_1\sin\theta_1\vec{k} \tag{B-38}$$

Similarly to brace surface, chord surface can be derived in its local coordinate (x',y',z') as:

$$\vec{S}^{CL}(x,\theta_2) = x'\vec{i}' + r_2\cos\theta_2\vec{j}' + r_2\sin\theta_2\vec{k}' \tag{B-39}$$

Mapping the local and global coordinate, the transformation matrix, Equation B-7, is introduced.

$$\begin{aligned}\vec{S}^{CL}(x',\theta_2) &= x'\left(\cos\alpha\vec{i} + \sin\alpha\vec{j}\right) + r_2\cos\theta_2\left(\cos\alpha\vec{j} - \sin\alpha\vec{i}\right) + r_2\sin\theta_2\vec{k} \\ &= \left(x'\cos\alpha - r_2\sin\alpha\cos\theta_2\right)\vec{i} + \left(x'\sin\alpha + r_2\cos\alpha\cos\theta_2\right)\vec{j} + r_2\sin\theta_2\vec{k}\end{aligned} \tag{B-40}$$

The vector normal left-side chord surface, $\vec{\mathbf{n}}_{33}^{CL}$ is:

$$\vec{\mathbf{n}}_{33}^{CL} = \vec{N}^{CL}(\theta_2) = r_2 \sin\alpha \cos\theta_2 \vec{i} + r_2 \cos\alpha \cos\theta_2 \vec{j} - r_2 \sin\theta_2 \vec{k} \tag{B-41}$$

Because θ_2 is not varied from 0 to π, for simplicity, $\vec{N}^{CL}$ should be written as a function of θ_1 using the relationship from Equation B-12 yield:

$$\begin{aligned} \vec{\mathbf{n}}_{33}^{CL} = \vec{N}^{CL}(\theta_1) =& r_2 \sin\alpha \cos\left[\sin^{-1}\left(\frac{r_1}{r_2}\sin\theta_1\right)\right]\vec{i} \\ &+ r_2 \cos\alpha \cos\left[\theta_2 = \sin^{-1}\left(\frac{r_1}{r_2}\sin\theta_1\right)\right]\vec{j} \\ &- r_1 \sin\theta_1 \vec{k} \end{aligned} \tag{B-42}$$

For brace and chord on the right-hand-side, the normal vector can be derived similarly to Equation B-41, however, α must be change corresponding to the definition of the local coordinate system. For right-side chord and right-side brace, α should be $\frac{-2\pi}{3}$ rad. and $\frac{-5.17\pi}{1000}$ rad. respectively. The vectors normal to the weld toe and tangent to member surface, $\vec{\mathbf{n}}_{11}$, are:

$$\vec{\mathbf{n}}_{11}^{BL} = \vec{\mathbf{n}}_{22}^{L} \times \vec{\mathbf{n}}_{33}^{BL} \tag{B-43}$$

$$\vec{\mathbf{n}}_{11}^{CL} = -\vec{\mathbf{n}}_{22}^{L} \times \vec{\mathbf{n}}_{33}^{CL} \tag{B-44}$$

$$\vec{\mathbf{n}}_{11}^{BR} = -\vec{\mathbf{n}}_{22}^{R} \times \vec{\mathbf{n}}_{33}^{BR} \tag{B-45}$$

$$\vec{\mathbf{n}}_{11}^{CR} = \vec{\mathbf{n}}_{22}^{R} \times \vec{\mathbf{n}}_{33}^{CR} \tag{B-46}$$

Figure B-5 shows that the angle between the vector $\vec{\mathbf{n}}_{22}$, and $\vec{\mathbf{n}}_{33}$ are less than 1° which is very small and not affect the direction of the vector $\vec{\mathbf{n}}_{11}$. There for the two assumptions made in section 4.2.1 are valid. Figure B.7 shows that SCFs from detailed method and simplified method are comparable. Both methods are applicable in this study.

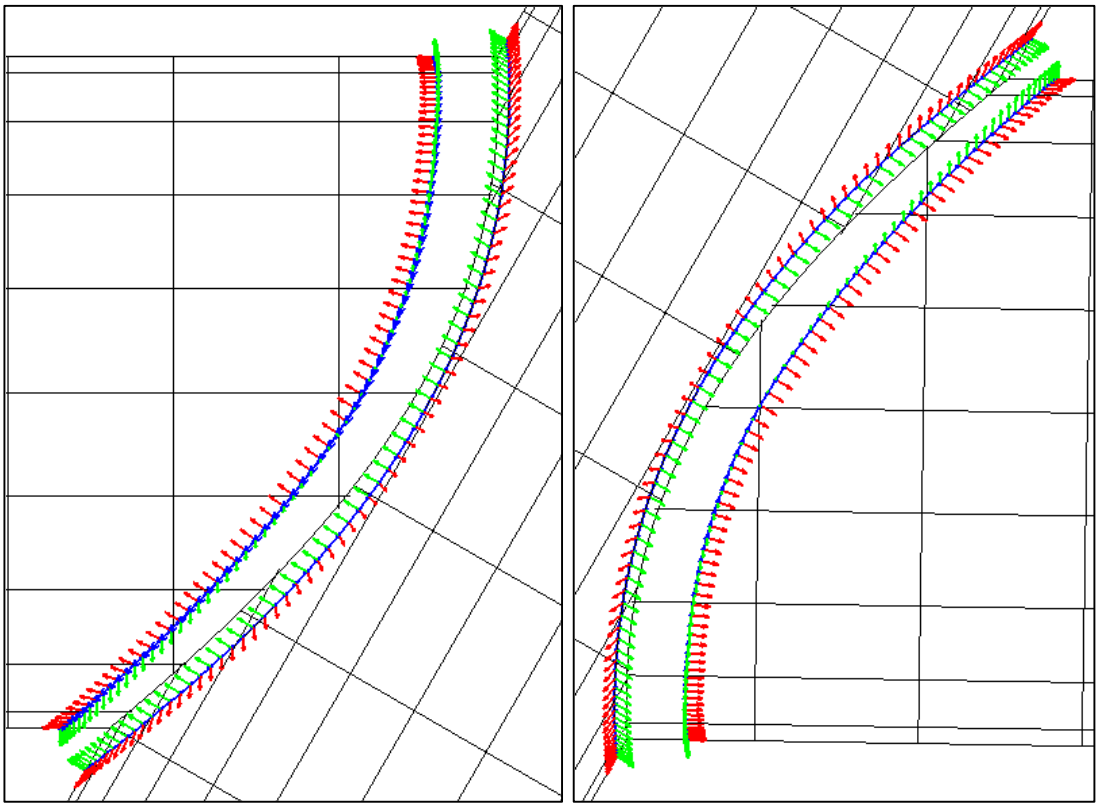

Figure B-5: Vector n_{11} (red), n_{22} (blue), n_{33} (green) of chord and brace members

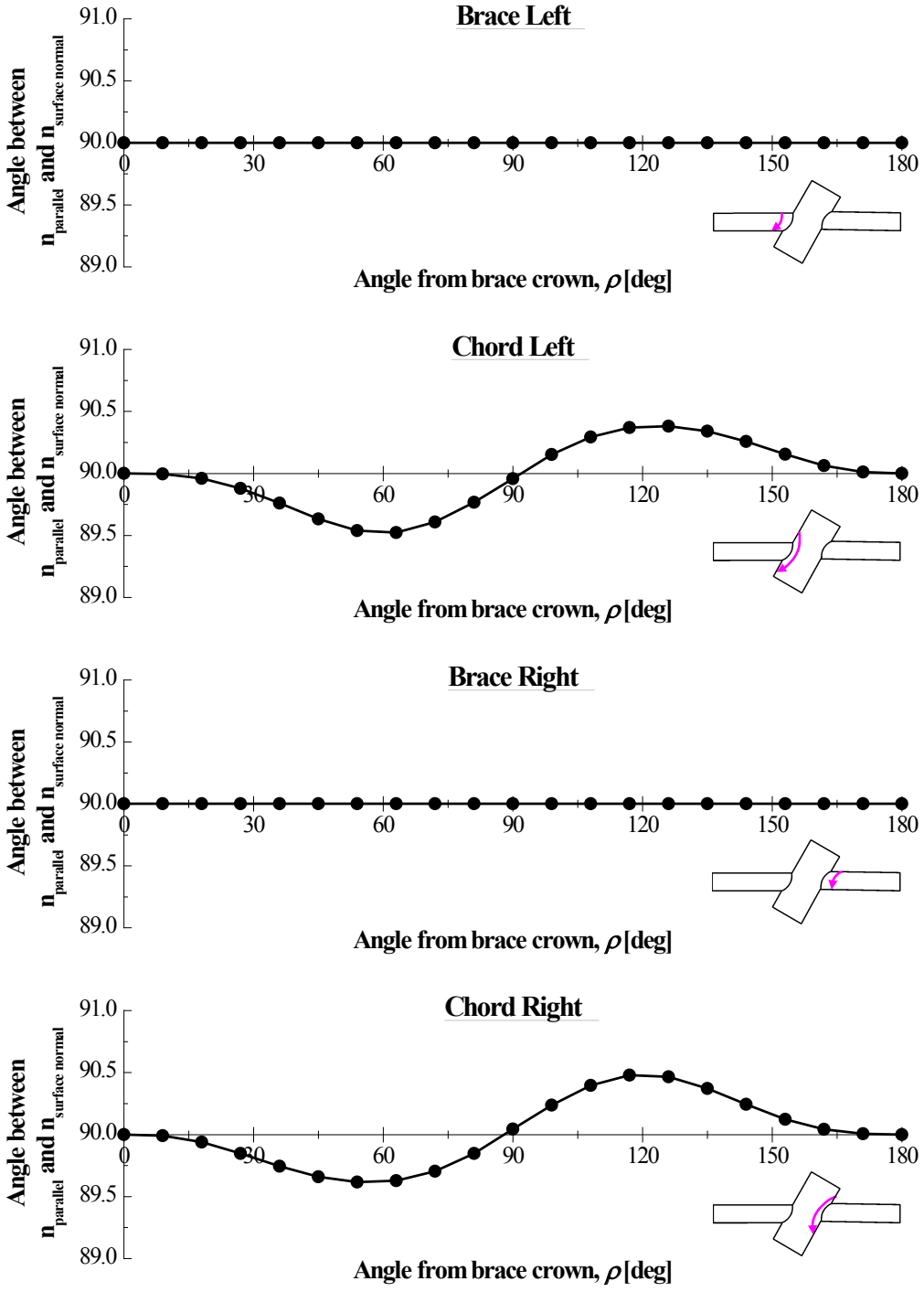

Figure B-6: Angle between n_{22} and n_{33}

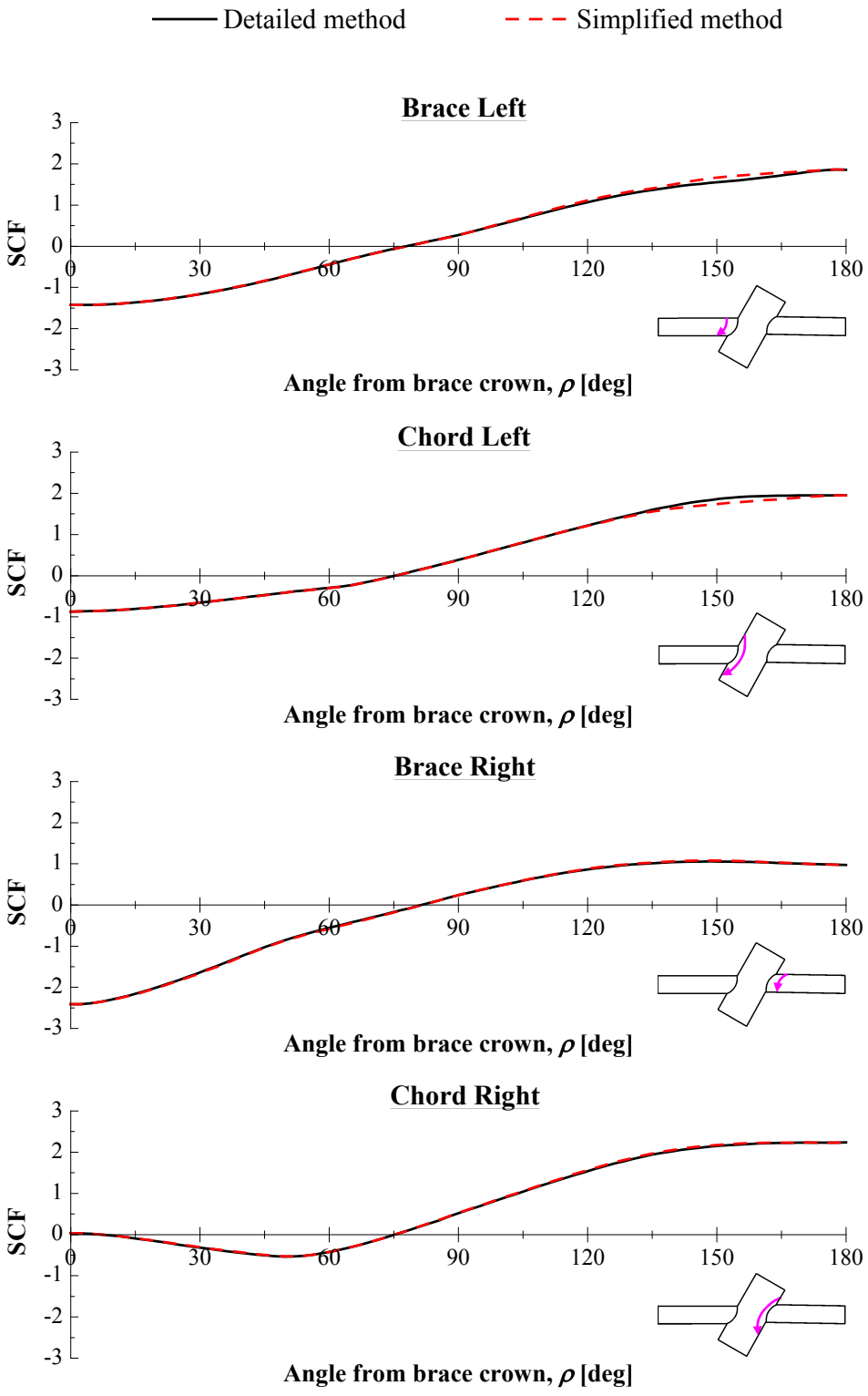

Figure B-7: Comparison of detailed method and simplified method